Handbook of
Thin Film
Technology

EDITED BY

LEON I. MAISSEL and REINHARD GLANG

International Business Machines Corporation
Components Division, East Fishkill Facility
Hopewell Junction, N.Y.

Chapter 1

Vacuum Evaporation

REINHARD GLANG

IBM Components Division, East Fishkill, New York

LIST OF SYMBOLS

a first coefficient in series expressions for heat capacity
a_B activity of constituent B in an alloy
A constant in molecular-distribution functions
A_w wall area upon which gas is impinging
A_e surface area from which evaporation takes place
A_r surface area receiving deposit
A_m effective cross-sectional area of an evaporation-rate monitor

α	plane angle
α_v	evaporation coefficient
α_c	condensation coefficient
α_T	thermal-energy accommodation coefficient
b	second coefficient in series expressions for heat capacity
β	plane angle
c	(1) third coefficient in series expressions for heat capacity; (2) speed of a gas atom or molecule
$\overline{c^2}$	mean-square speed
c_m	most probable speed $\Big\}$ in Maxwellian speed distributions
$\bar{c}$	arithmetic-average speed
c_t	propagation velocity of an elastic wave normal to the major surfaces of a thin quartz wafer
C_p	heat capacity at constant pressure
$\mathbf{C}_p$	molar heat capacity at constant pressure
C	conductance (gas-flow rate divided by pressure difference)
C_{visc}	conductance for viscous flow
C_{mol}	conductance for molecular flow
C_{trans}	conductance for transition flow
C_f	mass-determination sensitivity of resonating quartz-crystal wafer, Hz g^{-1} cm^2
d	film thickness
d_q	thickness of quartz wafer
d'	film-deposition rate, Å s^{-1}
D	diffusion coefficient
D'	ionization-rate monitor gauge constant
E_k	kinetic energy
E_v	evaporation energy
η	viscosity coefficient of gases
f	statistical factor in gas-viscosity equation
f_B	activity coefficient of constituent B in an alloy
f_0	resonance frequency of a quartz-crystal wafer
Δf	change of f_0 due to accumulated mass
F	force
φ	angle of vapor emission
g	gravitational constant
G	weight of deposit, g wt
G	Gibbs' free energy
$\Delta_e \mathbf{G}^\circ$	standard free energy of evaporation
$\Delta_d \mathbf{G}$	molar free energy of decomposition
Γ	mass-evaporation rate, g cm^{-2} s^{-1}
h	height, normal source-to-substrate distance
H	enthalpy or heat content at constant pressure
$\mathbf{H}$	molar enthalpy
$\Delta_e \mathbf{H}$	molar heat of evaporation
$\Delta_e \mathbf{H}^\circ$	standard heat of evaporation
$\Delta_e \mathbf{H}^*$	molar heat of evaporation at 0°K
I	electron current
I_e	electron-emission current
I_i	ion current
k	Boltzmann's constant
K	(1) material specific factor in the evaporation equation of binary alloys; (2) torsional constant for impingement-rate monitors; (3) deposit-distribution factor (≈ 1) in quartz-crystal oscillators
$K_p(T)$	temperature-dependent thermodynamic constant for equilibria involving gaseous constituents
l	lengths, distances
λ	(1) mean free path of gas particles; (2) wavelength of light
m	mass of an atom or molecule

M	molar mass (N_A molecules)
$\mathfrak{M}_e$	mass of material evaporated from an area A_e
$\mathfrak{M}_r$	mass of deposit received by an area A_r
$\mathfrak{u}$	chemical potential
$\mathfrak{u}°$	standard chemical potential (at 1 atm)
n	number of moles of material
n_f	refractive index of film material
N	(1) number of gas particles; (2) frequency constant of AT cut quartz wafers
N_A	Avogadro's number
N_i	number of gas particles impinging on a surface
N_u	number of gas particles having the velocity component u in the x direction
N_c	number of gas particles having the speed c in any direction
N_e	number of gas particles evaporating from a surface
N_m	number of gas particles arriving at a rate-monitor device
ν	oscillation frequency of surface atoms
ω	(1) solid angle; (2) angular velocity
p	gas pressure
p^*	thermodynamic equilibrium pressure
p_B	partial pressure of constituent B in a gas mixture
p_r	evaporation pressure at the substrate surface (or at distance r from source)
P	probability of evaporation
π	3.14159
Q	macroscopic flow rate of gases, torr l s^{-1}
Q_v	kinetic-energy partition function for a vapor phase
Q_c	kinetic-energy partition function for a condensed phase
Q_R^*	rotational-energy partition function for activated molecules in the liquid state
Q_{R_v}	rotational-energy partition function for molecules in the vapor state
r	direct distance between a small vapor source and a receiving point (substrate)
R	universal gas constant
R	resistance, ohms
R_s	sheet resistance, ohms/sq
ρ	(1) resistivity, ohm-cm; (2) density of film material
ρ_q	density of crystalline quartz
s	(1) radius of a thin-ring source; (2) radius of the receiving cylinder in impingement-rate monitors
S	entropy at constant pressure
$\mathbf{S}$	molar entropy at constant pressure
$\Delta_e \mathbf{S}°$	standard entropy of evaporation
S_0	dynamic sensitivity of ionization-rate monitor gauges
σ	(1) diameter of gas atoms or molecules; (2) mass per unit wall area in impingement-rate monitors
t	time
T	temperature, °K
τ	time constant
θ	(1) angle of vapor or light incidence; (2) surface coverage of metal films with oxygen, whereby $\theta = 1$ corresponds to formation of stoichiometric oxide
u	velocity component of gas particle in the x direction
v	(1) velocity component of gas particle in the y direction; (2) rate, cm s^{-1}, at which an evaporating solid surface recedes from its original position
V	(1) volume; (2) voltage
$\mathbf{V}$	molar volume
w	(1) velocity component of gas particle in the z direction; (2) lateral dimension, width
x	axis in an orthogonal coordinate system
x_B	mole fraction of constituent B in an alloy
y	axis in an orthogonal coordinate system
z	(1) axis in an orthogonal coordinate system; (2) number of nearest surface sites in the adsorption of oxygen on metal films
Z	numerical factor characterizing transition flow of gases

1. INTRODUCTION

The first evaporated thin films were probably the deposits which Faraday[1] obtained in 1857 when he exploded metal wires in an inert atmosphere. Further experimentation in the nineteenth century was stimulated by interest in the optical phenomena associated with thin layers of materials and by investigations of the kinetics and diffusion of gases. The possibility of depositing thin metal films in a vacuum by Joule heating of platinum wires was discovered in 1887 by Nahrwold[2] and a year later adapted by Kundt[3] for the purpose of measuring refractive indices of metal films. In the following decades, evaporated thin films remained in the domain of academic interest until the development of vacuum equipment had progressed far enough to permit large-scale applications and control of film properties. During the last 25 years, evaporated films have found industrial usage for an increasing number of purposes. Examples are antireflection coatings, front-surface mirrors, interference filters, sunglasses, decorative coatings on plastics and textiles, in the manufacture of cathode-ray tubes, and most recently in electronic circuits, the topic of prime interest in this book.

Although commonly referred to as a single process, the deposition of thin films by vacuum evaporation consists of several distinguishable steps:

1. Transition of a condensed phase, which may be solid or liquid, into the gaseous state

2. Vapor traversing the space between the evaporation source and the substrate at reduced gas pressure

3. Condensation of the vapor upon arrival on the substrates

Accordingly, the theory of vacuum evaporation includes the thermodynamics of phase transitions from which the equilibrium vapor pressure of materials can be derived, as well as the kinetic theory of gases which provides models of the atomistic processes. Further investigations of the sometimes complex events occurring in the exchange of single molecules between a condensed phase and its vapor led to the theory of evaporation, a specialized extension of the kinetic theory. From this basis, the distribution of deposits on surfaces surrounding a vapor source can be derived. The kinetic aspects of condensation processes are a topic in their own right and are therefore treated separately in Chap. 8, which is devoted to nucleation and growth phenomena.

Experimentally, vacuum evaporation and its applications have benefited from various disciplines which have contributed toward solutions of practical problems. These pertain to the construction of suitable vapor sources, the development of special techniques for the evaporation of alloys, compounds, and mixtures, and to questions of process control and automation. Finally, thin film deposition requires a properly evacuated chamber; however, vacuum technology is such a complex topic that it is treated separately in Chap. 2.

2. THERMODYNAMIC AND KINETIC FOUNDATIONS

The transition of solids or liquids into the gaseous state may be treated as a macroscopic or as an atomistic phenomenon. The former approach is based on thermodynamics and yields a quantitative understanding of evaporation rates, interactions between evaporants and their containers, stability of compounds, and compositional changes encountered during the evaporation of alloys. The atomistic approach is derived from the kinetic theory of gases and provides models which describe evaporation processes in terms of properties of individual particles. The latter theory also applies to the evacuation of vessels and thus relates to Chap. 2. Although thermodynamic and kinetic theories are treated in various textbooks, aspects pertinent to vacuum evaporation will be reviewed, and some of the widely used equations will be introduced.

a. The Equilibrium Vapor Pressure of Materials

In thermodynamics, the condensed and the gaseous states of materials are characterized by functions which depend on the macroscopic variables of pressure, temperature,

volume, and mass. Of particular significance is the thermodynamic equilibrium, a situation where two states, for instance, a condensed phase and its vapor, exist at the same temperature and in contact with each other without undergoing net changes. This means that the amounts of evaporating and condensing material are equal at all times as long as the equilibrium is maintained. Under these conditions, solids and liquids have characteristic vapor pressures which are unique functions of temperature.

At first sight the equilibrium vapor pressure may appear unrelated to vacuum evaporation since the latter is not an equilibrium process but involves transfer of material from one state to the other. However, atomic theory and extensive experiments have shown that evaporation rates cannot exceed an upper limit which is proportional to the equilibrium vapor pressure. Therefore, the saturation pressure of a vapor over its condensed phase is an important quantity to assess the amenability of a substance to evaporation and the temperatures required to achieve practical transfer rates.

The transformation of a condensed phase into vapor involves the conversion of thermal energy supplied to the evaporant into mechanical energy as represented by the expansion into vapor. According to the second law of thermodynamics, the conversion efficiency of thermal energy is limited because a fraction of it must serve to increase the entropy of the system and is not available for the production of mechanical energy. The conversion takes place with the greatest efficiency if the system changes reversibly.[4] Depending on the macroscopic variables under consideration, there are several ways to express the energy balance of such reversible phase transitions. The most commonly used form is

$$\Delta G = \Delta H - T \, \Delta S \tag{1}$$

where ΔG, ΔH, and ΔS are the changes in Gibbs' free energy G, in enthalpy H, and entropy S associated with the process. Equation (1) leads to simple thermodynamic relationships if the pressure p and the temperature T are treated as independent macroscopic variables; the volume V is thereby defined as a dependent quantity. The characteristic functions occurring in Eq. (1) are extensive properties, and hence the amount of substance involved is an additional variable.

For practical applications, it is necessary to know the dependence of the thermodynamic functions on the macroscopic variables which can be measured. These relationships are obtained by considering a closed system undergoing an infinitesimal change at equilibrium which leads to the following fundamental and often used partial derivatives:[4]

$$\frac{\partial G}{\partial T} = -S \qquad (p = \text{const}) \tag{2}$$

$$\frac{\partial G}{\partial p} = V \qquad (T = \text{const}) \tag{3}$$

V is the volume of the substance in the closed system. The total differential of the free energy is accordingly

$$dG = -S \, dT + V \, dp \tag{4}$$

The temperature dependences of the enthalpy and the entropy at constant pressure are defined by the partial differential equations

$$\frac{\partial H}{\partial T} = C_p \tag{5a}$$

and

$$\frac{\partial S}{\partial T} = \frac{C_p}{T} \tag{5b}$$

where C_p is the heat capacity of the system at constant pressure.

Per definition, the free-energy change ΔG is obtained only with reversible processes occurring at the thermodynamic equilibrium between the two states. An actual

process conducted under such conditions would be infinitely slow and is therefore hypothetical. The importance of ΔG lies in the fact that it constitutes a quantitative measure for the driving force associated with a possible system change from one state to another. Knowledge of ΔG thus makes it possible to determine the stability of one state relative to another. If there is no driving force between two states, they can coexist without change and therefore are at equilibrium. Consequently, the particular values which the macroscopic variables assume under equilibrium conditions can be derived by stipulating $\Delta G = 0$. In the case of a pure condensed phase in contact with its own vapor, the resulting relationship defines the equilibrium pressure of a material as a function of temperature.

For systems containing more than one phase or several substances, it is practical to consider the free energy of each component separately. This is done by introducing the chemical potential $\mathbf{\mu}$, which has the same significance and variables as G but refers to 1 g mol of material in a particular state. In regard to the vapor-solid or vapor-liquid equilibrium containing only a single substance, the relations established for G are also valid for $\mathbf{\mu}$ without any modification other than designating the extensive properties as molar quantities. This will be done by using the notations $\mathbf{H}$, $\mathbf{S}$, $\mathbf{V}$, and $\mathbf{C}_p$.

(1) Clausius-Clapeyron's Equation The vapor-solid or vapor-liquid equilibrium can be defined as an equality of the chemical potentials

$$\mathbf{\mu}_c = \mathbf{\mu}_g \tag{6}$$

whereby the subscripts c and g identify quantities associated with the condensed and gaseous states, respectively. Equation (6) also holds in differential form,

$$d\mathbf{\mu}_c = d\mathbf{\mu}_g \tag{7}$$

because these increments refer to changes from one equilibrium point to another. Substitution of the total differentials according to Eq. (4) into Eq. (7) yields

$$\frac{dp^*}{dT} = \frac{\mathbf{S}_g - \mathbf{S}_c}{\mathbf{V}_g - \mathbf{V}_c} \tag{8}$$

where dp^* is the change in equilibrium pressure resulting from the small temperature change dT. The symbol p^* has been introduced to denote that the pressure defined by Eq. (8) is no longer a variable to be chosen at liberty.

Equation (6) can also be expressed in terms of the enthalpy and entropy functions,

$$\mathbf{H}_c - T\mathbf{S}_c = \mathbf{H}_g - T\mathbf{S}_g$$

which may be substituted into Eq. (8) to yield Clausius-Clapeyron's equation:

$$\frac{dp^*}{dT} = \frac{\mathbf{H}_g - \mathbf{H}_c}{T(\mathbf{V}_g - \mathbf{V}_c)} \tag{9}$$

To solve Eq. (9), two approximations are made. The molar volume of the condensed phase is neglected since it is very small compared with the molar volume of the vapor. Furthermore, the vapor is assumed to obey the ideal-gas law, thereby neglecting deviations due to van der Waals forces between gaseous particles:

$$\mathbf{V}_g - \mathbf{V}_c \simeq \mathbf{V}_g = \frac{\mathbf{R}T}{p}$$

The difference of the enthalpies in Eq. (9) is the molar heat of evaporation,

$$\mathbf{H}_g - \mathbf{H}_c = \Delta_e\mathbf{H}$$

With these modifications, Eq. (9) transforms into

$$\frac{dp^*}{p^*} = \frac{\Delta_e\mathbf{H}\,dT}{\mathbf{R}T^2} \tag{10}$$

As a first approximation, the heat of evaporation may be assumed to be constant so that Eq. (10) can be integrated:

$$\ln p^* \simeq -\frac{\Delta_e H}{R T} + \text{const} \tag{11}$$

Equation (11) holds only for small temperature intervals. A more accurate vapor-pressure function is obtained by considering the temperature dependence of the molar heat of evaporation. The latter is determined by changes which the molar specific heats in both states undergo with temperature:

$$\frac{d(\Delta_e H)}{d T} = C_{p,g} - C_{p,c} = \Delta C_p \tag{12}$$

Near and above room temperature, the specific heats may be expressed in the general form $C_p = a + bT + cT^{-2}$, where the coefficients a, b, and c are numerical factors specific for a particular substance. Insertion of the C_p functions into Eq. (12) and subsequent integration give the heat of vaporization as a function of temperature:

$$\Delta_e H = \Delta_e H^* + \Delta a\, T + \frac{\Delta b}{2}\, T^2 - \Delta c\, T^{-1} \tag{13}$$

where $\Delta_e H^*$ is an integration constant which must be determined experimentally. Further substitution of Eq. (13) into Eq. (10) and integration of the latter yield

$$\ln p^* = -\frac{\Delta_e H^*}{R T} + \frac{\Delta a}{R} \ln T + \frac{\Delta b}{2R}\, T + \frac{\Delta c}{2R}\, T^{-2} + I \tag{14}$$

I is another constant of integration which is specific for a given material.

Theoretically, Eq. (14) permits the calculation of vapor pressures from fundamental material constants. However, the constants $\Delta_e H^*$ and I cannot be derived from first principles. Instead they are commonly calculated from vapor pressures which have been either measured by one of several experimental methods[5,6] or computed from spectroscopically determined energy levels.[7] The compilations of thermochemical data rarely list these constants. Therefore, an expression equivalent to Eq. (14) but containing only standard thermochemical data is desirable to calculate vapor pressures for different temperatures.

(2) Calculation of Vapor Pressures from Standard Thermochemical Data Numerical values of thermodynamic functions are commonly listed for the standard state, and the symbols referring to it are identified by adding the superscript °. The standard state is represented by 1 g mol of material at 1 atm of pressure and 298°K.[8] Thus, $\mu_g°(T)$ and $\mu_g°(T)$ are the chemical potentials of a pure substance at the temperature T and 1 atm in the condensed and in the gaseous states. Equilibrium between the two states can be established hypothetically in van't Hoff's equilibrium box by expanding (or compressing) both phases isothermally and reversibly. In this operation, the two chemical potentials change until they become equal at the equilibrium pressure p^*:

$$\mu_g°(T) + \int_1^{p^*} \left(\frac{\partial \mu_g}{\partial p}\right)_T dp = \mu_c°(T) + \int_1^{p^*} \left(\frac{\partial \mu_c}{\partial p}\right)_T dp \tag{15}$$

The effect of pressure on the chemical potential of the condensed phase is again neglected, and partial differentiation of $\mu_g°$ yields the molar volume according to Eq. (3)

$$\left(\frac{\partial \mu_g}{\partial p}\right)_T = V = \frac{R T}{p}$$

Integration of Eq. (15) leads to the equilibrium condition

$$\mu_g°(T) + R T \ln p^* = \mu_c°(T)$$

Introducing $\mu_g°(T) - \mu_c°(T) = \Delta_e G°(T)$, the standard free energy of evaporation, the vapor pressure becomes

$$\log p^* = -\frac{\Delta_e G°(T)}{RT} \log e \tag{16}$$

Thus, the equilibrium pressure (in atmospheres) can be calculated for any temperature at which the free energy of evaporation is known, if the latter is divided by $4.575T$ cal mol^{-1}. Conversion into torr is easily possible according to

$$\log p^* \text{ (torr)} = \log p^* \text{(atm)} + \log 760$$

Since $\Delta_e G°$ is often listed only for the reference state at 298°K, it is useful to know the temperature dependence of Eq. (16). Starting with

$$\Delta_e G°(T) = \Delta_e G°(298) + \int_{298}^{T} \left(\frac{\partial \Delta_e G°}{\partial T}\right)_p dT$$

and substituting the standard entropy of evaporation according to Eq. (2)

$$\left(\frac{\partial \Delta_e G°}{\partial T}\right)_p = -\Delta_e S°(T)$$

whereby the temperature dependence of the entropy follows from Eq. (5b)

$$\Delta_e S°(T) = \Delta_e S°(298) + \int_{298}^{T} \frac{\Delta C_p}{T} dT$$

one obtains

$$\Delta_e G°(T) = \Delta_e G°(298) - \int_{298}^{T} \left[\Delta_e S°(298) + \int_{298}^{T} \frac{\Delta C_p}{T} dT\right] dT$$

Further substitution of the standard enthalpy and entropy for $\Delta_e G°(298)$ according to Eq. (1) and solving the first integral term yield

$$\Delta_e G°(T) = \Delta_e H°(298) - T \Delta_e S°(298) - \iint_{298}^{T} \frac{\Delta C_p}{T} dT^2$$

Insertion of this expression for the temperature dependence of the standard free energy into Eq. (16) leads to

$$\log p^* = -\frac{\Delta_e H°(298)}{4.575T} + \frac{\Delta_e S(298)}{4.575} + \frac{1}{4.575T} \iint_{298}^{T} \frac{\Delta C_p}{T} dT^2 \tag{17}$$

In contrast to the former Eq. (14), this expression relates the vapor pressure to the standard enthalpy and entropy, the quantities which are most commonly given in thermodynamic tables.[9-15] If these data are not available either, it is often possible to estimate their approximate values by methods as discussed, for instance, by Kubaschewski.[6]

The complete solution of Eq. (17) depends on the form of the specific-heat term. A first-order approximation is obtained by neglecting specific-heat changes and assuming $\Delta C_p = 0$. More accurate values result if a constant average of $\overline{\Delta C_p} = \Delta a$ is applied over the entire interval from 298 to $T°$K. The integral term is then given by

$$\Delta a \iint_{298}^{T} \frac{dT^2}{T} = \Delta a T \left(\ln \frac{T}{298} + \frac{298}{T} - 1\right) = \Delta a Tf\left(\frac{T}{298}\right)$$

and can be evaluated by means of Table 1.

TABLE 1   Numerical Values of the Function $Tf\left(\dfrac{T}{298}\right)^{16}$

T, °K	$Tf\left(\dfrac{T}{298}\right)$	T, °K	$Tf\left(\dfrac{T}{298}\right)$
400	15.7	1400	1063
500	56.6	1500	1222
600	118	1600	1386
700	195	1700	1558
800	288	1800	1734
900	392	1900	1917
1000	508	2000	2105
1100	634	2500	3115
1200	769	3000	4224
1300	912	3500	5418

If the specific-heat functions are given as series for both the gaseous and the condensed state, the temperature dependence of the heat-capacity change may be considered,

$$\Delta C_p \doteq \Delta a + \Delta b\,T + \Delta c\,T^{-2}$$

and consequently the following terms occur:

$$\frac{1}{T}\int\limits_{298}^{T}\!\!\int \frac{\Delta C_p}{T}\,dT^2 = \Delta a\,f\left(\frac{T}{298}\right) + \frac{\Delta b}{2}\,T\left(1 - \frac{298}{T}\right)^2 + \frac{\Delta c}{2}\left(\frac{1}{T} - \frac{1}{298}\right)^2 \tag{18}$$

Equation (18) can be solved and terms with equal powers of T combined with the standard enthalpy and entropy terms in Eq. (17). This operation leads to vapor-pressure expressions of the form

$$\log p^* \text{ (torr)} = A T^{-1} + B + C\log T + DT + ET^{-2} \tag{19}$$

The contributions of the first-, second-, and third-order specific-heat terms to the coefficients in Eq. (19) are as follows:

$$A = -\;\frac{\Delta_e H°(298) - 298(\Delta a + 149\,\Delta b) + 3.35 \times 10^{-3}\,\Delta c}{4.575}$$

$$B = \frac{\Delta_e S°(298) - 6.70\,\Delta a - 298\,\Delta b + 5.6 \times 10^{-6}\,\Delta c}{4.575} + 2.8808 \tag{20}$$

$$C = \frac{\Delta a}{1.987} \qquad D = \frac{0.5\,\Delta b}{4.575} \qquad E = \frac{0.5\,\Delta c}{4.575}$$

Vapor-pressure data are often given in the form of Eq. (19). The coefficients C and D are considered only if the specific heats are known with sufficient accuracy and confidence in the standard enthalpy and entropy values merit refined calculations. There are few cases where the latter conditions warrant the use of the coefficient E.

(3) Vapor-pressure Data   The vapor pressures of all common elements have been determined, usually by several authors independently. Temperatures producing vapor pressures sufficiently high for practical evaporation rates range from about 600°C on up. With increasing temperatures, vapor-pressure measurements are more and more subject to experimental problems such as errors in the evaporation temperature, excessive residual gas pressure, and reaction of the condensed evaporant phase with the container. Consequently, the accuracy of vapor-pressure data is limited, and numerical values vary from author to author. A judicious choice is therefore necessary, particularly if the data are relatively old. To illustrate the situation, the

vapor pressure of liquid aluminum will be examined. Figure 1 shows experimental points which Nesmeyanov[5] selected from several investigations as being the most reliable. Based on these data, he derived the equation

$$\log p^* \text{ (torr)} = -15{,}993 T^{-1} + 12.409 - 0.999 \log T - 3.52 \times 10^{-6} T$$

which is also shown in Fig. 1. Kelley[17] gives the free energy of evaporation for liquid aluminum as

$$\Delta_e G^\circ(T) = 65{,}680 - 43.72 T + 4.61 \log T$$

from which the vapor pressure can be derived according to Eq. (16). Kubaschewski's[6] vapor-pressure equation

$$\log p^* \text{ (torr)} = -16{,}450 T^{-1} + 12.36 - 1.023 \log T$$
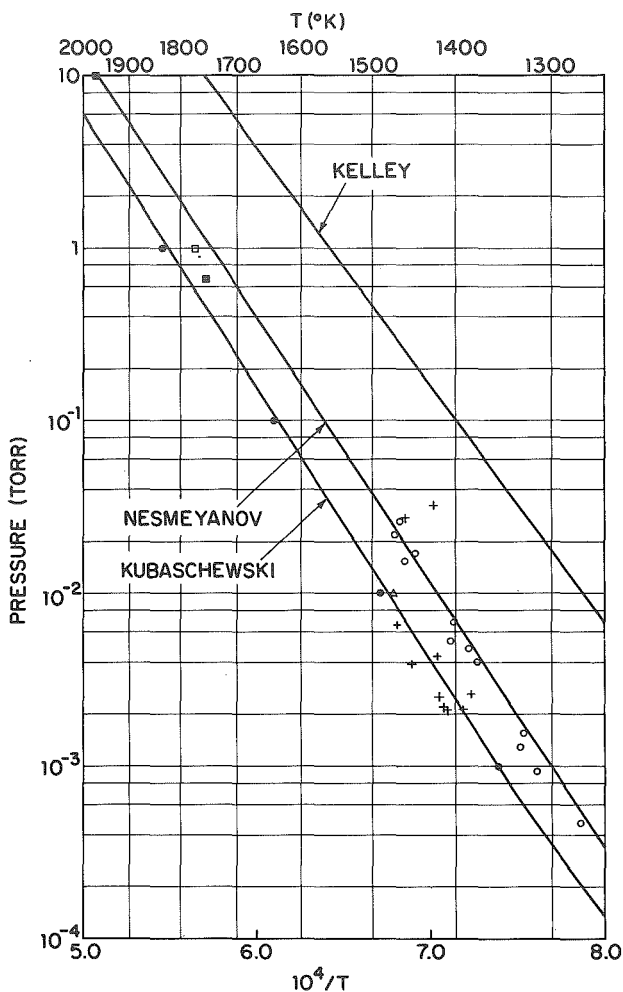
Fig. 1 Vapor pressure of liquid aluminum as measured by various authors (symbols), according to different vapor-pressure equations (lines), and tabulated by Honig (full circles).

is based on data[18] not included in Nesmeyanov's[5] review. As Fig. 1 shows, the discrepancies are substantial even if the older values of Kelley are disregarded. The values used by Honig[19] (full circles in Fig. 1) agree closely with Kubaschewski's curve.

The three vapor-pressure equations reflect different standard enthalpies and entropies, which have been evaluated according to Eqs. (20) and are listed below.

	$\Delta_e H°$ (298), kcal mol^{-1}	$\Delta_e S°$ (298), Cl mol^{-1}	ΔC_p, cal mol^{-1} deg^{-1}
Nesmeyanov[5]............	72.58	30.28	$-1.99 - 3.2 \times 10^{-5}\, T$
Kelley[17]................	65.08	30.32	-2.0
Kubaschewski[6].........	74.65	29.77	-2.03

The specific heat for liquid aluminum is 7.00 cal mol^{-1} deg^{-1} while that of aluminum vapor is known more accurately: $C_p = 4.97 + 1.2 \times 10^4 T^{-2}$ cal mol^{-1} deg^{-1}.[11] However, it would be pointless to consider the third-order C_p term in view of the uncertainty in the enthalpy value. The latter problem is illustrated in Fig. 2, which shows
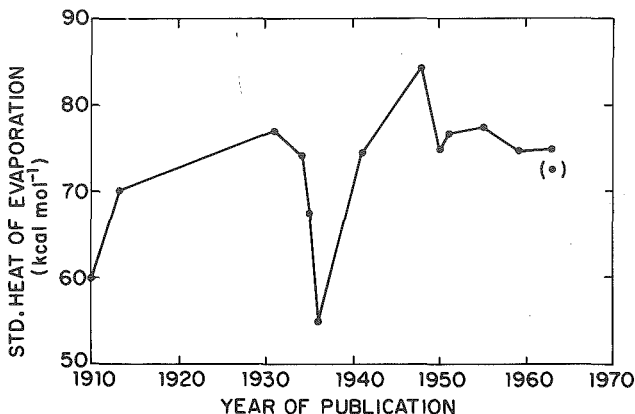
Fig. 2 Standard heat of evaporation of liquid aluminum as calculated by Nesmeyanov[5] from reported vapor-pressure data.

standard enthalpies calculated by Nesmeyanov[5] from vapor-pressure measurements of different authors in historical sequence. The more recent values converge at about 75 kcal mol^{-1}, and therefore, the vapor pressures given by Kubaschewski[6] and Honig[19] seem to be the most reliable ones. The enthalpy obtained from Nesmeyanov's vapor-pressure equation (parenthetical dot in Fig. 2) is at variance with this conclusion, although he, too, lists 75 kcal mol^{-1} as the most probable value (see Ref. 5, p. 433).

The vapor pressures of other metals are often affiliated with uncertainties similar to those demonstrated for aluminum. Data compilations in the form of tables or coefficients for Eq. (19) have been published by various authors.[5,6,17,20,21] The widely used vapor-pressure charts by Honig[19] allow a quick assessment of pressures to be expected at a given temperature; his numerical values are reproduced in Table 2 and generally preferred in this chapter.

b. The Kinetic Theory of Gases

The atomistic model of the evaporation process is based on the kinetic theory, which treats gases as an assembly of a large number of atoms or molecules of identical mass m

and size. For many applications, the shape and the structure of these particles may be ignored and the molecules can be considered as elastic spheres with diameters very small compared with their average distance of separation. Furthermore, the gas molecules are assumed to be in a constant state of random motion, colliding with one another and with the walls of the vessel containing them. In analogy to the ideal-gas equation describing the macroscopic behavior of gases, no allowance is made for forces between molecules except at the moment of collision. According to this model, the pressure exerted by a gas on its confining vessel results from the momentums which individual molecules impart when they strike the walls.

(1) Atomistic Concept of Gas Pressure and Temperature   The relationships between the macroscopic gas pressure and the translational energy of individual molecules can be derived in several more or less rigorous ways.[22,23] The particle speed c is thereby thought to have three velocity components u, v, w perpendicular to each other. As the speeds vary among the different particles, mean-square velocities

$$\overline{u^2} = \frac{\Sigma u^2}{N} \tag{21}$$

and mean-square speeds

$$\overline{c^2} = \frac{\Sigma c^2}{N} = \overline{u^2} + \overline{v^2} + \overline{w^2} \tag{22}$$

are defined to represent the state of all molecules N in the enclosure. It can be shown by theoretical arguments[22,23] that the molecules having velocities u exert the pressure

$$p = \frac{N}{V} m\overline{u^2} \tag{23}$$

on a wall perpendicular to the direction of u.

The velocities in different directions are assumed to be uniformly distributed, $\overline{u^2} = \overline{v^2} = \overline{w^2}$, and therefore

$$\overline{u^2} = \tfrac{1}{3}\overline{c^2} \tag{24}$$

Substitution of Eq. (24) into Eq. (23) yields the gas pressure as the force which the impinging molecules exert upon the walls:

$$p = \frac{1}{3}\frac{N}{V} m\overline{c^2} \tag{25}$$

The temperature of the gas is introduced by comparing Eq. (25) with the universal-gas equation $p = n\mathbf{R}T/V$, where n is the number of gram moles of gas. According to Avogadro's law, the number of molecules per gram mole $\mathbf{N}_A$ is a constant for all substances. Consequently, the total number of molecules N in a volume containing n moles of gas is $n\mathbf{N}_A$, and therefore

$$p = \frac{N}{V}\frac{\mathbf{R}}{\mathbf{N}_A} T = \frac{N}{V} kT \tag{26}$$

where k is the Boltzmann constant.[4]

From Eq. (26), the number of molecules per cubic centimeter at various pressures and temperatures can be calculated. It is often referred to as Loschmidt's number, and for pressures given in torr the relationship is

$$\frac{N}{V} = 9.656 \times 10^{18} \frac{p}{T} \qquad \text{cm}^{-3}$$

The two expressions for the pressure [Eqs. (25) and (26)] establish the identity

$$\tfrac{1}{3}m\overline{c^2} = kT$$

or, after multiplication with $\tfrac{3}{2}$,

$$\tfrac{1}{2}mc^2 = \tfrac{3}{2}kT \tag{27}$$

TABLE 2   Vapor-pressure Data for the Solid and Liquid Elements*

Symbol	Element	Data temp range, °K	Temperatures (°K) for vapor pressures, torr														
			10^{-11}	10^{-10}	10^{-9}	10^{-8}	10^{-7}	10^{-6}	10^{-5}	10^{-4}	10^{-3}	10^{-2}	10^{-1}	1	10^{1}	10^{2}	10^{3}
Ac	Actinium	1873, est.	1045	1100	1160	1230	1305 ⊙	1390	1490	1605	1740	1905	2100	2350	2660	3030	3510
Ag	Silver	958–2200	721	759	800	847	899	958	1025	1105	1195 ⊙	1300	1435	1605	1815	2100	2490
Al	Aluminum	1220–1468	815	860	906 ⊙	958	1015	1085	1160	1245	1355	1490	1640	1830	2050	2370	2800
Am	Americium	1103–1453	712	752	797	848	905	971	1050 ⊙	1140	1245	1375	1540	1745	2020	2400	2970
As₄	Arsenic(s)		323	340	358	377	400	423	447	477	510	550	590	645	712	795	900
At₂	Astatine	Est.	221	231	241	252	265	280	296	316	338	364	398	434	480	540 ⊙	620
Au	Gold	1073–1847	915	964	1020	1080	1150	1220	1305 ⊙	1405	1525	1670	1840	2040	2320	2680	3130
B	Boron	1781–2413	1335	1405	1480	1555	1640	1740	1855	1980	2140	2300 ⊙	2520	2780	3100	3500	4000
Ba	Barium	1333–1419	450	480	510	545	583	627	675	735	800	883 ⊙	984	1125	1310	1570	1930
Be	Beryllium	1103–1552	832	878	925	980	1035	1105	1180	1270	1370	1500 ⊙	1650	1830	2080	2390	2810
ΣBi	Bismuth		510	540 ⊙	568	602	640	682	732	790	860	945	1050	1170	1350	1570	1900
ΣC	Carbon(s)	1820–2700	1695	1765	1845	1930	2030	2140	2260	2410	2560	2730	2930	3170	3450	3780	4190
Ca	Calcium	730–1546	470	495	524	555	590	630	678	732	795	870	962	1075 ⊙	1250	1475	1800
Cd	Cadmium	411–1040	293	310	328	347	368	392	419	450	490	538	593 ⊙	665	762	885	1060
Ce	Cerium	1611–2038	1050 ⊙	1110	1175	1245	1325	1420	1525	1650	1795	1970	2180	2440	2780	3220	3830
Co	Cobalt	1363–1522	1020	1070	1130	1195	1265	1340	1430	1530	1655 ⊙	1790	1960	2180	2440	2790	3220
Cr	Chromium	1273–1557	960	1010	1055	1110 °	1175	1250	1335	1430 °	1540	1670	1825	2010 ⊙	2240	2550	3000
ΣCs	Cesium	300–955	213	226	241	257	274	297 ⊙	322	351	387	428	482	553	643	775	980
Cu	Copper	1143–1897	855	895	945	995	1060	1125	1210	1300 ⊙	1405	1530	1690	1890	2140	2460	2920
Dy	Dysprosium	1258–1773	760	801	847	898	955	1020	1090	1170	1270	1390	1535 ⊙	1710	1965	2300	2780
Er	Erbium	1773, est.	779	822	869	922	981	1050	1125	1220	1325	1450	1605 ⊙	1800	2060	2420	2920
Eu	Europium	696–900	469	495	523	556	592	634	682	739	805	884	981 ⊙	1100	1260	1500	1800
Fr	Francium	Est.	198	210	225	242	260	280 ⊙	306	334	368	410	462	528	620	760	980
Fe	Iron	1356–1889	1000	1050	1105	1165	1230	1305	1400	1500	1615	1750 ⊙	1920	2130	2390	2740	3200
Ga	Gallium(l)	1179–1383	755	796	841	892	950	1015	1090	1180	1280	1405	1555	1745	1980	2300	2730
Gd	Gadolinium	Est.	880	930	980	1035	1100	1170	1250	1350	1465 ⊙	1600	1760	1955	2220	2580	3100
ΣGe	Germanium	1510–1885	940	980	1030	1085	1150 ⊙	1220	1310	1410	1530	1670	1830	2050	2320	2680	3180
Hf	Hafnium	2035–2277	1505	1580	1665	1760	1865	1980	2120	2270 ⊙	2450	2670	2930	3240	3630	4130	4780
Hg	Mercury	193–575	170	180	190	201	214	229 ⊙	246	266	289	319	353	398	458	535	642
Ho	Holmium	923–2023	779	822	869	922	981	1050	1125	1220	1325	1450	1605 ⊙	1800	2060	2410	2910
In	Indium(l)	646–1348	641	677	716	761	812	870	937	1015	1110	1220	1355	1520	1740	2030	2430
Ir	Iridium	1986–2600	1585	1665	1755	1850	1960	2080	2220	2380	2560 ⊙	2770	3040	3360	3750	4250	4900
K	Potassium	373–1031	247	260	276	294	315 ⊙	338	364	396	434	481	540	618	720	858	1070
La	Lanthanum	1655–2167	1100	1155 ⊙	1220	1295	1375	1465	1570	1695	1835	2000	2200	2450	2760	3150	3680
Li	Lithium	735–1353	430	452 ⊙	480	508	541	579	623	677	740	810	900	1020	1170	1370	1620
Lu	Lutetium	Est.	1000	1060	1120	1185	1260	1345	1440	1550	1685	1845 ⊙	2030	2270	2550	2910	3370
Mg	Magnesium	626–1376	388	410	432	458	487	519	555	600	650	712	782	878 ⊙	1000	1170	1400

Symbol	Element	Range															
Mn	Manganese	1523–1823	660	695	734	778	827	884	948	1020	1110	1210	1335	1490 ⊙	1695	1970	2370
Mo	Molybdenum	2070–2504	1610	1690	1770	1865	1975	2095	2230	2390	2580	2800 ⊙	3060	3390	3790	4300	5020
Na	Sodium	496–1156	294	310	328	347	370 ⊙	396	428	466	508	562	630	714	825	978	1175
Nb	Niobium	2304–2596	1765	1845	1935	2035	2140	2260	2400	2550	2720 ⊙	2930	3170	3450	3790	4200	4710
Nd	Neodymium	1240–1600	846	895	945	1000	1070	1135	1220 ⊙	1320	1440	1575	1770	2000	2300	2740	3430
Ni	Nickel	1307–1895	1040	1090	1145	1200	1270	1345	1430	1535	1655 ⊙	1800	1970	2180	2430	2770	3230
Os	Osmium	2300–2800	1875	1965	2060	2170	2290	2430	2580	2760	2960	3190	3460	3800	4200	4710	5340
P₄	Phosphorus(s)		283	297	312	327	342	361	381	402	430	458	493	534	582	642	715
Pb	Lead	1200–2028	516	546	580 ⊙	615	656	702	758	820	898	988	1105	1250	1435	1700	2070
Pd	Palladium	1294–1640	945	995	1050	1115	1185	1265	1355	1465	1590	1735 ⊙	1920	2150	2450	2840	3380
ΣPo	Polonium	711–1286	332	348	365	384	408	432	460	494 ⊙	537	588	655	743	862	1040	1250
Pr	Praseodymium	1423–1693	900	950	1005	1070	1140 ⊙	1220	1315	1420	1550	1700	1890	2120	2420	2820	3370
Pt	Platinum	1697–2042	1335	1405	1480	1565	1655	1765	1885	2020 ⊙	2180	2370	2590	2860	3190	3610	4170
Pu	Plutonium(l)	1392–1793	931	983	1040	1105	1180	1265	1365	1480	1615	1780	1975	2230	2550	2980	3590
Ra	Radium	Est.	436	460	488	520	552	590	638	690	755	830	920 ⊙	1060	1225	1490	1840
Rb	Rubidium		227	240	254	271	289	312 ⊙	336	367	402	446	500	568	665	802	1000
Re	Rhenium	2494–2999	1900	1995	2100	2220	2350	2490	2660	2860	3080	3340 ⊙	3680	4080	4600	5220	6050
Rh	Rhodium	1709–2205	1330	1395	1470	1550	1640	1745	1855	1980	2130 ⊙	2310	2520	2780	3110	3520	4070
Ru	Ruthenium	2000–2500	1540	1610	1695	1780	1880	1990	2120	2260	2420	2620 ⊙	2860	3130	3480	3900	4450
ΣS	Sulfur		230	240	252	263	276	290	310	328	353	382 ⊙	420	462	519	606	739
ΣSb	Antimony	693–1110	477	498	526	552	582	618	656	698	748	806	885 ⊙	1030	1250	1560	1960
Sc	Scandium	1301–1780	881	929	983	1045	1110	1190	1280	1380	1505	1650 ⊙	1835	2070	2370	2780	3360
ΣSe	Selenium	550–950	286	301	317	336	356	380	406	437	472 ⊙	516	570	636	719	826	972
ΣSi	Silicon	1640–2054	1090	1145	1200	1265	1340	1420	1510	1610 ⊙	1745	1905	2090	2330	2620	2990	3490
Sm	Samarium	789–833	542	573	608	644	688	738	790	853	926	1015	1120	1260 ⊙	1450	1715	2120
Sn	Tin(l)	1424–1753	805	852	900	955	1020	1080	1170	1270	1380	1520	1685	1885	2140	2500	2960
Sr	Strontium		433	458	483	514	546	582	626	677	738	810	900	1005 ⊙	1160	1370	1680
Ta	Tantalum	2624–2948	1930	2020	2120	2230	2370	2510	2680	2860	3080 ⊙	3330	3630	3980	4400	4930	5580
Tb	Terbium	Est.	900	950	1005	1070	1140	1220	1315	1420	1550 ⊙	1700	1890	2120	2420	2820	3370
Tc	Technetium	Est.	1580	1665	1750	1840	1950	2060	2200	2350	2530 ⊙	2760	3030	3370	3790	4300	5000
Te₂	Tellurium	481–1128	366	385	405	428	454	482	515	553	596	647	706 ⊙	791	905	1065	1300
Th	Thorium	1757–1956	1450	1525	1610	1705	1815	1935 ⊙	2080	2250	2440	2680	2960	3310	3750	4340	5130
Ti	Titanium	1510–1822	1140	1200	1265	1335	1410	1500	1600	1715	1850 ⊙	2010	2210	2450	2760	3130	3640
Tl	Thallium	519–924	473	499	527	556 ⊙	592	632	680	736	803	882	979	1100	1255	1460	1750
Tm	Thulium	809–1219	624	655	691	731	776	825	882	953	1030	1120	1235	1370	1540	1760 ⊙	2060
U	Uranium	1630–2071	1190	1255	1325 ⊙	1405	1495	1600	1720	1855	2010	2200	2430	2720	3080	3540	4180
V	Vanadium	1666–1882	1235	1295	1365	1435	1510	1605	1705	1820	1960	2120 ⊙	2320	2560	2850	3220	3720
W	Tungsten	2518–3300	2050	2150	2270	2390	2520	2680	2840	3030	3250	3500 ⊙	3810	4180	4630	5200	5900
Y	Yttrium	1774–2103	1045	1100	1160	1230	1305	1390	1490	1605	1740	1905	2105	2355	2670	3085	3650
Yb	Ytterbium	Est.	436	460	488	520	552	590	638	690	755	830	920	1060	1225	1490	1840
Zn	Zinc	422–1089	336	354	374	396	421	450	482	520	565	617	681	760	870	1010	1210
Zr	Zirconium	1949–2054	1500	1580	1665	1755	1855	1975	2110	2260	2450	2670	2930	3250	3650	4170	4830

* With permission, from Ref. 19.
⊙ indicates melting point.

which shows that the temperature of a gas is proportional to the average kinetic energy of the molecules. Furthermore, since the mean-square speed $\overline{c^2}$ is composed of three equal mean-square velocities parallel to the orthogonal coordinates, Eq. (27) also implies that the total translational energy of gas molecules is equally distributed among three mutually perpendicular directions of motion with average increments of $\frac{1}{2}kT$ per degree of freedom. This is the equipartition principle of kinetic energy as it applies to the three degrees of translational freedom. Polyatomic molecules can store additional energy in the form of rotation and oscillation. These internal energies are also distributed in average increments of $\frac{1}{2}kT$ per degree of freedom, provided kT is not small compared with the energy of the excited state.

   (2) Molecular-distribution Functions Instead of characterizing the motion of gas molecules by a mean-square value, the entire range of possible values and their relative frequencies will now be considered. The functions governing the distributions of molecular properties were first derived by J. C. Maxwell and L. Boltzmann. Maxwell started with the assumption that the number of molecules having a certain speed between c and $c + dc$ is determined only by the kinetic energy and is therefore a function of $c^2 = u^2 + v^2 + w^2$. The use of even exponents allows for the fact that positive and negative velocities occur with equal probability, an obvious requirement since gases never accumulate preferentially near any one particular wall. Furthermore, the distribution function for the speed c must be the product of three independent but identical distribution functions for the components u, v, w, which determine the direction and magnitude of c. These considerations lead to the following definition equations:

$$\frac{dN_u}{N} = \phi(u^2)\, du \qquad \frac{dN_v}{N} = \phi(v^2)\, dv \qquad \frac{dN_w}{N} = \phi(w^2)\, dw$$

$$\text{and} \qquad \frac{dN_{u,v,w}}{N} = \psi(u^2 + v^2 + w^2)\, du\, dv\, dw = \phi(u^2)\phi(v^2)\phi(w^2)\, du\, dv\, dw \tag{28}$$

dN_u/N is the fraction of all molecules having velocities between u and $u + du$, and $\phi(u^2)$ is their distribution function. Analogous relations hold for the velocities v and w. $dN_{u,v,w}/N$ is the fraction of all molecules having simultaneously velocities between u and $u + du$, v and $v + dv$, w and $w + dw$, and ψ is the corresponding distribution function.

   The mathematical solution to satisfy these differential equations is an exponential function for ϕ with two constants A and c_m:

$$\phi(u^2) = A \exp\left(-\frac{u^2}{c_m{}^2}\right)$$

Analogous expressions hold for $\phi(v^2)$ and $\phi(w^2)$. From these follows

$$\psi(u^2 + v^2 + w^2) = A^3 \exp\left(-\frac{c^2}{c_m{}^2}\right)$$

The constant A can be determined by considering that the integrals of Eqs. (28) must represent the total number of molecules N:

$$\int_{-\infty}^{+\infty} dN_u = \int_{-\infty}^{+\infty} NA \exp\left(-\frac{u^2}{c_m{}^2}\right) du = N$$

Therefore, $A = (\pi c_m{}^2)^{-\frac{1}{2}}$, and the distribution functions become

$$\phi(u^2) = (\pi c_m{}^2)^{-\frac{1}{2}} \exp\left(-u^2/c_m{}^2\right)$$

$$\text{and} \qquad \psi(u^2 + v^2 + w^2) = (\pi c_m{}^2)^{-\frac{3}{2}} \exp\left(-\frac{c^2}{c_m{}^2}\right)$$

The distribution function $\psi(u^2 + v^2 + w^2)$ gives the fraction of molecules with speeds $c = (u^2 + v^2 + w^2)^{\frac{1}{2}}$ in one particular direction. There are other molecules with speeds of the same magnitude c but composed of different velocities and moving in

different directions. If molecular speeds are represented in a three-dimensional velocity space, the function $\psi(u^2 + v^2 + w^2)$ can be interpreted as indicating the frequency of speeds at a point with the coordinates u, v, w. Since the volume in the velocity space between the speeds c and $c + dc$ is $4\pi c^2\, dc$, a new distribution function $\Phi(c^2)$ can be derived which represents the fraction of molecules with a random speed c:

$$\frac{dN_c}{N} = \Phi(c^2)\, dc = 4\pi c^2 \psi(u^2 + v^2 + w^2)\, dc \tag{29}$$

Explicitly, the random speed distribution is

$$\Phi(c^2) = \frac{4}{c_m{}^3 \sqrt{\pi}}\, c^2 \exp\left(-\frac{c^2}{c_m{}^2}\right) \tag{30}$$

Differentiation of $\Phi(c^2)$ with respect to c shows that the distribution has a maximum at c_m. Therefore, c_m is the most probable speed. The relationship to the mean-square speed $\overline{c^2}$ can be derived by defining the latter through an integral rather than a summation:

$$\overline{c^2} = \frac{1}{N} \int_0^\infty c^2\, dN_c \equiv \frac{\Sigma c^2}{N} \tag{31}$$

Substituting dN_c/N from Eqs. (29) and (30) into Eq. (31) and solving the integral yields $c_m{}^2 = \frac{2}{3}\overline{c^2}$. Since $\overline{c^2} = 3kT/m$, the most probable speed is $c_m = (2kT/m)^{\frac{1}{2}}$. Restating the distribution functions in terms of gas temperature and mass rather than c_m, the fraction of molecules having velocities between u and $u + du$ in one particular direction is

$$\frac{dN_u}{N} = \phi(u^2)\, du = \left(\frac{m}{2\pi kT}\right)^{\frac{1}{2}} \exp\left(-\frac{mu^2}{2kT}\right) du \tag{32}$$

The fraction of molecules having random speeds between c and $c + dc$ is

$$\frac{dN_c}{N} = \Phi(c^2)\, dc = 4\pi \left(\frac{m}{2\pi kT}\right)^{\frac{3}{2}} c^2 \exp\left(-\frac{mc^2}{2kT}\right) dc \tag{33}$$

In addition to $\overline{c^2}$ and c_m, there is a third characteristic speed, the arithmetic average $\bar{c}$, which is defined as

$$\bar{c} = \frac{1}{N} \int_0^\infty c\, dN_c \tag{34}$$

Substituting dN_c/N from Eq. (33) into Eq. (34) and solving the definite integral yields

$$\bar{c} = \left(\frac{8kT}{\pi m}\right)^{\frac{1}{2}} = 14{,}551 \left(\frac{T}{M}\right)^{\frac{1}{2}} \qquad \text{cm s}^{-1} \tag{35}$$

where M = molar mass in grams. The three characteristic speeds form the numerical ratios

$$\sqrt{\overline{c^2}} : \bar{c} : c_m = \sqrt{\tfrac{3}{2}} : \sqrt{4/\pi} : 1 = 1.225 : 1.128 : 1$$

Speed distributions $\Phi(c^2)$ for aluminum vapor at 1200°C ($p^* \approx 10^{-2}$ Torr) and for hydrogen at the same temperature as well as at 25°C are shown in Fig. 3. The molecular speeds are of the order of 10^5 cm s^{-1}. Because of their smaller mass, hydrogen molecules travel faster than aluminum atoms. The effect of temperature is to increase the dispersion of the speed distribution.

The distribution of kinetic energies E_k among molecules is similar to that of the random speeds and can be derived from Eq. (33) by substituting $E_k = \frac{1}{2}mc^2$ and $dE_k = mc\, dc$, which yields

$$\frac{dN_{E_k}}{N} = \Phi(E_k)\, dE_k = \frac{2}{kT\sqrt{\pi}} \left(\frac{E_k}{kT}\right)^{\frac{1}{2}} \exp\left(-\frac{E_k}{kT}\right) dE_k$$
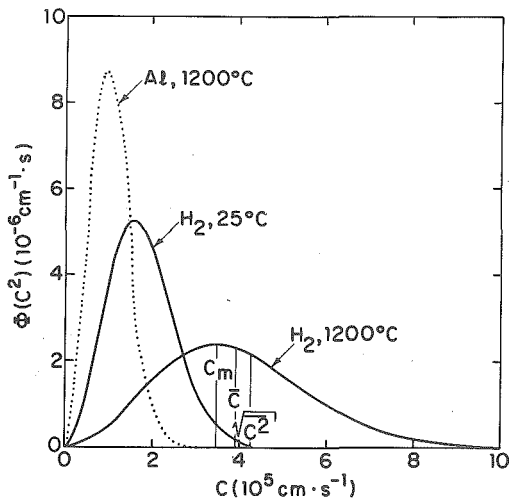
Fig. 3 Speed distributions for aluminum vapor and hydrogen gas.
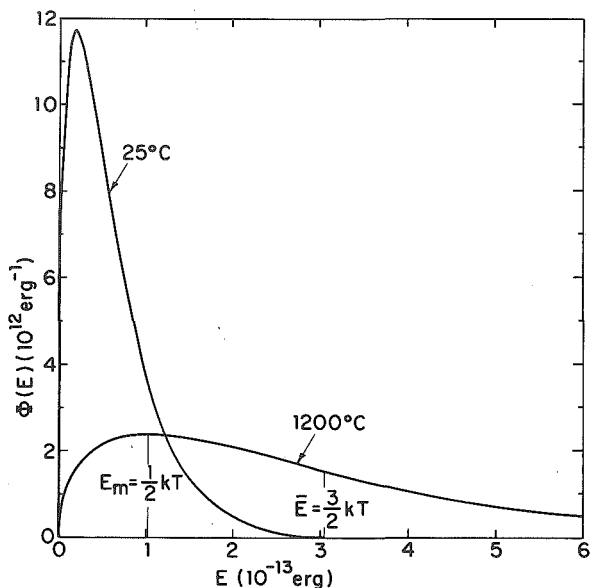
Fig. 4 Kinetic-energy distributions for two gas temperatures.

Figure 4 shows the kinetic-energy distributions corresponding to the speed distributions given in Fig. 3.   The kinetic energies are distributed only according to the temperature of the gas but independent of the molecular mass.   It is also of interest to note that the average energy $\overline{E_k} = \frac{3}{2}kT$ is three times greater than the most common energy $\frac{1}{2}kT$. This is due to the tail of the distribution at high multiples of kT. Particularly at higher temperatures, some molecules have energies far in excess of the average value.

(3) Impingement Rate of Molecules on a Surface   The impingement rate is the number of molecules which strike 1 cm² of a surface in unit time in a gas at rest. It is often needed in calculations of atomistic events and may be derived by considering only velocities perpendicular to the surface.   If the volume V contains N molecules, the number of those having a certain velocity u is given by Eq. (32):

$$dN_u = N\Phi(u^2)\, du$$

Only a fraction of these can reach the surface within a time interval dt, namely, those which are within the striking distance $u\, dt$. If A_w is the wall area under consideration, the fraction of the total volume which contributes to the impingement rate is $(u\, dt\, A_w)/V$.   Therefore,

$$d^2N_u = \frac{N}{V} A_w u\Phi(u^2)\, du\, dt \qquad\qquad (36)$$

is the number of particles impinging with velocities u.   Since the molecular velocities range from zero to infinity, Eq. (36) must be integrated for all velocities.   Proceeding from Eq. (32), this operation yields

$$\int_0^\infty u\Phi(u^2)\, du = \left(\frac{kT}{2\pi m}\right)^{\frac{1}{2}}$$

and therefore the impingement rate is

$$\frac{dN_i}{A_w\, dt} = \frac{N}{V}\left(\frac{kT}{2\pi m}\right)^{\frac{1}{2}}$$

or, after substituting the average molecular speed from Eq. (35),

$$\frac{dN_i}{A_w\, dt} = \frac{1}{4}\frac{N}{V}\bar{c} \qquad \text{cm}^{-2}\ \text{s}^{-1}$$

The relation between impingement rate and gas pressure is obtained by inserting p/kT for N/V:

$$\frac{dN_i}{A_w\, dt} = (2\pi mkT)^{-\frac{1}{2}}p \qquad\qquad (37)$$

For pressures given in torr, the impingement rate is

$$\frac{dN_i}{A_w\, dt} = 3.513 \times 10^{22}(MT)^{-\frac{1}{2}}p \qquad \text{cm}^{-2}\ \text{s}^{-1}$$

where M is the molar mass in grams.

(4) Free Paths of Gas Molecules   Although gas molecules move at very high speeds, they do not traverse large distances because of frequent collisions and deflection from their course.   For physical phenomena involving mass transport through the gaseous state, it is of interest to know the distances which molecules travel between collisions. The quantity which is used to characterize the ability of gas particles to cover distances is the mean free path (mfp) λ.   It is defined as the average distance of travel between subsequent collisions.   An oversimplified but instructive derivation of the mfp follows from the assumption that all gas molecules are at rest except one.   If the traveling molecule has the average speed $\bar{c}$, its path length after a time dt is $c\, dt$. Assuming further that all molecules have the same diameter σ, the traveling molecule collides with all particles whose centers are within a cross-sectional area $\pi\sigma^2$ along its path.   Thus, the volume within which collisions are possible is $\pi\sigma^2\bar{c}\, dt$.   By multiplying with the number of molecules per cubic centimeter, the collision frequency becomes $(N/V)\pi\sigma^2\bar{c}\, dt$.   These collisions divide the molecule's traveling distance $\bar{c}\, dt$ into equal intervals which are considered as the mean free path:

$$\lambda \approx \left(\frac{N}{V}\pi\sigma^2\right)^{-1}$$

A rigorous derivation, which takes into account the relative motion of all gas molecules, yields the more accurate expression

$$\lambda = \left(\frac{N}{V} \pi \sigma^2 \sqrt{2} \right)^{-1}$$

or, if the gas pressure is substituted for N/V,

$$\lambda = \frac{kT}{p \pi \sigma^2 \sqrt{2}} \tag{38}$$

Thus, the mean free path is inversely proportional to the gas pressure.

Since intermolecular collisions are statistical events, the actual free paths vary. Their distribution is given by an exponential decay function

$$\frac{N}{N_0} = \exp\left(\frac{-l}{\lambda} \right) \tag{39}$$

where N/N_0 is the fraction of molecules which have not suffered a collision as yet after traveling a free path of length l. According to Eq. (39), only 37% of all molecules traverse a distance as long as the mfp without being deflected. On the other hand, 1% of the molecules reach distances of at least 4.5λ before they collide.

To obtain numerical values of the mfp, it is necessary to know the molecular diameter σ. For some materials, this quantity has been determined by directing a beam of metal vapor into a gas and analyzing the deposit obtained at various distances from the vapor source. The molecular diameter plays a role in several other physical processes which involve interaction between gas molecules. An important example is the flow of gases through narrow tubes where the observed property, the coefficient of viscosity, is related to σ through the mechanism of momentum transfer during intermolecular collisions. Another example is the deviation of real gases from the ideal-gas law.

Fig. 5 Mean free paths of common gases as functions of pressure.

Since one of the coefficients in van der Waals' equation represents the actual volume of the gas particles, molecular diameters can also be derived from the empirical volume correction of van der Waals' equation of state. Additional methods for the determination of σ are based on the density of solids consisting of closely packed molecules, or on observations of the intensity decrease of an electron beam passing through a gas.

While the principal effects of molecular diameters in physical phenomena such as scattering of particle beams or viscous flow of gases are well established, the derivation of exact relationships poses theoretical difficulties. This is due to the fact that the hard-sphere model for gas molecules is an oversimplification. Gas molecules have complex structures and are not necessarily spherical. Furthermore, molecules exert attractive and repulsive forces upon each other which vary with distance. Thus, instead of visualizing molecules as hard spheres of well-defined size, it is more realistic to associate them with effective collision cross sections whose diameters may vary depending on the type of experiment made. A comparison of molecular diameters as obtained by different methods has been given by Dushman (Ref. 21, p. 39). For the common gases He, H_2, O_2, N_2, Ar, CH_4, CO_2, and H_2O, the effective cross-sectional diameters range from 2 to 5 Å. The mean free paths corresponding to these values at various pressures according to Eq. (38) are shown in Fig. 5. Since the particle diam-

eters are not too different, the mean free paths of all common gases fall into a narrow band bounded by the largest and the smallest molecules, H_2O and He.

(5) Gas Viscosity and Flow The mean free paths and viscosities of gases are of interest in assessing the vapor distribution around evaporation sources, but their role in vacuum technology is more important. The evacuation of a vessel by means of pumps involves connecting passages through which the gas must flow in order to be removed. The behavior of streaming gases, however, is determined by the motion of individual molecules and their collisions. For a broad treatment of the subject, the reader is referred to Dushman (Ref. 21, p. 80). The following section merely introduces the concept of viscosity and characterizes the different types of gas flow as related to molecular events.

A gas streaming through a narrow tube encounters resistance at the tube walls. As a result, the gas layer closest to the wall is slowed down and does not participate in the collective motion. This layer in turn delays the propagation of the next layer, and so forth. Consequently, every layer of gas moves at a different velocity depending upon its distance from the wall. This situation is shown schematically in Fig. 6. Since there is a velocity gradient between adjacent layers, the latter exert forces in the direction of gas flow (tangential) upon each other. The tangential force per unit area F_{tg} is transmitted by collisions between molecules from adjacent layers and results from the ensuing exchange of momentum. It is proportional to the radial velocity gradient dv/dx:

$$F_{tg} = \eta \frac{dv}{dx}$$

Fig. 6 Schematic representation of particle velocities for viscous flow through a narrow tube.

The proportionality factor η is the viscosity coefficient and expresses that property of a moving gas which results from internal friction caused by intermolecular collisions. It is specific for different gases and is measured in poise. A substance has a viscosity of 1 Poise if a tangential force of 1 dyn cm^{-2} arises from a radial velocity gradient of 1 cm s^{-1} cm^{-1}. The viscosities of the common gases are of the order of 10^{-4} Poise.

In order to relate η to properties of individual gas particles such as mass, velocity, and mean free path, the tangential force F_{tg} must be derived from kinetic theory. This has been attempted by different authors, and their results are of the general form

$$\eta = fm \frac{N}{V} \bar{c}\lambda \qquad (40)$$

The factor f varies between 0.3 and 0.5 depending on the assumed model of molecular interaction. The derivation of Chapman and Cowling[24] yields $f = 0.499$, and this value is now preferred over previous ones which were obtained without consideration of attractive and repulsive forces between molecules. By substituting $\bar{c}$ from Eq. (35) and λ from Eq. (38), Eq. (40) can be transformed into

$$\eta = \frac{2f}{\pi\sigma^2} \left(\frac{mkT}{\pi} \right)^{\frac{1}{2}}$$

From this relation follow the conclusions that the viscosity of gases is independent of pressure and, in contrast to the viscosity of liquids, increases with temperature. Both these predictions have been confirmed experimentally for that region of pressures where intermolecular collisions are more frequent than wall collisions. Furthermore, since the viscosity η is amenable to experimental determination by macro-

scopic gas-flow measurements, numerical values of effective molecular diameters can be derived. These are shown in Table 3.

The macroscopic flow rate of gases Q is that quantity of gas which passes through the cross section of a duct in unit time. It may be expressed as a volume of gas at a certain pressure or as a molecular current

$$Q = p\frac{dV}{dt} = kT\frac{dN}{dt}$$

The most common units for Q are torr $l\,s^{-1}$. At relatively high pressures, the flow rate is dependent on the viscosity of the gas and is characterized by a distribution of particle velocities as pictured in Fig. 6. Accordingly, this type of gas flow is called *viscous laminar flow*. The rate of viscous flow can be derived from the laws of hydrodynamics, which lead to different expressions depending on the geometrical shape of

TABLE 3   Effective Molecular Diameters from Viscosity Measurements at 0°C*

Gas	σ, 10^{-8} cm	Gas	σ, 10^{-8} cm
He............	2.18	Ar..........	3.67
H_2............	2.75	Kr..........	4.15
Ne............	2.60	Xe.........	4.91
O_2............	3.64	CO_2........	4.65
Air...........	3.74	H_2O........	4.68

* From Ref. 22, p. 149.

the duct. The simplest ducts are straight cylindrical tubes of uniform cross section for which the rate of viscous flow was first given by Poiseuille,

$$Q_{\text{visc}} = \frac{\pi r^4}{8\eta l}\bar{p}(p_2 - p_1)$$

where r is the radius and l the length of the tube; $(p_2 - p_1)$ is the pressure difference across the length of the tube, and $\bar{p}$ the average of p_2 and p_1.

In analogy to Ohm's law, the quantity

$$C = \frac{Q}{p_2 - p_1}$$

is called the conductance and is commonly used to characterize the gas-carrying ability of ducts. Thus, the conductance of a cylindrical tube in the range of viscous flow is

$$C_{\text{visc}} = \frac{\pi r^4}{8\eta l}\bar{p}$$

i.e., it is inversely proportional to the viscosity and decreases toward lower pressures. For air, which has a viscosity of 1.845×10^{-4} Poise at 25°C, numerical values can be derived from

$$C_{\text{visc}} = 2{,}840\frac{r^4}{l}\bar{p}_{\text{torr}} \qquad l\,s^{-1} \tag{41}$$

(r and l in cm).

The laws of viscous flow follow from the assumption of frequent intermolecular collisions which are responsible for the behavior of the gas as a coherent medium. These laws cannot be extended to very low pressures where wall collisions are more frequent than intermolecular collisions. As shown schematically in Fig. 7, gas flow at very low particle densities is characterized by molecules traveling independently of each other with random motion superimposed upon the direction of gas transport.
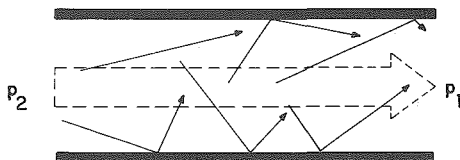
Fig. 7 Schematic representation of particle velocities for free molecular flow through a narrow tube.

This behavior is called *free molecular flow*. It was first analyzed by Knudsen,[25] who derived the molecular-flow equation for long cylindrical tubes:

$$Q_{\text{mol}} = \frac{2}{3}\pi\frac{r^3}{l}\bar{c}(p_2 - p_1)$$

Substitution of $\bar{c}$ from Eq. (35) and dividing by the pressure difference $p_2 - p_1$ across the tube length l yields the conductance in the molecular-flow region,

$$C_{\text{mol}} = 30.48\frac{r^3}{l}\left(\frac{T}{M}\right)^{\frac{1}{2}}\qquad l\,\text{s}^{-1}$$

It should be noted that the conductance in the region of molecular flow is independent of the gas pressure. Numerical values for air flow ($\sqrt{T/M} = 3.207$ at 25°C) can be derived from

$$C_{\text{mol}} = 97.75\frac{r^3}{l}\qquad l\,\text{s}^{-1} \tag{42}$$

(r and l in cm).

A comparison of Eqs. (41) and (42) shows that the conductance of a cylindrical tube is much greater in the region of viscous flow than for molecular flow. The transition from one type of flow to the other is not sharp but gradual. The movement of gases in this interval is referred to as *transition flow*. The gas flow in this intermediate range cannot be derived from first principles. It is customarily described by empirical equations which assume that the total gas flow consists of a viscous and a molecular contribution. For long cylindrical tubes, the conductance for transition flow has been formulated by Knudsen,

$$C_{\text{trans}} = C_{\text{visc}} + ZC_{\text{mol}} \tag{43}$$

where
$$Z = \frac{1 + 2.507r/\bar{\lambda}}{1 + 3.095r/\bar{\lambda}}$$

and $\bar{\lambda}$ is the mean free path associated with the average pressure $\bar{p}$.

To assess the fractions of flow attributable to viscous and molecular flow, Eq. (43) may be rewritten as

$$C_{\text{trans}} = C_{\text{mol}}\left(\frac{C_{\text{visc}}}{C_{\text{mol}}} + Z\right) = C_{\text{mol}}\left(\frac{0.1472r}{\bar{\lambda}} + Z\right) \tag{44}$$

The parameter Z is 0.810 for $r/\bar{\lambda} \gg 1$ (viscous flow) and approaches 1.000 for $r/\bar{\lambda} \ll 1$ (molecular flow). Since Z does not vary widely, the first term of Eq. (44) determines the predominant type of flow. Values of the mean free paths may be taken from Fig. 5 or calculated from Eq. (38). The latter yields for air at 25°C

$$\bar{\lambda} = \frac{5.10^{-3}}{\bar{p}_{\text{torr}}}\qquad \text{cm}$$

which transforms Eq. (44) into

$$C_{\text{trans}} = C_{\text{mol}}(29r\bar{p}_{\text{torr}} + Z) \tag{45}$$

Comparison of the two terms in Eq. (45) shows that the gas flow is at least 95 % viscous if $r\bar{p}_{\text{torr}} > 0.5$ while for $r\bar{p}_{\text{torr}} < 0.005$ the flow may be treated as molecular. Thus, the region of transition flow encompasses two decades of pressure.

The flow of gas induced by high-vacuum pumps (below 10^{-3} Torr) is molecular, and the paths of molecules are frequently interrupted by wall collisions. The presence of pipes, elbows, and baffles makes it difficult to derive a mathematical expression for the conductance of that region which connects a vacuum chamber with its pump. Methods of estimating the transmission probability through a complex system of tubes, diaphragms, and baffles are of great interest in determining the effective speed of pumps and have been reviewed by Steckelmacher.[26] Most powerful are Monte Carlo techniques, which were first applied to the problem by Levenson, Milleron, and Davis.[27] In this analysis, the molecular conductance of irregularly shaped channels is computed from possible trajectories of individual molecules. If a sufficiently large number of molecular paths is taken into account, the conductance of channels as complex as diffusion-pump baffles can be derived fairly accurately.

3. EVAPORATION THEORY

The application of the kinetic-gas theory to interpret evaporation phenomena resulted in a specialized evaporation theory. Early attempts to express quantitatively the rates at which condensed materials enter the gaseous state are connected mainly with the names of Hertz, Knudsen, and Langmuir. The observation of deviations from the originally postulated ideal behavior led to refinements of the transition mechanisms, which became possible as the understanding of molecular and crystalline structures increased. As a result, the evaporation theory includes concepts of reaction kinetics, thermodynamics, and solid-state theory. The questions pertaining to the directionality of evaporating molecules are primarily answered by statistical considerations derived from gas kinetics and sorption theory.

a. Evaporation Rates

(1) The Hertz-Knudsen Equation The first systematic investigation of evaporation rates in a vacuum was conducted by Hertz in 1882.[28] He distilled mercury at reduced air pressure and observed the evaporation losses while simultaneously measuring the hydrostatic pressure exerted on the evaporating surface. By using an evaporant of good thermal conductivity such as mercury, he excluded the possibility of limiting the evaporation rates because of insufficient heat supply to the surface. For all conditions chosen, Hertz found evaporation rates proportional to the difference between the equilibrium pressure of mercury at the surface temperature of the reservoir p^* and the hydrostatic pressure p acting on that surface.

From these observations, he drew the important and fundamental conclusion that a liquid has a specific ability to evaporate and cannot exceed a certain maximum evaporation rate at a given temperature, even if the supply of heat is unlimited. Furthermore, the theoretical maximum evaporation rates are obtained only if as many evaporant molecules leave the surface as would be required to exert the equilibrium pressure p^* on the same surface while none of them must return. The latter condition means that a hydrostatic pressure of $p = 0$ must be maintained. Based on these considerations, the number of molecules dN_e evaporating from a surface area A_e during the time dt is equal to the impingement rate given by Eq. (37) with the equilibrium pressure p^* inserted, minus a return flux corresponding to the hydrostatic pressure p of the evaporant in the gas phase:

$$\frac{dN_e}{A_e \, dt} = (2\pi mkT)^{-\frac{1}{2}}(p^* - p) \qquad \text{cm}^{-2}\,\text{s}^{-1} \qquad (46)$$

The evaporation rates originally measured by Hertz were only about one-tenth as high as the theoretical maximum rates. The latter were actually obtained by Knudsen[29] in 1915. Knudsen argued that molecules impinging on the evaporating surface may be reflected back into the gas rather than incorporated into the liquid. Conse-

quently, there is a certain fraction $(1 - \alpha_v)$ of vapor molecules which contribute to the evaporant pressure but not to the net molecular flux from the condensed into the vapor phase. To account for this situation, he introduced the evaporation coefficient α_v, defined as the ratio of the observed evaporation rate in vacuo to the value theoretically possible according to Eq. (46). The most general form of the evaporation rate equation is then

$$\frac{dN_e}{A_e\,dt} = \alpha_v(2\pi mkT)^{-\frac{1}{2}}(p^* - p)$$

which is commonly referred to as the Hertz-Knudsen equation.

Knudsen found the evaporation coefficient α_v to be strongly dependent on the condition of the mercury surface. In his earlier experiments, where evaporation took place from the surface of a small quantity of mercury, he obtained values of α_v as low as 5×10^{-4}. Concluding that the low rates were attributable to surface contamination as manifest in the discolored appearance of the metal, he allowed carefully purified mercury to evaporate from a series of droplets which were falling from a pipette and thus continually generated fresh, clean surfaces. This experiment yielded the maximum evaporation rate

$$\frac{dN_e}{A_e\,dt} = (2\pi mkT)^{-\frac{1}{2}}p^* \tag{47}$$

(2) Free Evaporation and Effusion   It was first shown by Langmuir[30] in 1913 that the Hertz-Knudsen equation also applies to the evaporation from free solid surfaces. He investigated the evaporation of tungsten from filaments in evacuated glass bulbs and assumed that the evaporation rate of a material at pressures below 1 Torr is the same as if the surface were in equilibrium with its vapor. Since recondensation of evaporated species was thereby excluded, he derived the maximum rate as stated by Eq. (47). Knowing the weight loss which the filaments had suffered during a certain time of evaporation, Langmuir was able to calculate the vapor pressure of tungsten. In order to do so, the molecular evaporation rate [Eq. (47)] is multiplied with the mass of an individual molecule. This yields the mass evaporation rate

$$\Gamma = m\frac{dN_e}{A_e\,dt} = \left(\frac{m}{2\pi kT}\right)^{\frac{1}{2}}p^* \tag{48}$$

or $$\Gamma = 5.834 \times 10^{-2}\left(\frac{M}{T}\right)^{\frac{1}{2}}p^* \qquad \text{g cm}^{-2}\text{ s}^{-1}$$

for pressures in torr.

The mass evaporation rate per unit area Γ is related to the total amount of evaporated material $\mathfrak{M}_e$ through the double integral

$$\mathfrak{M}_e = \int_t\int_{A_e} \Gamma\,dA_e\,dt \tag{49}$$

Assuming a uniform evaporation rate across the entire evaporation area and no variations with time, Γ can be determined from experimental data and inserted into Eq. (48) to obtain the vapor pressure. Numerical values of mass evaporation rates for metals at various vapor pressures have been tabulated by Dushman.[21] At $p^* = 10^{-2}$ Torr, Γ is of the order of 10^{-4} g cm^{-2} s^{-1} for most elements.

Phase transitions of this type, which constitute evaporation from free surfaces, are commonly referred to as Langmuir or free evaporation. Since the assumption $\alpha_v = 1$ is not always valid, as will be discussed later, an evaporation coefficient $\alpha_v < 1$ is often needed in Eq. (48). An alternate evaporation technique which avoids the uncertainty introduced by α_v being possibly smaller than 1 was established by Knudsen[31] and is associated with his name. In Knudsen's technique, evaporation occurs as effusion from an isothermal enclosure with a small orifice (Knudsen cell). The evaporating surface within the enclosure is large compared with the orifice and maintains the

equilibrium pressure p^* inside.   The diameter of the orifice must be about one-tenth or less of the mfp of the gas molecules at the equilibrium pressure p^*, and the wall around the orifice must be vanishingly thin so that gas particles leaving the enclosure are not scattered or adsorbed and desorbed by the orifice wall.   Under these conditions, the orifice constitutes an evaporating surface with the evaporant pressure p^* but without the ability to reflect vapor molecules; hence $\alpha_v = 1$.   If A_e is the orifice area, the total effusion from the Knudsen cell into the vacuum is $A_e(2\pi mkT)^{-\frac{1}{2}}(p^* - p)$ molecules per second.

Langmuir's and Knudsen's techniques have been employed in many experimental versions to determine the vapor pressure of materials and heats of vaporization.[5] Knacke and Stranski[32] have reviewed these methods, and a critical examination of both techniques with their limitations has been published by Rutner.[33]   Langmuir's method suffers from the uncertainty of whether or not an observed rate of weight loss truly reflects the equilibrium rate of evaporation.   It is often used, however, to determine α_v by comparing its results with independently known vapor-pressure data or with evaporation-rate measurements from Knudsen cells.   The principal problem with Knudsen's technique is that an ideal cell with an infinitely thin-walled orifice yielding free molecular flow can only be approximated.   In practice, orifices of finite thickness must be used, which necessitates the application of corrective terms in the effusion equation.   Expressions for the conductance of various orifices and tubes are derived and discussed in Dushman's book.[21]   Freeman and Edwards[34] solved the transmission problem for nonideal orifices by machine computations.

b. Evaporation Mechanisms

The evaporation coefficient α_v was introduced into the Hertz-Knudsen equation to account for observed evaporation rates smaller than those permitted by the equilibrium pressure.   Its theoretical justification, however, was obtained from the kinetics of a condensation process which included the possibility of elastic reflection of vapor molecules on the evaporant surface.   Because of this derivation, the same coefficient is sometimes referred to as the condensation coefficient α_c and is defined as the ratio of molecules condensing to those colliding with the surface of the condensed phase.*   In evaporations of the Langmuir type, however, recondensation of evaporated molecules is excluded by definition, and an understanding of the evaporation coefficient in the sense of α_c is therefore fictitious.   The assumption $\alpha_v = \alpha_c$, which is implied when the terms evaporation and condensation coefficients are used synonymously, is contingent upon identical mechanisms governing both processes and therefore is not generally true.

The necessity of having to resort to a condensation model to interpret the evaporation coefficient α_v has led many investigators to attempt the derivation of an expression equivalent to the Hertz-Knudsen equation strictly from the point of evaporation. The aim of these approaches is to establish an atomistic model for the evaporation process capable of yielding $\alpha_v < 1$ without the assumption that evaporation and condensation are the results of oppositely directed but otherwise identical mechanisms. Hence it is necessary to consider conditions which may inhibit or delay the departure of atoms or molecules from the surface of a condensed phase.   Various assumptions about such constraining factors and different approaches to treat them mathematically have been tried, and the interested reader is referred to the review article by Knacke and Stranski,[32] to the more recent and shorter treatment by Dettorre, Knorr, and Hall,[37] or to Hirth and Pound's book,[35] which offers the most comprehensive coverage and bibliography on the subject.   The following sections about evaporation mechanisms and representative experimental results are largely based on Hirth and Pound's work.

---

* Neither α_v nor α_c is identical with the accommodation coefficient α_T, which is used to describe the degree of energy exchange toward equilibrium between incident gas molecules and a condensed phase (see Chap. 8).   If energy exchange does play a retarding role in the process of evaporation, α_T enters the evaporation coefficient as one of several possible constraining factors.   Definitions of the various coefficients and their relationships among each other are discussed by Hirth and Pound (Ref. 35, p. 1) and by Winslow.[36]

(1) Liquids In the simplest model for the evaporation process, the condensed phase is considered as a system of oscillators whose surface molecules are bound by a certain energy of evaporation E_v. Transition into the gas phase is assumed to occur if a surface molecule possesses an energy of oscillation equal to or greater than E_v. It is also implied that all surface molecules have the same binding energy and an equal chance to evaporate. Based on this model, the probability of evaporation P was first estimated by Polanyi and Wigner.[38] Taking into account interaction among molecules by interference of eigenfrequencies, they arrived at

$$P \approx \frac{2E_v}{kT}\, \nu \exp\left(-\frac{E_v}{kT}\right)$$

where ν is the oscillation frequency of the surface atoms.

A more refined statistical model evolved from the work of Herzfeld,[39] Pelzer,[40] and Neumann.[41] They characterized the state of the surface molecules by a Maxwellian energy distribution and a spatial distribution, the latter relating the displacement of a molecule from its equilibrium position to its potential energy. A molecule evaporates if it is displaced far enough for its potential energy to equal the energy of evaporation. This treatment yields an evaporation probability per unit area and unit time of

$$P = \left(\frac{kT}{2\pi m}\right)^{\frac{1}{2}} \frac{Q_v}{Q_c} \exp\left(-\frac{E_v}{kT}\right) \tag{50}$$

where Q_v and Q_c are the partition functions of the vapor and of the condensed phase, respectively. Equation (50) can be transformed by equating the evaporation probability P with the molecular evaporation rate $dN_e/A_e\,dt$ and substituting $\frac{1}{4}\bar{c}$ for $(kT/2\pi m)^{\frac{1}{2}}$ [see Eq. (35)]. Furthermore, it can be shown that

$$\frac{Q_v}{Q_c} \exp\left(-\frac{E_v}{kT}\right) = \frac{N}{V}$$

is the statistical expression for the law of mass action. Consequently, Eq. (50) is equivalent to the Hertz-Knudsen equation for maximum evaporation rates as stated previously in Eq. (47). The same solution has also been obtained by Penner,[42] who treated the evaporation process in terms of the reaction-rate theory.[43]

The significance of these results is that the simple oscillator model of an evaporating surface is capable of explaining only maximum rates with a coefficient $\alpha_v = 1$ in the Hertz-Knudsen equation. Experience has shown that the model applies to liquids which evaporate by exchange of single atoms with a monatomic vapor. Most molten metals fall into this category, and $\alpha_v = 1$ has been confirmed experimentally for liquid mercury, potassium, and beryllium. Certain organic liquids whose molecules have spherical symmetry and small entropies of evaporation follow the same behavior; an example is CCl_4.

To explain evaporation coefficients smaller than 1, the possibility of changes in the internal energy states of molecules has been examined. In substances where molecules in the condensed state have fewer degrees of freedom than in the gaseous state, evaporation requires the exchange of internal energy in addition to translational energy. Herzfeld[44] was the first to consider the effect of internal energy changes on evaporation rates, and several authors have treated the problem thereafter (see Refs. 41, 42, 44 to 48). It is statistically unlikely that a surface molecule receives the internal and translational energies necessary for evaporation under the thermal-equilibrium conditions at exactly the same instance. More probable is a sequence of events in which the molecule is first activated by obtaining sufficient translational energy and then must wait for an internal energy quantum before evaporation can occur. Among the different forms of internal energy, rotational terms are considered to have the strongest effect on α_v because the relaxation time required to activate a rotational degree of freedom in the translationally activated state is estimated to be longer than for any other process.[47]

The mathematical treatment of evaporation involving internal energy changes is again based on the theory of absolute reaction rates,[43] with some variations among the different authors in the characterization of the activated state and in the assignment of partition functions. An illustrative example is the case where a rotational degree of freedom is restricted in the liquid but operative in the gaseous state. Derivation based on the rate theory yields the Hertz-Knudsen equation in the form

$$\frac{dN_e}{A_e\,dt} = \left(\frac{Q_R{}^*}{Q_{R_v}}\right)(2\pi mkT)^{-\frac{1}{2}}(p^* - p)$$

where $Q_R{}^*$ and Q_{R_v} are the rotational partition functions for the activated liquid state and for the vapor, respectively. Thus, the evaporation coefficient α_v takes on the significance of the ratio of two partition functions. Here, restricted evaporation ($\alpha_v < 1$) is due to the lack of one degree of freedom, which reduces the number of possible states for molecules in the liquid. This form of hindered phase transition is referred to as an entropy constraint.[35]

Hirth and Pound (Ref. 35, p. 83) have compiled and critically evaluated experimental α_v data from several authors. They conclude that the mechanism of activation in two steps with $\alpha_v < 1$ holds for liquids with small polar molecules evaporating from static surfaces. Examples are benzene, chloroform, ethanol, methanol, glycerol, and water. Conflicting results of $\alpha_v \approx 1$ have also been published for glycerol and water; the discrepancy may arise from differences in the experimental conditions such as turbulence in the vapor stream which could continually disturb the vapor-liquid interface. Liquids consisting of polar molecules which are either of the long-chain type or large and planar show a different behavior insofar as their evaporation coefficients are approximately equal to 1. Examples are 2-ethyl-hexyl phthalate, lauric acid, hexadecanol, n-dibutyl phthalate, tridecyl methane, n-hexadecane, and similar compounds. A possible explanation is that in these molecules the rotational degrees of freedom are operative in the translationally activated state; hence $Q_R{}^* = Q_{R_v}$ and $\alpha_v = 1$.

The evaporation rate of liquids is also retarded by surface contamination, as was experienced by Knudsen[29] in his earlier experiments ($\alpha_v \approx 10^{-3}$). The mechanisms by which impurities act as interface constraints during evaporation are presently understood only qualitatively. The most plausible explanations are that impurity atoms affect surface molecules by increasing the activation energy of evaporation, or that slow diffusion of evaporant molecules through an impurity film is the rate-determining step. Understandably, little experimental evidence exists since great care is generally taken to avoid surface contamination in evaporation-rate studies.

(2) Crystalline Solids While an evaporation model based on equal binding energies for all surface molecules is a reasonable point of departure for liquids, it is not applicable to crystalline solids. The model for crystal surfaces as established by Kossel[49] and Stranski[50,51] distinguishes different sites with variable numbers of nearest and second-nearest neighbor atoms. Since the binding forces exerted by adjacent atoms are additive, the evaporation energies for atoms on different sites must also be different. As shown in Fig. 8, the atoms S in a completed surface plane and L' in a ledge are surrounded by more than the average number of neighbors and therefore can be removed only by supplying an energy greater than the lattice energy. Conversely, a free surface atom like A or one at a ledge like L has less than the average number of neighbors and therefore may be removed by relatively small energies. The atom K in the kink or half-crystal position is most significant because its binding energy is equal to the lattice energy. Consequently, a crystal can be built in repeatable steps of equal energy by adding kink atoms. The removal or addition of a kink atom is therefore the microscopically reversible step which controls the evaporation and growth equilibrium on a crystal surface.

The probability of direct transitions of atoms from kink sites into the vapor as calculated from the binding energies is still too small to account for actually observed evaporation rates. This was first shown by Volmer[40] and led to the theory of stepwise evaporation. According to this concept, evaporation is initiated by an atom

dissociating from a kink position, followed by dissociation from the ledge position and diffusion across the crystal surface. This sequence is indicated by the arrows in Fig. 8. Before desorption can occur, the diffusing adatom must be activated by receiving the required translational energy. The theory of stepwise evaporation has been further developed by Hirth and Pound,[52] who predicted that crystal edges act as sources for monomolecular ledges which subsequently move across the crystal surface. It is therefore possible to evaporate perfect crystals bounded by singular surfaces without having to nucleate evaporation steps within the surfaces. This important function of crystal edges in the kinetics of evaporation is distinctly different from the minor role which edges play as nucleation sites in the kinetics of crystal growth.
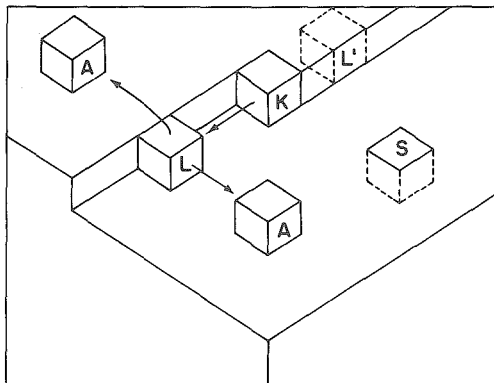
Fig. 8 Schematic of a crystal surface with atomic sites having different numbers of nearest neighbors. S: surface atom within a completed crystal plane. L': atom within a monatomic ledge. K: kink position. L: atom at a monatomic ledge. A: single atoms adsorbed on the surface.

A rigorous treatment of the metastable equilibrium population of adatoms on the crystal surface as determined by the supply (dissociation and diffusion) and annihilation (activation and desorption) processes has been given by Hirth and Pound (Ref. 35, p. 92). Simultaneous solution of the equations governing the individual process steps yields a general evaporation-flux equation from which numerical predictions for evaporation coefficients can be obtained in certain specific cases. An important parameter in the solutions is the average spacing between monatomic ledges on the crystal surface. On large low-index surfaces of single crystals, the ledge spacing is wider than the mean random-walk distance of the adatoms. Consequently, the evaporation rate is controlled by the interplay of ledge generation at crystal edges and surface diffusion of adatoms. Under these conditions, the evaporation coefficient for monatomic vapors should tend toward a minimum value of $\alpha_v = \frac{1}{3}$.

On high-index crystal planes, the surface is likely to form many ledges with spacings comparable with the mean diffusion distance which adatoms can cover before they are activated and desorbed. This situation leads to $\alpha_v \approx 1$. Other cases which have been considered include the possibilities of an entropy constraint for atoms dissociating from a ledge and of a high activation energy required for dissociation of atoms from a kink site. Both cases give values of $\alpha_v < \frac{1}{3}$. Evaporation coefficients smaller than 1 may also be due to adsorbed impurities. Their restraining influence on the evaporation process is attributed to the protective action of firmly adsorbed molecules on crystal edges so that the formation of new evaporation ledges is inhibited. Consequently, adatoms are supplied only from already existing ledges which grow to macroscopic size and thereby lower the rate of evaporation.

Experimental evidence pertaining to perfect single crystals to confirm these concepts is sparse. Sears[53] was able to show that evaporation from crystal edges occurs readily if the external vapor pressure is lowered as little as 2% below the equilibrium pressure. Conversely, no evaporation took place from a singular surface of the same crystal at external pressures as low as half the equilibrium value. This behavior supports the argument that crystal edges serve as sources for evaporation ledges.

The theory of stepwise evaporation can be extended to imperfect crystals and polycrystalline materials (Ref. 35, p. 107). Such solids follow the same evaporation kinetics as perfect crystals except for differences in the spacing of evaporation ledges. Spiral dislocations, for example, serve as additional sources for monatomic ledges, but the spacing of the latter should eventually assume the same values during evaporation as those between edge-generated ledges. Therefore, imperfect crystals should have evaporation coefficients similar to those of perfect crystals; i.e., α_v should approach one-third. In polycrystalline materials, ledge sources in the form of grain boundaries, cracks, crystal edges, and dislocations are numerous. The average ledge spacing will therefore be small, which leads one to expect evaporation coefficients approaching 1 unless the process is subject to entropy or impurity constraints.

Hirth and Pound have critically reviewed published evaporation coefficients for a number of polycrystalline solids and imperfect single crystals.[54] These data were obtained by comparing the results of Langmuir- and Knudsen-type vapor-pressure measurements. In agreement with the theory, polycrystalline metals with monatomic vapors such as Ag, Cu, Be, Cd, Hg, Fe, Cr, and Pt yielded evaporation coefficients of about 1. However, this result is contingent upon the availability of clean crystal surfaces, and coefficients smaller than 1 have been obtained in a number of instances where this condition was not satisfied. The effect of impurities on evaporation has been demonstrated for beryllium, whose coefficient α_v was reduced to 0.02 by allowing the metal surface to chemisorb oxygen.

Evaporation rates for low-index planes on imperfect single crystals have been determined for Ag, KCl, KI, rhombic sulfur, CsI, CsBr, NaCl, and LiF. Except for the latter two compounds, evaporation coefficients between 0.3 and 0.8 have been found. While these data are compatible with the theoretical value of $\frac{1}{3} < \alpha_v < 1$ for surface-diffusion-controlled evaporation, the possibility of entropy constraints has also been considered and cannot be excluded in several cases. Uncertainties in the interpretation of some data also arise from the use of vacuum pressures too high to rule out impurity adsorption. The evaporation coefficient of NaCl ($\alpha_v = 0.1$ to 0.2) and LiF ($\alpha_v = 0.1$ to 1) were found to be temperature-dependent, which is attributed to varying degrees of formation of polyatomic gaseous species.

The evaporation behavior of polycrystalline solids which evaporate as polymers (Se, Te, As, P, C) and of compounds which dissociate upon evaporation (NH_4Cl, AlN, BN, Al_2O_3) is governed by more complex kinetic processes than heretofore discussed. The observed values vary from $\alpha_v \approx 1$ for Te_2 vapor to $\alpha_v \approx 10^{-7}$ for P_2 and P_4 vapor. A detailed theoretical analysis of these cases has not been possible yet, one reason being the lack of sufficient information about the identity and concentration of the evaporating species as dependent on time, temperature, and crystal morphology.

c. Directionality of Evaporating Molecules

In the preceding discussion of evaporation mechanisms, only the total number of molecules leaving a surface was of interest. It is to be expected that the interaction between the surface of the condensed phase and an individual atom about to evaporate also determines the direction into which the particle will be emitted. The answer to this question must be statistical in nature and contingent upon assumptions about the energy states of molecules at the instant of evaporation. Since the distribution of kinetic energies among molecules is well known for the gaseous state, the spatial distribution of particles can be derived for the effusion of gases from an ideal Knudsen cell.

(1) The Cosine Law of Emission An isothermal enclosure with an infinitesimally small opening dA_e bounded by vanishingly thin walls is shown schematically in Fig. 9. It is assumed to contain N molecules which have a Maxwellian speed distribution.

Most of these molecules will impinge on the enclosure walls and be reflected without causing a net change in the total speed distribution. Those molecules moving toward the opening, however, will leave the enclosure in the same direction and at the same speed that they possessed immediately prior to their escape. The total population of gas molecules in the enclosure is assumed to remain constant because of the presence of a condensed phase. The distribution of molecules in the evaporant stream is then determined by the distribution of molecular speeds inside the effusion cell and may be described by an expression which gives the number of molecules within a small solid angle $d\omega$ for every direction of emission. The latter is defined by its angle φ with the normal to the surface element dA_e.

Considering first molecules of only one particular speed c, their total number in the enclosure is $dN_c = N\Phi(c^2)\,dc$. Within a time dt, only those molecules can reach dA_e and leave in the direction φ which are in the slanted prism indicated in Fig. 9. Thus, the fraction of molecules within striking distance of the opening is $c\,dt\cos\varphi\,dA_e/V$. The number of molecules actually crossing the opening is further reduced because their speeds c within the slanted prism are randomly distributed in all directions. Hence, only the fraction $d\omega/4\pi$ is actually moving toward dA_e. Multiplication of dN_c with the volume fraction and the angular fraction yields the number of molecules having a speed c and leaving in the direction φ:

$$d^4N_{e,c}(\varphi) = \frac{N}{V}\,c\,\Phi(c^2)\,dc\,dA_e\,dt\cos\varphi\,\frac{d\omega}{4\pi}$$

Integration over all speeds c gives the total number of molecules per angle increment $d\omega$, whereby

$$\int_0^\infty c\,\Phi(c^2)\,dc = \bar{c}$$

and therefore

$$d^3N_e(\varphi) = \frac{1}{4}\frac{N}{V}\,\bar{c}\,dA_e\,dt\cos\varphi\,\frac{d\omega}{\pi}$$

Fig. 9 Effusion from an isothermal enclosure through a small orifice.

The small increment of mass carried by these molecules is $d^3\mathfrak{M}_e(\varphi) = m\,d^3N_e(\varphi)$, and since $m \times \frac{1}{4}(N/V)\bar{c} = \Gamma$, one obtains

$$d^3\mathfrak{M}_e(\varphi) = \Gamma\,dA_e\,dt\cos\varphi\,\frac{d\omega}{\pi} \tag{51a}$$

or, substituting the total mass of evaporated material $\mathfrak{M}_e$ according to Eq. (49),

$$d\mathfrak{M}_e(\varphi) = \mathfrak{M}_e\cos\varphi\,\frac{d\omega}{\pi} \tag{51b}$$

Equations (51a) and (51b) represent the cosine law of emission and are equivalent to Lambert's law in optics. According to the cosine law, emission of material from a small evaporating area does not occur uniformly in all directions but favors directions approximately normal to the emitting surface where $\cos\varphi$ has its maximum values.

The amount of material which condenses on an opposing surface also depends on the position of the receiving surface with regard to the emission source. As shown in Fig. 10, the material contained in an evaporant beam of solid angle $d\omega$ covers an area which increases with distance as well as with the angle of incidence θ. The element

of the receiving surface which corresponds to $d\omega$ is $dA_r = r^2\,d\omega/\cos\theta$. Therefore, the mass deposited per unit area is

$$\frac{d\mathfrak{M}_r(\varphi,\theta)}{dA_r} = \frac{\mathfrak{M}_e}{\pi r^2}\cos\varphi\cos\theta \tag{52}$$

The validity of the cosine law for the effusion of gases was first tested by Knudsen,[55] who showed that the expected distribution is obtained at vapor pressures low enough to permit a mean free path of at least ten times the diameter of the effusion opening. Mayer[56] confirmed the cosine-law distribution for the effusion of air, hydrogen, and carbon dioxide by measuring the momentum of impinging molecules at various angles φ opposite the opening with a torsion balance.
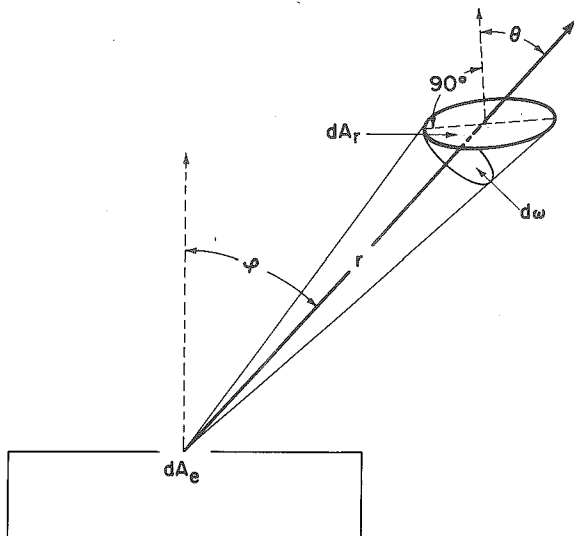
Fig. 10   Surface element dA_r receiving deposit from a small-area source dA_e.

The extension of the cosine law to emission from liquid or solid surfaces is generally taken to be permissible, thereby implying that free-evaporating molecules, too, have Maxwellian speed distributions. This assumption can be justified theoretically in those cases where evaporation takes place without surface constraints, i.e., if $\alpha_v = 1$. Then, the distribution of energies and directions of molecules emerging from a surface cannot differ from those which would impinge from an equilibrated vapor without violating the second law of thermodynamics. However, if the evaporation process is subject to entropy constraints, this argument cannot be applied, and deviations from the cosine law are possible (Ref. 35, p. 8). In practice, the condition $\alpha_v = 1$ holds for the free evaporation of simple solids and liquids with monatomic vapors, and therefore the cosine law may be extended to the greater portion of evaporant materials of current interest.

Experimental evidence to prove the validity of the cosine law for free evaporation was furnished by Knudsen,[57] who evaporated crystals of sulfur, zinc, silver, and antimony trisulfide from a point on the surface of a spherical glass flask. The experimental arrangement, which is shown schematically in Fig. 11, provides for $\cos\varphi = \cos\theta = r/2r_0$ at every point of the receiving surface. Thus, the amount of deposit according to Eq. (52) should be independent of the location on the receiving surface, and Knudsen observed that the glass sphere was indeed uniformly coated. More recently, Heald and Brown[58] analyzed the angular distribution of CO_2 molecules impinging on and being reemitted from a polished copper surface; their results, too, were in accord with the cosine law.
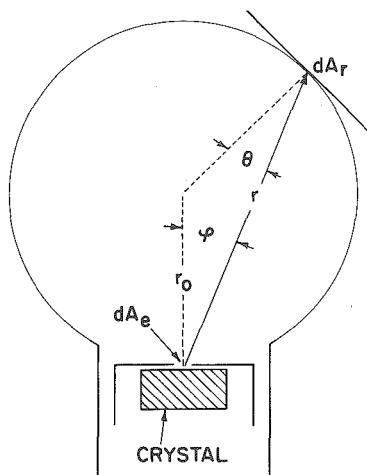
Fig. 11 Evaporation from a small-area source dA_e onto a spherical receiving surface.

(2) Emission from a Point Source As shown in the preceding section, molecules evaporating from a small surface element yield a directional emission pattern. At least hypothetically it is possible to change that condition and visualize molecules emerging from an infinitesimally small sphere ("point") of surface area dA_e. Provided the molecules have again a Maxwellian speed distribution at the moment of departure, they will move away from the point source in all directions with equal probability, as shown schematically in Fig. 12. Consequently, the mass evaporation
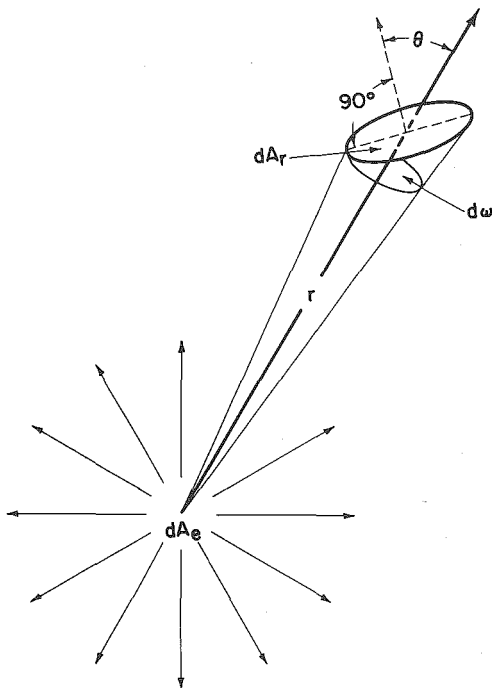
Fig. 12 Evaporation from a point source dA_e onto a receiving surface element dA_r.

rate Γ is uniform in all directions, and the mass contained in a narrow beam of solid angle $d\omega$ is

$$d^3\mathfrak{M}_e = \Gamma \, dA_e \, dt \, \frac{d\omega}{4\pi} \qquad (53a)$$

or, since $\displaystyle\iint_{t,A_e} \Gamma \, dA_e \, dt$ is the total evaporated mass $\mathfrak{M}_e$,

$$d\mathfrak{M}_e = \mathfrak{M}_e \frac{d\omega}{4\pi} \qquad (53b)$$

For a receiving element dA_r within the solid angle $d\omega$, the dependence on source distance and beam direction is the same as for a small surface source, $dA_r = r^2 \, d\omega/\cos\theta$, and therefore the amount of deposit received from a point source is

$$\frac{d\mathfrak{M}_r}{dA_r} = \frac{\mathfrak{M}_e}{4\pi r^2} \cos\theta \qquad (54)$$

The receiving surface of uniform deposit is a sphere with the point source in the center so that $\cos\theta = 1$ and $r = \text{const}$.

The nondirectional emission pattern of an idealized point source is of limited interest insofar as it is a fair approximation for only a few practical sources. Equation (53a) is sometimes used to derive deposit distributions obtained by evaporating from linear or ring-shaped wire sources, which are then considered to form an array of point sources.

4. THE CONSTRUCTION AND USE OF VAPOR SOURCES

The evaporation of materials in a vacuum system requires a vapor source to support the evaporant and to supply the heat of vaporization while maintaining the charge at a temperature sufficiently high to produce the desired vapor pressure. The rates utilized for film deposition may vary from less than 1 to more than 1,000 Å s^{-1}, and the vaporization temperatures of any particular element differ accordingly. Rough estimates of source operating temperatures are commonly based on the assumption that vapor pressures of 10^{-2} Torr must be established to produce useful film condensation rates. For most materials of practical interest, these temperatures fall into the range from 1000 to 2000°C.

To avoid contamination of the deposit, the support material itself must have negligible vapor and dissociation pressures at the operating temperature. Suitable materials are refractory metals and oxides. Further selection within these categories is made by considering the possibilities of alloying and chemical reactions between the support and evaporant materials. Alloying is often accompanied by drastic lowering of the melting point and hence may lead to rapid destruction of the source. Chemical reactions involving compounds tend to produce volatile contaminants such as lower oxides which are incorporated into the film. Additional factors influencing the choice of support materials are their availability in the desired shape (wire, sheet, crucible) and their amenability to different modes of heating. The former determines the amount of evaporant which the source can hold (capacity), while the latter affects the complexity of the source structure and the external power supply.

Attempts to reconcile these demands have led to numerous source designs, which have been reviewed by Holland (Ref. 59, p. 108) and Behrndt.[60] Specialized sources of rather complex construction are nearly always required to evaporate quantities in excess of a few grams. Table 4 shows the temperatures of interest in this context for the more common elements, along with existing experience concerning suitable support materials. The melting points and approximate temperatures required to produce 10^{-2} Torr are taken from Honig.[19] For several elements, these data differ from the older values given in Holland's[59] widely used table. Pirani and Yarwood's[61] compilation of evaporation techniques for the elements has also been used. Most of the evaporation coefficients α_v are from Hirth and Pound[35] except those of Sb and and As.[62] Individual source materials and types of vapor sources are reviewed in more detail in the following sections.

TABLE 4   Temperatures and Support Materials Used in the Evaporation of the Elements

Element and predominant vapor species	Temp, °C mp	$p^* = 10^{-2}$ Torr	Wire, foil	Crucible	Remarks
Aluminum (Al)	659	1220	W	C, BN, TiB$_2$-BN	Wets all materials readily and tends to creep out of containers. Alloys with W and reacts with carbon. Nitride crucibles preferred
Antimony (Sb$_4$, Sb$_2$)	630	530	Mo, Ta, Ni	Oxides, BN, metals, C	Polyatomic vapor, $\alpha_v = 0.2$. Requires temperatures above mp. Toxic
Arsenic (As$_4$, As$_2$)	820	~300	. . . .	Oxides, C	Polyatomic vapor, $\alpha_v = 5.10^{-5}$– 5.10^{-2}. Sublimates but requires temperatures above 300°C. Toxic
Barium (Ba)...	710	610	W, Mo, Ta, Ni, Fe	Metals	Wets refractory metals without alloying. Reacts with most oxides at elevated temperatures
Beryllium (Be)	1283	1230	W, Mo, Ta	C, refractory oxides	Wets refractory metals. Toxic, particularly BeO dust
Bismuth (Bi, Bi$_2$)	271	670	W, Mo, Ta, Ni	Oxides, C, metals	Vapors are toxic
Boron (B).....	2100 ± 100	2000	. . . .	C	Deposits from carbon supports are probably not pure boron
Cadmium (Cd)	321	265	W, Mo, Ta, Fe, Ni	Oxides, metals	Film condensation requires high supersaturation. Sublimates. Wall deposits of Cd spoil vacuum system
Calcium (Ca)..	850	600	W	Al$_2$O$_3$	
Carbon (C$_3$, C, C$_2$)	~3700	~2600	. . . .	. . . .	Carbon-arc or electron-bombardment evaporation. $\alpha_v < 1$
Chromium (Cr)	~1900	1400	W, Ta	. . . .	High evaporation rates without melting. Sublimation from radiation-heated Cr rods preferred. Cr electrodeposits are likely to release hydrogen
Cobalt (Co)...	1495	1520	W	Al$_2$O$_3$, BeO	Alloys with W, charge should not weigh more than 30 % of filament to limit destruction. Small sublimation rates possible
Copper (Cu)...	1084	1260	W, Mo, Ta	Mo, C, Al$_2$O$_3$	Practically no interaction with refractory materials. Mo preferred for crucibles because it can be machined and conducts heat well
Gallium (Ga)..	30	1130	. . . .	BeO, Al$_2$O$_3$	Alloys with refractory metals. The oxides are attacked above 1000°C
Germanium (Ge)	940	1400	W, Mo, Ta	W, C, Al$_2$O$_3$	Wets refractory metals but low solubility in W. Purest films by electron-gun evaporation
Gold (Au).....	1063	1400	W, Mo	Mo, C	Reacts with Ta, wets W and Mo. Mo crucibles last for several evaporations
Indium (In)...	156	950	W, Mo	Mo, C	Mo boats preferred
Iron (Fe)......	1536	1480	W	BeO, Al$_2$O$_3$, ZrO$_2$	Alloys with all refractory metals. Charge should not weigh more than 30 % of W filament to limit destruction. Small sublimation rates possible
Lead (Pb).....	328	715	W, Mo, Ni, Fe	Metals	Does not wet refractory metals. Toxic
Magnesium (Mg)	650	440	W, Mo, Ta, Ni	Fe, C	Sublimates
Manganese (Mn)	1244	940	W, Mo, Ta	Al$_2$O$_3$	Wets refractory metals

TABLE 4 Temperatures and Support Materials Used in the Evaporation of the Elements (Continued)

Element and predominant vapor species	Temp, °C		Support materials		Remarks
	mp	$p^* = 10^{-2}$ Torr	Wire, foil	Crucible	
Molybdenum (Mo)	2620	2530	....	....	Small rates by sublimation from Mo foils. Electron-gun evaporation preferred
Nickel (Ni)....	1450	1530	W, W foil lined with Al_2O_3	Refractory oxides	Alloys with refractory metals; hence charge must be limited. Small rates by sublimation from Ni foil or wire. Electron-gun evaporation preferred
Palladium (Pd)	1550	1460	W, W foil lined with Al_2O_3	Al_2O_3	Alloys with refractory metals. Small sublimation rates possible
Platinum (Pt)	1770	2100	W	ThO_2, ZrO_2	Alloys with refractory metals. Multistrand W wire offers short evaporation times. Electron-gun evaporation preferred
Rhodium (Rh)	1966	2040	W	ThO_2, ZrO_2	Small rates by sublimation from Rh foils. Electron-gun evaporation preferred
Selenium (Se_2, Se_n: $n = 1$–8)[63]	217	240	Mo, Ta, stainless steel 304	Mo, Ta, C, Al_2O_3	Wets all support materials. Wall deposits spoil vacuum system. Toxic. $\alpha_v = 1$
Silicon (Si)....	1410	1350	....	BeO, ZrO_2, ThO_2, C	Refractory oxide crucibles are attacked by molten Si and films are contaminated by SiO. Small rates by sublimation from Si filaments. Electron-gun evaporation gives purest films
Silver (Ag)....	961	1030	Mo, Ta	Mo, C	Does not wet W. Mo crucibles are very durable sources
Strontium (Sr).	770	540	W, Mo, Ta	Mo, Ta, C	Wets all refractory metals without alloying
Tantalum (Ta)	3000	3060	....	....	Evaporation by resistance heating of touching Ta wires, or by drawing an arc between Ta rods. Electron-gun evaporation preferred
Tellurium (Te_2)	450	375	W, Mo, Ta	Mo, Ta, C, Al_2O_3	Wets all refractory metals without alloying. Contaminates vacuum system. Toxic. $\alpha_v = 0.4$
Tin (Sn)......	232	1250	W, Ta	C, Al_2O_3	Wets and attacks Mo
Titanium (Ti)	1700	1750	W, Ta	C, ThO_2	Reacts with refractory metals. Small sublimation rates from resistance-heated rods or wires. Electron-gun evaporation preferred
Tungsten (W)	3380	3230	....	....	Evaporation by resistance heating of touching W wires, or by drawing an arc between W rods. Electron-gun evaporation preferred
Vanadium (V).	1920	1850	Mo, W	Mo	Wets Mo without alloying. Alloys slightly with W. Small sublimation rates possible
Zinc (Zn).....	420	345	W, Ta, Ni	Fe, Al_2O_3, C, Mo	High sublimation rates. Wets refractory metals without alloying. Wall deposits spoil vacuum system
Zirconium (Zr)	1850	2400	W	....	Wets and slightly alloys with W. Electron-gun evaporation preferred

a. Wire and Metal-foil Sources

The simplest vapor sources are resistance-heated wires and metal foils of various types, as shown in Fig. 13. They are commercially available in a variety of sizes and shapes at sufficiently low prices to be discarded after one experiment if necessary. Materials of construction are the refractory metals, which have high melting points and low vapor pressures. Most commonly used are tungsten, molybdenum, and tantalum. Platinum, iron, or nickel are sometimes employed for materials which evaporate below 1000°C. As shown in Table 5, the volatility of the support materials will generally not be a problem except for molybdenum at temperatures above 1800°C. However, tungsten and molybdenum form volatile oxides by reaction with residual water vapor or dissolved oxygen and thus may contribute condensable impurities.

TABLE 5 Properties of Refractory Metals

Property	Tungsten	Molybdenum	Tantalum
Melting point, °C[19].	3380	2610	3000
T, °C, for $p* = 10^{-6}$ Torr[19].	2410	1820	2240
Electrical resistivity,[64] 10^{-6} ohm-cm:			
At 20°C.	5.5	5.7	13.5
At 1000°C.	33	32	54
At 2000°C.	66	62	87
Thermal expansion, %[64]:			
From 0–1000°C.	0.5	0.5	0.7
From 0–2000°C.	1.1	1.2	1.5

The sources shown in Fig. 13a and b are commonly made from 0.02 to 0.06-in.-diameter tungsten wire. Their utility is limited to evaporants which can be affixed to the source, typically in the form of wire. Upon melting, the evaporant must wet the filament and be held by its surface tension. Spreading of the molten evaporant across the wire is desirable to increase the evaporation surface and thermal contact. This is encouraged by distributing the initial charge evenly over the entire length of the source. Suitable techniques are electroplating of the evaporant onto the filament, multistrand filaments where the evaporant is added as one of the fibers, or hanging short loops of evaporant wire onto each coil of a helix (Fig. 13b). Multistrand filaments are generally preferred because they offer a greater surface area than single-wire filaments. Because of their simplicity and low cost, wire sources are also used to evaporate metals such as Al, Ni, Fe, or Pt which are known to alloy with tungsten. Under these conditions, the evaporant charge should be small compared with the mass of the filament, and the latter is quickly destroyed if the molten evaporant collects in one spot.

Even if the evaporant does not alloy with the filament, the capacity of wire sources is small. Provided that uniform wetting and distribution of the melt over a few centimeters of filament length are obtained, such sources may hold amounts up to 1 g. Wire baskets as shown in Fig. 13c are used to evaporate pellets or chips of dielectrics or metals which either sublime or do not wet the wire material upon melting. If wetting occurs, the turns of the basket are shorted and the temperature of the source drops.

Metal foils as shown in Fig. 13d, e, and f have capacities of a few grams and are the most universal types of sources for small evaporant quantities. They are fabricated from 0.005- to 0.015-in.-thick sheets of tungsten, molybdenum, or tantalum. The dimpled sources have reduced widths in the center to concentrate the heating in the area of the evaporant. The recessed circles or ovals are only ⅛ to ¼ in. deep since refractory metals are not easily drawn to greater depths. Canoe or boat sources may be made in the laboratory by bending metal sheets into the desired shape. This is readily done with tantalum and not too difficult with molybdenum. Tungsten, however, is very brittle and breaks if it is bent at room temperature. Deformation is possible at elevated temperatures in a nonoxidizing atmosphere (Ref. 59,

p. 109). All three metals embrittle after having been heated in vacuum, especially if alloying with the evaporant has occurred. Their mechanical properties are reviewed in detail by Kohl.[64]

Wetting of the metal-foil surface by the molten evaporant is desirable in the interest of good thermal contact. However, molten metals also lower the electrical resistance of the foil in the contact area, thereby causing the temperature to drop. This problem is avoided with oxide-coated foils as shown in Fig. 13e. Oxide-coated metal sources were first described by Olsen et al.,[65] who embedded tungsten-wire baskets in sintered Al_2O_3 or BeO. Nowadays oxide coatings are applied by plasma-spray processes. Typical commercial sources consist of 0.010-in. Mo foils (or sometimes Ta) covered with an equally thick layer of alumina. The oxide layer is claimed to be nonporous and withstands temperature cycling without chipping. Maximum operating temperatures of 1850 to 1900°C are possible, but the vapor pressure of molybdenum
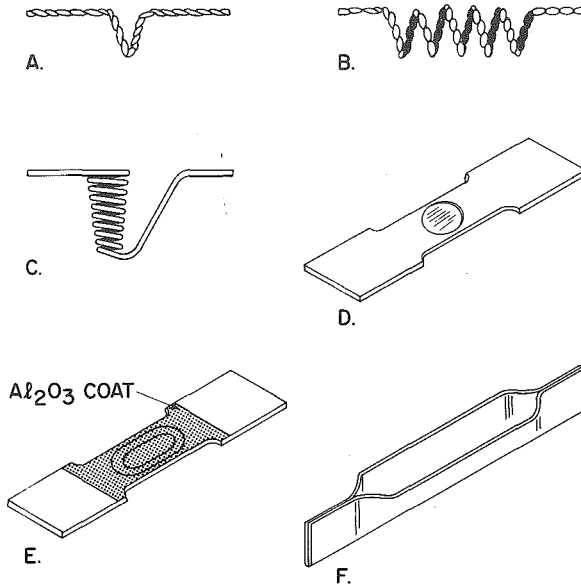
Fig. 13 Wire and metal-foil sources. (A) Hairpin source. (B) Wire helix. (C) Wire basket. (D) Dimpled foil. (E) Dimpled foil with alumina coating. (F) Canoe type.

exceeds 10^{-6} Torr in this range and that of alumina is even higher. The power requirements of such sources are 30 to 50% above those of comparable uncoated foils since the thermal contact between the resistance-heated metal and the evaporant is reduced by the oxide coat. Molten metals do not wet the alumina surface but coalesce into a sphere. Whereas alloying is inhibited, the possibility of forming volatile oxides from the Al_2O_3 and the evaporant metal should be considered.

Electrical connections to wire and foil sources are made by attaching their ends to heavy copper or stainless-steel clamps. The latter are usually part of massive metal bars connected rigidly to a pair of electrical feedthroughs. To avoid warping of the source due to thermal expansion (see Table 5), flexible cables such as braided copper wire or multilayered copper foil are often used. Since the electrical resistance of wire and foil sources is small, low-voltage power supplies rated at 1 to 3 kW are required. Typical arrangements consist of a step transformer (5 to 20 V) whose primary side is connected to a variable 110- or 220-V transformer. The latter is necessary to raise the operating voltage as the resistance of the refractory metals increases strongly with temperature (see Table 5). The secondary current may be as low as 20 A for

some of the wire sources, or as high as 500 A for some foil sources.   If the source current exceeds 100 A, it is advisable to use water-cooled feedthroughs.

There are wire or foil sources to evaporate small charges of nearly all elements except the refractory metals themselves.   Films of W, Mo, and Ta have been prepared by spring-loading two wires (0.02 in. diameter) of the respective metals such that their ends touch and form a high-resistance junction.   Melting of the junction and evaporation are induced by passing an electric current through the arrangement.[66] An alternate technique is vacuum-arc evaporation.   Lucas et al.[67] established short arcs between zone-purified rods of Ta, Nb, and V by means of a dc welding generator. A similar arrangement has been described by Massey,[68] who sustained an arc between two carbon rods and produced carbon films up to 1 μ thick.   In general, however, heating by electron bombardment is the preferred technique to evaporate refractory metals.

b. Sublimation Sources

The problem of finding nonreactive supports for materials evaporating above 1000°C can be circumvented in those cases where the 10^{-2} Torr vaporization temperature is near the melting point of the evaporant.   The elements Cr, Mo, Pd, V, Fe, and Si reach vapor pressures of 10^{-2} Torr before they melt and hence can be sublimated. This allows evaporation from wires or foils of the film materials by direct resistance heating without contact with any foreign material.   High-purity nickel and iron films have been prepared in this manner by Behrndt.[69]   Kilgore and Roberts[70] produced silicon films by sublimation from resistance-heated ribbons at 1300 to 1350°C.   The technique is of particular interest for silicon because the molten element rapidly alloys with and destroys refractory-metal filaments.   Although silicon has also been evaporated from ThO_2, Al_2O_3, and SiO_2 boats,[71] it has a strong tendency to attack refractory oxides and to form volatile SiO.   Thus, without resorting to electron-gun evaporation, high-purity silicon films are best obtained by sublimation.

The sublimation technique can be extended to a few more metals with vapor pressures in the 10^{-3} Torr range at their respective melting points.   Examples are Ni,[72] Rh, and Ti.   Sublimation of titanium is widely practiced in vacuum technology to getter chemically reactive gases, an application which requires only small deposition rates (see Chap. 2).   For the purpose of depositing films with thicknesses of 1,000 Å or more, however, the sublimation rates are generally too small.   This disadvantage can be somewhat compensated by using filaments of large surface area and by reducing the source-to-substrate distance to a few centimeters.   But an enlarged sublimation surface increases the power requirement of the source, and the short evaporation distance reduces the area of uniform deposit thickness while it enhances radiation heating of the substrates.   For these reasons, sublimation of metals is not widely practiced.

An important exception from this rule is chromium because its vapor pressure reaches 10^{-2} Torr about 500°C below the melting point.   Consequently, high deposition rates can be obtained by sublimation from compact sources and with substrate distances of the order of 50 cm.   The simplest arrangement is to place chromium chips in a tungsten or tantalum boat.[73]   However, since the chips do not melt, their thermal contact with the filament is poor and variable, which makes it difficult to maintain constant evaporation rates.   Better heat contact is obtained if the chromium is electroplated onto a tungsten filament.[74]   Heavily chrome-plated tungsten rods are also commercially available.   However, electrodeposited metals tend to occlude significant amounts of hydrogen, which may contribute substantially to the residual gas load of the vacuum system.

A practical chromium sublimation source has been developed by Roberts and Via.[75] As shown in Fig. 14, a chromium rod is supported within a dual-wall cylinder.   The latter is fabricated from pieces of 0.002 in. (inner cylinder) and 0.005 in. (outer cylinder) thick tantalum sheet which are spot-welded together to form a continuous current path.   Since the source is compact and well shielded, the power requirements are less than 750 W.   Sublimation occurs from the entire surface area of the rod, which is uniformly heated by radiation.   Therefore, ejection of particles does not occur, and

the evaporation rates are constant over extended periods of time. By increasing the voltage, condensation rates of 100 Å s⁻¹ or more across normal bell-jar distances may be obtained. The source capacity amounts to at least 50% of the initial rod charge. The latter may be prepared from chromium powder by pressing and sintering, but the purest films are obtained from zone-refined rods.
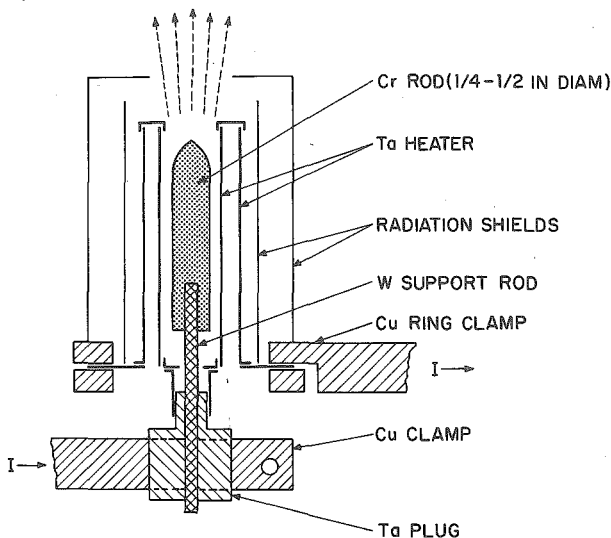
Fig. 14 Chromium sublimation source after Roberts and Via.[75] The electric current flows through the tantalum cylinder (heavy lines).

Sublimation sources are frequently used for the vaporization of thermally stable compounds. These are commonly obtained as powders or loosely sintered chunks containing large quantities of absorbed or occluded gases. Upon heating, spontaneous release of gases often causes violent ejection of evaporant particles which are incorporated into the films. To avoid this problem, baffled sources have been designed which inhibit direct line-of-sight transmission from the evaporant charge to the substrates. The simplest of these sources are made by spot welding two dimpled tantalum foils together to form an enclosure. The upper dimple has an aperture to allow the vapor to escape. Within the enclosure and opposite the aperture is a small sheet-metal baffle to restrain evaporant particles. These sources are suitable for the evaporation of moderate quantities of II-VI compounds.[76]

Large source capacities and high evaporation rates are often an important requirement in the deposition of dielectric films. The first source to satisfy these objectives was the well-known Drumheller[77] design shown in Fig. 15a. It is charged with SiO chunks packed around a resistance-heated tantalum cylinder. The latter is perforated and acts as a chimney through which the externally generated SiO vapors escape. A ring-shaped lid prevents the ejection of oxide particles. In many ways, it is an example of good source design: compact, well shielded for minimum power requirements, of large capacity, demanding little maintenance, and capable of yielding high rates because of its large internal surface area. Accordingly, it has become one of the most widely used sources in the laboratory.

Since 0.001- to 0.005-in. tantalum sheet can easily be cut, bent, and spot-welded, dielectric sublimation sources of the "optically dense" type exist in a great variety of designs. Vergara et al.[78] introduced a new family of these sources, where the generation and emission of vapor take place in two separate parts of the source. An example is shown in Fig. 15b. A disadvantage compared with the Drumheller source is

the need for a second power supply to heat the vapor-emitting box. But present vendor catalogs list many designs also based on functional separation by internal baffles, where both compartments form one continuous current path and are energized by only one power supply. Although primarily developed for SiO, these sources are also suitable to evaporate the sulfides, selenides, and tellurides of Zn and Cd as well as MgF_2.
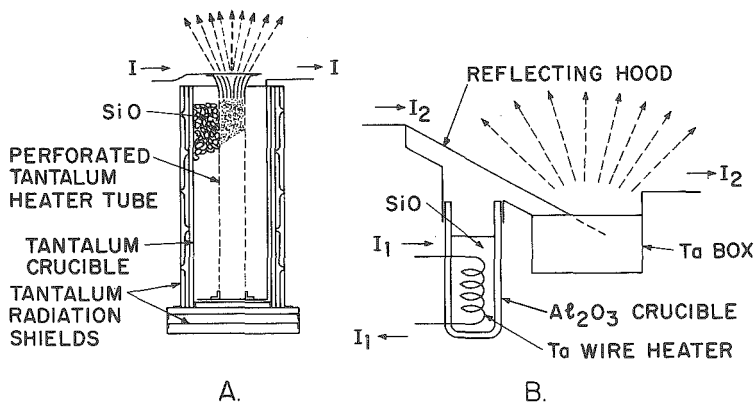
Fig. 15 Optically dense SiO sources. (A) The Drumheller[77] source. (B) Compartmentalized source. (*After Vergara, Greenhouse, and Nicholas.*[78])

c. Crucible Sources and Materials

(1) Refractory Metals Crucible sources are required to support molten metals in quantities of a few grams or more. Since the melt is in contact with the container for prolonged periods of time, the selection of thermally stable and noncontaminating support materials must be made very carefully. The compatibility of molten evaporants with refractory metals can be assessed by studying the phase diagram of the two materials.[79] The metal combination should have very small mutual solubilities and no low-melting eutectic. If a suitable refractory metal can be found, it is preferable over oxide crucibles since slight interaction of the latter with molten metals and vaporization of contaminant oxides are sometimes difficult to recognize. Moreover, metal crucibles can be obtained in a greater variety of shapes and sizes, and they are better heat conductors and also less sensitive to rapid temperature changes than oxide crucibles.

Referring back to Table 4, a number of metals can be evaporated from molybdenum crucibles. Of the three refractory metals, molybdenum is the least expensive and can be machined more easily than tungsten. A source design which is particularly useful for the evaporation of Cu, Ag, or Au is shown in Fig. 16. The solubilities of these three metals in molybdenum and vice versa are very small. Hence the crucible is not attacked, and the author has obtained up to 50 copper depositions from the same container. The stability toward silver appears to be equally good, while gold has been observed to penetrate the molybdenum walls after fewer than 10 evaporations. The resistance-heated filament consists of two halves cut from tantalum foil and spot-welded together as shown in the upper part of Fig. 16. Held by copper clamps at both ends, it maintains its cylindrical shape without contacting other parts of the source. An additional advantage of the meandering sheet-metal filament over a wire helix is its larger radiating surface. Because of the multiple heat shields, a power input of about 500 W is sufficient for Cu or Ag evaporations. The rates are very stable and respond well to feedback control from ionization or crystal-oscillator rate monitors.
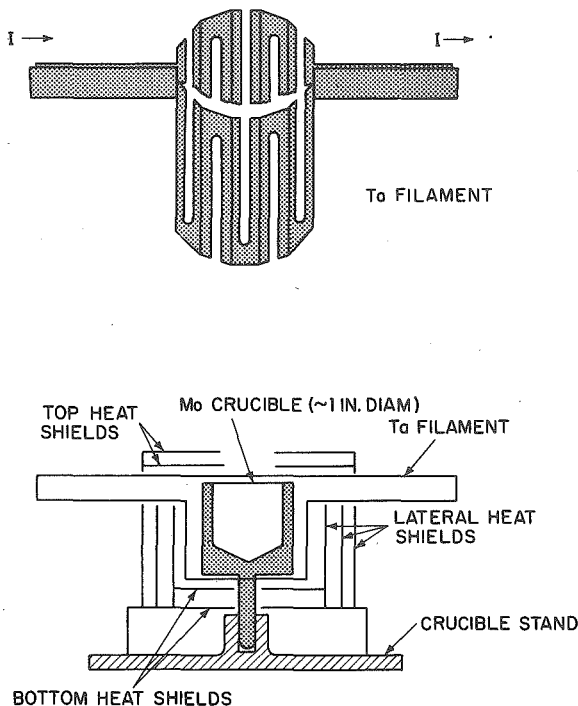
Fig. 16 Molybdenum crucible source with meandering tantalum sheet filament.

(2) Refractory Oxides Refractory-oxide crucibles are available in certain standard shapes and sizes from manufacturers of vacuum accessories.[80] A thorough review of refractory oxide properties has been given by Kohl,[64] and the data in Table 6 are selected from that source. The physical properties of ceramic oxides show consider-

TABLE 6 Properties of Refractory Oxides*

Oxide	Porosity, vol %	Fusion temp, °C	Max normal use temp, °C	Thermal conductivity, cal s^{-1} deg^{-1} cm^{-2} cm	Thermal stress resistance
Sintered ThO_2	3–7	3050	2500	0.007	Fair–poor
Sintered BeO	3–7	2570	1900	0.046	Excellent
Sintered ZrO_2 (stabilized[92]: ZrO_2, $4HfO_2$, $4CaO$)	3–10	2550	2200	0.005	Fair–good
Sintered Al_2O_3	3–7	2030	1900	0.014	Good
Sintered MgO	3–7	2800	1900	0.016	Fair–poor
Vitreous SiO_2	0	1710	1100	0.012	Excellent
Sintered TiO_2	3–7	1840	1600	0.008	Fair–poor

* From Kohl.[64]

able variations depending on the manufacturing process. Generally, the purest products have superior thermal stability and mechanical strength. Oxide crucibles for vacuum evaporation are typically sintered from powder of at least 99.8% purity and retain a small pore volume. Wall thicknesses are of the order of 1 to 3 mm, and high thermal conductivities are desirable for reasons of heat transfer as well as thermal shock resistance. The fusion temperatures in Table 6 are somewhat lower than the melting points of the pure oxides but still far above those temperatures at which these materials can be safely used. Similarly, the maximum normal use temperatures in Table 6 do not necessarily hold for vacuum applications since there may be additional restrictions.

An important factor in assessing the suitability of an oxide support material is its thermodynamic stability. The first five oxides listed in Table 7 have sufficiently large free energies of dissociation to maintain oxygen partial pressures of less than 10^{-12} Torr at 2000°C. TiO_2 and NiO are not useful evaporation-support materials because they decompose too readily. The utility of SiO_2 is limited because it gives up its oxygen to several metals which are capable of forming oxides of greater thermodynamic stability. Thus, SiO_2 in contact with Al or Mg is rapidly attacked even below 1000°C. Other metals such as Ag, Au, or Pt do not react chemically but require evaporation temperatures which are too close to or even above the softening point of vitreous silica. Consequently, only the first five oxides in Table 7 merit serious

TABLE 7 Thermodynamic Stability of Refractory Oxides as Represented by Their Free Energies of Dissociation at 1800°C[81]

Dissociation Process	Std Free Energy at 1800°C, kcal/g-at of oxygen
$\frac{1}{2}ThO_2(s) = \frac{1}{2}Th(s) + \frac{1}{2}O_2(g)$	+111
$BeO(s) = Be(l) + \frac{1}{2}O_2(g)$	+100
$\frac{1}{2}ZrO_2(s) = \frac{1}{2}Zr(s) + \frac{1}{2}O_2(g)$	+ 84
$\frac{1}{3}Al_2O_3(s) = \frac{2}{3}Al(l) + \frac{1}{2}O_2(g)$	+ 82
$MgO(s) = Mg(g) + \frac{1}{2}O_2(g)$	+ 53
$\frac{1}{2}SiO_2(s) = \frac{1}{2}Si(l) + \frac{1}{2}O_2(g)$	+ 49
$3TiO_2(s) = Ti_3O_5(s) + \frac{1}{2}O_2(g)$	+ 18
$NiO(s) = Ni(l) + \frac{1}{2}O_2(g)$	+ 13

consideration. Within this group, the sublimation pressure of some of the oxides imposes an upper temperature limit on their utility in vacuum. MgO, for instance, sublimates noticeably at 1600 to 1900°C, Al_2O_3 at 1900°C, and BeO at 1900 to 2100°C.

In principle, the compatibility of an evaporant metal with an oxide support material can be judged by comparing the free energies of dissociation of both metal oxides at the anticipated use temperature. However, the kinetics of the reactants cannot be predicted, and in some cases the reaction may be slow enough to permit limited use of a combination whose thermodynamic stability is marginal. Unfortunately, not all the metal–metal oxide interface reactions of potential interest have been investigated. Johnson[82] studied the stability of 21 metal–metal oxide pairs in vacuum at temperatures from 1500 to 2300°C. Economos and Kingery,[81,83] in a similar study, classified the observed interface reactions according to their severity. The slightest forms of interaction are discoloration of the oxide surface and metal penetration along the oxide grain boundaries. More severe reaction may result in visible corrosion of the oxide surface or in the formation of a new phase at the interface. The significance of these observations for the evaporation of metals from oxide crucibles is not always obvious. Relatively heavy interaction with new-phase formation, for example, may be acceptable if none of the reaction products is volatile. Conversely, the absence of even discoloration at the interface may obscure the fact that a volatile suboxide has been emitted. A stability matrix which combines the observations of Johnson,[82] Economos and Kingery[81,83] with data from Kohl[64] is shown in Table 8.

The stability matrix demonstrates that the refractory metals W, Mo, and Ta cannot be evaporated from oxide supports. The data are also of interest in judging the stability of refractory-metal filaments in contact with oxide crucibles or boats. Among the

TABLE 8   Thermal Stability of Refractory Oxides in Contact with Metals*

Metal	Temp, °C for 10^{-2} Torr	Refractory oxides				
		ThO$_2$	BeO	ZrO$_2$	Al$_2$O$_3$	MgO
W....	3230	Slight reduction at 2200°C	Stable at 1700°C; reaction >1800°C	Stable <1600°C; little reaction up to 2000°C	Limited by the onset of Al$_2$O$_3$ sublimation at 1900°C	Limited by the onset of MgO sublimation at 1600–1900°C
Mo...	2530	Little reaction up to 2300°C	Stable at 1900°C but not above	Stable at 2000°C; ZrO$_2$ decomposes at 2300°C		
Ta....	3060	Stable up to 1900°C	Stable up to 1600°C	Stable up to 1600°C		
Zr....	2400	Interaction begins at 1800°C	Interaction begins at 1600°C	Slight interaction at 1800°C	Oxide attacked at 1600°C	
Be....	1230	Only slight interaction at **1600°C**			Oxide discolored at **1400°C**	Stable at **1400°C** but not at **1600°C**
Si.....	1350	Little or no attack at **1400°C**; noticeable reaction at 1600°C			Slight reaction at 1400°C	Slight reaction at 1400°C, strong at 1600°C
Ti....	1750	Slight interaction at **1800°C**	Little reaction at 1600°C but considerable at 1800°C		Little reaction at 1400°C but considerable at 1800°C	
Ni....	1530	Ni(l) is stable in contact with all oxides at **1800°C**				

Boldface type indicates metal-oxide pairs which can be used for thin film deposition.
* After Johnson,[82] Economos and Kingery,[81,83] and Kohl.[64]

other metals, only Ni and Be are either nonreactive or have sufficiently slow reaction kinetics to be safely evaporated from oxide boats.   The cases of Si and Ti in some of the most stable oxides are marginal.   Although the oxide supports are not strongly attacked, both elements are known to form volatile suboxides, which leads one to expect deposits with a certain oxide content.   There are, however, many other metals not listed in Table 8 which can be evaporated from refractory oxide enclosures. Examples are As, Sb, Bi, Te, Ca, Mn, and others with vaporization temperatures below 1000°C, as well as Co, Fe, Pd, Pt, Rh which require temperatures between 1500 and 2100°C.

Oxide crucibles are commonly heated by radiation from refractory-metal filaments. The simplest arrangement is a wire coil as shown in Fig. 17.   The filament touches the crucible in several places, thus enhancing the heat transfer by conduction.   However, this involves the risk of interaction between filament and oxide.   The source should be surrounded by radiation shields since the filament emits only a small fraction of its energy in the direction of the crucible.
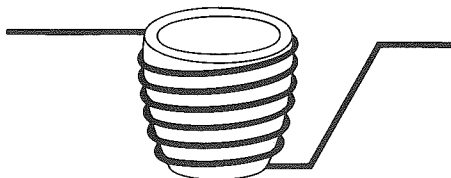
Fig. 17   Oxide crucible with wire-coil heater.

A more efficient design is the DaSilva[84] source shown in Fig. 18. It is made from 0.0025-in. Ta foil rolled into a cylinder and spot-welded to circular top and bottom electrodes. The source requires cylindrical crucibles and yields rates which can be well controlled through the power input to the cylinder. With proper heat shielding, the power requirements are less than 500 W. Many other heater arrangements, for example, modifications of the crucible source shown in Fig. 16, are possible.
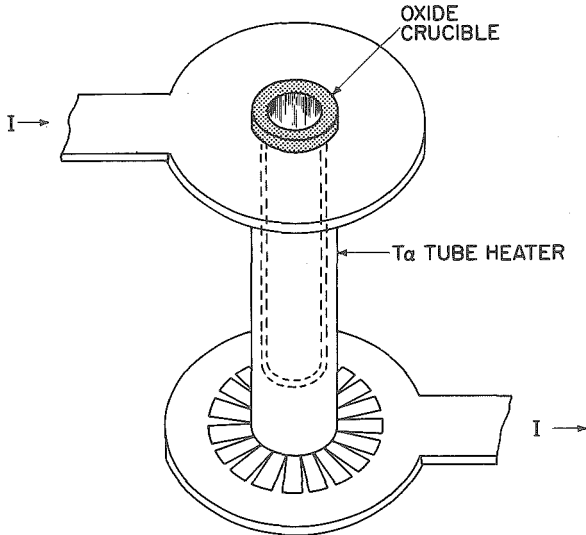
Fig. 18   DaSilva[84] crucible source.

(3) Boron Nitride   A number of borides, carbides, silicides, and nitrides have excellent thermal stabilities. Reviews of their physical properties and availability have been given by Hauck[85] and Kohl.[64] One of these "space-age materials," boron nitride (BN), has found application for evaporation crucibles. It is a white insulating material with a structure similar to graphite. Like the latter, it is relatively soft and can be machined with ordinary cutting tools into a great variety of shapes. The thermal conductivity of BN is similar to that of alumina, and its heat-shock resistance is excellent. Its mechanical strength is about one-half that of alumina. It has a tendency to absorb water and therefore requires outgassing prior to metal evaporation. The maximum use temperature is determined by the nitrogen dissociation pressure, which reaches 10^{-2} Torr at 1600°C and exceeds 10^{-1} Torr at 1800°C.[86]

The density and also the amount of gas evolving when boron nitride is heated depend on the manufacturing process. Pyrolytic boron nitride* deposited from boron halide and ammonia has the highest purity and density and is impervious to gases. Manufacturing processes which sinter powders with organic binders yield products with a stronger tendency to contribute impurities to the evaporant. A composition consisting of 50% of BN and titanium diboride (TiB_2) each is also well established as a crucible material.† Titanium diboride has a thermal conductivity similar to BN but is harder and melts at 2940°C. The composite material is gray and machinable like the pure nitride. Its electrical resistivity at 1100 to 1200°C is of the order of a few milliohm-centimeters.[87]

The most important application of boron nitride crucibles is in the evaporation of aluminum. Contrary to nearly all ceramic oxides, neither the nitride nor the com-

---

* For example, Boralloy, Union Carbide Corp., New York, N.Y.

† Marketed as HDA Composite Ceramic by Union Carbide Corp., New York, N.Y.

posite is appreciably attacked by molten aluminum. Evaporation of the latter from a boron nitride crucible has been described by Thompson and Libsch,[88] while Ames et al.[87] used the composite ceramic. Both groups of investigators employed rf induction heating. The crucible developed by Ames et al.[87] is of particular interest and is shown in Fig. 19. It is designed to avoid the well-known problem of molten aluminum
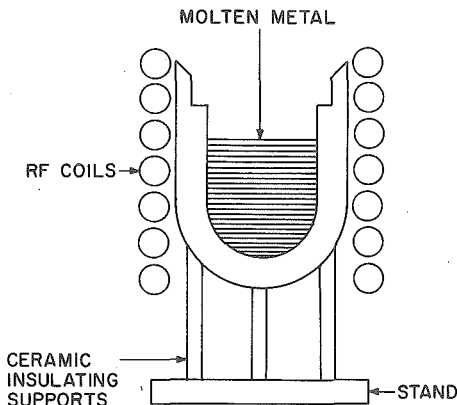
Fig. 19 RF heated aluminum source with boron nitride–titanium diboride crucible. (*After Ames, Kaplan, and Roland.*[87])

migrating upward and spilling over the brim of the container. This is overcome by the reduced thickness of the upper portion of the crucible, which is approximately one-third of the skin depth of the rf field. Consequently, coupling in this region is sufficiently strong to affect complete vaporization of the migrating aluminum layer. The wall thickness of the lower portion is about equal to the skin depth. It permits adequate coupling to evaporate the metal but shields the melt from the rf field enough to minimize turbulence and droplet ejection. The source is capable of producing reliably spatter-free aluminum films of bulk resistivity.

Rf induction heating, whether in conjunction with boron nitride, refractory oxide, or metal crucibles, has some advantages over radiation heating. Since at least part of the energy is coupled directly into the evaporant metal, it is not necessary to produce filament or crucible temperatures in excess of the vaporization temperature for the purpose of maintaining a heat flow. Thus, interactions between evaporant and container walls are minimized. Also, the utilization of the energy supplied to the source is more efficient than in the case of filament heating since radiation and conduction heat losses are smaller. The need for radiation shields is obviated by the water-cooled coupling coils surrounding the crucible.

Disadvantages are the greater cost and space requirement of the rf power supply, the need for more thoroughly insulated vacuum feedthroughs, and the necessity of having to experiment with coil spacing, diameter, and external tuning for efficient coupling. For guidelines in the design of rf heated sources, their power requirements and depth of penetration as functions of frequency, the reader is referred to the book by Pirani and Yarwood.[61] The essential consideration is that most of the power is induced near the surface of the charge. The thickness of the layer, within which two-thirds of the energy is generated, is called the skin depth. The latter is inversely proportional to the square root of the radio frequency [see Chap. 2, Sec. 4a(3)]. Therefore, uniform heating of large metal charges is effectively accomplished with lower frequencies, while small or thin objects require very high frequencies. To give some examples, commercial equipment operating at about 10 kHz is suitable to heat metal charges of several pounds. Quantities of several grams require generators operating at a few hundred kilohertz, while satisfactory energy transfer into charges of a few cubic milli-

meter volume (milligram quantities) is obtained at frequencies greater than 50 MHz.[89]

(4) Carbon   Another material frequently used for the evaporation of metals is carbon.   It is available in several forms with properties varying widely as a result of different manufacturing processes.   An extensive review of carbon products has been given by Kohl,[64] and the properties of possible interest in vacuum evaporation are listed in Table 9.

TABLE 9   Properties of Carbon[64,82]

Vapor pressure:
  At 1900°C.............................. $\sim 10^{-6}$ Torr
  At 2500°C.............................. $\sim 10^{-2}$ Torr
Density, commercial graphites:.............. 1.6–1.8
  Vitreous carbon........................ 1.3–1.5
  Pyrolytic graphite...................... Up to 2.26
  Theoretical............................ 2.265
Electrical resistivity, 10^{-3} ohm-cm:
  Commercial graphites.................... 0.5–2.5
  Vitreous carbon........................ 1–5
  Pyrolytic graphite...................... 0.5–500
Coefficient of thermal expansion, 10^{-6} deg^{-1}:
  Commercial graphites.................... 2–6
  Vitreous carbon........................ 2–4
  Pyrolytic graphite...................... <1–10
Thermal stability in contact with metals and oxides:
  W.................................... Carbide formation >1400°C
  Mo................................... Carbide formation >1200°C
  Ta................................... Carbide formation >1000°C
  Pt, Pd, Rh............................ Reactions at temperatures closely below the eutectic melting points
  Al................................... The molten metal forms carbides
  Si, Ti............................... The molten metals react rapidly and form nonvolatile carbides
  Cu, Be............................... Can be evaporated without reaction
  Alkali metals......................... The molten metals penetrate graphite and form compounds
  ThO_2................................ Reduction observed after 4 min at 2000°C
  BeO.................................. Reduction observed after 2 min at 2300°C
  ZrO_2................................ Reduction observed after 4 min at 1600°C
  MgO.................................. Reduction observed after 8 min at 1800°C

Ordinary commercial graphites have a large pore volume and are relatively soft. Pyrolytic graphite is denser and harder.   A relatively new material is vitreous carbon,[90] which is prepared by thermal decomposition of organic polymers.   Contrary to graphite, which has a dull surface and tends to flake or abrade easily, vitreous carbon has a high luster, does not flake, and yields conchoidal fractures.   Its density is relatively low because of a pore volume of about 30%.[91]   But the pores are of spherical shape and not accessible to gases; hence the material has a very small permeability even for helium.   The purity and ash content (<50 ppm) are superior to ordinary graphites (several hundred ppm).   Vitreous carbon has been recommended for melting of III-V compounds, tellurides, and MgF_2.   It is not wetted by molten aluminum and even resists the attack of molten Na_2O_2 for a limited time.   Although it appears quite promising as an evaporant-support material, very little has been reported to date about its actual usage.   Vitreous carbon is available in the form of crucibles or thin plates which can be machined.*

All carbon products are electrically conductive and may be resistance or induction heated.   They are also good heat conductors and have low coefficients of thermal expansion; hence their thermal shock resistance is excellent.   The various graphites can be machined into intricate shapes such as slotted bars or crucibles for direct resistance heating.   However, objects of small cross sections are fragile.

* For example, from The Plessey Company (U.K.) Ltd.; or from Gallard-Schlesinger Chemical Mfg. Corp., Carle Place, L.I., N.Y.

While the vapor pressure of carbon permits vacuum applications up to 2000°C, the practical limits are often much lower. As shown in Table 9, many metals including the refractories form carbides or eutectics at moderate temperatures. Another problem is the large internal surface area of ordinary graphites. The gases released upon heating are CO_2, CO, N_2, and H_2, and complete outgassing is obtained only at temperatures above 1700°C. In evaporating copper from graphite crucibles, the author encountered very persistent gas evolution, which was sufficiently violent to eject micron-size droplets of copper onto substrate surfaces at 20 in. distance. This difficulty should not occur with some of the denser "vacuum-tight" graphites.

A study of aluminum evaporation from graphite boats has been published by Moriya et al.[92] The molten metal wets graphite and flows over the brim, thus continually changing the effective evaporation area. The flow can be prevented by fitting the brim with an Al_2O_3 barrier since the contact angle between liquid aluminum and the oxide is nearly 90°. Another problem is the formation of Al_4C_3, which floats on the melt and thereby reduces the free surface area. The addition of 1 to 2% titanium to the melt was found to suppress this reaction. Finally, to achieve a constant liquid level for uniform evaporation rates, the charge was continually replenished by feeding aluminum wire into the boat. Wire-feed mechanisms are commercially available[93] and also useful to enhance the capacitance of small sources.[94,95]

The application of carbon heaters can be extended to materials which normally form carbides if ceramic inserts are used. As shown at the bottom of Table 9, the reduction temperatures of refractory oxides approach or exceed 2000°C. Boron nitride, too, is stable in contact with carbon. Hemmer and Piedmont[96] built the evaporation source shown in Fig. 20, which consisted of a dual-wall resistance-heated graphite cylinder with a boron nitride liner. The tantalum reflectors allowed temperatures of 2000°C to be obtained at 700 W power input. The maximum temperature achieved was 2600°C, and compounds such as SiO_2, CeO_2, and Si_3N_4 were evaporated. However, in view of the vapor pressure of carbon and the dissociation of BN, the resulting films were probably not very pure.
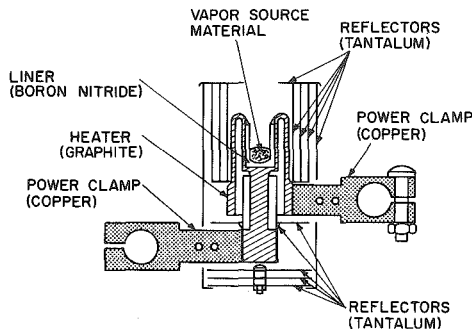
Fig. 20. Graphite evaporation source with boron nitride liner. (*After Hemmer and Piedmont.[96]*)

d. Electron-bombardment Heated Sources

Instead of supplying energy by resistance or induction heating, vaporization of substances can also be accomplished by electron bombardment. A stream of electrons is accelerated through fields of typically 5 to 10 kV and focused onto the evaporant surface. Upon impingement, most of the kinetic particle energy is converted into heat, and temperatures exceeding 3000°C may be obtained. Since the energy is imparted by charged particles, it can be concentrated on the evaporating surface while other portions of the evaporant are maintained at lower temperatures. Hence, interactions between evaporant and support materials are greatly reduced.

Experimentally, the method may be implemented in a number of ways. This is reflected in the great variety of source arrangements described in the literature and reviewed by Holland[97] and Behrndt.[60] The sources may be classified according to the modes of electron acceleration or by the techniques used to support the evaporant. The choice of the latter is fairly independent of the former and allows considerable freedom of combination, as will be illustrated by examples in each category.

Devices operating on the principle of electron-bombardment heating are referred to as electron guns. A hot cathode is universally employed as the electron source, with tungsten wire the preferred filament material because it retains its strength and shape at the high temperatures required for efficient electron emission.[98] The filament life is limited by possible reactions with the evaporant vapors and by sputtering due to impingement of high-energy positive ions. Hence, electron guns should be constructed so that the filament can be replaced easily.

A potential of several kilovolts is needed to accelerate the electrons emitted from the cathode. If the electric field is maintained between the cathode and the evaporant (the "work"), the structure is called work-accelerated. The alternative is self-accelerated guns. These have a separate anode with an aperture through which the electron beam passes toward the work. The electron energy is sufficient to ionize residual gas or evaporant molecules encountered along the way. Since ionization causes loss of beam energy and focus, the pressure in the vacuum chamber must be below 10^{-4} Torr. Additional problems due to ionization are specific for particular types of gun structures.

(1) Work-accelerated Electron Guns Typically, work-accelerated structures have a hot cathode in form of a wire loop in close proximity to the evaporant. The electrons converge radially upon the work. The simplest arrangement is the pendant-drop configuration introduced by Holland[99] and shown in Fig. 21a. The metal to be evaporated must be in rod or wire form and centered within the cathode loop. Evaporation takes place from the molten tip, and the substrates are located below the source. The drop of molten metal at the tip is held by its surface tension and requires careful control of the electric energy supplied. If the drop temperature exceeds the melting point too far, the metal rod melts back and the drop falls off. Therefore, applicability of the method is limited to metals with high surface tension and vapor
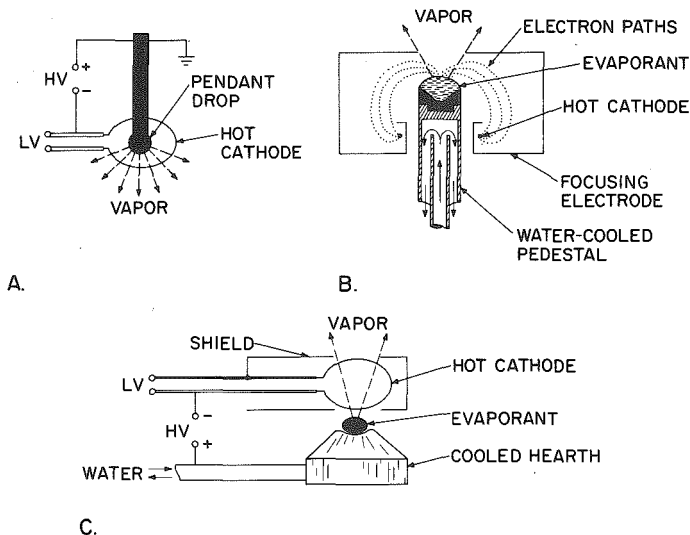
Fig. 21 Work-accelerated electron-bombardment sources. (A) Pendant-drop method. (B) Shielded filament (Unvala[103]). (C) Shielded filament (Chopra and Randlett[104]).

pressures greater than 10^{-3} Torr at their melting points. The evaporation rates from molten drops of maximum supportable size have been measured by Heavens.[100] They decrease in the order Fe, W, Ni, Ta, Ag, Mo, Pt. Titanium[97] and zirconium[101] are also amenable to this technique.

In addition to being rate-limited, the pendant-drop method poses other difficulties. Some of these are apparent in a more complex design described by Milleron.[102] In this version, Mo or Ti wire is supplied from a spool and fed upward through a cooled copper tip which aids in maintaining a stable molten ball of metal. The wire-feed rate and the power input must be matched to the evaporation rate as determined by the vapor pressure and size of the molten drop. Heavy outgassing upon melting is suppressed by resistance heating of the wire on its way up from the spool to the guiding tip.

Another problem arises from exposure of the cathode to high vapor densities generated by the hot source. The resulting ionization leads to cathode erosion by sputtering with ensuing film contamination. To avoid these difficulties, it has become customary to offset the cathode filament away from the work and to surround it by metal shields. These are arranged so that straight line-of-sight transmission from the filament to the source as well as to the substrates is eliminated. Furthermore, the shields are at cathode potential to repel electrons and force them into curved paths ending on the evaporant.

Although cathode shielding and electrostatic focusing have been used in conjunction with the pendant-drop method,[101] it has found much wider application in work-accelerated guns with water-cooled supports. As shown in Fig. 21b and c, the cathode loop may be below (Unvala and Booker[103]) or above (Chopra and Randlett[104]) the work. Configurations similar to Fig. 21c are relatively easy to implement and have been used to evaporate such metals as Ta,[105] Si,[71] and Mo.[106] The high voltage is generally applied to the cathode, whose power supply must therefore be electrically insulated, while the evaporant support is grounded. If the cathode is grounded, the strongest electric field coincides with the region of highest vapor density surrounding the work, a condition which often results in a glow discharge.

Even with the potential applied to the cathode, work-accelerated guns are rate-limited because the vapor density decreases only moderately across the short distance between source and filament. The ionization of vapor within the electrostatic shield produces a space charge which reduces the accelerating voltage. At higher evaporation rates, a glow discharge between the cathode and the bell-jar walls may be established. This instability makes the control of power input and evaporation rates somewhat difficult. The close proximity of vapor source and filament shield is also responsible for heavy accumulation of deposits on parts of the shield. Hence, frequent cleaning or change of shields is necessary. To avoid these shortcomings, electron guns have been designed where the cathode and accelerating structure are remote from the evaporant source.

(2) Self-accelerated Electron Guns This class of guns is similar to and actually evolved from x-ray tubes. A small tungsten helix or hairpin filament constitutes the electron source. Rough focusing may be achieved electrostatically by means of a cylindrical shield and an anode disk as shown in Fig. 22a. The space between the anode and the work is field-free. Increased pressure due to outgassing in the anode-cathode region, however, may lead to ionization and defocusing. If the beam is to traverse longer distances, or focusing into a very small spot is desired, better control is obtained with a magnetic lens. An example is shown in Fig. 22b, where the electron beam is focused by a negatively biased filament shield, a conical anode, and a magnetic coil. For purposes of evaporation, focal spots of a few millimeters diameter are used. Telefocus guns of the type shown in Fig. 22b have been successfully employed to evaporate refractory metals such as Nb[109] or Ta[110] which require temperatures above 3000°C. Their history and design have been reviewed by Denton and Greene.[108] Thun and Ramsey[111] developed a different gun structure which utilized only electrostatic focusing between spherically shaped cathode and anode surfaces.

Contrary to work-accelerated guns, which operate with voltages of less than 10 kV, considerably higher voltages are used in telefocus guns. Consequently, the danger

of x-rays emanating from the vacuum system must be considered.   Aluminum or glass walls absorb x-rays generated by electrons of up to about 10 keV energy.   Radiation generated by more energetic electrons is only partially retained by stainless-steel walls.[98]   It is therefore advisable to monitor the radiation near high-energy electron-gun evaporation systems and to use lead shields if necessary.
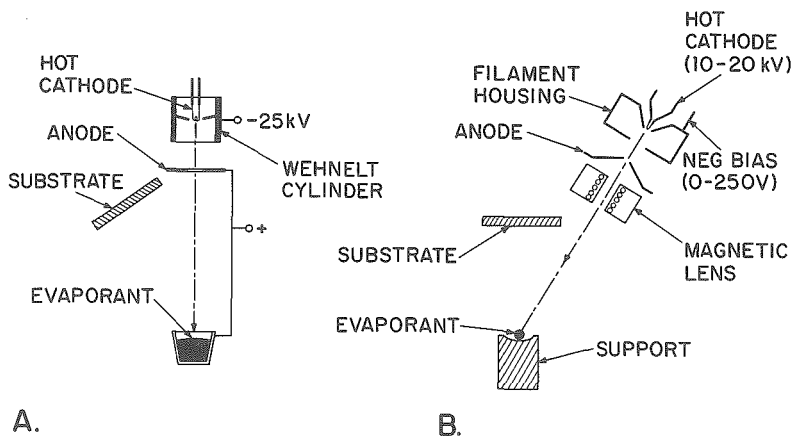
Fig. 22 Self-accelerated electron guns. (*A*) Electrostatically focused. (*Reichelt and Mueller.*[107])   (*B*) Electrostatically and magnetically focused. (*Denton and Greene.*[108])

(3) Bent-beam Electron Guns   In the electron guns shown in Fig. 22, the path of the electron beam is a straight line.   Therefore, either the gun or the substrates must be mounted off to the side.   This restriction in the arrangement of electron source and substrate can be removed by bending the electron beam through a transverse magnetic field.[108]   Forcing the electrons into curved paths also allows effective separation of gun structure and vapor source without resorting to long distances.   This possibility was first realized by Holland,[99] and compact electron guns which combine the advantages of other structures have been developed since.

An example of a bent-beam electron gun is shown in Fig. 23.   The transverse field is provided by an electromagnet which permits focusing during operation.   Other models have permanent magnets and variable operating voltage to adjust the beam.   Relatively large area elongated cathodes are employed to increase the electron-emission current.   This facilitates gun operation at voltages below 10 kV without sacrificing power.   The cathode, although close to the evaporant, is in an offset position and shielded, hence protected against deposits and erosion by ion bombardment.
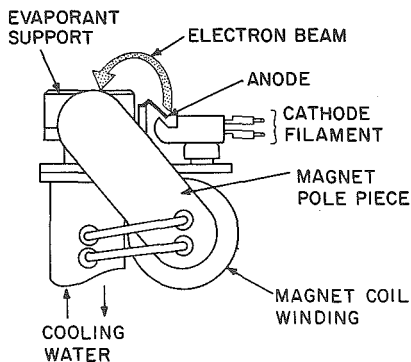
Fig. 23 Bent-beam electron gun with water-cooled evaporant support. (*With permission of Temescal Metallurgical Co., Berkeley, Calif.*)

Work-accelerated guns similar to those shown in Fig. 21*b* and *c* as well as telefocus structures of the types shown in Fig. 22 are commercially available.   For laboratory- and bell-jar-type operations, however, the bent-beam guns have become most popular

because they are compact, of universal applicability, and not rate-limited. Commercial models offer powers between 2 and 10 kW with accelerating voltages from 3 to 10 kV. They all use a water-cooled copper hearth to support the evaporant, and most of the guns are bakeable to facilitate outgassing. Depending upon the degree of thermal contact between evaporant and support, temperatures up to 3500°C may be achieved so that refractory metals as well as oxides can be evaporated.

A general problem encountered in electron-gun evaporation is rate monitoring. The uncontrolled generation of positive ions interferes with the performance of most ionization-rate monitors. Crystal-oscillator monitors, too, tend to give erroneous rate indications because of the accumulation of charges. However, it is possible to remove charged particles from the vapor entering the monitoring device by means of an electrostatic grid. Stray electrons may also be collected by the substrates and, if these are insulating, establish potentials of several hundred volts. Rairden and Neugebauer[112] observed catastrophic discharges associated with surface damage upon formation of a thin continuous metal film. This can be avoided if the substrates are either allowed to float electrically or kept at the filament potential. The latter situation results in a moderate substrate bombardment by positive ions, which may improve film purity but also affects nucleation and growth processes.[104]

(4) Evaporant Support and Materials   The various methods of supporting materials during electron-bombardment heating have already been introduced in Figs. 21 to 23. Because of the limitations of the pendant-drop technique, the water-cooled copper hearth is the preferred type of support. Although the evaporant is in contact with the support surface, chemical interaction is negligible. This is due to the fact that a "skull" of solid evaporant is maintained at the interface and separates the melt from the support.[113] Overheating and spreading of such a molten button may, however, lead to excessive heat losses and reduced evaporation rates. As shown in Fig. 21b, Unvala and Booker[103] avoided this problem by evaporating from a short rod to separate the molten surface from the pedestal. Denton and Greene[108] used a massive tungsten heat sink without water cooling, but the duration of the experiment had to be limited to a few minutes. Siddall and Probyn[114] reduced heat losses by employing refractory compound rather than metal hearths.

The advantage of evaporation without support interaction is lost if the container is allowed to heat up or if the vaporization energy is supplied indirectly by bombarding the crucible. The choice of support materials for a given evaporant is then subject to the same rules as in resistance or induction heating. Yet, electron-beam heating sometimes offers other advantages such as greater simplicity of construction, more directional heat supply, or less stirring of the melt. Examples are the evaporation of Ni and Fe from molybdenum crucibles lined with Al_2O_3 or ZrO_2,[115] of Ge from SiO_2[107] or tungsten[116] containers, and of Be, Cu, Au from BeO, Al_2O_3, or ZrO_2 crucibles.[117] Electron-bombardment heating of dimpled molybdenum and tantalum boats[118] as well as the use of graphite crucibles[111] have also been described.

Electron-bombardment heating may be used to evaporate compounds, provided these do not decompose upon heating. This problem is discussed in more detail in Sec. 6 of this chapter. Examples of compounds which have been evaporated from electron guns are SiO, SiO_2, MgF_2, Al_2O_3, CeO_2, TiO_2, ZrO_2,[108] and ZnS.[119] When dielectric materials are evaporated, it is necessary to use an electrically conductive support to avoid accumulation of charges and deflection of oncoming electrons.

Although electron-bombardment heating is a very versatile and almost universal evaporation technique, it is generally not chosen if the more easily controlled alternative of resistance heating is available. The method is of practical importance in those cases where the greatest film purity is desired and no suitable support material exists. Examples are the evaporation of expitaxial silicon films[103] and of high-purity refractory metals such as Ta, Nb, W, and Mo[109,110,112,120] which require temperatures between 3000 and 3500°C. Of special interest are also the evaporation of carbon[121] and of boron[122] by means of electron bombardment. Finally, electron guns with water-cooled hearths are used with increasing frequency to evaporate platinum metals as well as some of the more reactive metals like Al, Ni, and Fe.

5. THICKNESS DISTRIBUTION OF EVAPORATED FILMS

In addition to materials and modes of construction, an important consideration in the design of vapor sources is their emission characteristics. The latter manifests itself in the distribution of condensate on the substrates. Since most practical applications require a certain film thickness, the substrate area which can be covered uniformly is a significant figure of merit for vapor sources. Assuming condensation coefficients of $\alpha_c = 1$, the distribution of deposits can be derived in principle from the emission laws, Eqs. (51) and (52) in Sec. 3c. In practice, however, it is found that the emission patterns of many useful sources deviate from the idealized behavior. The causes of such modified emission patterns are collisions of evaporant molecules among each other and with walls constituting part of the source. The mathematical formulation of modified emission laws has often been attempted but is difficult, and the resulting expressions apply only to effusion cells with well-defined orifices. No emission theory exists for sources of the open-crucible type, and their behavior can be discussed only on an empirical basis.

a. Thickness Profiles Resulting from the Basic Emission Laws

The distribution of evaporated material is given by Eqs. (52) and (54) (Sec. 3c) as a function of source-to-substrate distance and angle of incidence. Hence, thickness profiles can be derived for substrate areas of any given shape or position relative to the source. Normally, however, the substrates are planar and parallel to the plane of the emitting surface, and only this case is treated here.
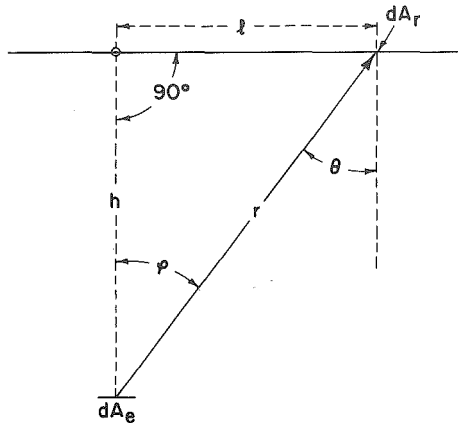
Fig. 24 Evaporation onto a plane-parallel receiver.

(1) Small Surface and Point Sources The mass received at a point on the substrate defined in terms of r, φ, and θ is given directly by Eqs. (52) and (54). To convert mass into film thickness d, one may visualize the small mass $d\mathfrak{M}_r$ occupying a volume of $dA_r\, d$. If ρ is the density of the film material, then

$$d = \frac{1}{\rho} \frac{d\mathfrak{M}_r}{dA_r} \tag{55}$$

For a plane-parallel receiver at a distance h from the source, the angle of incidence θ equals the emission angle φ, and $\cos \theta = \cos \varphi = h/r$ as shown in Fig. 24. The evaporation distance r for a surface element dA_r varies with the distance l from the center of the substrate area according to $r^2 = h^2 + l^2$. Substituting these relations and Eq. (55) into Eqs. (52) and (54) yields

For the small-area source:

$$d = \frac{\mathfrak{M}_e}{\pi \rho h^2 [1 + (l/h)^2]^2}$$

For the point source:

$$d = \frac{\mathfrak{M}_e}{4\pi \rho h^2 [1 + (l/h)^2]^{\frac{3}{2}}}$$

Since both sources have infinitesimally small evaporation areas dA_e, the evaporated mass $\mathfrak{M}_e$ and hence d, too, are differential quantities. Without assuming that Eqs. (52) and (54) also apply for small but finite areas, the emission characteristics of the two source types may be defined in terms of the ratio d/d_0, where d_0 is the center thickness at $l = 0$ (see Fig. 24). This leads to the expressions

For the small-area source:

$$\frac{d}{d_0} = \left[1 + \left(\frac{l}{h}\right)^2 \right]^{-2} \tag{56}$$

For the point source:

$$\frac{d}{d_0} = \left[1 + \left(\frac{l}{h}\right)^2 \right]^{-\frac{3}{2}} \tag{57}$$

The thickness distributions corresponding to Eqs. (56) and (57) are shown in Fig. 25. Because of the smaller negative exponent, the thickness obtained from a point source decreases less rapidly than that of a small-surface source. Characteristic for the small-surface source is a thickness decrease of 2% at a center distance l equal to 10% of the evaporation distance h.
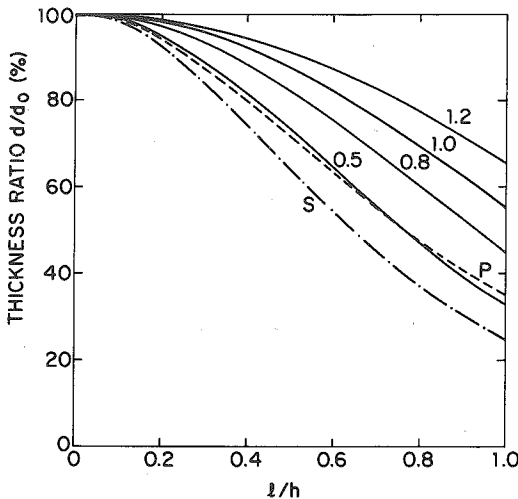
Fig. 25 Film-thickness distributions for a small-surface source (S) and a point source (P). The drawn lines are profiles for circular-disk sources, whereby the numbers indicate the ratios of source radius to substrate distance s/h.

(2) Ring and Circular-disk Sources In practice evaporations are performed with sources whose evaporating surfaces are not vanishingly small. The distributions obtained from sources of finite dimensions can be derived by integrating Eqs. (51a) and (53a) in Sec. 3c, i.e., by adding the thickness increments received at one point from all emitting elements dA_e. In doing so it is assumed that the entire source surface emits at a uniform rate Γ. Such integrations have been performed by Steckel-

macher and Holland[123] for infinitely thin linear and ring-shaped sources consisting of many emitting points or surface elements. The case of a truly two-dimensional evaporation source was first solved by von Hippel[124] and is treated in the following part.

The source is assumed to be a circular disk of radius s emitting toward a plane-parallel receiver. Therefore, the distribution of material on the substrate plane is centrosymmetrical and can be described by one coordinate, the center distance l. The arrangement is shown schematically in Fig. 26. A particular emitting element representing a small fraction of a thin ring may be expressed as $dA_e = s\,d\alpha\,ds$, where α is the angle between l and the projection of s onto the substrate plane. Since the latter is parallel to the source plane, it is again $\cos\varphi = \cos\theta = h/r$. Substituting
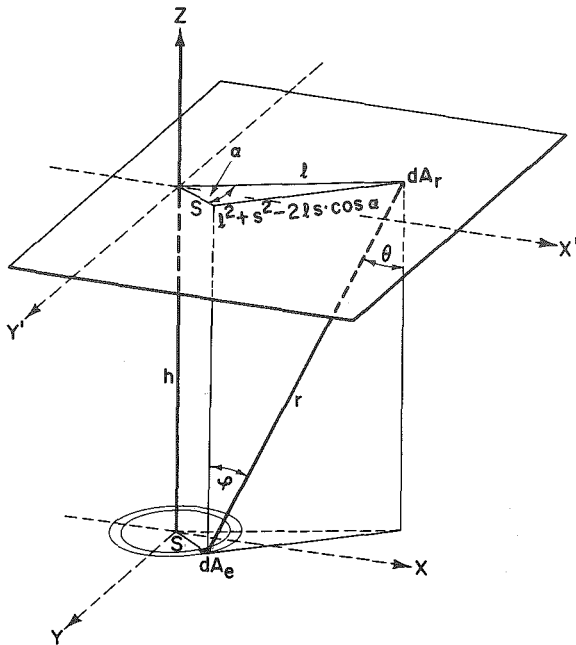
Fig. 26 Evaporation from an element dA_e of a ring to a point dA_r on the substrate plane x', y'.

this relationship and Eq. (55) into the small-surface source Eq. (52), the thickness received from a disk source is given by

$$d = \iiint\limits_{t,s,\alpha} \frac{\Gamma s\,d\alpha\,ds}{\pi\rho}\frac{h^2}{r^4}\,dt$$

The triple integral arises from Eq. (49) [Sec. 3a(2)] since the total evaporated mass $\mathfrak{M}_e$ of all surface elements dA_e and their time dependence must be considered. After substituting the evaporation distance r by quantities which characterize the position of the receiving point relative to the source, $r^2 = h^2 + l^2 + s^2 - 2ls\cos\alpha$ (see Fig. 26), integration over α from 0 to 2π can be performed. From the resulting expression

$$d = \iint\limits_{t,s} \frac{2\Gamma h^2}{\rho}\frac{h^2 + l^2 + s^2}{[(h^2 - l^2 + s^2)^2 + (2lh)^2]^{\frac{3}{2}}}\,s\,ds\,dt \qquad (58)$$

the distribution obtained from an infinitely thin ring source is easily derived since $2\pi s \, ds \int_t \Gamma \, dt = \mathfrak{M}_e$ is the total mass evaporated from such a source. Therefore, Eq. (58) becomes

$$d = \frac{\mathfrak{M}_e}{\pi \rho h^2} \frac{1 + (l/h)^2 + (s/h)^2}{\{[1 - (l/h)^2 + (s/h)^2]^2 + 4(l/h)^2\}^{\frac{3}{2}}} \qquad \text{for thin-ring-surface sources} \quad (59)$$

The thickness uniformity resulting from thin-ring-surface sources is again best described by introducing the center thickness (at $l = 0$)

$$d_0 = \frac{\mathfrak{M}_e}{\pi \rho h^2} \frac{1}{[1 + (s/h)^2]^2} \qquad (60)$$

and forming the ratio d/d_0. In addition to the relative center distance l/h, Eqs. (59) and (60) contain a second parameter, the relative source radius s/h. Machine-calculated distributions for thin-ring-surface sources having large ratios of s/h are
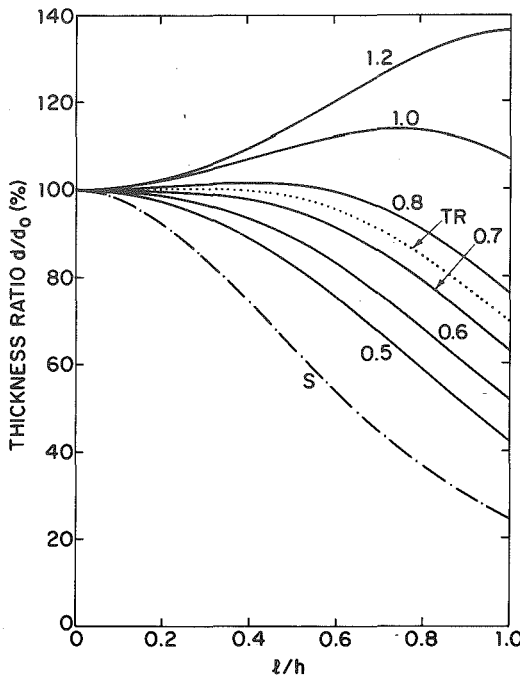
Fig. 27 Film-thickness distributions for a small-surface source (S) and for infinitesimally thin ring-surface sources (drawn lines). The numbers indicate the ratios of source radius s to shortest evaporation distance h. The dotted curve TR represents a ring source of finite dimensions with an inner radius $s_i = 0.7h$ and an outer radius $s_o = 0.8h$.

shown in Fig. 27. If the source radius is relatively small ($s \leqq 0.1h$), the ring-source distributions are nearly the same as obtained from a single-element-surface source. This conclusion can be derived from Eq. (59) directly by assuming $(s/h)^2 \ll 1$. Substantial improvements in thickness uniformity across large substrate areas result only if ring sources are employed whose diameter is comparable with the source-to-substrate spacing h. The most uniform thickness around the center of the substrate area is obtained with $s/h = 0.7$ to 0.8. At larger radii, the throw of ring sources

toward the substrate center becomes smaller than the emission toward more periph-
eral areas.

To continue the derivation of material distributions for circular-disk sources,
Eq. (58) must be integrated over the disk radius s. Integration by parts yields

$$d = \int_t \frac{\Gamma}{2\rho} \left[1 - \frac{h^2 + l^2 - s^2}{\sqrt{(h^2 - l^2 + s^2)^2 + (2lh)^2}} \right] dt \tag{61}$$

In this case, the total evaporated mass $\mathfrak{M}_e$ can be substituted for Γ according to
$\mathfrak{M}_e = \pi s^2 \int_t \Gamma \, dt$, which gives the thickness expressions for circular-disk sources:

$$d = \frac{\mathfrak{M}_e}{2\pi\rho s^2} \left\{ 1 - \frac{1 + (l/h)^2 - (s/h)^2}{\sqrt{[1 - (l/h)^2 + (s/h)^2]^2 + 4(l/h)^2}} \right\} \tag{62}$$

and

$$d_0 = \frac{\mathfrak{M}_e}{2\pi\rho s^2} \frac{2(s/h)^2}{1 + (s/h)^2}$$

Machine-calculated thickness distributions for disk sources of comparatively large
diameters are shown in Fig. 25. Surprisingly, a source of radius $s = 0.5h$ yields
a distribution which is similar to that of a single-point source. Further increases of
the source radius contribute toward better thickness uniformity around the center but
not as effectively as ring sources. For small-diameter-disk sources, Eq. (62) can be
approximated by a series development which leads to

$$\frac{d}{d_0} \approx \frac{1 + (s/h)^2}{[1 + (l/h)^2]^2 + [1 - (l/h)^2](s/h)^2} \qquad \text{for } s \leqq 0.1h$$

Numerical evaluation of this expression gives distributions which are within a few
tenths of 1 % of the single-surface-element source.

Equation (62) may also be used to derive distributions for ring sources of finite width
by subtracting the emission of an inner disk from that of an outer disk. The profile
resulting from such a "true" ring source of optimum dimensions ($s = 0.7$ to $0.8h$)
is indicated in Fig. 27 (dotted line, TR). Although the width of this source is rela-
tively large, the distribution is very similar to that which an infinitely thin ring of
$s = 0.75h$ would yield.

In conclusion, the thickness distributions obtained from disk and ring sources whose
diameters or widths are finite but smaller than the source-to-substrate spacing are
adequately represented by the formulas derived for single-element and thin-ring-
surface sources. While large-diameter ring sources produce uniform film thickness
over a much greater deposition area than a small source at the center, one cannot
improve the deposit distribution significantly by enlarging the size of an ordinary flat
filament or crucible source. The advantage of a source with a large evaporation sur-
face is primarily the attainment of reasonably high deposition rates at moderate
filament temperatures with correspondingly low vapor pressures. Thereby, the
chances of chemical interaction between the evaporant and the container material are
also reduced.

b. Emission Characteristics of Practical Vapor Sources

In applying the results of the previous section to practical source design, limitations
are encountered which are best illustrated by an example. In order to obtain a deposi-
tion rate of 10 Å s^{-1} for a material of density $\rho = 10$ g cm^{-3} with an assumed mass
evaporation rate of $\Gamma = 10^{-4}$ g cm^{-2} s^{-1}, which would be typical for an evaporant
pressure $p^* = 10^{-2}$ Torr, one needs a disk source with a radius of $s = 0.1h$ according
to Eq. (61). Since source-to-substrate distances in bell-jar systems are usually of the
order of 10 in. or larger, a source with a diameter amounting to 20 % of that distance
poses several problems: It is difficult to maintain a uniform evaporation temperature
across such a large area; the radiation heat losses are likely to overtax the capability
of the power supply, and they will also cause outgassing of various surfaces inside the
system. For these reasons, relatively small area sources are nearly always used,

and one may conclude that evaporant pressures in excess of 10^{-2} Torr occur frequently in practical deposition processes. Such high vapor densities in the immediate vicinity of the source cause reduced evaporation rates because of back diffusion, and deviations from the basic emission law due to the scattering of colliding molecules. These problems are aggravated if the source is not flat but has sidewalls to enhance the evaporant capacity.

(1) Approximate Small-area and Point Sources There are several evaporation sources whose distribution patterns follow the basic emission laws. Flat metal strips or shallow dimpled boats of the type shown in Fig. 13d and e, for example, have repeatedly been found to yield cosine-law emission.[125,126] Even if the molten evaporant does not wet the filament but forms an approximate sphere as does silver on tungsten, the emission characteristics of the small-surface source are still maintained. This is attributable to the fact that vapor molecules impinging on the hot filament surface are adsorbed and reemitted diffusely within a time period corresponding roughly to the Debye frequency of the lattice of the filament material.[127] Consequently, hot surfaces which are not in contact with the condensed evaporant phase but are exposed to its vapor act effectively as extensions of the emitting surface. As long as these surfaces are within the source plane, no deviations from the cosine emission law result. This is still true if the plane of the source is not perfectly parallel to the substrate plane but is tilted. However, the latter condition affects the symmetry of the distribution around the center of the substrate area.[126]

Distributions approaching that of an ideal point source are obtained from two configurations. One is the hairpin filament shown in Fig. 13a; the other is the pendant-drop arrangement shown in Fig. 21a. Both sources are of limited practical value, either because the source capacity is too small or because the instability of the drop does not permit sufficiently high evaporation temperatures. The small surface of such sources prevents the attainment of high evaporation rates in principle.

(2) Effusion Cells Directional emission patterns which do not obey the cosine law but favor the substrate region opposite to the source ("beaming") were first investigated in conjunction with the effusion of gases from nonideal orifices. Clausing[128] derived a distribution equation for effusion from short tubes which is based on cosine-law emission but modified to account for the effect of tube walls preventing direct passage of some of the molecules. The resulting distributions have cusp-shaped maxima in the center and fall off more rapidly at higher emission angles than the straight cosine-law distribution. While fairly successful in describing the effusion of gases, Clausing's approach has often been modified for orifices of different shapes or to achieve a more adequate representation of observed distribution patterns. A review of this subject may be found in Dushman's book.[21]

As for evaporant distributions emanating from effusion cells, Clausing's formula is at best an approximation. This is due to the many forms of molecular interaction—within the orifice, in the beam, with residual gases, and on neighboring surfaces—which cannot always be prevented and whose effects on the emission pattern are difficult to assess quantitatively. An illustrative example is the complex evaporation mechanism suggested by Ruth and Hirth,[129] which takes into account adsorption, surface diffusion, and desorption of evaporant vapor in the orifice region. As a result of this interaction with the walls, the evaporant beam contains molecules of different history. There are those which come directly from the interior of the effusion cell. Others have been adsorbed on the orifice walls, diffused toward the opening, and reemitted. A third fraction arises from the fact that the concentration of adsorbed molecules does not decrease to zero at the upper orifice rim. Instead, the diffusion process continues and covers part of the outer lid surface, where further desorption occurs. Assuming diffuse reemission of adsorbed molecules according to the cosine law, the authors used machine calculations to determine emission patterns of SiO for various shapes of effusion openings. Their results for a tubular opening of equal length and diameter are shown in Fig. 28 and demonstrate that the contributions of adsorbed and reemitted molecules are far from negligible. Moreover, the computed curve agrees very well with SiO effusion measurements carried out independently by Guenther.[130] Figure 28 also shows Clausing's distribution, which was calculated

for the same type of tubular opening but does not take into account surface diffusion and yields an exaggeratedly steep thickness decrease.
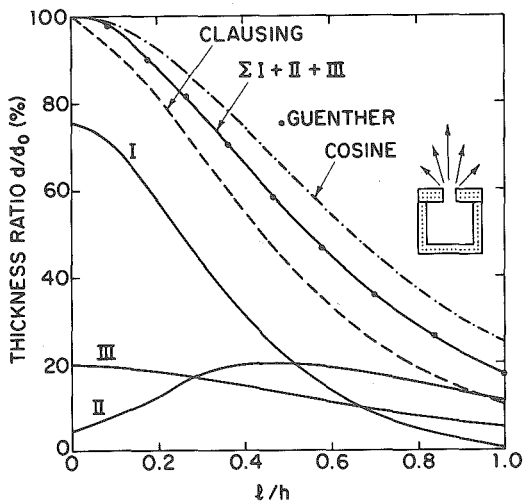
Fig. 28   Thickness distributions for a short tubular orifice (length = diameter).   After Clausing,[128] experimental points from Guenther,[130] and calculated for Guenther's effusion cell by Ruth and Hirth[129]: I = direct effusion from the interior of the cell; II = reemitted from the orifice wall; III = diffused onto and reemitted from the lid of the effusion cell.

The curvature and steepness of the profiles in Fig. 28, however, cannot be generalized.   Learn and Spriggs,[131] for example, found a distribution for lead and tin vapor effusing from a tubular opening, which falls off even more rapidly than Clausing's equation applied to their case would yield.   The factors which, in addition to sorption and surface diffusion, cause deviations from the ideal cosine effusion are not fully understood as yet.   Ehrler and Kraus[132] conducted effusion experiments with SiO at cell pressures in excess of 10^{-1} Torr.   They observed not only beam dispersion but also a distribution of molecular speeds which was narrower than the Maxwellian. They argue that both effects are due to scattering within the relatively dense molecular beam where molecules collide as the faster ones try to pass slower particles and thus bring about deflection as well as a tendency to assume more uniform speeds.   Another factor pertaining to the evaporation of compounds such as KCl, which enter the gas phase partly as monomer, partly as di- and trimer molecules, was recently reported by Grimley and LaRue.[133]   For the same effusion cell, they observed different angular flux distributions for the different molecular species as well as a dependence on cell temperature.

In conclusion, the only generalization presently possible is that emission patterns from effusion cells tend to be more directional and have a more pointed maximum in the center than the cosine emission pattern.   The severity of the effect is strongly influenced by the orifice geometry, but other factors such as molecular species, cell temperature, and vapor density, too, play a role.

(3) Surface Sources with Perpendicular Sidewalls   This category includes most practical sources, particularly the various crucible types, since sidewalls in one form or another are required to hold evaporant quantities in excess of a few grams.   As previously discussed, hot surfaces exposed to evaporant vapors act as extended emitting surfaces.   If these protrude from the primary source plane, they are likely to affect the emission pattern through sorption and surface-diffusion processes like effusion orifice walls.   Contrary to effusion cells, however, typical crucible sources

have openings which are as large as the evaporating surface, and the evaporant pressure inside is below the equilibrium value corresponding to the source temperature. Therefore, one would expect only moderate beaming effects from relatively short crucible sources. This is indeed the case. A crucible-source distribution reported by Behrndt and Jones,[134] for example, shows only slight deviations from the cosine law near the substrate center and falls off somewhat more rapidly toward the periphery. The chromium sublimation source shown in Fig. 14, although considerably deeper, is also only slightly directional. The long and narrow inner tube of the Drumheller SiO source, however, has a strong beaming effect and yields an emission pattern which resembles a Clausing distribution.[126]

An interesting source and its distribution have been reported by Spriggs and Learn.[135] These authors evaporated CdS from an array of cylindrical bores in a relatively large ($s/h \approx 0.25$) molybdenum block. The thickness profiles obtained deviate noticeably from the cosine distribution at distances $l > 0.4h$. Beaming also manifests itself in deposition rates around the center which are about twice as high as the calculated values. The effect of the source walls is further enhanced because CdS is a poor heat conductor and therefore evaporates predominantly from the hot walls rather than from the entire cross section of the bores. The latter phenomenon produced a doughnut-shaped thickness profile if the evaporant beam from a single bore was made to pass through a small aperture some distance above the source.

The effects of obstacles in the vapor path, either alone or in conjunction with high residual gas pressure, have been investigated by Rohn.[136] When evaporating LiF from a small surface source at a residual gas pressure of 10^{-4} Torr, he obtained a nearly perfect cosine distribution. Under these conditions, a small obstacle in the form of a wire loop placed in the vapor stream as shown in Fig. 29 did not distort
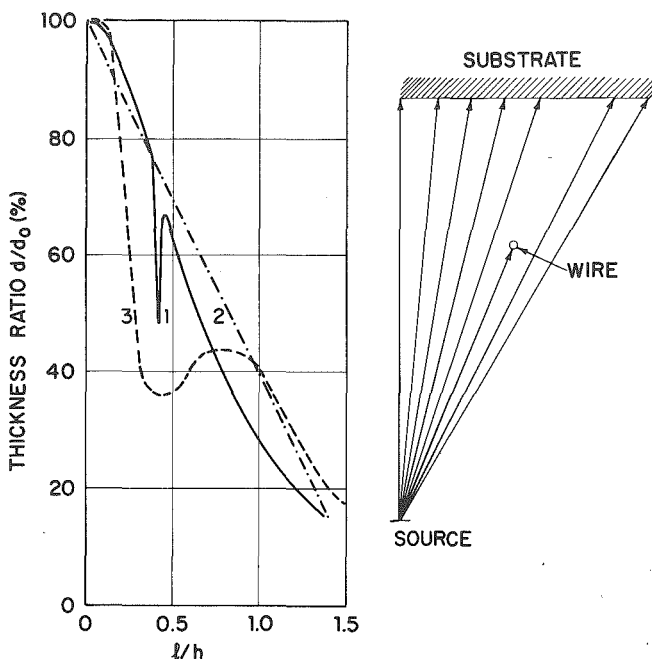
Fig. 29 Distribution profiles as affected by a heated wire and increased gas pressure. (*After Rohn.*[136]) 1. Residual gas pressure $< 10^{-4}$ Torr, wire hot or cold. 2. Residual gas pressure $= 10^{-1}$ Torr, wire cold. 3. Residual gas pressure $= 10^{-1}$ Torr, wire heated.

the cosine distribution except for casting a geometrical shadow.   If the residual gas pressure was raised to 10^{-1} Torr without heating the wire, the evaporant molecules were scattered toward larger emission angles and gave an almost linear thickness profile as shown by curve 2 in Fig. 29.   Very strong beaming as represented by curve 3 was obtained by heating the wire at 10^{-1} Torr gas pressure.   The drastic distortion of this profile and the relatively flat (not cusp-shaped) thickness profile around the center spot are clearly not due to vapor adsorption and reemission from the surface of the wire loop.   Instead, the effect must be attributed to rising currents of hot gas generated by the wire loop ("chimney action").   A hot crucible wall around a surface from which evaporation takes place at relatively high vapor pressures may cause similar thermal currents and thereby distort the basic emission pattern.

The combined effects of reemission from sidewalls, intermolecular collisions, thermal currents, and nonuniform temperature of different source parts are generally not predictable.   Hence, an empirical approach to source design is often necessary and may, through minor variations of the source geometry, lead to more uniform distributions.   An example is the two thickness profiles in Fig. 30 which were obtained by flash evaporation of Cr-SiO pellets.[137]   The complete flash filament is shown in Sec. 6c(3), Fig. 43.   Evaporation of the pellets occurs almost exclusively from the flat bottom (filament) of the source, but the sidewalls necessary to prevent ejection of the evaporant exert a significant influence on the shape of the profile.   It is estimated that the pellet feed rates (about 1 g min^{-1}) generate momentary and local evaporant pressures in excess of 2.10^{-1} Torr.   Consequently, interactions with the walls as well as in the released vapor itself can be substantial.   Comparison of the two profiles in Fig. 30 shows a significant reduction of the beaming effect if the deflection shield is conical and thus offers a wider path for the vapor bursts.   The absolute evaporation rates reflect the degree of beaming insofar as the cylindrical shield yielded center
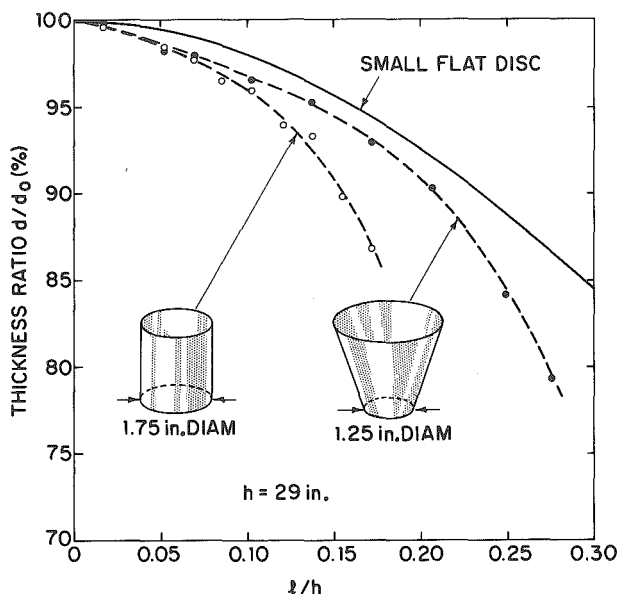
Fig. 30 Thickness profiles obtained by flash evaporation of sintered Cr-20 at. % SiO pellets from cylindrical and cone-shaped crucible sources.   For comparison, the regular cosine-law distribution expected from a small flat disk is also shown.

thicknesses of 1.45 times the value calculated from Eq. (62), whereas the cone-shaped source gave 1.35 times the theoretical maximum.

In this context, an observation of Beavitt, Turnell, and Campbell[138] is of interest. When flash-evaporating gold from a filament at 2000°C, these authors found a particle-speed distribution in the vapor that was narrower than the Maxwellian. This result is similar to Ehrler and Kraus'[132] findings for the effusion of SiO at high pressures, and if interpreted in terms of their concept, one would conclude that flash evaporation is especially inducive to heavy molecular interaction in the vapor.

In conclusion, the most uniform thickness distributions which one can hope to attain with small-area crucible or similar sources are slightly inferior to or at best approach those of flat-surface sources. While moderate improvements in uniformity can be achieved by making the ratio of sidewall height to source diameter as small as possible, the most effective measure is to increase the evaporation distance and thereby enlarge the relatively uniform area circumscribed by incidence angles near 0°. This method is, of course, limited by the available system dimensions and by the absolute rates which the source can produce. Therefore, different source arrangements capable of yielding better uniformity are of considerable interest.

c. Sources for Uniform Coverage of Large Areas

Successful attempts to achieve uniform large-area coverage are almost all based on the emission patterns obtained from large-diameter ring sources and have been reviewed by Behrndt.[139] In its simplest form a ring source consists of a circular wire loop emitting material from its entire surface. The integration of the emission flux from such a wire-ring source has been performed by Oberg et al.,[140] while Bugenis and Preuss[141] measured actual thickness profiles of evaporated gold films containing a radioactive isotope. They found slightly greater thickness variations and center thicknesses than Oberg's formula predicts, both indications of possible beaming effects or, as suggested by the authors, due to deviations of the source geometry from the ideal circular shape and planar position. Behrndt and coworkers[134,142-145] experimented extensively with more complex configurations such as multiple rings and crisscrossing wires to obtain uniform large-area coverage with Ni-Fe films. Although film-thickness variations as low as ±1% over substrate areas of several inches diameter could be achieved, these types of wire sources are difficult to operate and limited in their application to those metals which can either be sublimated or loaded uniformly onto refractory-metal wires. Therefore, alternate possibilities to produce distributions similar to those of ring sources have been studied.

One approach to achieve uniform coverage utilizes a rotating shutter in the evaporant beam to alter the amount of vapor admitted to the substrate.[146] Evaporations may be performed from crucibles, which are the most universal sources, and the resulting emission patterns are modified by the contour of the shutter. It is essential that the axis of rotation coincides with the centers of the source and the substrate area. The design of the shutter is determined by the distribution pattern of the source and the size of the area to be coated. To minimize the inevitable reduction of evaporation rates, no material is intercepted at the most peripheral points of the deposition area. From there toward the geometrical center, the shutter blade must represent arcs of increasing length such that the amount of material intercepted at any center distance reduces the deposition rate to the rate at the most peripheral points. The shutter contours required for uniform distributions are spirals whose exact outlines for deposition areas of various diameters have been calculated by Behrndt.[146] He was able to coat substrate areas of 10 × 10 cm² uniformly within ±0.35%.

The most stringent demands concerning thickness uniformity arise in the fabrication of optical coatings,[147] and therefore, the techniques for accomplishing this objective have been developed in conjunction with the deposition of multilayer dielectric films. The methods originated from the idea that distributions identical to those of ring sources are also obtained if either an eccentrically located source is rotated opposite stationary substrates or if the substrates are rotated vis-à-vis a stationary eccentric source. Since rotating the source poses experimental problems in regard to power leads and temperature control, rotation of substrates is the preferred solution.

The latter arrangement also allows uniform coating of several substrates positioned at equal center distances.

The identity of thickness distributions resulting from an eccentric small-area source on rotating substrates and those from thin-ring sources was first recognized by Fisher and Platt,[148] and the principle has been utilized by several investigators.[139]   The distribution equation (59) for ideal ring sources is immediately applicable to rotating substrates if the parameter s is taken to be the horizontal distance of the small-area source from the axis of rotation, and l as the radial distance of a point on the substrate plane from the center of rotation.   Behrndt[149] has shown that minimum thickness variations at a radial substrate distance $l = 0.1h$ are obtained if the eccentricity s of the small-area source equals $0.71h$.   He introduced a further refinement by placing several substrates equidistant from a common axis of rotation and making them revolve individually around their own axes.[150]   The resulting planetary motion of individual substrates reduces even those thickness variations which would be caused by beaming of crucible sources.   Another advantage is the greater homogeneity of those film properties which may be affected by different angles of incidence.   The thickness of films produced under these conditions varied by as little as $\pm 0.16\%$ on substrates of 6 in. diameter.   The construction of such a revolving substrate holder is, however, a major mechanical task and rarely warranted by the more modest uniformity requirements in electronic-film applications.

6. THE EVAPORATION OF COMPOUNDS, ALLOYS, AND MIXTURES

Relatively few inorganic compounds, alloys, or mixtures evaporate congruently because the constituents which are present in the solid or liquid state usually differ in their vapor pressures.   Consequently, the composition of the vapor and hence of the condensate is not the same as that of the source material.   In principle, compositional changes associated with the transition into the gaseous state can be predicted from thermodynamics.   In practice, however, the available thermochemical data are rarely sufficient to describe quantitatively the complex processes which may occur.   Empirical information is therefore the most reliable guide in determining the experimental conditions necessary to produce films of the desired composition.   This objective cannot always be reached by direct evaporation, and special techniques such as reactive, two-source, and flash evaporation have been developed.   These are attempts to control the vapor composition regardless of differences in volatility of the constituents, and sometimes they are the only way to prepare certain films of considerable practical interest.

a. Evaporation Phenomena of Compounds

In the evaporation of metals, the predominant species in the gas phase are single metal atoms, and only a small fraction—usually less than 0.1%—associate into diatomic molecules.   As indicated in Table 4, there are a few elements—C, S, Se, Te, P, As, Sb—whose vapors consist of polyatomic species.   In the evaporation of compounds, however, transition into the gas phase rarely occurs without changes of the molecular species.   This has been established by mass-spectroscopic investigations of the vapors evolving from compounds heated in vacuo.[151]   The evidence shows that vaporization of compounds is usually accompanied by dissociation or association or both processes. Whereas association does not affect the stoichiometry of the constituents, dissociation often does, namely, if one of the dissociation products is not volatile.   The latter case represents thermal decomposition and makes direct evaporation impractical.   Thus, deposition of compound films from a single vapor source requires that the material enters the gaseous state either in the form of complete molecules or—if dissociation occurs—that the constituents are equally volatile.   If this condition is satisfied, one speaks of congruent evaporation.   Table 10 lists pertinent information for a number of compounds which are of interest in thin film work and amenable to direct evaporation.   The various mechanisms involved are discussed in the following.

TABLE 10 Direct Evaporation of Inorganic Compounds

Compound	Vapor species observed (in order of decreasing frequency)	mp, °C	T, °C, at which $p^* = 10^{-2}$ Torr	Comments on actual evaporation temperatures, support materials used, and related experience
			Oxides	
Al_2O_3.....	Al, O, AlO, Al_2O, O_2, $(AlO)_2$	2030^{154}	$\sim 1800^{17,152}$	From W and Mo supports at 1850–2250°C.[159] With telefocus gun at 2200°C, no decomposition[152] From W support: Al_2O_3 films have small oxygen deficits.[153] O_2-dissociation pressure at 1780°C: 1.5×10^{-18} Torr[153]
B_2O_3......	B_2O_3[151]	450^{154}	$\sim 1700^{154}$	From Pt and Mo supports at 940–1370°C[151]
BaO......	Ba, BaO, Ba_2O, $(BaO)_2$, Ba_2O_3, O_2[159]	1925^{154}	$154^{17,154}$	From Al_2O_3 crucible at 1200–1500°C.[159] From Pt crucible with only slight decomposition, p_{O_2} (1540°C) = 3.5×10^{-18} Torr[153]
BeO......	Be, O, $(BeO)_n$, $n = 1$–6, Be_2O[151]	2530^{154}	2230^{154}	From W support at 2070–2230°C.[151] With telefocus gun at 2400–2700°C, no decomposition[152]
Bi_2O_3.....	....	817^{154}	1840^{153}	From Pt support[153]
CaO......	Ca, CaO, O, O_2[151]	$\sim 2600^{154}$	$\sim 2050^{17}$	Support materials: ZrO_2, Mo, W. The latter two form volatile oxides, molybdates, and wolframates at 1900–2150°C[151]
CeO_2......	CeO, CeO_2[151]	1950^{153}	....	From W support without decomposition[153]
In_2O_3.....	In, In_2O, O_2[151]	....	....	From Pt support with only little decomposition.[153] Vapor species observed at 1100–1450°C. At 1000–1450°C from Al_2O_3 crucible, more In_2O than In[151]
MgO......	Mg, MgO, O, O_2[151]	2800^{154}	$\sim 1560^{152}$	Mo or W supports at 1840–2000° form volatile oxides, molybdates, and wolframates.[151] With telefocus gun at 1925°C, no decomposition.[152] From Al_2O_3 at 1670°C[159]
MoO_3.....	$(MoO_3)_3$, $(MoO_3)_n$, $n = 4,5$[155,159]	795^{154}	610^{155}	From Mo oven at 500–700°C, the trimer is the main species. Above 1000°C, there is some decomposition into $MoO_2(s)$ + $O_2(g)$.[155] At 730°C, the oxygen-decomposition pressure is 1.1×10^{-14} Torr.[153] From Pt at 530–730°C[158]
NiO......	Ni, O_2, NiO, O[151]	2090^{153}	1586^{153}	From Al_2O_3 crucible at 1300–1440°C.[151] Heavy decom-

TABLE 10 Direct Evaporation of Inorganic Compounds (Continued)

Compound	Vapor species observed (in order of decreasing frequency)	mp, °C	T, °C, at which $p^* = 10^{-2}$ Torr	Comments on actual evaporation temperatures, support materials used, and related experience
			Oxides	
Sb_2O_3	. . . .	656[154]	~450[154]	position with $p_{O_2} = 4 \times 10^{-1}$ Torr at 1586°C[153] Lower oxides result if evaporated from W supports. Pt heaters do not produce decomposition[153]
SiO	SiO	. . . .	1025[156,157]	Usually evaporated from Ta or Mo heaters at residual gas pressures below 10^{-5} Torr and at temperatures between 1150 and 1250°C. Dissociation into Si and O_2 begins above 1250°C and may lead to oxygen-deficient films[153]
SiO_2	SiO, O_2[153,158]	1730[152]	~1250[152]	With telefocus gun at 1500–1600°C, no decomposition.[152] Ta, Mo, W supports are attacked by SiO_2 and contribute volatile oxides.[153] From Al_2O_3 at 1630°C, SiO_2 vapor species is present[159]
SnO_2	SnO, O_2[151]	. . . .	. . . .	From SiO_2 crucible at 975–1250°C.[151] Films directly evaporated from W support are slightly oxygen-deficient[153]
SrO	Sr, O_2, SrO[159]	2460[154]	~1760[17]	From Al_2O_3 at 1830°C.[159] Evaporation from Mo or W at 1700–2000°C produces volatile Mo and W oxides, molybdates, and wolframates[151]
TiO_2	TiO, Ti, TiO_2, O_2[153,159]	1840[154]	. . . .	TiO_2 source material decomposes into lower oxides upon heating.[152,153] p_{O_2} at 2000°C is 10^{-10} Torr. Nearly stoichiometric films by pulsed electron-beam heating[169]
WO_3	$(WO_3)_3$, WO_3[155]	1473[154]	1140[155]	From Pt oven at 1040–1300°C.[155] From Pt support at 1220°C.[159] From W heater with only slight decomposition; p_{O_2} at 1120°C is 3×10^{-10} Torr[153]
ZrO_2	ZrO, O_2	2700[154]	. . . .	From Ta support at 1730°C, volatile TaO.[159] From W support, oxygen-deficient films.[153] ZrO_2 source material loses oxygen when heated by electron beams[152]

TABLE 10   Direct Evaporation of Inorganic Compounds (Continued)

Compound	Vapor species observed (in order of decreasing frequency)	mp, °C	T, °C, at which $p^* = 10^{-2}$ Torr	Comments on actual evaporation temperatures, support materials used, and related experience
		Sulfides, Selenides, Tellurides		
ZnS.......	....	1830[168] ($p \approx 150$ atm)	1000[154]	From Mo support. Minute deviations from stoichiometry if allowed to react with residual gases. From Ta at 1050°C[167]
ZnSe......	....	1520[168] ($p \approx 2$ atm)	820[160]	
CdS......	S_2, Cd, S, S_3, S_4[151]	1750[168] ($p \approx 100$ atm)	670[161]	From Pt oven at 740°C.[151] Films tend to deviate from stoichiometry.[153] Suitable support materials: graphite, Ta, Mo, W, SiO_2, Al_2O_3-coated W; evaporation at 600–700°C[167]
CdSe.....	Se_2, Cd	1250[168]	660[162,163]	From Al_2O_3 crucible[167]
CdTe.....	Te_2, Cd[164]	1100[168]	570[164]	From Ta boat at 750–850°C; film stoichiometry depends on condensation temperature[76]
PbS.......	PbS, Pb, S_2, $(PbS)_2$[151]	1112[154]	675[154]	From quartz crucible at 625–925°C.[151] From Mo support.[153] Purest films from quartz furnace at 700°C; Fe or Mo boats react and form volatile sulfides[165]
Sb_2S_3.....	....	546[154]	550[153]	From Mo support[153]
Sb_2Se_3....	Sb_4, $(SbSe)_2$, Sb_2, SbSe[151]	611[166]	....	From graphite at 725°C.[151] From Ta oven at 500–600°C, fractionation and films of variable stoichiometry[166]
		Halides		
NaCl.....	NaCl, $(NaCl)_2$,[151] $(NaCl)_3$	801[154]	670[17,154]	From Ta, Mo, or Cu ovens at 550–800°C[151]
KCl......	KCl, $(KCl)_2$[151]	772[154]	635[17,154]	From Ni or Cu ovens at 500–740°C[151]
AgCl......	AgCl, $(AgCl)_3$[151]	455[154]	690[154]	At 710–770°C.[151] From Mo support, $p^* = 10^{-2}$ Torr at 790°C[153]
MgF_2.....	MgF_2, $(MgF_2)_2$, $(MgF_2)_3$[151]	1263[154]	1130[154]	From Pt oven at 950–1230°C.[151] From Mo support.[153] Very little dissociation into the elements[158]
CaF_2......	CaF_2, CaF[151]	1418[154]	~1300[154]	From Ta oven at 980–1400°C.[151] From Mo support[153]
$PbCl_2$.....	....	678[154]	~430[154]	Direct evaporation possible[153]

(1) Evaporation without Dissociation   The simplest transition of a compound AB into the gas phase is described by the equation

$$AB \ (s \text{ or } l) \ = \ AB(g)$$
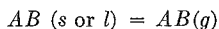
As in the evaporation of the elements, the free energy of evaporation associated with this process is only a function of the temperature and hence is given by the standard value $\Delta_e \mathbf{G}°(T)$.   In analogy to Eq. (16), vapor pressures can be derived from

$$\log \ p_{AB}{}^* \ = \ - \ \frac{\Delta_e \mathbf{G}°(T)}{4.575T} \qquad p_{AB}{}^* \text{ in atm}$$

A glance at the observed vapor species in Table 10 shows that very few compounds evaporate in this simple mode.   Examples are SiO and MgF_2, which are among the most widely used film materials.   The evaporation behavior of B_2O_3, CaF_2, and most of the divalent group IV oxides (SiO homologs like GeO or SnO) is very similar.   The degree of dissociation or association which some of these compounds show is negligible for most practical purposes and hardly affects the vapor pressure.   Generally, the tendency to dissociate is greater the higher the evaporation temperature and the lower the pressure.   An example is the onset of the dissociation of SiO into Si and O_2 at 1250°C.

Most metal halides are known to form polymolecular species according to

$$nAB(s \text{ or } l) \ = \ A_n B_n(g)$$
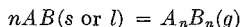
where typically $n = 2$ or 3.   The fraction of di- and trimers in alkali chloride vapors is significant, particularly at lower temperatures.   The tendency to associate is even stronger in the case of MoO_3 and WO_3 where the trimer represents more than 80% of the vapor species.   This fact must be considered when vapor pressures and molecular weights are inserted into Eq. (48) to determine mass-evaporation rates.   The evaporation coefficients α_v are seldom known except for some of the alkali halides which have values between 0.1 and 1.

(2) Evaporation with Dissociation: Chalcogenides   Evaporation by dissociation into the elements according to

$$AB(s) \ = \ A(g) \ + \ \tfrac{1}{2}B_2(g) \tag{63}$$

is often found with binary compounds.   If the heat of evaporation into A and B atoms and the heat of dissociation of AB molecules are both known, it is possible to assess the thermal stability of the compound molecules and to predict the resulting gas species.[170]

Well-known examples of complete dissociation are the II-VI compounds.   Somorjai[171] investigated the free evaporation of CdS and CdSe at 600 to 900°C.   He concluded that the kinetics involves diffusion of A and B surface atoms with recombination of the latter to form B_2 molecules prior to entering the gas phase.   According to the law of mass action, equilibrium is obtained when the product of the two gas pressures equals a temperature-dependent constant $K_p(T)$,

$$p_A p_{B_2}{}^{\frac{1}{2}} \ = \ K_p(T)$$

whereby

$$\log K_p(T) \ = \ - \ \frac{\Delta_e \mathbf{G}(T)}{4.575T}$$

The total pressure over the compound AB, $p_t = p_A + p_{B_2}$, may vary according to the ratio of partial pressures and assumes its minimum value if the vapor composition is stoichiometric: $p_{B_2} = \tfrac{1}{2}p_A$.   For this case, the total equilibrium pressure is given by

$$\log \ p_t{}^* \ = \ - \ \frac{2}{3} \frac{\Delta_e \mathbf{G}(T)}{4.575T} + \log 3 - \frac{2}{3} \log 2 \qquad p_t{}^* \text{ in atm}$$

Comparing the free evaporation rates with vapor pressures obtained under equilibrium conditions, Somorjai[171] found coefficients α_v between 0.01 and 0.1, which indicates that one of the processes preceding the evaporation of Cd and S_2 or Se_2 particles is

constrained by an activation energy. This is the reason why source temperatures measured during the evaporation of II-VI compounds tend to be somewhat higher than those expected from equilibrium-vapor-pressure data (see Table 10).

Volatility of both constituents of a compound is only a necessary but not a sufficient requirement for the deposition of stoichiometric films. When arriving at the substrate, A and B_2 particles must also become absorbed in the proper ratio and recombine to form the AB compound. Differences in the sticking coefficients may lead to films which either are deficient in the nonmetallic constituent or contain excess metal as a second phase. Inhomogeneous films may also be the result of incomplete recombination. The presence of second phases in II-VI compounds can be detected by measuring the optical transmittance of the films. The pure compounds have a sharp absorption edge at that wavelength which corresponds to the forbidden energy gap of the semiconductor. In CdTe films condensed at room temperature, for example, the absorption is shifted toward greater wavelengths by the presence of free tellurium, whereas pure compound films were obtained at 150 to 250°C.[76] The importance of the substrate temperature in determining the film composition has also been observed with other II-VI compounds. CdS films deposited at 150°C are transparent and yellow whereas room-temperature condensates are black, probably because of the presence of excess Cd.[167]

The other II-VI compounds are less well investigated but should show similar behavior; i.e., they can be evaporated directly from single sources at temperatures below 1000°C, and the substrate temperature is an important control parameter to ensure proper film composition. The chalcogenides of divalent group IV elements are also volatile but differ in the degree of dissociation. Thus, compounds like SiS, GeS, SnS, and PbS evaporate primarily as molecular species.[151] As the thermodynamic stability of the sulfides decreases from Si toward Pb, one has to be increasingly concerned about possible reactions with the support material. In this respect, quartz containers are safer than metal boats.[165] The same considerations apply to the selenides and tellurides of group IV elements.[172] The chalcogenides of group V have been of little practical interest as thin films, and their evaporation behavior is exemplified by Sb_2Se_3 in Table 10. Fractionation due to differences in volatility and stratified films with variable composition are typical for this class of compounds.

(3) Evaporation with Dissociation: Oxides The evaporation of most oxides requires temperatures in excess of 1500°C. The binary oxides of Be, Mg, Ca, Sr, Ba, and Ni evaporate predominantly by dissociation according to Eq. (63). But as shown in Table 10, their vapors also contain molecular species, oxygen atoms, and in some cases lower oxides. The tendency to form suboxides is stronger among group III metals as exemplified by Al or In, and most pronounced in the fourth group whose elements are capable of forming relatively stable and volatile binary oxides:

$$AB_2(s) = AB(g) + \tfrac{1}{2}B_2(g)$$

Because of the high temperatures required, the evaporation kinetics of the oxides is essentially unexplored. Only in the case of Al_2O_3 has an evaporation coefficient of $\alpha_v = 2.10^{-4}$ been published (Ref. 35, p. 139). Generally, congruent evaporation is more likely to be attained with binary oxides than with sesqui- or dioxides. This is due to the fact that the higher oxides tend to lose oxygen at temperatures which are too low for the volatilization of the resulting suboxides. Hence, slightly oxygen-deficient and therefore discolored films are often obtained.

Another difficulty is the interaction of oxides with support materials. Tungsten and molybdenum are generally unstable because they recombine with the dissociated oxygen and thereby affect the stoichiometry of the evaporant. Moreover, the reaction products are volatile either in the form of MoO_3 and WO_3 or as molybdates and wolframates which are incorporated into the films. Tantalum, too, forms a volatile suboxide as, for example, in contact with ZrO_2:[169]

$$ZrO_2(s) + Ta = ZrO(g) + TaO(g)$$
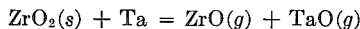
Many metal oxides are also reduced if heated in graphite boats. Evaporation from platinum containers minimizes the risk of secondary reactions but is possible only with some of the more volatile oxides such as BaO. The less stable oxides such as In_2O_3 yield slightly oxygen-deficient films even if evaporated from platinum. Refractory oxide crucibles have been used, but they involve the risk of chemical attack by the highly reactive alkali-earth oxides, or of evaporating themselves at the high temperatures required.

The best method to evaporate refractory oxides directly is electron-beam heating. Reichelt and Mueller[152] avoided the container problem by focusing the beam on a small part of relatively large source crystals. Because of the poor heat conductivity of the oxides, the focal spot assumed temperatures which were 200 to 400°C higher than those corresponding to equilibrium pressures of 10^{-2} Torr. Under these conditions, MgO, BeO, Al_2O_3, SiO_2, and ThO_2 films could be directly evaporated. The oxides of Ti, Zr, Nb, Ta, and Cr, however, did not evaporate congruently but decomposed as indicated by the discoloration of the source crystals. The deposition of stoichiometric TiO_2 films is of particular interest because of the high index of refraction. However, TiO_2 loses oxygen very easily, and the nonstoichiometric products normally obtained are intensely colored as well as semiconducting. Reichelt[169] succeeded in depositing insulating TiO_2 films which were stoichiometric within a fraction of 10^{-10} by utilizing electron-beam pulses of 0.5 s duration. With this technique, decomposition of the source material adjacent to the focal spot is minimized since the latter is rapidly heated to temperatures where the vapor pressure of the suboxide is sufficiently high for congruent evaporation to take place. The same technique has also been used to prepare SiO_2 films.[169] Cariou et al.[173] obtained HfO_2, ZrO_2, and Ta_2O_5 films of good dielectric properties by direct electron-beam evaporation. An oil-free vacuum was used to avoid oxide reduction by residual hydrocarbons. The direct evaporation of SiO_2, Al_2O_3, and ThO_2 with an electron gun has also been reported by Cox et al.[174] It is noteworthy that most oxides are very effective getters for residual water vapor whose presence in the films may cause variations in density, stress, and optical properties.[175] Pliskin[176] found electron-gun evaporated SiO_2 films to be very reactive because of bond straining and porosity. They also contained some Si_2O_3 and tended to absorb water. Finally, it has been observed that electron-beam-evaporated Al_2O_3 films incorporate free electrical charges.[177]

In summary, a number of inorganic compounds, including most halides, the II-VI compound semiconductors, and several important oxides, are amenable to direct evaporation. The evaporation kinetics in most cases is complex and involves dissociation or association of molecules so that the vapor consists of different species. This must be taken into account when mass-evaporation rates are derived from vapor-pressure data. Figure 31 shows the vapor pressures for compounds as far as they are presently known. The curves represent total pressures including all species in stoichiometric proportions (p_t^*). Because of the experimental difficulties in establishing true vapor-solid equilibria at high temperatures, the accuracy of the data is seldom very high. Furthermore, it should be kept in mind that the temperatures required for free evaporation will often be higher than the curves suggest because of evaporation constraints as reflected in α_v-values < 1. Additional vapor-pressure data covering the 1- to 760-Torr range of many inorganic compounds have been compiled by Stull.[178]

(4) Decomposition A large number of compounds evaporate incongruently; i.e., the volatilities of their constituents at elevated temperatures differ so strongly that the vapor and hence the condensate do not have the same chemical composition as the source. The simplest decomposition reactions are of the type

$$AB(s) = A(s) + \tfrac{1}{2}B_2(g)$$
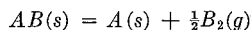
where the metal A forms a separate phase. In this case, the free energy of the decomposition process $\Delta_d G$ is fixed by the standard chemical potentials of both solid phases

and dependent merely on temperature. The decomposition pressure is therefore given by

$$\tfrac{1}{2} \log p_{B_2}{}^* = -\frac{\Delta_d \mathbf{G}°(T)}{4.575 T} \qquad p^* \text{ in atm}$$

The free energy of decomposition $\Delta_d \mathbf{G}°(T)$ is identical with the free energy of formation of AB from the elements except for its sign. Hence, the decomposition pressure can be calculated from the appropriate free-energy-of-formation data, which have been tabulated by several authors for most common compounds.[6,159,179,180]
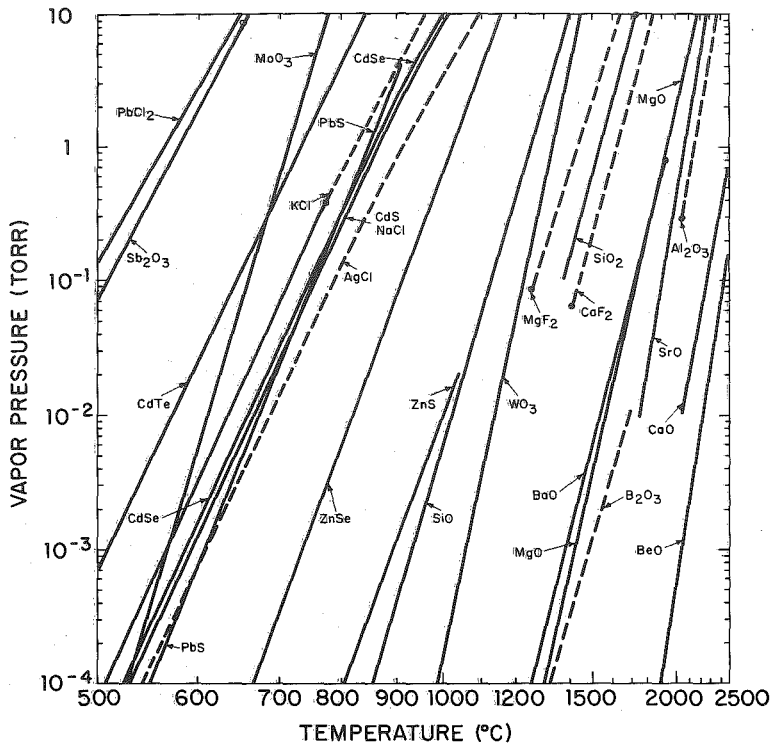
Fig. 31 Equilibrium vapor pressures of inorganic compounds. Drawn lines: over solids; broken lines: over liquids. The full circles indicate melting points. The sources of the data are referenced in the fourth column of Table 10.

The kinetics of decomposition reactions has been investigated by Rickert[181] using Ag_2S, Ag_2Se, and CuI as model substances. Evaporation is preceded by formation of B_2 molecules in the absorbed state, while the metal atoms diffuse and form nuclei and crystallites. Most of the metal borides,[182] carbides, and nitrides[151] follow similar mechanisms. Incongruent evaporation involving the formation of lower carbides ($WC \rightarrow W_2C$) or nitrides ($CrN \rightarrow Cr_2N$) has also been observed. In all these cases, either no films are obtained or their composition is different from the source material. Known exceptions of nearly congruent evaporation in this category are TiC, ZrC,[183] and AlN.[86]

Among the oxides, Cr_2O_3 and Fe_2O_3 are examples of decomposition into suboxides of low volatility. Attempts to deposit films of these compounds have been described by Holland.[153] If evaporated from tungsten boats, lower oxide films of undefined

composition are obtained. In the case of Fe_2O_3, the source material decomposes into a mixture of Fe_3O_4 and metallic iron, whereas Cr_2O_3 yields oxygen-deficient films although volatile oxides do exist.[151] Generally, lower oxides or oxygen-deficient deposits can be converted into higher oxides by heating in air. However, the required temperatures are often too high for the film substrate, or the post-deposition reaction may yield highly stressed, porous, or nonadherent films. Therefore, methods other than direct evaporation such as reactive evaporation, reactive sputtering, or rf sputtering are preferable for these materials.

Another important family of compounds whose evaporation is preceded by decomposition are the III-V compounds. Their pressure-temperature-composition diagrams have been reviewed by Weiser,[184] and their predominant mode of decompositions is

$$AB(s) = A(l) + \frac{1}{n} B_n(g) \qquad (n = 2, 4) \tag{64}$$
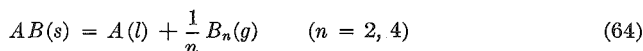
The relatively volatile group V constituents (P, As, and Sb) reach pressures of 10^{-2} Torr at temperatures of 700 to 900°C. In this interval, the group III metals Al, Ga, and In are molten, but their vapor pressures are orders of magnitude lower than those of the group V elements. Therefore, the vapor consists predominantly of B_n molecules and contains virtually no metal atoms or, in the case of indium compounds, a nonstoichiometric amount.[151]

The direct evaporation of III-V compounds is further complicated by the fact that the residual source materials $AB(s)$ and $A(l)$ form solid or liquid solutions. Consequently, the free energy of the decomposition reaction Eq. (64) is also dependent on the concentration of residual B in the source and therefore varies as decomposition proceeds. Accordingly, the vapor pressure of the constituent B can only be derived if the free energy is given as a function of both the temperature and the activity a_B in the remaining solution:

$$\frac{1}{n} \log p_{B_n} = - \frac{\Delta_d \mathbf{G}(T, a_B)}{4.575T} \qquad p_{B_n} \text{ in atm}$$

An experimental investigation leading to the determination of thermodynamic constants and of a vapor-pressure equation for GaP has been published by Lee and Schoonmaker.[185]

Attempts to deposit III-V compound films by direct evaporation in spite of these difficulties have been reported by Paparoditis.[186] The indium compounds are most promising because In is a little more volatile than Ga or Al. Evaporating InSb and InAs to completion, Paparoditis obtained fractionation and stratified films. The films could be homogenized and their stoichiometry restored by post-deposition annealing at temperatures around 300°C. Dale et al.[187] tried to counteract the fractionation of InSb by replenishing the source repeatedly with new material, thereby approaching an indium-rich melt from which InSb evaporates nearly in the proper stoichiometric ratio.[188] However, these techniques are not applicable to the other III-V compounds which have greater vapor-pressure differences and higher melting points. Because of the latter, restoration of the compound by interdiffusion of the condensed elements requires relatively high temperatures which involve the risk of losing the volatile constituent during the crystallization process.[186] Therefore, special techniques such as two-source and flash evaporation are usually considered when III-V compounds are to be deposited.

b. Evaporation Phenomena of Alloys

(1) Raoult's Law The constituents of alloys evaporate independently of each other and, like the pure metals, mostly as single atoms. Monatomic vapor may be observed over alloys even in those cases where the pure element is known to form molecules. An example is the occurrence of monatomic antimony vapor over Pt-Sb[189] and Au-Sb[190] alloys. The vapor pressure of an alloy constituent, however, is different from that of the pure metal at the same temperature. This is due to the change in

chemical potential which a metal B experiences when it is dissolved in another metal A to form an alloy A-B. If the concentration is given by the mole fraction x_B, the chemical potential in the alloy, $\mu_{B,c}(T)$, differs from that of the pure metal, $\mu°_{B,c}(T)$, by the energy spent to disperse B[191]:

$$\mu_{B,c}(T) = \mu°_{B,c}(T) + RT \ln x_B \qquad (65)$$

The use of the mole fraction in Eq. (65) implies an ideal solution; i.e., the energy of atomic interactions between two different constituents must be the same as between two equal constituents.

The chemical potential of an ideal gas at the pressure p is related to the potential of the standard state, $\mu°_{B,g}(T)$ at 1 atm, by the equation [see Sec. 2a(2)]:

$$\mu_{B,g}(T) = \mu°_{B,g}(T) + RT \ln p_B \qquad (66)$$

Equilibrium between the alloy and its adjacent vapor phase $B(g)$ is obtained if the two potentials [Eqs. (65) and (66)] are equal. This yields the vapor-pressure relation

$$RT \ln p_B = -[\mu°_{B,g}(T) - \mu°_{B,c}(t)] + RT \ln x_B \qquad (67)$$

The difference in standard chemical potentials is the standard free energy of evaporation for the pure metal, $\Delta_e G°(T)$, whch according to Eq. (16) must be divided by RT to yield the vapor pressure of the pure metal. Thus, Eq. (67) simplifies to

$$p_B = x_B p_B{}^*$$

This expression is one form of Raoult's law, which states that the pressure of an element over an ideal solution is reduced in proportion to its mole fraction. It can be verified experimentally by measuring the vapor pressure over alloys of known composition. Deviations from Raoult's law are common because most alloy systems are not ideal solutions. In order to describe the behavior of real solutions, the activity a_B has been introduced. It is defined as the actual ratio of vapor pressures,

$$a_B = \frac{p_B}{p_B{}^*}$$

and related to the mole fraction by the activity coefficient f_B:

$$a_B = f_B x_B$$

By substituting a_B for x_B, the usual thermodynamic relationships can be applied to systems which are not ideal solutions. Therefore, the activity and its coefficient are important empirical parameters which have been tabulated for a number of binary systems.[192] Since the activity of a material is temperature- as well as system-dependent, the existing data are far from being complete. The examples shown in Figs. 32 and 33 are of particular interest because Ni-Fe and Ni-Cr are the most widely used alloy systems in the thin film field. The deviations from Raoult's law in the nickel-iron system are relatively small and negative. In the nickel-chromium system, positive as well as negative deviations occur. They are especially large at small concentrations. The diagram also shows the activity behavior in a two-phase solid.

Since the vapor pressure of alloys is affected by the energy state of the atoms in the condensed phase, the activity is related to the phase diagram of the system. Activity plots and phase diagrams for a few binary systems have been compared by Koller.[194] Ideal behavior ($f_B \approx 1$) can be expected only but not always from simple systems which show complete miscibility. Compound formation in the solid state is likely to reduce the vapor pressure since stronger bonds have to be broken. This usually causes negative deviations ($f_B < 1$) even when the temperature is above the melting point of

the compound.   Positive deviations from Raoult's law indicate that the attractive forces between unlike atoms in an alloy are weaker than the interaction in the pure phase (Ref. 6, p. 36).   If there is a miscibility gap in the liquid state, the activity of the lighter component floating on top of the melt will be close to 1.

A.   B.
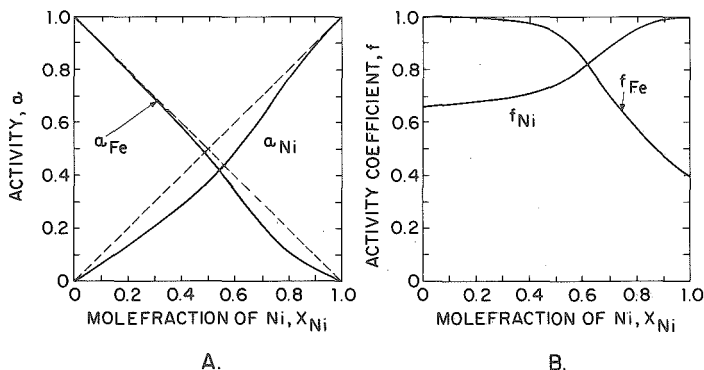
Fig. 32   (A) Activities of Ni and Fe in liquid nickel-iron alloys at 1600°C.   Ideal behavior according to Raoult's law: broken lines.   Experimentally determined: solid lines.   (B) Activity coefficients for the same conditions.   (*After data from Zellars, Payne, Morris, and Kipp.*[193])

A.   B.
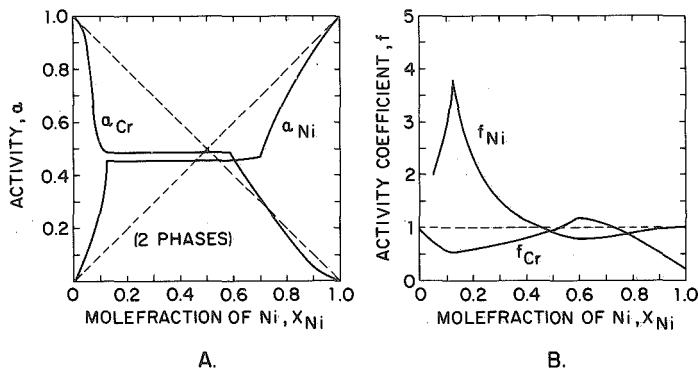
Fig. 33   (A) Activities of Ni and Cr in solid nickel-chromium alloys at 1100°C.   Raoult's law: broken lines.   Experimentally determined: solid lines.   (B) Activity coefficients for the same conditions.   (*After data from Hultgren et al.*[192])

(2) Compositional Changes during Evaporation   The application of Raoult's law to the evaporation of *liquid alloys* introduces the mole fraction and—for real solutions— the activity coefficient into the Hertz-Knudsen equation.   After dividing Eq. (48) by the molecular weight, the evaporation rates for the constituents of a binary alloy are

$$\frac{dn_A}{dt} = \frac{5.834 \times 10^{-2}}{\sqrt{M_A T}} f_A x_A p_A^*   \qquad \text{mol cm}^{-2} \text{ s}^{-1} \tag{68a}$$

and

$$\frac{dn_B}{dt} = \frac{5.834 \times 10^{-2}}{\sqrt{M_B T}} f_B x_B p_B^*   \qquad \text{mol cm}^{-2} \text{ s}^{-1} \tag{68b}$$

The ratio of A and B particles in the vapor stream at any moment is therefore

$$\frac{dn_A}{db_B} = \frac{f_A x_A p_A^*}{f_B x_B p_B^*} \left(\frac{M_B}{M_A}\right)^{\frac{1}{2}} \tag{69}$$

whereby $x_A + x_B = 1$. The ratio is dependent on time since x_A and x_B change as the evaporation proceeds. Assuming that the activity coefficients remain constant, the system specific material parameters can be combined into one factor

$$K = \frac{f_A p_A^*}{f_B p_B^*} \left(\frac{M_B}{M_A}\right)^{\frac{1}{2}}$$

The integration of Eq. (68a) has been performed by Zinsmeister[188] and leads to

$$\frac{x_A}{x_A^\circ} \left(\frac{1 - x_A^\circ}{1 - x_A}\right)^K = \left(\frac{n}{n^\circ}\right)^{K-1} \tag{70}$$

where x_A° = mole fraction of A in the initial alloy charge
$\quad n^\circ$ = total number of moles A and B in the initial alloy charge
$\quad n = n_A + n_B$ = number of moles left in the source

It is implied that the composition of the alloy remains homogeneous throughout the evaporation process, in other words, that there are no concentration gradients between the surface and the interior. From Eq. (70), one can compute x_A as a function of the fraction of material already evaporated, $(n^\circ - n)/n^\circ$. The mole fraction x_B is obtained from an expression analogous to Eq. (70). Substitution of x_A and x_B into Eq. (69) permits computation of the molar ratio dn_A/dn_B in the vapor and hence at the moment of condensation as a function of the evaporated fraction of the charge. Such calculations have been performed by Zinsmeister,[188] and his results are shown in Fig. 34. The change of the molar ratio during the evaporation is significantly affected by the system specific parameter K and by the mole fraction of the initial alloy charge x_A°.

From Fig. 34, several conclusions can be drawn. Unless K happens to be 1, in which case an alloy evaporates congruently, the composition of the vapor deviates from that of the melt. Initially, the more volatile constituent evaporates preferentially, but the proportions are reversed as the charge is used up. Directly evaporated films are therefore stratified and have a vertical concentration gradient. This effect is more pronounced the more K differs from 1. If K is close to 1, it may be attempted to deposit nearly homogeneous films by evaporating only a small fraction of the total charge. The initial concentration x_A° must then be carefully selected to compensate for the different volatilities in order to obtain the desired composition.

When the curves shown in Fig. 34 are used to assess the chances of direct evaporation, a number of complications must be considered. The assumption of constant activity coefficients may not be warranted. It is then necessary to perform the integration of Eq. (68) in steps for intervals of constant K values. Furthermore, mass transfer from the interior to the surface of the melt may not be instantaneous. In this case, the surface concentration and its relation to the composition in the interior enter the calculation.[188] Lastly, it should be remembered that surface contaminations such as oxide or slag films act as evaporation constraints and may introduce evaporation coefficients $\alpha_v \ll 1$ into the starting equations (68).

Compositional changes during the *sublimation of alloys* have been treated by Huijer et al.[195] In the absence of convection and stirring effects as encountered in melts, the source surface is depleted of the more volatile constituent B. The evaporation rate of B therefore decreases. At the same time, B atoms diffuse from the interior of the solid to the surface. Eventually, the two processes balance and reach a stationary state.

During the transient state, the diffusion process is governed by Fick's second differential equation

$$\frac{\partial x_B}{\partial t} = D \frac{\partial^2 x_B}{\partial y^2} \tag{71}$$

where y is the distance of a point in the interior of the alloy from the surface. Since both constituents are continually evaporating, the alloy surface recedes from its original position. Huijer et al.[195] treated this complication by letting the origin of the y axis move along a parallel z axis whose origin is fixed at the initial surface.
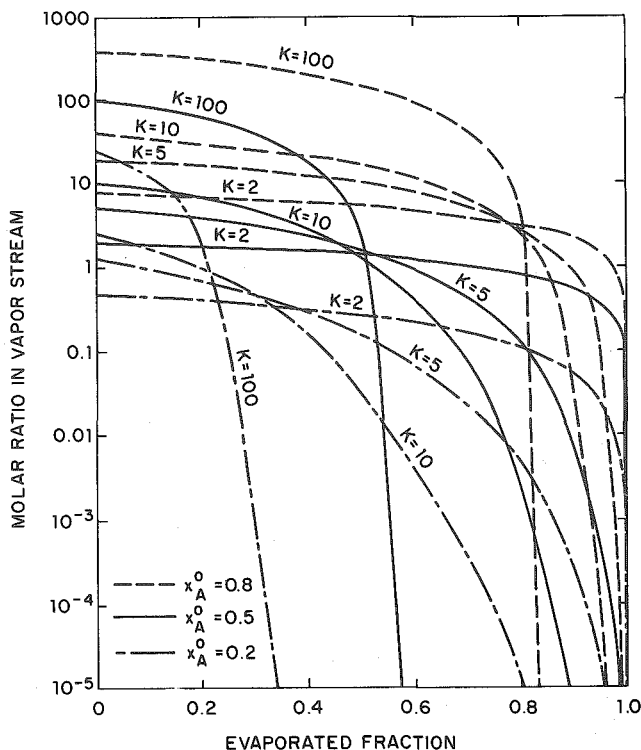
Fig. 34 Molar ratio in the vapor of binary alloys as function of the fraction already evaporated. (*From Zinsmeister.*[188])

Assuming the surface recedes at a constant rate of v cm s^{-1}, the relationship between the coordinates is $z = y - vt$. Equation (71) is thereby transformed into

$$\frac{\partial x_B}{\partial t} = D \frac{\partial^2 x_B}{\partial z^2} + v \frac{\partial x_B}{\partial z} \tag{72}$$

In the steady state, $\partial x_B/\partial t = 0$, and Eq. (72) has the solution

$$x_B = x_B{}^\circ - C \exp\left(-\frac{v}{D}z\right)$$

where $x_B{}^\circ$ is the mole fraction of B in the initial charge and C a constant which depends on the evaporation rates and densities of the constituents.

An analytic solution of Eq. (72) for the transient states is not available. Huijer et al.[195] obtained numerical solutions with the aid of a computer. The assumed boundary conditions are a constant initial concentration $x_B{}^\circ$ throughout the alloy, and a material-removal rate v determined by the evaporation equations (68a) and (68b) with varying values of x_A and x_B at the surface. Figure 35 shows their results

for one specific value of v/D. During the transient state, the concentration profiles intersect the receding material surface at successively smaller values until the steady state is reached. The shaded area represents the amount of B evaporated during a steady-state period. Since the surface concentration is constant, the ratio of $A:B$ in the vapor does not change any more. Furthermore, the profiles at t_6 and t_7 are parallel to each other and therefore include exactly the same amount of constituent B as would have been contained in the equally thick layer which was actually removed, assuming the latter had had a uniform concentration $x_B°$ (area between dotted lines in Fig. 35). It follows that an alloy evaporates in its original composition once the steady state has been obtained. The latter happens faster, and the surface layer affected by the outward-diffusion process is thinner, the larger the ratio v/D. Thus, high evaporation rates and small diffusion coefficients favor the applicability of this method.
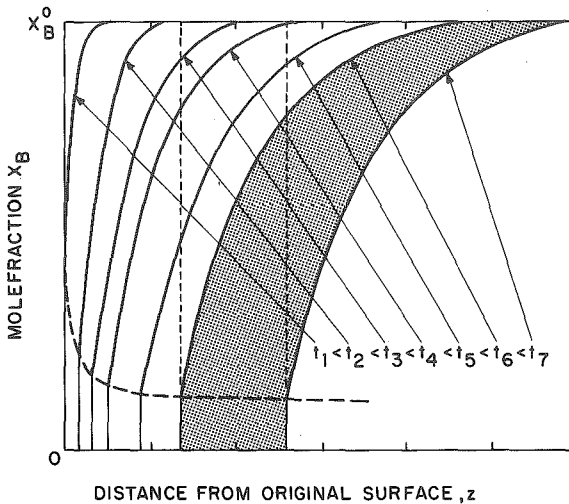
Fig. 35 Mole fraction of constituent B in a solid alloy as function of distance from the original source surface and time. The broken line represents the intersects of the distributions with the receding surface and hence the momentary surface concentration. The shaded area indicates losses of B during a period of steady-state evaporation. (*After Huijer, Langendam, and Lely.*[195])

(3) Examples of Direct Alloy Evaporation The direct evaporation of alloys for the purpose of thin film fabrication has been investigated primarily with the systems Ni-Fe and Ni-Cr. Nickel-alloy films containing around 15% Fe (Permalloy) are widely utilized for magnetic memory elements, while 80% Ni–20% Cr films (Nichrome) often serve as microminiature resistors. The two systems are eminently suited to illustrate the evaporation behavior of alloys because one has a low and the other a high ratio of vapor pressures. Both are often evaporated from tungsten boats, although the melts react with the support material. Alumina or zirconia crucibles are therefore preferred for Ni-Fe alloys. This does not appear to be true for Nichrome, probably because of the affinity of chromium for oxygen and the noticeable volatility of its suboxides. Resistance, electron bombardment, and induction heating have all been tried whereby the latter has the advantage of stirring the melt while the other methods provide only thermal convection.

A number of methods are available to determine the ratio of evaporated constituents. The direct approach is to analyze the vapor with a mass spectrometer.[196] More common is the use of shuttering techniques to condense separate fractions

and then analyze the deposits. Time resolution of deposit fractions has also been obtained by condensation on a moving Mylar tape.[197] The film composition may be determined by x-ray fluorescence[197] or chemical microanalysis[198] with techniques such as emission spectroscopy[199] or colorimetry.[200]

The preceding section about compositional changes allows an a priori assessment of the results to be expected from the direct evaporation of alloys, and Table 11 shows such data for Permalloy.

TABLE 11   Evaporation Data for Permalloy (85% Ni–15% Fe) at Two Temperatures*

	1600°C (liquid)		2000°C (liquid)	
Activity coefficients...............	$f_{Ni} = 1$ $f_{Fe} = 1$	$f_{Ni} = 0.97$ $f_{Fe} = 0.52$	$f_{Ni} = 1$ $f_{Fe} = 1$	$f_{Ni} = 0.97$ $f_{Fe} = 0.52$
Material parameter K..............	2	1.1	1.6	0.9
Initial evaporation rate $\Gamma(Ni + Fe)$, g cm^{-2} s^{-1}..........	3×10^{-4}	2.5×10^{-4}	2.5×10^{-2}	2.2×10^{-2}
Initial Ni:Fe ratio in the vapor.....	75:25	85:15	78:22	87:13

* Based on vapor pressures by Honig[19] and activity coefficients from Fig. 32.

Since the material parameter K introduced in Sec. 6b(2) is close to 1 and the evaporation rates are 10^{-4} g cm^{-2} s^{-1} or higher, one would conclude that Permalloy is amenable to direct evaporation. If ideal behavior is assumed, the films should be somewhat richer in iron than the source material. However, the negative deviation from Raoult's law of Fe in Ni should allow nearly 1:1 transfer of the source composition to the films. This has been confirmed experimentally. The fact that Ni-Fe films are less iron-rich than expected on the basis of $f_{Fe} = 1$ was first reported by Blois[201] for evaporation at 1600°C. Brice and Pick[115] evaporated at 2000°C and established that charges of 85% or more Ni produce initial deposits of nearly the same composition. When using large melts which maintain their composition fairly well for longer periods of time, the iron content of the films is typically within 2 to 4% of the charge. Evaporation of a major portion of the melt (70 to 75%), however, yields stratified films with concentration gradients of about 5% per 1,000 Å.[202] Thus, theory and experiment agree very well in the case of Ni-Fe, and Permalloy films may indeed be fabricated by direct evaporation.

TABLE 12   Evaporation Data for Nichrome (80% Ni–20% Cr) at Two Temperatures*

	1100°C (solid)		1450°C (liquid)
Activity coefficients.......................	$f_{Ni} = 1$ $f_{Cr} = 1$	$f_{Ni} = 0.9$ $f_{Cr} = 0.8$	$f_{Ni} = 1$ $f_{Cr} = 1$
Material parameter K.....................	11	10	7.5
Initial evaporation rate $\Gamma(Ni + Cr)$, g cm^{-2} s^{-1}.................	6.5×10^{-8}	5.3×10^{-8}	1×10^{-4}
Initial Ni:Cr ratio in the vapor	30:70	31:69	50:50

* Based on vapor pressures by Honig[19] and activity coefficients from Fig. 33. Activities in the liquid state are not known.

Evaporation data for Nichrome are listed in Table 12. At the lower temperature, evaporation is impractical in view of the small rates. Lakshmanan[203] obtained deposition rates of 0.17 Å s^{-1} from a sublimation source operating at 1000°C. The most common source temperatures for Nichrome are between 1400 and 1500°C (mp = 1395°C). Although the spread in the vapor pressures of Ni and Cr is smaller

at higher temperatures, the parameter K is still too high to expect constant film composition from a significant fraction of the melt. This has been confirmed by Degenhart and Pratt,[198] who evaporated 12% of a small Nichrome charge at 1400 to 1500°C. The initial fractions of the deposit had the approximate composition 15% Ni–85% Cr, whereas the last fractions consisted of about 80% Ni and 20% Cr. Similar results were obtained when Nichrome vapors were analyzed by a mass spectrometer.[196] Here, the initial vapor composition was 17:83, and after 12 min of evaporation 80:20. These results indicate that the material-transfer ratio is even worse than calculated in Table 12, which means the activity coefficients in this system tend to increase the K value. Deviations from Raoult's law have been reported for Ni-Cr alloys containing small amounts of Al and Cu.[199,204] The activity of chromium is greater than its mole fraction ($f_{Cr} > 1$), which agrees with Degenhart and Pratt's results. The evaporation of Ni appears to be somewhat retarded ($f_{Ni} < 1$), whereas the copper evaporation is enhanced ($f_{Cu} > 1$). Aluminum shows large negative deviations from the ideal behavior.

These studies demonstrate that the controlled deposition of homogeneous Nichrome films by direct evaporation from the melt is not easily accomplished. It would be necessary to use a very large charge of substantially lower Cr content than desired for the films, and to evaporate only a small fraction of it. This approach has been tried by Wied and Tierman,[205] but the results are not described in terms of composition.

An interesting alternative is the evaporation of the solid alloy. The analysis of compositional changes during the sublimation of alloys given by Huijer et al.[195] was applied to Nichrome. Evaporating from a wire at 1300°C, the steady-state distribution was reached after 3 h of evaporation. From the decrease in wire diameter and an analysis of the steady-state profile, Huijer et al. determined the diffusion coefficient of Cr in Ni to be 6.7×10^{-10} cm² s⁻¹. The steady-state surface concentration of Cr was found to be 3%, which upon substitution into the evaporation equation yields a vapor ratio Ni:Cr of 83:17 in close agreement with the 80:20 ratio in the wire. However, the vapor pressures of the two metals at 1300°C are 0.25×10^{-3} and 1.8×10^{-3} Torr, respectively, which amounts to a total evaporation rate as low as 3×10^{-6} g cm⁻² s⁻¹. Therefore, the sublimation technique, too, is of little practical value. More successful methods of depositing Nichrome films with controlled composition are flash evaporation[200] and dc bias sputtering.[206]

Compositional changes during the evaporation of other alloys are not as thoroughly investigated as those of the two nickel systems. An example of successful direct evaporation is Cr-Ge. Since the vapor pressures of these two elements are nearly identical, Riddle[207] obtained almost congruent evaporation at 1310°C from melts containing equal amounts of Cr and Ge. Sauer and Unger[208] studied the evaporation of Ag-Cu, Ag-Al, Ag-Sn, Cu-Sn, and Pb-Sn alloys. The compositions of the deposited fractions agreed quite well with predictions based on Raoult's law. Alloys of the brass type like Cu-Zn and Cu-Cd cannot be directly evaporated because Cu is non-volatile at temperatures where Zn and Cd have vapor pressures exceeding 1 Torr. The behavior of several bronzes has been described by Holland (Ref. 59, p. 182); there are some compositions in the Cu-Sn and Cu-Al systems which can be evaporated with little fractionation.

c. Special Evaporation Techniques

The preceding discussions of the behavior of compounds and alloys show that several materials which are of interest as thin films are not amenable to direct evaporation. Heavy fractionation, compositional changes, and stratified films are also predictable if mixtures such as cermets (ceramics and metals) are heated jointly in one source. For these situations, special evaporation techniques have been developed which utilize different experimental principles to obtain films of controlled composition.

(1) Reactive Evaporation In the deposition of metal films, the background pressure is usually kept as low as possible because the interaction of residual gases with the evaporant has mostly detrimental effects on film properties.[209] In reactive evaporation, however, relatively high oxygen pressures from 10^{-5} to 10^{-2} Torr are deliberately

maintained to produce fully oxidized metal films. Thus, the technique is applicable in those cases where metal oxides cannot be evaporated directly because of complete or partial decomposition. A controlled oxygen leak is generally used to provide the desired atmosphere, but the thermal decomposition of MnO_2 has also been employed to establish the oxygen pressure.[210] For the kinetics of reactive evaporation, it is important to remember that the mean free path of gas particles at 10^{-4} Torr is of the order of 50 cm (see Fig. 5). Hence, the probability of forming metal oxide molecules through collisions in the gas phase is very small. Instead, recombination takes place on the substrate surface, which is exposed to high incidence rates of metal and oxygen particles.

The formation of an oxide film by reactive evaporation begins with the impingement of metal atoms and O_2 molecules on the substrate surface. Some of these are adsorbed; others are reflected or desorbed after brief contact with the surface. The ratio of permanently adsorbed to total impinging particles is the condensation coefficient α_c. The adsorbed vapors must then react to form the metal oxide. This reaction is essentially an ordering process whereby the adsorbed atoms diffuse across the surface until they fall into the potential wells represented by the regular lattice sites. Consequently, the film-growth process is controlled by the impingement rates of metal atoms and O_2 molecules, the condensation coefficients of the two species, and the substrate temperature.

For practical purposes, the rate at which metal atoms arrive at the substrate is best expressed in terms of the deposition rate as obtained from the same source at the same temperature and distance but in the absence of oxygen:

$$\frac{dN_{Me}}{A_r\,dt} = \mathbb{N}_A \frac{\rho_{Me}}{M_{Me}} d' \qquad \text{atoms cm}^{-2}\text{ s}^{-1}$$

where ρ_{Me} = density of the metal film, g cm^{-3}
   M_{Me} = molar mass of the metal, g mol^{-1}
   d' = pure metal condensation rate, cm s^{-1}
   A_r = receiving (substrate) surface, cm^2

The impingement rate of oxygen molecules is given by the Eq. (37) of Sec. 2b(3):

$$\frac{dN_{O_2}}{A_r\,dt} = 3.513 \times 10^{22}(M_{O_2}T)^{-\frac{1}{2}}p_{O_2} \qquad \text{molecules cm}^{-2}\text{ s}^{-1}$$

where M_{O_2} = molar mass of O_2, 32 g mol^{-1}
   T = gas temperature, usually 300°K
   p_{O_2} = O_2 partial pressure, torr

Impingement rates for a number of evaporants and common gases can be determined with the aid of the nomogram in Fig. 36. As indicated by the broken lines, a chromium condensation rate of 1 Å s^{-1} corresponds to 8×10^{14} atoms cm^{-2} s^{-1}. If the evaporation is carried out at an oxygen pressure of 10^{-6} Torr, the competing rate is about 4×10^{14} O_2 molecules cm^{-2} s^{-1}. Since oxygen is strongly chemisorbed by chromium, a substantial fraction will be incorporated into the film, which therefore consists partially of chromium oxide.[211] O_2:Cr impingement ratios of less than 10^{-2} are required to produce essentially metallic films.[212] If the impinging gas is not adsorbed, however, it may be present in much greater concentrations without being incorporated. An example is the evaporation of Cr at similar rates in 3×10^{-3} Torr of He, which resulted in metallic films of nearly bulk resistivity.[213]

The condensation coefficient α_c may reflect two mechanisms which are responsible for particles being rejected by the film surface. One is the immediate rebounding of molecules whose translational energy was not taken up by the solid upon impact. The other mechanism is rapid desorption as caused by either a small energy of adsorption or high substrate temperatures (see Chap. 2, Sec. 3a). Oxygen is strongly chemisorbed by all metals of interest for reactive evaporation (see Chap. 2, Fig. 37). Even if these energies are substantially reduced because the metal surface is partially oxidized, the corresponding residence times of adsorbed oxygen at room temperature

are still long compared with the film-growth rate. Hence, condensation coefficients $\alpha_c < 1$ indicate mostly lack of energy accommodation (see Chap. 8, Sec. 2a).

The accommodation coefficients of vapors on solids are largely unknown. Available data pertain to the common gases on clean surfaces of a few metals such as Mo and W.[214-217] The values at room temperature are between 0.1 and 0.5, with oxygen at the lower end of the range. The condensation coefficients of metals are usually assumed to be 1 because the impingement rates used in vacuum evaporation cor-

MOLECULES

$p(TORR)$ $cm^{-2}s^{-1}$ $d'(\overset{\circ}{A}\,s^{-1})$

EVAPORANT

$6.0225 \cdot 10^{15} \cdot \dfrac{\rho}{M}$

RESIDUAL GAS

$\dfrac{3.513 \cdot 10^{22}}{\sqrt{M \cdot T}}$

Fig. 36 Nomogram to determine impingement rates. The appropriate point on the evaporant axis is to be connected with the observed (pure) deposition rate on the d' axis. For residual gases, points on the far right and on the pressure axes should be connected. The intersects with the center axis give the impingement rates. (A gas temperature of 300°K has been assumed in locating the common gases on the far right axis.)

respond to pressures far greater than the equilibrium values at ordinary substrate temperatures. Experimentally, the condensation rates of metals evaporated from the same source under identical conditions are usually found to be independent of the substrate temperature from $-195°C$ up to several hundred degrees Celsius. For a few metals, condensation coefficients of 1 have actually been measured (Ref. 35, p. 117).

The reactive evaporation of metals or lower metal oxides onto substrates at moderate temperatures produces amorphous or poorly crystallized films whose stoichiometry is largely determined by the impingement ratio of the constituents. However, because of differences in the condensation of species, the film composition is not necessarily the same as the impingement ratio. This is best illustrated by the mechanism proposed by Ritter[218,219] for the reactive evaporation of Si and SiO. He assumed that the state of film oxidation is determined by the rate at which oxygen is chemisorbed:

$$\left(\frac{dN_{O_2}}{dt}\right)_{ads} = \left(\frac{dN_{O_2}}{dt}\right)_{imp} \frac{z(1-\theta)^2}{z-\theta} \alpha_c \exp\left(-\frac{E}{RT}\right)$$

where θ = surface coverage with oxygen
z = number of nearest surface sites
E = activation energy for the chemisorption of oxygen
α_c = condensation coefficient of O_2 molecules

The Si or SiO particles which arrive simultaneously are thought to condense with $\alpha_c = 1$. Accordingly, the ratio of O : Si atoms in the film is

$$\left(\frac{N_O}{N_{Si}}\right)_{film} = 2\frac{(dN_{O_2})_{ads}}{(dN_{Si})_{imp}} = 2\left(\frac{dN_{O_2}}{dN_{Si}}\right)_{imp} \frac{z(1-\theta)^2}{z-\theta} \alpha_c \exp\left(-\frac{E}{RT}\right) \qquad (73a)$$

and

$$\left(\frac{N_O}{N_{Si}}\right)_{film} = 2\frac{(dN_{O_2})_{ads}}{(dN_{SiO})_{imp}} + 1 = 2\left(\frac{dN_{O_2}}{dN_{SiO}}\right)_{imp} \frac{z(1-\theta)^2}{z-\theta} \alpha_c \exp\left(-\frac{E}{RT}\right) + 1 \qquad (73b)$$

The composition of film samples condensed at room temperature was determined by chemical microanalysis and plotted against the known impingement ratios as shown in Fig. 37. Equations (73a) and (73b) were evaluated by assuming $z = 4$ nearest neighbors and by relating the coverage to the state of film oxidation such that $\theta = 1$ for fully oxidized films with $(N_O/N_{Si})_{film} = 2$, and $\theta = 0.5$ for SiO films with $(N_O/N_{Si})_{film} = 1$. The product $\alpha_c \exp(-E/RT)$ was derived empirically by seeking the best fit for the experimental data. Values of 0.6 for Si and 0.2 for SiO were thus obtained. Further analysis led to the conclusion that the activation energy E was less than 1 kcal mol^{-1} for both reactions, which agrees with the known fact that the chemisorption of oxygen on metals is usually not activated (see Chap. 2, Sec. 3a).

As Fig. 37 demonstrates, Ritter's mechanism describes the empirical relation between film composition and impingement ratio quite well. To produce Si_2O_3 films, an impingement ratio of 20 as represented by a deposition rate of 5 Å s^{-1} in 10^{-4} Torr of oxygen is required. In a subsequent study, Anastasio[220] found a ratio slightly greater than 10 in substantial agreement with Ritter's data. Anastasio's investigation also showed that the same relationship between film composition and impingement ratio holds for a range of deposition rates from 10 to 110 Å s^{-1} and for oxygen pressures between 2×10^{-5} and 2×10^{-4} Torr.

The large excess of impinging oxygen molecules required might suggest that completely oxidized films are obtained with the greatest assurance if the oxygen pressure is increased beyond the necessary minimum. While this is true, it has detrimental consequences for the film properties. When evaporating TiO, Ritter[219] found a decrease in hardness and refractive index of the TiO films condensed at 300°C as the oxygen pressure was increased from 10^{-4} to 10^{-3} Torr. He attributes this to the greater frequency of collisions and associated energy losses which TiO molecules

suffer at the higher oxygen pressure. The effect should be less significant at higher substrate temperatures, which automatically supply the thermal energy required for surface diffusion and ordering processes. This expectation is confirmed by the study of Feuersanger et al.,[221] who evaporated Ba and Ti at 10^{-2} Torr of oxygen. Here, the probability of collisions in the gas phase was high, yet crystalline $BaTiO_3$ films were obtained by maintaining condensation temperatures of 800 to 1000°C.
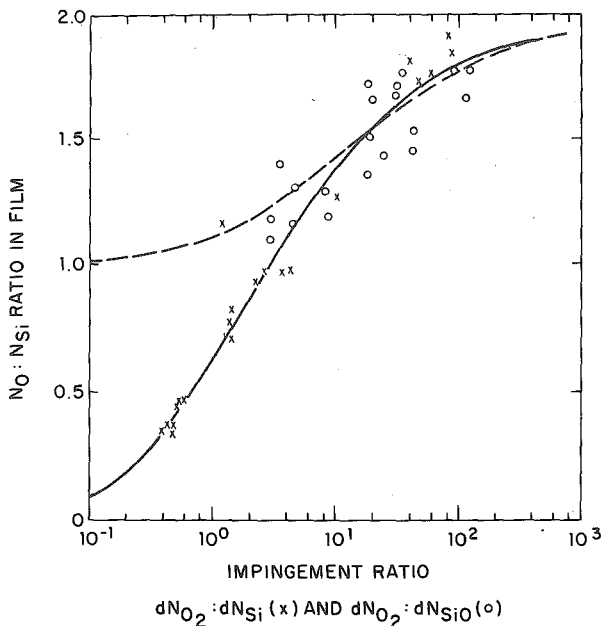
Fig. 37 Oxygen-to-silicon ratio in reactively evaporated films as determined experimentally (points) and calculated from Eqs. (73a) and (73b) (curves). (*After Ritter.*[219])

The reactive evaporation of dielectric films whose properties depend on the attainment of a crystalline structure requires elevated substrate temperatures even if the metal atoms do not lose their kinetic energy by collisions. In these cases, the surface reaction or atomic ordering process is the rate-controlling step. This process is thermally activated in contrast to Ritter's mechanism for Si_2O_3, where nonactivated chemisorption determines the degree of oxygen incorporation. Surface-reaction-controlled deposition has been observed by Krikorian[222] in her study of epitaxial oxide films formed by reactive evaporation onto sapphire substrates. Her results in Fig. 38 show that the growth rates of crystalline Ta_2O_5 films increase with temperature. Since the impingement rates of metal atoms and oxygen molecules are constant for each curve, a significant fraction must be rejected by the growing surface. At the substrate temperatures used, one can expect relatively poor energy accommodation of impinging particles. This holds even for Ta atoms, as the declining growth rates for the pure metal in Fig. 38 show. In addition, the residence times of adsorbed oxygen atoms at these temperatures are short enough to reduce α_c further.

Although the film-growth process is surface-reaction-controlled, the oxygen-to-metal impingement ratio must still be carefully chosen. A minimum O_2 impingement rate is required for complete oxidation. With Ta rates of the order of 2 Å s^{-1}, the minimum oxygen pressure at 700°C is about 10^{-3} Torr, whereas a somewhat lower pressure is sufficient at 900°C, where the reaction rate is higher.[222] The expectation that an

excessive amount of oxygen is tolerable because the film surface rejects it is true only in regard to film composition. The film structure, however, is adversely affected. In the case of Ta_2O_5 growing on single crystalline substrates, epitaxy could not be achieved if the oxygen pressure approached 10^{-3} Torr. For Al_2O_3 films growing at 400 to 500°C, the pressure dividing single-crystal and polycrystalline growth conditions was about 10^{-5} Torr.[222]
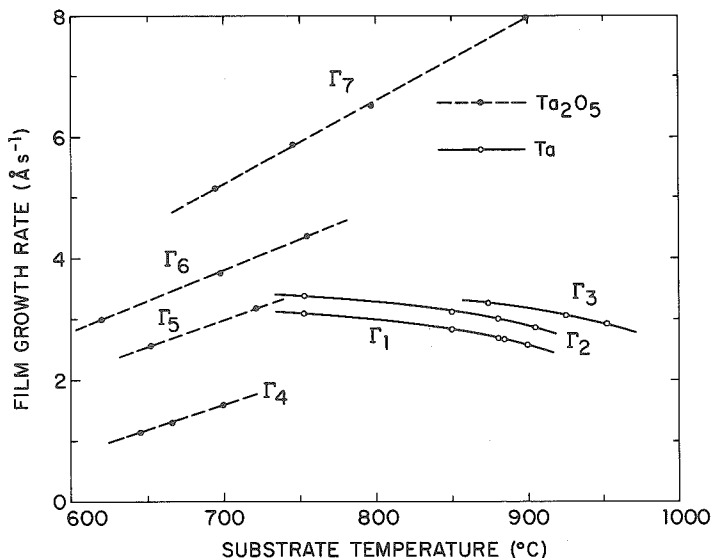
Fig. 38 Film growth rates vs. substrate temperature for constant evaporation rates Γ. The solid lines are for pure tantalum evaporation (Γ_1, Γ_2, Γ_3), the broken lines for reactive evaporation (Γ_4, Γ_5, Γ_6, Γ_7). (*After Krikorian.*[222])

Examples of metal oxides which have been reactively evaporated and the conditions employed are listed in Table 13. In nearly all cases, the deposition rates are small to ensure a high impingement ratio without having to increase the oxygen pressure beyond 10^{-4} Torr. Elevated substrate temperatures are used if film properties such as crystallinity, density, hardness, optical absorption, or dielectric constants are of interest rather than merely film composition. Although the existing studies pertain mostly to oxides, reactive evaporation is applicable to other classes of compounds. An example is CdS, which tends to yield slightly nonstoichiometric, cadmium-rich films of low resistivity if evaporated alone. Pizzarello[230] obtained stoichiometric films of high resistivity by evaporating CdS in the presence of sulfur vapor. Titanium and zirconium nitrides have been prepared by evaporating the respective metals in a nitrogen atmosphere.[231] The formation of carbide films by metal evaporation in the presence of hydrocarbons has apparently not been investigated as yet, possibly because the required substrate temperatures are likely to be impractically high.

(2) Two-source Evaporation The installation of two or more sources for the evaporation of different materials in the same vacuum system is widely practiced to produce multilayer films. By operating two sources simultaneously, it is possible to deposit multiconstituent films which are not amenable to direct evaporation. The types of sources employed are the same as in single-source evaporation. Resistance-heated effusion cells,[232-235] electron guns,[236,237] and wire-ring sources[238] have been successfully used. To avoid cross contamination, the sources must be separated by shields which shadow one source from the vapor of the other without blocking passage to the sub-

TABLE 13 Reactive Evaporation of Metal Oxides

Deposition process	Oxygen pressure, Torr	Deposition rate, Å s^{-1}	Substrate temp, °C	Comments on film properties	References
$2Al(g) + \frac{3}{2}O_2 = Al_2O_3(s)$	5×10^{-4}	. . . .	. . . .	50-Å-thick pinhole-free films of 10^8 ohms cm^{-1} dc resistance	223
	10^{-5}–10^{-4}	4–5	. . . .		224
	2×10^{-6}–5×10^{-5}	$\sim$1	400–500	Epitaxial Al_2O_3 films on sapphire at $p_{O_2} \leqq 10^{-5}$ Torr	222
$2Cr(g) + \frac{3}{2}O_2 = Cr_2O_3(s)$	2×10^{-5}	$\sim$2	300–400	Dielectric films of poor crystallinity	225
	$\sim 10^{-5}$	$\sim$1	25	Film density approaches that of bulk Cr_2O_3	211
$2Fe(g) + \frac{3}{2}O_2 = Fe_2O_3(s)$	10^{-4}–10^{-3}	. . . .	. . . .	Nearly amorphous Fe_2O_3 films	226
$2Cu(g) + \frac{1}{2}O_2 = Cu_2O(s)$	10^{-4}–10^{-2}	. . . .	. . . .	Cu_2O films converted into CuI films by exposure to I_2 vapors	227
$SiO(g) + \frac{1}{2}O_2 = Si_2O_3(s)$	10^{-5}–10^{-4}	. . . .	−195 to 500	Absorption coefficient is a function of Si:O ratio in films	228, 229
	9×10^{-5}	4.5	Up to 350°C	Essentially Si_2O_3 films without absorption of visible light	174
	10^{-4}	5	25	O_2:Si impingement ratio must be about 20 to obtain Si_2O_3 films	218, 219
	2×10^{-5}–2×10^{-4}	10–110	. . . .	Film composition depends only on the O_2:Si impingement ratio. This must be $\sim$10 for Si_2O_3	220
$2Ta(g) + \frac{5}{2}O_2 = Ta_2O_5(s)$	10^{-4}–10^{-3}	$\sim$2	700–900	Epitaxial Ta_2O_5 films on sapphire and CaF_2 substrates	222
$TiO(g) + \frac{1}{2}O_2 = TiO_2(s)$	$\sim 10^{-4}$	. . . .	300	Hardness and refractive index of films suffer if $p_{O_2} > 10^{-4}$ Torr	219
$Ba(g) + Ti(g) + \frac{1}{2}O_2 = BaTiO_3(s)$	10^{-2}	2–8	770–1025	Films on polished Pt-Rh substrates had dielectric constants up to 1,330	221

TABLE 14   Two-source Evaporation, Experimental Conditions, and Types of Films Obtained

Evaporated constituents	Evaporation conditions and method of control	Sub-strate temp, °C	Films obtained	References
Alloy and Multiphase Films				
Cu + Ni................	Sequential evaporation	Low	Stratified films. Annealing at 200°C yields two-phase alloy films	241
Cu, Ag, Au, Mg, Sn, Fe, Co.	Simultaneous evaporation from two sources. Ionization-rate monitor control, $\pm 1\%$	-193	Binary alloy films of metastable structures	240
Cu, Ag, Au, Al, Ni, and others	Simultaneous evaporation from two sources. Rates adjusted by varying source temperatures	25–600	Binary alloy films of varying composition and structure	242
Ni + Fe.................	Two wire-ring sources, evaporation rates controlled by quartz-crystal oscillator	300	Permalloy films. $d' \approx 10$ Å s^{-1}	238
Nb + Sn................	Two sources, rates monitored by particle impingement–rate monitor. Impingement ratio $N_{Nb} : N_{Sn} = 3$	25–700	Superconducting Nb$_3$Sn films. $d' \approx 2$ Å s^{-1}, $\alpha_c \approx 1$	243
V, Nb + Si, Sn............	Two electron-gun sources, rates monitored by measuring ionization current	....	Superconducting films of approx composition Nb$_3$Sn and V$_3$Si	237
ZnS + LiF...............	Two sources, rates monitored by a microbalance. Variable impingement ratios	30–40	Mixed dielectric films of different composition. $d' = 10$–30 Å s^{-1}	244
Au, Cr + SiO, MgF$_2$.......	Two-source evaporation with ionization-rate monitor control (± 1–2 %)	25–300	Au-SiO, Au-MgF$_2$, Cr-SiO, and Cr-MgF$_2$ resistor films of different compositions	245
Cr + SiO................	SiO source at 1100°C, Cr source at 1500°C. Impingement ratio varied with location on substrate	400	High-resistivity Cr-SiO films of variable composition	246

TABLE 14   Two-source Evaporation, Experimental Conditions, and Types of Films Obtained (Continued)

Evaporated constituents	Evaporation conditions and method of control	Sub-strate temp, °C	Films obtained	References
		Compound Films		
Cd + S.................	Two effusion ovens, Cd at 400–450°C, S at 120–150°C. Cd excess	400–650	Stoichiometric CdS crystals	232
Cd + Se................	Impingement fluxes controlled by source temperature. $N_{Cd} = 2 \times 10^{16}$, $N_{Se} = 10^{16}$–10^{17} cm^{-2} s^{-1}	200	Stoichiometric CdSe films	247, 248
PbSe + PbTe...........	Source temperatures varied around 700°C	300	Epitaxial films of PbSe$_{1-x}$Te$_x$ on NaCl crystals	233
Bi + Te................	Bi source at 750°C, Te source temperature variable. $N_{Te}:N_{Bi} = 10$–40	400–500	Stoichiometric films of Bi$_2$Te$_3$. n-type, 2×10^{19} electrons cm^{-3}	249
Bi + Se................	Rate control by quartz-crystal oscillator. Se source at 250°C; Bi source temperature variable	52	Vitreous, semiconducting films of nonstoichiometric composition	250
Al + Sb................	Source temperatures adjusted by quartz-crystal oscillator to yield $N_{Sb}:N_{Al}$ ratios of 1.6–16	550	Stoichiometric AlSb films. $d' \approx 10$ Å s^{-1}	234
Ga + As................	Ga source at 940–970°C, As source at 300°C. $N_{As}:N_{Ga} \approx 10$; Ga impingement flux: 10^{15} cm^{-2} s^{-1}	550	Stoichiometric GaAs films. Epitaxial on (100) NaCl, polycrystalline on quartz	251
Ga + As................	Ga source at 910°C, As source at 295°C. Deposition rate: <2 Å s^{-1}	375–450	Stoichiometric GaAs films on GaAs, Ge, and Al$_2$O$_3$ single-crystal substrates. Fiber texture to single-crystalline	252
In + As................	Incident fluxes: $N_{In} = 5 \times 10^{16}$ cm^{-2} s^{-1}, $N_{As} = 5 \times 10^{16}$–$5 \times 10^{17}$ cm^{-2} s^{-1}	230–680	Stoichiometric InAs films; n-type	247, 248
In + Sb................	Incident fluxes: $N_{In} = 5 \times 10^{16}$ cm^{-2} s^{-1} $N_{Sb} = 5 \times 10^{16}$–$5 \times 10^{17}$ cm^{-2} s^{-1}	400–520	Stoichiometric InSb films; n-type	247, 248
	Source temperatures adjusted by microbalance to yield $N_{Sb}:N_{In} = 1.1$	250	Stoichiometric InSb films; α_c of Sb ≈ 0.6	253

strate.   Thermal insulation of the sources is also important to facilitate independent temperature adjustments.[233]

The evaporation of two materials at different temperatures followed by joint condensation on the same substrate circumvents the problems of fractionation and decomposition encountered in the direct evaporation of most alloys and certain compounds.   It is also possible to codeposit materials which form neither compounds nor solid solutions.   Because of the random arrival of single atoms and their limited mobility in the absorbed state, these multiphase films consist of very small particles which are intimately mixed.   Important examples are resistor films of ceramic oxides and metals (cermets), whose multiphase nature becomes apparent only after annealing and recrystallization.[239]   Segregation of phases can also be suppressed in binary metal systems.   This was demonstrated by Mader,[240] who obtained metastable alloy films by condensation onto liquid-nitrogen-cooled substrates.   A list of coevaporated materials, their experimental conditions, and the resulting films is shown in Table 14.

The objective of two-source evaporation is the deposition of films having one particular composition.   Therefore, the central problem in this technique is the control of condensation rates in the exact constituent ratio desired.   These rates are primarily determined by the equilibrium pressure of the evaporant, $p^*(T_1)$, at the source temperature.   As the evaporant spreads omnidirectionally, the particle density decreases with increasing distance from the source.   Assuming a small-surface source with an emission characteristic according to Eq. (52), and expressing $\mathfrak{M}_r$ by the corresponding impingement pressure [Eq. (37)] and $\mathfrak{M}_e$ by the mass-evaporation rate [Eqs. (48) and (49)], the vapor pressure p_r at the receiving surface is given by

$$p_r = \frac{A_e \cos \varphi \cos \theta}{\pi r^2} p^*(T_1) \tag{74}$$

where A_e = area of vapor source
$\varphi,\ \theta$ = angles of emission and incidence, respectively
r = distance between source and point receiving deposit

Most metals and congruently evaporating compounds have very small equilibrium pressures at practical substrate temperatures T_3.   Accordingly, p_r is much larger than the equilibrium pressure $p^*(T_3)$.   If a vapor is highly supersaturated with respect to the surface temperature, condensation occurs generally with $\alpha_c = 1$.   Consequently the composition of alloy and metal-dielectric films is determined by the constituent pressures p_r at the substrate.   The control of the film composition may then be achieved by direct measurements of the particle density in the vapor stream, using ionization-rate monitors,[236,240,245] quartz-crystal oscillators,[238,250] electromagnetic microbalances,[253] or mechanisms which are actuated by the momentum received from impinging particles.[243,244]   The two monitoring devices required must be located so that they are exposed to the vapor of only one but not the other constituent.   The source temperatures are adjusted manually to yield predetermined condensation rates, or the electric signal of the monitor may be used to maintain the rates constant at the desired levels (see Sec. 7d).   Feedback control in conjunction with ionization-rate monitors has allowed film-composition control within ± 1 to 2%.[240,245]

A general problem is the positioning of two sources such that the substrate area is exposed uniformly to both vapor streams.   According to Eq. (74), the effective vapor pressure p_r depends on the angle of incidence θ.   While a few percent thickness variation across the substrate area is often acceptable, differences in angles of incidence from two sources also cause compositional deviations, as illustrated in Fig. 39.   This effect is minimized if concentric two-source arrangements are used.[238,247,248]   An alternate solution is to tilt the effusion ovens such that both are aimed at the substrate surface under the same angle of inclination.[232]   In general, angle-of-incidence effects can be reduced by increasing the source-to-substrate distance.   If films of continuously varying composition are to be deposited, this may be accomplished by deliberately spacing the two sources far apart.[246]

The composition of compound films is less sensitive to source positioning and requires less stringent control of the impingement fluxes than alloy or metal dielectric

films.   The reason is that the condensation rate of compounds is not solely a function of the ratio of constituent vapor pressures but is also determined by surface reaction. Thus, two-source evaporation of compounds is similar to reactive evaporation where the substrate temperature controls the film growth.   The preferential condensation of compounds from binary vapors has been analyzed by Guenther[247,248] and developed into an experimental technique known as the three-temperature method.   The latter exploits the fact that the free energies required for the dissociation of compounds according to

$$AB(s) = A(g) + \tfrac{1}{2}B_2(g)$$
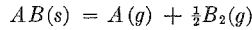
are greater than the free energies of evaporation of the constituents

$$A(s) = A(g) \qquad \text{and} \qquad B(s) = \tfrac{1}{2}B_2(g)$$
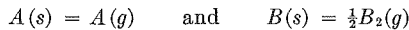
This difference is reflected in constituent vapor pressures which are lower over the compound than over the pure elements.   Figure 40 illustrates the situation for CdSe.   At fixed constituent pressures p_r over the substrate surface, there exists a wide temperature interval within which the vapors are supersaturated only in regard to the compound but not for the elements.

The degree of supersaturation required to deposit the compound but not the pure elements depends further on the condensation coefficients α_c, which are generally not known a priori.   Guenther[248] determined the condensation coefficients of Cd and

Fig. 39   Two-source evaporation arrangement yielding variable film composition.
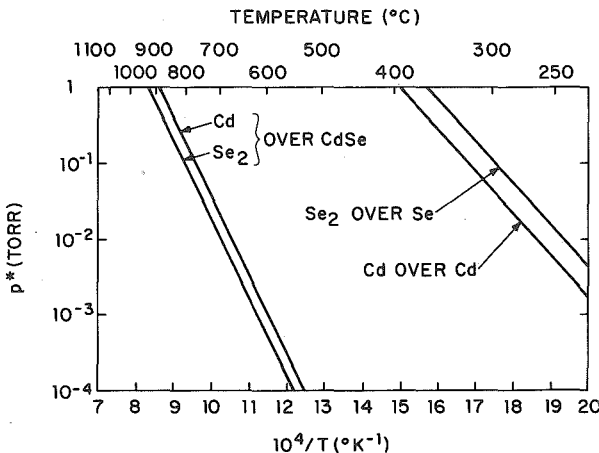
Fig. 40   Equilibrium vapor pressures of Cd and Se_2 over the compound (*Burmeister and Stevenson*[163]) and over the pure elements (*Honig*[19]).

Se_2 experimentally and derived temperatures and impingement rates which allow only compound formation.   As shown in Table 14, the stoichiometry of CdSe films condensed at 200°C with a Cd impingement rate of 2×10^{16} cm^{-2} s^{-1} is maintained if the selenium rates vary from 10^{16} to 10^{17} cm^{-2} s^{-1}.   This degree of freedom in the

constituent vapor-pressure ratio has been termed the stoichiometric interval.[248] Its extent is a function of the substrate temperature and the vapor pressures p_r.

The three-temperature method is also applicable if one of the constituents is not volatile at the substrate temperature. This is the case with III-V compounds and is illustrated for InAs in Fig. 41. In contrast to CdSe, indium vapor which is super-saturated with respect to the compound is also supersaturated in regard to the pure-metal phase. Therefore, stoichiometric intervals for III-V compounds require an excess of the more volatile constituent to ensure that the condensing group III element reacts to completion. The evaporation conditions listed in Table 14 show that the impingement ratios may vary from 1 to 10. The absolute rates generally used are of the order 10^{15} to 10^{17} cm^{-2} s^{-1}, which corresponds to pressures of 10^{-5} to 10^{-3} Torr over the substrate. Higher pressures are not recommended because of excessive scattering as the two vapor streams mix.
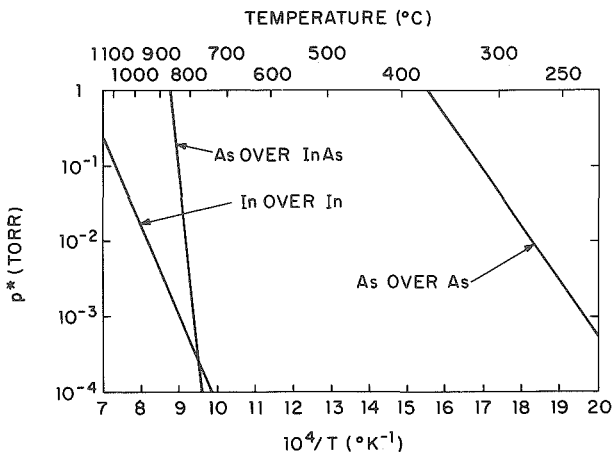
Fig. 41 Equilibrium vapor pressures of In and As over the elements (*Honig*[19]), and decomposition pressure of As over InAs (*Guenther*[248]).

Considerable freedom also exists in the choice of substrate temperatures. However, the useful temperature interval is often narrowed by factors other than film stoichiometry. To obtain highly ordered crystalline films, temperatures somewhat above the minimum values for single-phase condensation are required. Upper limits are imposed by the necessity to achieve supersaturation below about 10^{-3} Torr, or by the melting point of the compound as in the case of InSb. More subtle effects are slight deviations from stoichiometry which vary with temperature and determine the type and degree of semiconductivity. Thus, InAs films deposited at lower temperatures contain an As excess, while condensation at the upper end of the temperature range leads to an As deficit.[248]

The risk of obtaining large deviations from the stoichiometric composition is potentially greater if one or both constituents have substantial solubilities in the compound. This is the case for Bi and Te in Bi$_2$Te$_3$. However, Haenlein and Guenther[249] established that such compounds, too, may have stoichiometric intervals. As shown in Table 14, a large excess of Te vapor can be rejected and the film stoichiometry maintained. These considerations do not apply at low substrate temperatures, where impinging molecules are indiscriminately incorporated into the film as exemplified by the Bi-Se system in Table 14. The pseudo-binary system Pb (Se,Te) is comparable with Bi$_2$Te$_3$ insofar as one constituent, PbTe, has a fairly broad range of existence.[79] Mixed compound films of the III-V family have also been prepared by simultaneous evaporation from three sources.[235]

(3) Flash Evaporation   Flash evaporation is another technique for the deposition of films whose constituents have different vapor pressures.   In contrast to two-source evaporation, it does not require provisions to monitor the vapor density, nor is the control of the source temperature particularly critical.   The objective of film-composition control is accomplished by evaporating to completion small quantities of the constituents in the desired ratio.   Only one filament is used at a temperature sufficiently high to evaporate the less volatile material.   Although fractionation occurs during the evaporation of each particle, the latter are so small that stratification in the film is limited to a few atomic layers.   These potential inhomogeneities are further reduced by dispensing the evaporant in a steady trickle.   Thus, there are several particles in different stages of fractionation residing on the filament at all times.   The net result of these simultaneous, discrete evaporations is a vapor stream whose composition is uniform and identical to that of the source material.   Accordingly, excellent control of film composition can be achieved.   Young and Heritage[254] reported that Ni-Fe-Cr films prepared by flash evaporation showed less compositional variation than sputtered films.

The technique is applicable for the evaporation of alloys, metal-dielectric mixtures, and compounds, as shown by the examples in Table 15.   In most cases, the vapors impinging on the substrate are highly supersaturated so that the film composition is not affected by condensation coefficients.   The cuprous chalcogenides[271] are an exception, but generally the control of film composition is determined by how well the objective of complete evaporation of the source material is accomplished.   For this purpose, several experimental techniques are available.   They can be characterized by three criteria, namely, the form in which the evaporant material is introduced, the mechanism used to dispense the evaporant, and the type of flash filament employed.

In the case of metals and alloys, continuous evaporation of small quantities is possible by feeding wire from a spool through a guide tube against the hot filament.   Such mechanisms have been described by Tandeski et al.[257] for Permalloy and by Siddall and Probyn[114] for Nichrome.   A modified arrangement, which allows alternate flash evaporation of metals and organic insulators, utilizes knife-edges to cut short lengths of wire which are dropped onto the filament.[259]   In general, however, the evaporant is not available in wire form, and the greatest freedom in regard to materials is obtained by utilizing powders.

Various types of powder dispensers are shown in Fig. 42.   They all have storage hoppers but differ in the powder release and transport mechanisms.   The moving-belt feeder (Fig. 42a) was the first device employed in flash evaporation, but it has rarely been used after its introduction by Harris and Siegel in 1948,[255] since alternate approaches are mechanically simpler.   The worm-drive feeder in Fig. 42b moves the powder from the hopper to a release opening by means of an Archimedean screw.   Its application has been restricted to metal-dielectric mixtures because the worm gear tends to compress metal powders into lumps, while brittle compounds are ground into very small particles.   These effects make uniform and complete evaporation impossible.   The ratchet gear and spring mechanism is widely used in other types of feeders, too, to prevent the powder from sticking and accumulating in the chute.

Since particle grinding and jamming are common problems with worm-drive feeders, alternate solutions have been sought.   The disk feeder shown in Fig. 42c exerts no mechanical force on the powder.   Its feed rate is determined by the gap between hopper and disk and by the number of revolutions per minute.   The device can be modified to dispense pellets rather than powder by providing an orifice instead of a gap at the lower end of the hopper.[137]   This design offers a greater loading capacity than the disk magazine feeder in Fig. 42d, which is also used to dispense metal pellets or spheres.[258]

Powder dispensers which operate by either mechanically[266] or electromagnetically[276] induced vibrations (Fig. 42e and d) have been employed mostly for the evaporation of compounds.   They do not allow the same latitude in feed-rate adjustment as disk devices because the trickle of powder tends to become discontinuous or non-uniform under various conditions.   This is not too critical, since most compounds evaporate more easily and rapidly than refractory metals, and since each compound

TABLE 15 Flash Evaporation of Materials

Materials	Form of evaporant	Feeder mechanism	Filament temp, °C	Substrate temp, °C	Comments on films	Reference
			Metals and Alloys			
Au(64)-Cd(36), Cu(52)-Zn(48)...	Powdered alloys, 80/100 mesh	Moving belt	. . . .	. . . .	Au-Cd and β-brass films have composition of source	255
Ni + Fe......................	Mixed powders	Disk and wiper	~1930	. . . .	Ni-Fe films with ±1 % control of composition	256
Ni(86)-Fe(14).................	Alloy wire	Spool and guide tube	2000	300	Ni-Fe film composition equal to that of source ±0.2 %	257
Ni; Fe; Cu; constantan; chromel; alumel	Pellets	Disk magazine	2000	200–250	Thin film thermocouples. Rates: 5–300 Å s⁻¹ across 12 cm distance	258
Ni(80)-Cr(20).................	Alloy wire	Spool and guide tube	1620	. . . .	Nichrome films, Cr content varies with filament temperature	114
Ni + Cr (20, 55, 70 % Cr).......	Mixed powders, 100/300 mesh	Vibrating chute	1800	300	Alloy films within 1 % of source composition. Rates: 1–10 Å s⁻¹	200
Sn; nylon....................	Wire; strands	Two spools and cutting knives	200 (nylon)	~0	Alternate layers of metal and insulator	259
			Metal-Dielectric Mixtures			
Cu + SiO (1:5)...............	Mixed powders	Rotating tube	. . . .	−269	Highly disordered films of high resistivity	260
Cr + 30 mol % SiO............	Mixed powders, 325/400 mesh	Worm drive	~2000	200	250 ohms/sq resistor films with +20 to 50 % deviations	261
Cr + SiO (62 and 74 mol % Cr)..	Mixed powders, 125/325 mesh	Worm drive	2000	400	Resistor films; SiO content less than source. Rates: 4 Å s⁻¹ across 23 cm distance	262
Cr + SiO (50–100 mol % Cr)....	Sintered pellets, ~0.7 mm size	Disk and wiper	2050 ± 50	200	Resistor films, SiO content equals that of source ±1–3 %. Rates: 20–30 Å s⁻¹ across 70 cm distance	137, 239
Cr(15)-Si(85).................	Powdered alloy	Vibrating chute	2000	200–500	Resistor films	263
Cr₃Si + TaSi₂ + Al₂O₃..........	Mixed powders	Worm drive	2500	200–400	Resistor films with ± 10 % control	264

TABLE 15 Flash Evaporation of Materials (Continued)

Materials	Form of evaporant	Feeder mechanism	Filament temp, °C	Substrate temp, °C	Comments on films	Reference
		Compounds				
AlSb............................	Powder, 100/150 mesh	Vibrating trough	1400–1600	700	Imperfect epitaxial films on Ge	265, 266
GaP............................	Powder, 100/150 mesh	Vibrating trough	1500	540	Epitaxial films on Ge crystals	265, 266
GaAs............................	Powder, 100/200 mesh	Vibrating trough	1450	300–670	Epitaxial films on Ge crystals above 600°C. Rates: 2–30 Å s^{-1}	267
	Powder, 100/200 mesh	Worm drive	1400–1800	530 ± 10	Epitaxial films on GaAs crystals. Rates: 2–5 Å s^{-1} across 21 cm distance	268
	Powder, 100/150 mesh	Vibrating trough	1300–1800	475–525	Epitaxial films on Ge crystals	265, 266
	Powder, 40/60 mesh	Micrometer screw and piston	1325	525–575	Highly oriented films on Ge and GaAs crystals. Rates: 10–25 Å s^{-1} across 10 cm distance	269
GaSb............................	Powder, 100/150 mesh	Vibrating trough	1650	500	Epitaxial films on Ge crystals	265, 266
InP............................	Powder, 100/150 mesh	Vibrating trough	1400–1650	300	Epitaxial films on Ge crystals	265, 266
InAs............................	Powder, 100/150 mesh	Vibrating trough	1500	500	Epitaxial films on Ge crystals	265, 266
InSb............................	Granules	Vibrating trough	1600	450–460	Epitaxial films on InSb crystals, n-type, 10^{15}–10^{17} donors per cm^3	270
	Powder, 100/150 mesh	Vibrating trough	1650	300–400	Epitaxial films on Ge crystals	265, 266
Cu_2S; Cu_2Se....................	Powders of 250–300 μ	Vibrating chute	1400	25	Semitransparent, conductive films of $Cu_{1.8}S$ and $Cu_{1.8}Se$	271
$BaTiO_3$........................	Sintered powder, 100/200 mesh	Vibrating trough	2300	500–700	Crystalline films, dielectric constants of 400–700. Rate: 3 Å s^{-1} across 8 cm distance	272 272
	?	?	2100	900–1000	Epitaxial films on sapphire and Si crystals, $p(O_2)$ = 10^{-4} Torr. Rates: 0.1–0.3 Å s^{-1}	273
Various perovskites..............	Sintered powder, 100/200 mesh	Vibrating trough	2050–2300	500–700	Perovskite films, epitaxial on LiF crystals. Rates: 1–3 Å s^{-1} across 8 cm distance	274

particle contains the constituents in the proper ratio. An ultrasonic particle feeder consisting of a stainless-steel tube attached to a barium titanate transducer has been described by Eckardt and Peacock.[277] A vibratory feeder of large storage capacity is commercially available.* It is a cylindrical container with a helical grove cut into its interior wall. Vibrations induced by a solenoid convey a continuous stream of
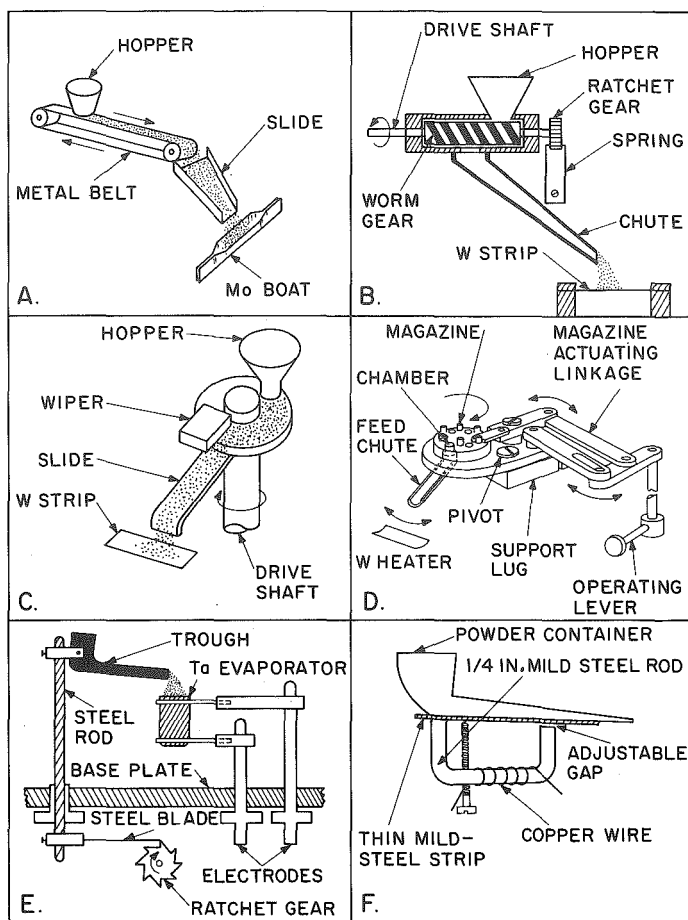
Fig. 42 Flash-evaporation mechanisms. (A) Belt feeder. (*Harris and Siegel.*[255]) (B) Worm-drive feeder with mechanical vibrator. (*Himes, Stout, and Thun,*[275] *Braun and Lood.*[262]) (C) Disk feeder. (*Beam and Takahashi.*[256]) (D) Disk magazine feeder. (*Marshall, Atlas, and Putner.*[258]) (E) Mechanically vibrated trough and cylindrical source. (*Richards.*[266]) (F) Electromagnetically vibrated powder dispenser. (*Campbell and Hendry.*[200])

evaporant upward in the helix and to an exit channel. The material must be available in the form of granules or pellets of 0.1- to 0.8-mm size.

Of considerable importance is the proper choice of material and design for the flash-evaporation filament. The latter must be capable of attaining temperatures of

---

* Bendix Corporation, Vacuum Division, Cincinnati, Ohio; in Europe: Balzers A.G., Liechtenstein.

typically 2000°C without volatilization or heavy reaction with the evaporant. Flat posts of refractory materials which are heated by electron bombardment have been used in conjunction with wire feeders.[114,257] Powder flash evaporation from an electron-beam-heated tungsten disk has been reported by Wilson and Terry.[264] By far the most common technique, however, is the evaporation from resistance-heated refractory-metal sources. The simplest filaments are flat strips of 0.005-in. tungsten sheet which are easily made and may be discarded after one experiment. The latter consideration is significant because tungsten alloys with most of the materials in Table 15 so that the useful life of the filament is limited. For the III-V compounds, which require somewhat lower evaporation temperatures, tantalum filaments are also suitable.[266,270] $BaTiO_3$ and the other perovskites, however, severely attack tungsten through oxidation. Therefore, these materials have been evaporated from iridium filaments.[272-274]

A universal problem encountered in the flash evaporation of powders from flat filaments is incomplete evaporation due to particle ejection and deflection. Since the evaporant has a large surface-to-volume ratio but can usually not be degassed prior to evaporation, the sudden release of gases upon impact on the filament is often sufficient to expel particles. Another loss mechanism is the deflection of falling powder away from the filament by the current of rising vapors. The latter effect is stronger the higher the evaporation rates, which are thereby limited. An example is the maximum feed rate of 0.15 g min^{-1} for Nichrome alloys found by Campbell and Hendry.[200] Small particles are more strongly deflected than larger ones,[268] which is the reason for using graded powders. The losses of unevaporated source material may be as high as 50%,[256] particularly if long source-to-substrate distances necessitate high feed and evaporation rates.[137]

Fig. 43 Flash-evaporation filament with spot-welded chimney and separate deflection cone. (*Glang, Holmwood, and Maissel.*[137])

In the evaporation of homogeneous powders such as compounds or alloys, particle ejection and deflection affect only the economy of the process and the maintenance of the vacuum system. There is, of course, also the risk that particles may be thrown against the substrate surface. To avoid these difficulties, coarser powders and cylindrical (see Fig. 42e) or conical crucibles have been used in the evaporation of perovskites[274] and III-V compounds.[266,270] Ellis[271] folded a tungsten sheet to form a resistance-heated filament shaped like an open envelope. When alloy or metal-dielectric films are evaporated from mixed powders, evaporant losses are also associated with unpredictable changes in film composition. This has been observed with Ni-Fe films, which tend to contain less iron than the source material,[256] and with Cr-SiO films, which are deficient in the lighter component, SiO.[137,262] Since the properties of resistor films, in particular the degree of resistance change during post-deposition annealing and stabilization, are very sensitive to variations in composition, flash evaporation is practical only if evaporant losses are avoided.

In the case of Cr-SiO, this has been accomplished by sintering the mixed powders into pellets which contain the constituents in the proper ratio and are sufficiently large to fall through the rising vapors without deflection.[137] To avoid losses from rebounding or decrepitating pellets, the flash filament may be provided with a spot-welded tantalum chimney and a separate metal cone, as shown in Fig. 43. The filament can be changed without having to discard the cone. Temperature control is facilitated by a thermocouple whose tip is spring-loaded against the filament bottom. With this arrangement, pellets containing up to 30 mol % SiO yielded films of identical composition with deviations of only ±1%. At higher SiO concentrations, the degree of
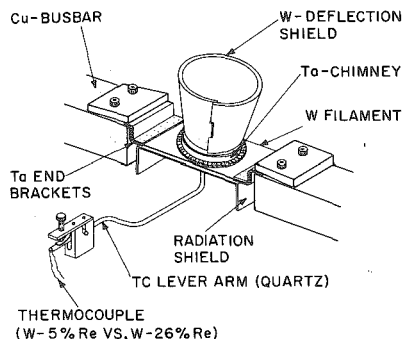
control is slightly inferior. Furthermore, since deflection losses are eliminated, the flash source is only power-limited; i.e., the feed rate can be increased until the filament temperature drops because of an overload of evaporant. Feed rates of about 1 g min^{-1} with deposition rates between 20 and 30 Å s^{-1} across 70 cm substrate distance have been obtained.

Flash evaporations have mostly been performed in poor vacua of 10^{-5} to 10^{-4} Torr. This is attributable to the high gas content of the evaporant powder and outgassing from the surfaces surrounding the relatively large-area flash filament. The effect of the high background pressure on film properties may be inconsequential, especially in the case of oxide films. However, this is not so if strongly electropositive metals are deposited. Siddall and Probyn[114] found that the chromium content of Nichrome films evaporated at 10^{-4} Torr varied significantly as a function of the filament temperature. At 1400°C, the films were deficient in chromium, while an excess was found at 1700°C. It is believed that the evaporation of Cr at low temperatures is retarded by the formation of chromium oxide which becomes volatile at the higher temperatures. In a few instances, pressures of 10^{-6} Torr or less have been maintained, for example, during the flash evaporation of InSb[270] and CrSiO.[137,262]

The temperatures of the substrates in Table 15 determine primarily the degree of order and crystallinity in the films. The temperatures listed for compounds are those required for homo- or heteroepitaxial films. In the case of III-V compounds, the upper limit is determined by reevaporation of the group V constituent, whereas lower temperatures yield polycrystalline films.[265] An excess of the group V constituent in the source material does not affect the film stoichiometry adversely since the condensation process is reaction-controlled as in two-source evaporation.[266] Flash evaporation has also been used to prepare single-phase pseudo-binary compounds of the III-V family.[278]

7. DEPOSITION MONITORING AND CONTROL

The objective in vacuum evaporation is nearly always to deposit films to certain specifications. If the latter pertain to film properties which are primarily extensive such as thickness or sheet resistance, it is sufficient to determine when the accumulated deposit has reached the desired value so that the process can be terminated. However, intensive film properties such as density, resistivity, stress, or crystallinity depend on the rates at which evaporant and residual gas molecules arrive at the substrate. It is therefore often necessary to maintain specified evaporation rates. The sensing devices which allow measurements during the evaporation process are referred to as either thickness or rate monitors. They exploit different physical effects to determine the density of the evaporant stream, the mass of the deposit, or a thickness-dependent film property.

Traditionally, monitoring devices have been constructed by individual investigators to suit their particular purpose, and numerous design modifications have been reported in each class. Several types of monitors have become commercially available during the last few years, after sufficient operational experience had been accumulated to judge their ruggedness and ranges of application and to select the most practical design features. Reviews of thickness and rate monitors have been given by Steckelmacher[279] and Behrndt.[139] The reader is referred to these articles for more detailed descriptions of individual devices, since the following treatment is limited to the operating principles and gives only a few representative examples.

a. Monitoring of the Vapor Stream

There are two methods of measuring the density of the evaporant vapor stream. In one technique, the vapor molecules are ionized by collisions with electrons, and the ions are collected. The other approach is based on measuring the dynamic force which impinging particles exert on a surface. Both methods indicate the *evaporation rate* at a particular instance. To derive the accumulated film thickness, the rates must be integrated. Furthermore, the methods require empirical calibration; i.e.,

the film thicknesses obtained for known deposition times have to be determined independently to correlate rate-meter indication and actual deposition rate. The resulting calibration curves are specific for the individual monitoring device and the material evaporated. Their reproducibility is also contingent upon leaving the source, rate meter, and substrates in fixed positions.

(1) **Ionization-gauge Rate Monitors**   Rate-monitoring devices based on the ionization of evaporant vapors are shown in Fig. 44. All have a hot-tungsten emission
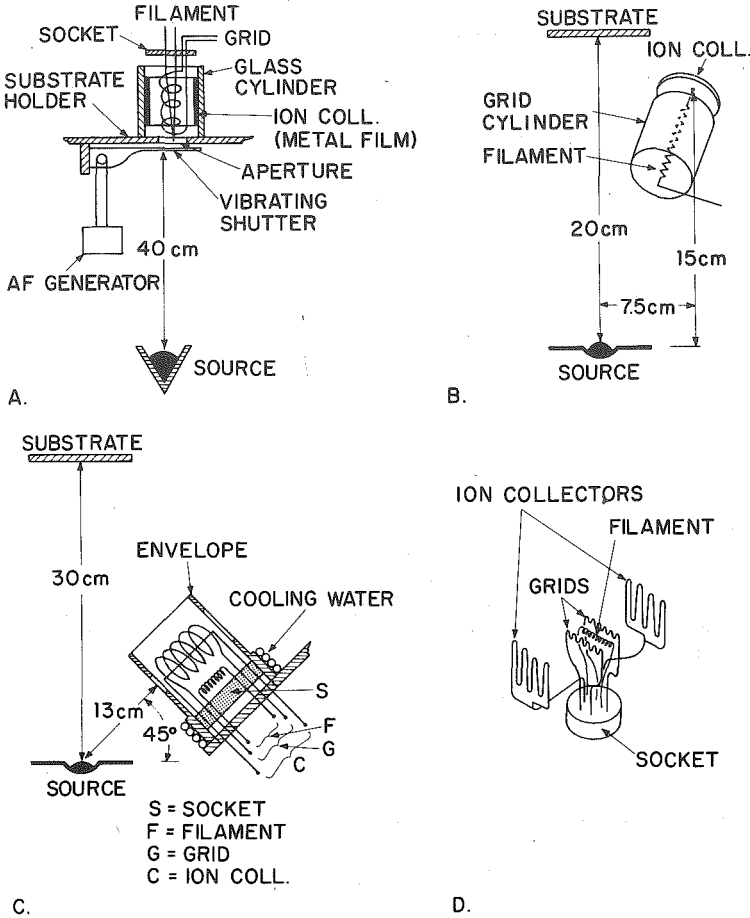
Fig. 44   Ionization-rate monitor designs and arrangements.   (*A*) After Schwarz.[280]   (*B*) After Giedd and Perkins.[284]   (*C*) After Perkins.[285]   (*D*) After Dufour and Zega.[282]

filament to provide electrons. The latter are accelerated with voltages of 150 to 200 V by means of grids (anodes) in the form of a helix, a cylinder, or a wire electrode. The ion collector may be a cylinder, a disk, or a simple wire to which negative voltages of the order of 20 to 50 V are applied. The monitors are mounted so that the ion collector and the entrance aperture point toward the vapor source. The distance to the source may be the same as the source-to-substrate separation or made shorter to enhance the sensitivity.

The ion current I_i which is produced by an electron-emission current I_e is given by[280]

$$I_i = D'I_e \left(\frac{N}{V}\right)_m$$

where $(N/V)_m$ is the number of vapor molecules per cubic centimeter in the monitor and D' is a gauge constant. The vapor density in the monitor depends on the rate of molecules arriving at the entrance aperture (area $= A_m$) and on their average velocity $\bar{c}$:

$$\frac{dN_m}{A_m \, dt} = \left(\frac{N}{V}\right)_m \bar{c}$$

The arrival rate can be derived from the emission law which is applicable to the vapor source. For a small-surface source it is given by Eq. (52) in Sec. 3c(1):

$$\frac{d\mathfrak{M}}{A_m \, dt} = m \frac{dN_m}{A_m \, dt} = \Gamma \frac{A_e \cos \varphi_m \cos \theta_m}{\pi r_m^2}$$

where A_e = effective vapor-source area
$\quad r_m$ = source-to-monitor distance
$\quad \varphi_m, \theta_m$ = angles of emission and incidence for the monitor
$\quad \Gamma$ = mass-evaporation rate per unit source area

By substituting $\bar{c}$ according to Eq. (35) and Γ from Eq. (48), the monitor ion current can be expressed as a function of the vapor pressure p^* of the evaporant at the source temperature T:

$$I_i = D'I_e \frac{A_e \cos \varphi_m \cos \theta_m}{\pi 4kT r_m^2} p^* \tag{75}$$

The significance of the gauge constant becomes more apparent in the relation[280]

$$D' = 7.5 \times 10^{-4} S_0 kT_0 \qquad \text{(for } p^* \text{ in torr, } T_0 = 300°\text{K)}$$

Here, S_0 is the dynamic gauge sensitivity, a parameter which measures the response of an ion gauge to the flow of vapor, as opposed to the static sensitivity, which is usually quoted for ion gauges but refers to stationary gases.[281] Dynamic gauge sensitivities as determined for rate monitors range from 0.05 to 0.5 Torr^{-1}.[280,282]

For practical purposes, it is of interest to correlate the measured ion current I_i with the deposition rate d' as observed on the thin film substrate. For emission from a small-area source, the deposition rate follows from Eq. (52) [Sec. 3c(1)] by differentiating with respect to time and also considering Eqs. (49) and (55):

$$d' = \left(\frac{m}{2\pi kT}\right)^{\frac{1}{2}} \frac{A_e \cos \varphi_s \cos \theta_s}{\rho \pi r_s^2} p^* \tag{76}$$

The subscript s refers to the substrate position, and ρ is the density of the deposit. Combination of Eqs. (75) and (76) yields the equation

$$\frac{I_i}{d'} = D'I_e \frac{r_s^2 \cos \varphi_m \cos \theta_m}{r_m^2 \cos \varphi_s \cos \theta_s} \rho N_A \left(\frac{\pi}{8MRT}\right)^{\frac{1}{2}} \tag{77}$$

Thus, the response of the monitor gauge in terms of measured ion current depends on the gauge structure as represented by D', on the distances and angular relationships, and on the material constants ρ and M, and it is proportional to the emission current I_e. The $T^{-\frac{1}{2}}$ dependence is usually neglected and considered a material constant since the range of useful evaporation temperatures encompasses at the most a few hundred degrees for any specific evaporant.

Although the performance ratio I_i/d' of a monitor is explicitly stated by Eq. (77), the gauge constant D' is not known a priori. Therefore, rate monitors must be empirically calibrated. For several experimental devices and specific materials, calibration curves have been published, and numerical values are listed in Table 16. The I_i/d' ratios are constant throughout the investigated ranges of deposition rates,

TABLE 16 Operational Features and Performance Ratios of Ionization-rate Monitors

Reference	Gauge structure	Residual gas discrimination	Emission current I_e	I_i/d', μA/Å s^{-1}	Evapo-rant	Readout
Haase[283]............	Commercial ionization gauge	Chopper wheel, 6 Hz	?	$\sim 10^{-4}$	Ag	Rates displayed on oscilloscope
Schwarz[280]..........	Cylindrical collector (Fig. 44a)	Vibrating shutter, 10–20 Hz	3 mA	1.5×10^{-4} 4.0×10^{-4} 4.5×10^{-4}	Al Cr Ni	Current indicator, and integrator to show thickness directly
Giedd and Perkins[284]..	Cylindrical grid, disk collector (Fig. 44b)	$p < 10^{-6}$ Torr: neglect; $p > 10^{-6}$ Torr: sub. $I_i = I_{total} - I_{res. gas}$	40 mA	10^{-1}	Sn	Rates registered on strip-chart recorder
Perkins[285]...........	Straight-wire collector (Fig. 44c)	Compensation with second gauge	10 mA	1.6×10^{-2} 4.7×10^{-2} 8.0×10^{-2} 12.0×10^{-2}	SiO Sn Pb CdTe*	Rates registered on strip-chart recorder
Dufour and Zega[282]...	Dual grid and collector structure (Fig. 44d)	Compensating gauge, chopper wheel, 20 Hz	$\leqq 4$ mA	8×10^{-5}	Al	Rates registered on strip-chart recorder
Brownell at al.[286].....	Straight-wire collector	Vibrating shutter, 170 Hz	?	0.4 V/Å s^{-1} 1.4 V/Å s^{-1} 1.7 V/Å s^{-1}	Ge SiO Au	Strip-chart recorder, and integrator to show thickness directly

* From Ref. 76.

and they are higher the greater the electron-emission current. The latter must be stabilized to facilitate stable monitor operation. A potentially disturbing factor is stray electrons emitted from the hot-vapor source. To guard against these, the source may be positively biased with 150 to 200 V,[283,284] or the monitor aperture may have magnetic and electric deflection plates to strip the arriving vapor of charged particles.[287]

A common difficulty with ionization-rate monitors is residual gas contributions to the ion current. The effect is illustrated by the data of Perkins,[285] whose gauge had a linear characteristic for residual gases with an ion current of 0.04 μA at 10^{-6} Torr. The evaporation of SiO at a rate of 20 Å s^{-1} yielded a current of 0.32 μA. Thus, even under rather favorable conditions, the background contribution to the total ion current amounts to 11%. One solution to the problem is to modulate the vapor stream entering the monitor by a chopper wheel or a vibrating shutter, thereby producing an alternating current which can be discriminated from the dc component attributable to the background. The alternate approach is to install a second, identical gauge which is exposed only to the residual gases but shielded against the vapor stream. Its output signal can be used to compensate for the background effect of the monitor gauge. Examples of both methods are listed in Table 16. The gauge of Dufour and Zega[282] shown in Fig. 44d utilizes the dual grid-collector structure for this compensatory function in combination with the beam-modulation technique.

Several additional points are essential for the successful operation of ionization-gauge rate monitors. If dielectric materials are to be evaporated, accumulation of deposits on grid and collector must be avoided. In Perkins'[285] device, both these filaments are electrically heated so that the evaporant vapors do not condense. In dc monitors of this type, it is also necessary to select a socket material of high insulation resistance ($>10^{12}$ ohms) and thereby maintain leakage currents between collector and grid at levels which are negligibly small compared with the ion current. The Joule heating of all three filaments tends to increase the temperature and therefore lower the insulation resistance of the alumina socket. This is prevented by water cooling of the socket holder. Shielding of the monitor structure against unnecessary deposits, particularly against metal films on the socket surface, is a general requirement which applies to all types. Finally, provisions for baking the monitor at temperatures around 300°C are desirable to minimize outgassing and background effects.

Since rate-monitor signals are very weak—typically a few tenths of 1 μA or less—they must be amplified for display and control purposes. Examples of instruments used are given in the last column of Table 16; for circuit diagrams, the reader is referred to the original publications. Electronic integrators which indicate accumulated thickness directly have been employed by Schwarz[280] and Brownell et al.[286] The latter were able to control film thicknesses within ± 10 Å. The rate monitor described by Perkins[285] gave thickness control of ± 2 to 5%.

A new type of ionization-rate monitor has recently been introduced by Zega.[288] It is distinguished from other models by the utilization of a small electron beam ($I_e = 0.2$ mA) to effect vapor ionization. The beam is swept at a frequency of 750 Hz across an entrance aperture through which the vapor passes. Thus, an ac signal is generated whose amplitude is proportional to the evaporant density while the background pressure contributes a dc reference level. The device is capable of controlling evaporation rates greater than a few angstroms per second, and its electronic controls include an integrator to monitor film thickness. The functional parts are enclosed in a small metal box and do not accumulate any deposits. Other advantages are the attainment of background discrimination without any moving parts, and the fact that no water cooling is required.

(2) Particle-impingement-rate Monitors Devices of this type were introduced by Neugebauer in 1964[243] but have not found wide usage as yet. Two different designs are shown in Fig. 45. Both consist of a light, thin-walled aluminum cylinder which is mounted off to the side of the source and partially shielded against the vapor. The exposed area of the cylinder receives a momentum whenever an atom impinges. The resulting torque tends to turn the cylinder. In Beavitt's[289] model (Fig. 45b), the

cylinder is pivoted and free to turn whereas the one in Fig. 45a is suspended from a wire whose torsion force opposes rotation. Thus, the pivot device revolves as long as molecules are impinging, whereas the torsion device turns only by a certain angle until torque and torsion forces balance. Both devices use magnetic damping to avoid oscillations.

A.   B.
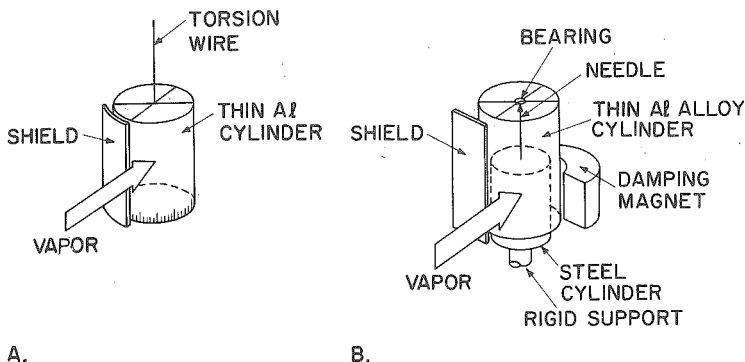
Fig. 45 Particle-impingement-rate monitors. (A) Torsion-wire device. (*After Neugebauer.*[243]) (B) Pivot-supported device. (*After Beavitt.*[289])

The equations relating deposition rate and meter response of impingement-rate monitors have been derived by Beavitt.[289] For wire-suspended cylinders, the deposition rate d' is proportional to the turning angle β:

$$d' = \frac{2K}{\rho \bar{c} s^2 h} \beta$$

where K = torsional constant of the suspension
ρ = density of deposit
$\bar{c}$ = average molecular velocity
s = cylinder radius
h = cylinder height

Neugebauer determined a sensitivity of 1.5 Å s^{-1} rad^{-1} for his device during the evaporation of tin.

The pivoted cylinder indicates deposition rates by its angular velocity ω. This quantity is difficult to measure unless one resorts to pulse-counting methods. It is, however, an integrating device which allows convenient monitoring of the accumulated deposit if the total number of revolutions $(2\pi\omega t)$ is counted:

$$d = 2\pi\omega t \, \frac{s\sigma(\frac{1}{2}s + 2h)}{\rho \bar{c} \tau h}$$

Here, σ = mass per unit wall and top area
τ = time constant of the damped rotor

A device made by Beavitt[289] turned 1 rad if 5.3 mg of Al or Au was evaporated from a source at 10 cm distance.

In comparing the two monitors, the torsion-wire device has a relatively slow response time and therefore does not indicate sudden changes in evaporation rate. The pivoted device does not suffer from this shortcoming as much as from the fact that a minimum impingement rate is required to overcome the friction of the bearing. The threshold value for Beavitt's model was 2 Å s^{-1} of Al. The $T^{-\frac{1}{2}}$ dependence, which enters through the presence of $\bar{c}$ in the denominators, can be neglected for practical purposes since the impingement rate rises exponentially with the source temperature. Both gauges measure the true impingement rate regardless of α_c since reevaporation of molecules occurs randomly in all directions and therefore does not cause additional torque.

Common advantages of both models are the simplicity of their construction, the absence of residual gas effects, independence from previously accumulated deposits, and the fact that no adjustment to obtain a null position is required.   The principle is not limited to cylindrical rotors but has also been applied to rotating disks which can be mounted in closer proximity to the substrates.   Although the vapor impinges nearly perpendicular onto the surface of such a device, Beavitt[289] showed that disk devices are more sensitive than cylinders.   He constructed a disk monitor from thin aluminum foil which had a sensitivity of 0.04 Å s^{-1} rad^{-1} for Al and a response time of 0.5 min.   The response time may be shortened but only at the expense of losing sensitivity.

b. Monitoring of the Deposited Mass

Mass-sensing devices may be used for all evaporant materials.   They operate either by determining the weight of the deposit, or by detecting the change in oscillating frequency of a small quartz crystal on which the evaporant condenses.   Both types of devices can be made very sensitive to the point where extraneous effects interfere critically with their operation.   Since the measured quantity is the accumulated mass of deposit, conversion into film thickness requires knowledge of the material's density. The latter is usually somewhat lower for films than for bulk materials.   Furthermore, the locations of the sensing device and of the substrates with respect to the source are often different so that the geometric factors must be considered in the same manner as discussed for ionization-gauge-rate monitors.   Lastly, the response of the device per unit mass of deposit is not always predictable with the required accuracy.   For these reasons, mass-sensing devices, too, are best calibrated after their installation by comparing their readings with independently measured film thicknesses on the substrates.

(1) **Microbalances**   Instruments suitable for the gravimetric determination of small quantities of mass are summarily referred to as microbalances.   Their design may be based on different principles such as the elongation of a thin quartz-fiber helix, the torsion of a wire, or the deflection of a pivot-mounted beam.[290]   Their applications encompass many areas other than thin film measurements, and the literature about microbalances and related topics is extensive.   A detailed review about the construction of such instruments including a table of different models and their sensitivities was given by Behrndt in 1956.[291]   For more recent developments, especially vacuum applications, the reader is referred to "Vacuum Microbalance Techniques," the proceedings of annual symposia on the same topic which have appeared regularly since 1961 (Plenum Press, New York).   The models selected for this review illustrate some of the more commonly used design features and are of established utility for thin film work, but they are by no means the only ones for which this claim can be made.

Campbell and Blackburn[244] constructed a relatively simple microbalance by converting the movements of a microammeter.   A later version of this instrument is due to Hayes and Roberts[292] and is shown in Fig. 46.   The meter arm is balanced by an adjustable weight and the meter spring.   In the null position, the two photodiodes receive equal amounts of light through the aperture in the centrally located shutter. Deviations from this position alter the resistance of the diodes and thereby unbalance the bridge circuit.   The resulting current flows through the meter coil and produces a restoring force on the meter arm.   The restoring current is proportional to the force acting on the mica vane at the other end and is amplified in the control system. A strip-chart recorder provides a permanent record of the evaporation.

In the position shown in Fig. 46a, the vane experiences two forces due to its exposure to the vapor stream.   The weight of the deposit,

$$G = A_m\rho d \quad \text{g wt} \quad \text{or} \quad \text{Equivalent force } F_1 = gA_m\rho d \quad \text{dyn} \quad (78)$$

where A_m = vane area
  ρ = deposit density
  d = deposit thickness, cm
  g = gravitational constant

tends to pull the meter arm down. An upward-directed force arises from the momentum imparted by the impinging vapor molecules. Assuming a sufficiently large source-to-monitor distance so that all molecules arrive at the same angle of
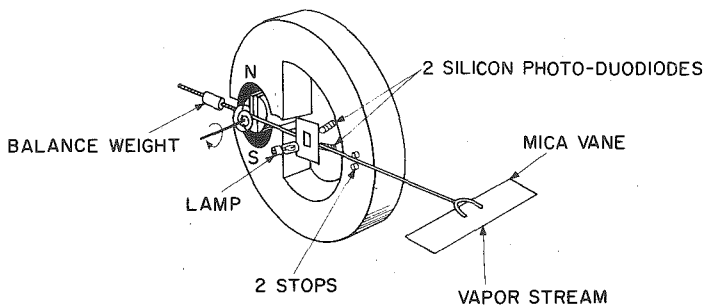
A.
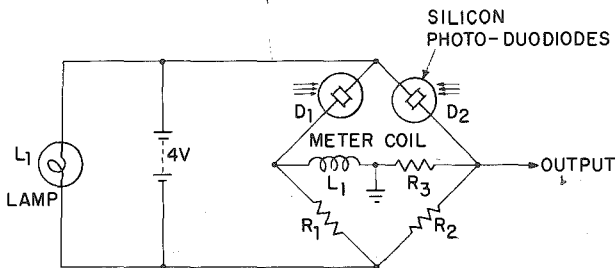
B.

Fig. 46 (*A*) Schematic drawing and (*B*) circuit diagram of a microbalance constructed from a microammeter movement. (*Hayes and Roberts.*[292])

incidence θ, the dynamic force generated by the vapor stream is

$$F_2 = \frac{d\mathfrak{M}}{dt} \bar{c} \cos \theta \qquad \text{dyn}$$

where $d\mathfrak{M}/dt$ = mass deposition rate on vane area, g s^{-1}

$$\bar{c} = 14{,}551 \sqrt{T/M}, \text{ cm s}^{-1} = \text{avg molecular velocity}$$

Since $d\mathfrak{M}/dt = A_m \rho d'$, the dynamic force is related to the deposition rate d', Å s^{-1} by

$$F_2 = 1.4551 \times 10^{-4} A_m \rho \sqrt{T/M}\, d' \cos \theta \qquad \text{dyn} \tag{79}$$

The net force $F_1 - F_2$, which is observed during evaporation at constant rate, is traced in Fig. 47. The line of gradual weight increase, $F_1 = g A_m \rho t d'$, is shifted downward by the constant impingement force F_2. A true weight indication is obtained when the evaporation stops.

The response to both deposit weight and particle-impingement forces is also found in microbalances of different construction. To separate the two effects, the vane must be oriented in a vertical direction and the vapor impinge horizontally. If the beam

axis is then left in the horizontal position as shown in Fig. 46a, the balance indicates only weight.   Conversely, if the meter movement is turned 90° so that its axis points toward the center of gravity, the instrument functions as a particle-impingement device.[292]   This latter option is usually not available on other microbalances.
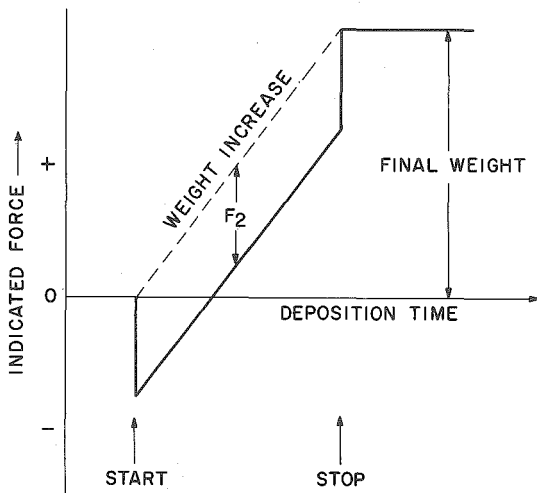
Fig. 47 Net force on a microbalance with horizontal axis and vane, for vertical vapor incidence.

To give an idea of the forces originating in film-deposition experiments, numerical values must be inserted into Eqs. (78) and (79).   A metal of density 10 contributes 10^{-7} g wt cm^{-2} of vane area for every angstrom of film thickness, which is equivalent to a force of 10^{-4} dyn cm^{-2}/Å.   The material constant $\rho \sqrt{T/M}$ in Eq. (79) may vary from 20 to 85 for different metals, whereby temperatures necessary to achieve 10^{-2} Torr evaporant pressure are assumed.   Values between 40 and 50 are most common. Thus, for perpendicular impact $(\theta = 0)$, 1 cm^2 of vane surface experiences a force of about 7×10^{-3} dyn for every Å s^{-1} of deposition rate.   Since practical vane areas are of the order of 1 cm^2, accuracies of ± 10 Å for thickness and ± 1 Å s^{-1} for rates require instruments which indicate accurately 10^{-6} g wt or about 10^{-2} dyn.   Most instruments exceed these specifications.   The meter-movement device of Roberts and Hayes had a maximum sensitivity of 2×10^{-6} g wt and could sense a dynamic force of 5×10^{-3} dyn.

The most common mode of microbalance construction utilizes a crossbeam which is balanced on a taut torsion fiber.   A number of models require that the beam deflection is observed—for instance, with a cathetometer or on the scale micrometer of a micro-scope—to derive the weight change.[293]   Sensitivities of 1.5×10^{-7} g wt have been obtained with such instruments.[294,295]   For monitoring and controlling processes in vacuum systems, it is more practical if the beam deflection generates a compensating force which provides a proportional electric signal.   Such balances are referred to as electromagnetic or electrostatic depending on the means employed to generate the restoring force.   The zero position of the beam is usually sensed with a light beam, but capacitive or inductive effects may also be utilized.

A schematic drawing of an electromagnetic torsion balance is shown in Fig. 48.   The model is entirely constructed from quartz rods with a 40-μ-diameter quartz torsion fiber.[296]   A small permanent magnet is fused to one end of the crossbeam and attracted by the solenoid which supplies the restoring force.   Oscillations are damped by the copper cylinder surrounding the magnet.   The balance reportedly indicates 10^{-7} g wt

with an accuracy of $\pm 10\%$. For comparison, a monolayer of iron weighs 1.8×10^{-7} g wt cm^{-2}.

The balance shown in Fig. 48 has also been modified into a model with electrostatic force compensation.[297] This version had a thin metallized quartz wafer instead of a magnet at the beam end. The wafer formed the center plate of a three-plate capacitor and could be charged electrostatically because a tungsten torsion wire was used instead of the quartz fiber. The restoring force was produced by applying voltage to the three plates. While mechanically quite rugged, the balance achieved high sensitivity—2.5×10^{-7} g wt gave an amplified output signal of 1 V—through the use of a very thin (10-μ-diameter) tungsten wire. If installed vibration-free, the zero position fluctuated by no more than the equivalent of 4×10^{-9} g wt. Oscillations were eliminated by a feedback circuit. Since it was constructed entirely from refractory mate-
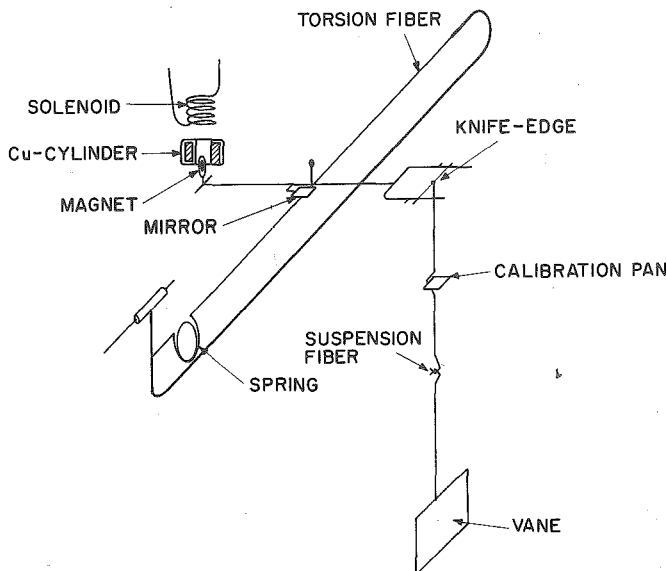
Fig. 48 Microbalance with torsion-fiber suspension and electromagnetic-force compensation at beam end. (*Mayer et al.*[296])

rials such as fused quartz and tungsten, the balance could be baked at temperatures above 400°C.

Figure 49 shows an electromagnetic balance with a moving coil to restore the zero position. This instrument, which was reported by Cahn and Schultz,[298] has a hollow aluminum beam suspended on a torsion ribbon. The latter is more rugged than a wire and self-centering so that no arresting mechanism is required. The deposit is received by a $\frac{3}{4}$-in.-diameter mica scale pan which may be suspended into the substrate area by means of a stirrup. Such an arrangement, which also includes a water-cooled shield to protect the balance against source radiation, has been described by Houde.[253] The zero position of the balance is detected by a phototube whose current varies according to the degree of illumination admitted by the shutter. The amplified current is applied to the coil and, in restoring the zero position, generates a voltage proportional to the weight change. This signal is then recorded. On the most sensitive range, the instrument gives a 5-μV output for 10^{-7} g wt of deposit (about 1.5 Å of SiO).

Microbalances of similar construction with sensitivities from 10^{-6} to 10^{-7} g wt and capacities of typically 0.2 to 2 g wt are commercially available from several manu-

facturers which are listed in Ref. 279. Among the more recent developments, an instrument described by Gast[299,300] is of particular interest because the sample holder is suspended magnetically and physically separated from the balance mechanism. A remarkably sensitive torsion balance has been described by Pearson and Wadsworth.[301] It can detect forces of 2×10^{-8} dyn, which is equal to the rms effects caused by the Brownian motion. Other disturbing effects are often encountered with less sensitive balances as well. Foremost among them is the shift of the zero position due to temperature inhomogeneities along the balance beam. Wolsky et al.[302] discuss modes of beam construction which enhance the chances of maintaining the arm-lengths constant within the desired 0.01 ppm. Mechanical vibrations, electrostatic effects, and gas adsorption, too, interfere with precision weighting.[291]
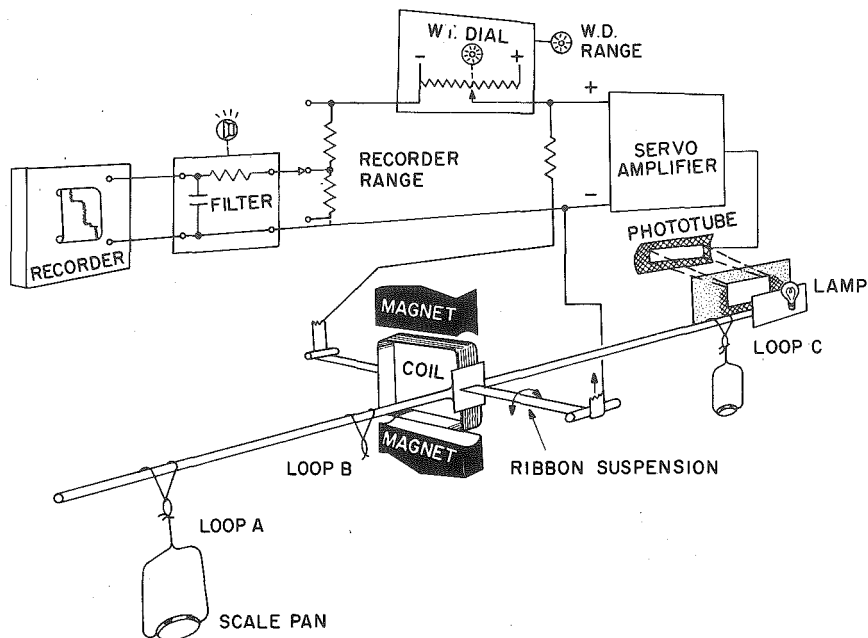
Fig. 49 Microbalance with torsion-ribbon suspension, coil movement, and signal recorder. (*Cahn and Schultz.*[298])

(2) Crystal Oscillators The use of quartz-crystal oscillators to determine small quantities of deposited matter was first explored by Sauerbrey[303,304] and Lostis.[305] The transducers required to monitor film thickness are of relatively simple construction and about as sensitive as microbalances while practically unaffected by mechanical shocks and external vibration. Therefore, crystal oscillators have received much interest during the last years and are currently the most widely used means for monitoring thin film depositions. The crystal-oscillator monitor utilizes the piezoelectric properties of quartz. A thin crystal wafer is contacted on its two surfaces and made part of an oscillator circuit. The ac field induces thickness-shear oscillations in the crystal whose resonance frequency is inversely proportional to the wafer thickness d_q,

$$f = \frac{c_t}{2d_q}$$

where c_t is the propagation velocity of the elastic wave in the direction of thickness. The major surfaces of the wafer are antinodal.

An important consideration in preparing the quartz wafer is the temperature dependence of the resonance frequency. The temperature coefficient of frequency (TCF) of quartz is related to the elastic constants. It has positive and negative terms whose magnitudes depend on the direction of the vibration with respect to the natural crystal axes. Since frequency changes resulting from temperature fluctuations affect the accuracy of mass determinations, the quartz crystals are cut in an orientation where the TCF terms compensate each other. This is the case if the plane of the cut forms an angle of about 35° with the c, x plane as illustrated in Fig. 50. The orientation is designated as an AT cut and is used in all thickness monitors.

The temperature dependence of the TCF for a number of AT crystals of slightly different orientation has been measured by Phelps.[306] Figure 51 shows the function for a cut made at 35°20'. The TCF reaches zero at about 30°C and remains smaller than $\pm 5.10^{-6}$ deg^{-1} in a temperature interval of about ± 30°C. Changes in the cutting angle of only 10' shift the temperature of zero TCF by as much as 50°C and also narrow the interval of small TCF values. The cutting angles generally preferred are between 35°10' and 35°20'. The resonance frequencies for thickness-shear mode oscillations of AT crystals are given by

$$f_0 = \frac{N}{d_q} \qquad (80)$$

Fig. 50 Quartz crystal with AT cut wafer.

where $N = 1.67 \times 10^6$ Hz mm.

If a small $\Delta \mathfrak{M}$ is added to either one or both sides of the wafer, it may be assumed that the original crystal surfaces remain antinodes of vibration; i.e., the foreign matter does not store elastic-deformation energy during the vibration cycle. Hence, the deposit affects the resonance frequency only through its mass whereas material
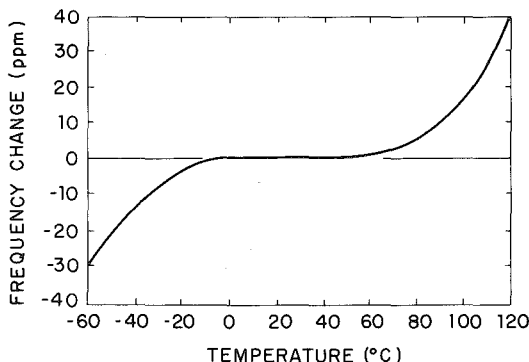
Fig. 51 Frequency change vs. temperature for an AT crystal cut at 35°20'.

specific properties such as density or elastic constants are inconsequential. The effect of mass loading on the frequency may be derived by differentiating Eq. (80) with respect to d_q and substituting the added increment of quartz Δd_q by an identical

mass $\Delta \mathfrak{M}$ of foreign matter and different thickness d_f.[304]   An alternate derivation was given by Stockbridge,[307] who applied perturbation analysis to a resonating plate and obtained essentially the same relation:

$$\Delta f = -\frac{Kf_0{}^2}{N\rho_q}\frac{\Delta \mathfrak{M}}{A_m} = -\frac{KN}{\rho_q d_q{}^2}\frac{\Delta \mathfrak{M}}{A_m} \qquad (81)$$

Here, ρ_q is the density of quartz (2.65 g cm^{-3}) and $K \approx 1$ is a constant which depends on the distribution of deposit over the monitor area A_m.   The latter should be the total surface area of the wafer.   However, if the electrodes applied to the wafer cover
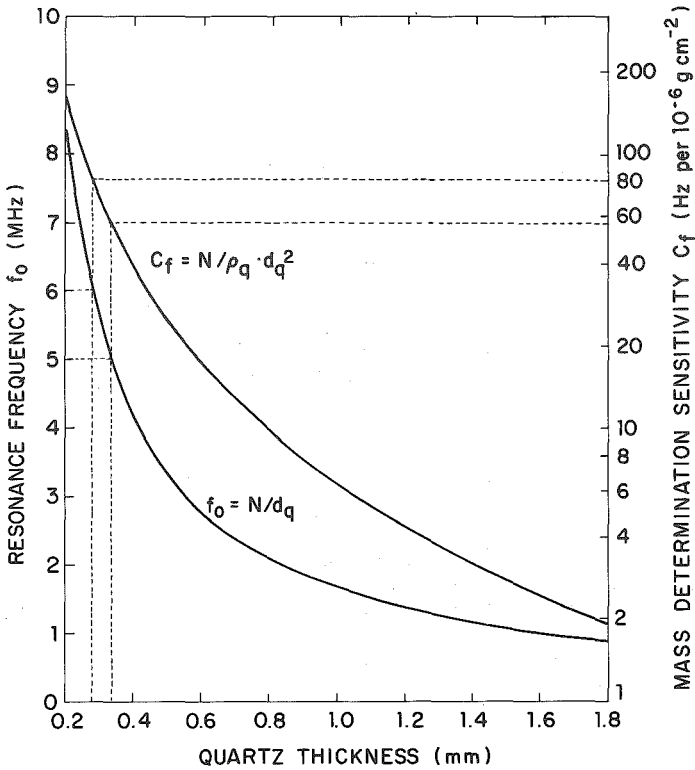
Fig. 52   Resonance frequency and mass-determination sensitivity of AT crystals as functions of wafer thickness.

only part of the crystal surface, as is often the case, then A_m is to be taken as the electrode area.   It has been shown that oscillations outside the electrode area are negligible and deposits there contribute only 1% to the frequency change Δf.[304]
    The proportionality factor in Eq. (81),

$$\frac{f_0{}^2}{N\rho_q} = \frac{N}{\rho_q d_q{}^2} = C_f \qquad \text{Hz g}^{-1}\text{ cm}^2 \qquad (82)$$

is called the mass-determination sensitivity of the crystal.   As shown in Fig. 52, the thinner crystals with the higher resonance frequencies give larger frequency changes per deposited mass per unit area.   Hence, in the interest of sensitivity, the crystal wafers should be made as thin as their fragility permits.   There is, however, another limitation.   The relationship between Δf and $\Delta \mathfrak{M}$ ceases to be linear if the thickness of

the deposited mass is no longer small compared with the wafer thickness. Estimates as to how far linearity may be assumed without committing significant errors vary from $\Delta f_{max} = 0.5\%$[139] to 5%[279] of the initial frequency f_0. Although the maximum permissible frequency change is larger for the thinner crystals, the mass which causes this Δf_{max} is greater for the less sensitive (thicker) crystals; this is illustrated in Fig. 53. Crystals of about 0.3 mm thickness with initial frequencies of 5 to 6 MHz are generally considered to offer the best compromise between high sensitivity and high mass-loading capacity. This range is indicated (dashed lines) in Figs. 52 and 53.
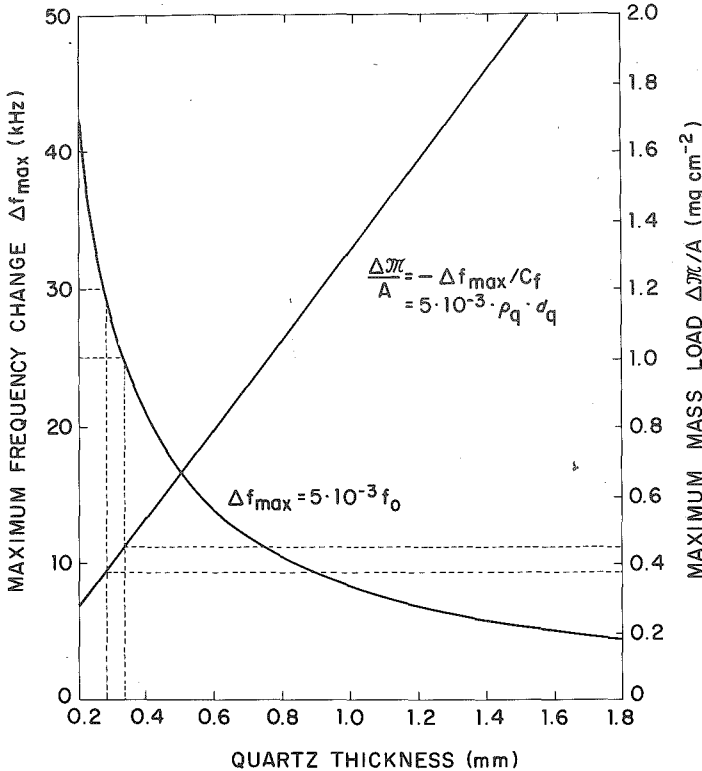
Fig. 53 Maximum frequency change and mass loading for AT crystals as functions of wafer thickness.

The mass-frequency equation (81) has repeatedly been verified by control experiments with microbalances. Eschbach and Kruidhof[308] obtained an experimental value of C_f which agreed within 0.4% with the value derived from the material parameters of quartz [Eq. (82)]. It is therefore not necessary to calibrate monitor wafers empirically, but Niedermayer et al.[309] point out that the temperature of the crystal should be taken into account. The interval of approximately linear frequency changes has also been investigated. Empirical values of Δf_{max} for 5-MHz crystals range from 50 to 100 kHz,[308,310,311] which is equivalent to deposits of 1 to 2 mg cm^{-2}. The corresponding maximum thickness

$$d = \frac{\Delta \mathfrak{M} \times 10^8}{\rho A_m} \qquad \text{Å}$$

varies from 5,000 to 50,000 Å depending on the density ρ of the film material.

The onset of nonlinear frequency response may be due to second-order terms neglected in the perturbation analysis of Stockbridge,[307] or the assumption of no energy storage in the deposit may be invalid. In the former case, deviations from linearity should be independent of the deposit material, whereas the latter possibility leads one to expect differences according to the mechanical properties of the film material.[307] If the nonlinear portion of the frequency-mass characteristics is known for the particular crystal, the useful range may be extended to thicknesses of several microns. Calibration of a monitor wafer by independent thickness measurements is possible because accumulated deposits can be etched off and the crystal may be used again. However, when the film thickness is no longer small compared with the thickness of the crystal, the deposit begins to store elastic energy and introduces vibrations other than in the thickness-shear mode. At some point, the oscillations of the crystal in the direction of thickness change irregularly (the frequency "jumps"), or they may cease altogether. In view of this limitation and the modest price of the quartz wafers, it is usually not worthwhile to extend the thickness range by an elaborate calibration procedure.

The crystals used in deposition monitors are either circular or square platelets of typically 13- to 14-mm size. They are mounted in holders which prevent them from shifting position, yet allow easy removal and replacement. Two examples of crystal holders are shown in Fig. 54. The electric field is applied through thin gold or some-
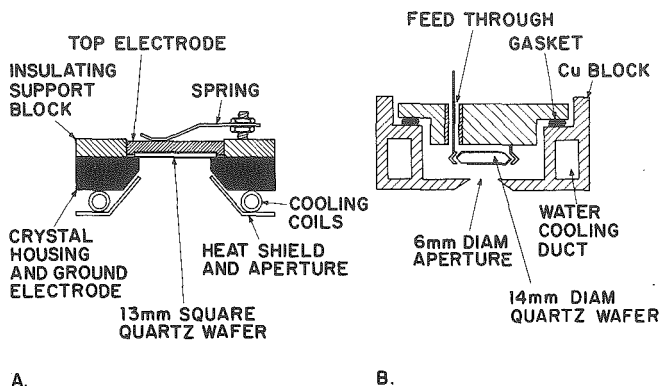
Fig. 54 Oscillator crystal holders for deposition monitoring. (A) After Behrndt and Love.[145] (B) After Pulker.[310]

times silver films evaporated onto both sides of the wafer. In Fig. 54a, the film electrodes extend over the entire surface whereas in Fig. 54b, only the center area is covered by 6- to 8-mm dots. In the latter case, evaporated leads permit contacts to be made at the wafer edge. In other arrangements, only the exposed surface of the wafer is metallized whereas the opposite side is contacted directly by a metal block. A holder whose materials of construction allow outgassing of the entire transducer at 450°C has been described by Langer and Patton.[312] The frequency characteristics of quartz crystals which have been heated to 400°C are fully restored after cooling.[310] Utilization of crystal oscillators in ultrahigh vacuum is therefore possible. The effect of pressure on the oscillation frequency has been found to be negligible throughout the entire high- and ultrahigh-vacuum range, provided there are no adsorption or desorption phenomena on the crystal surface.[313]

Although AT cut wafers have the smallest possible temperature coefficient of frequency, it is still necessary to protect the crystal against temperature changes due to radiation from the source and heat of condensation. Therefore, the crystal housing is usually water-cooled and forms a radiation shield which surrounds the entire crystal except for the deposition area. The heat received by this necessarily exposed area

still causes temperature increases of several degrees Celsius with ensuing frequency changes of 10 to 100 Hz[145,310,311] which are equivalent to mass changes of 10^{-7} to 10^{-6} g cm^{-2}.   The effect can be minimized by using a small-entrance aperture as in Fig. 54b, but it is not negligible when making precision measurements.   Behrndt[139] recommends delaying the opening of the substrate shutter for some time while exposing the monitor to the source and vapors.   With this procedure, the greater part of the crystal-temperature change takes place prior to the accumulation of deposit on the substrates.

The instrumentation required to operate a monitor consists basically of an oscillator and a suitable frequency meter.   While it is possible to measure the frequency change
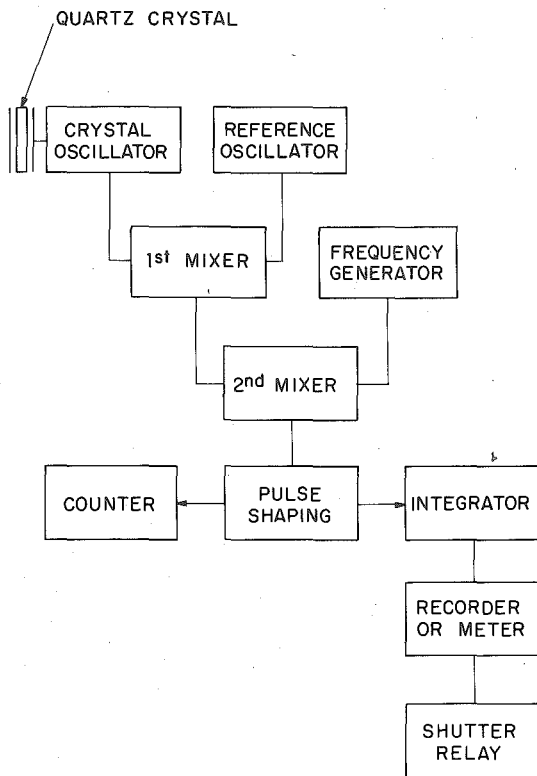
Fig. 55   Block diagram for quartz-crystal oscillator instrumentation.   (*After Pulker.*[310])

at the level of the resonance frequency f_0, this requires expensive equipment capable of giving accurate six-digit readings.   It is therefore common practice to use a reference oscillator, for instance, a second crystal, with a fixed frequency and to generate a difference frequency.   The latter is mixed again with the signal from a variable-frequency generator, as indicated in the block diagram in Fig. 55.   The advantage of this arrangement is that it permits operation in the most sensitive frequency range regardless of the film thickness accumulated on the crystal.   The output signal is in the audio-frequency range and drives the counter circuit.

The various methods of frequency measurement have been discussed recently by Steckelmacher[279] and Langer and Patton.[312]   Digital as well as analog-type instruments are capable of measuring frequencies accurately to within ± 1 ppm.   If digital equipment is used, a printer may serve to provide a permanent record, and deposition rates may be derived by comparing subsequent readings.   The differentiation may

also be performed electronically, and rates as well as total thickness may be displayed on separate indicators. For analog-type instruments, the frequency must be converted into a dc signal which may be displayed on a meter or recorded on a strip chart. Automatic termination of the deposition process by actuating a shutter relay at a preselected signal level is easily possible.

In practice, the accuracy of crystal-oscillator monitors is determined by the stability of the oscillator circuit. The effects of hydrostatic gas pressure and gas adsorption on oscillator frequency have been studied by Stockbridge[313] and are negligible for most practical purposes. If a frequency change of 1 Hz in a 5-MHz oscillator can be detected, the corresponding sensitivity of the monitor is about 2×10^{-8} g cm^{-2}. Ordinarily, however, the stability of the circuits is only of the order of 10 to 100 Hz h^{-1}. Thus, the practical mass-detection limit is 10^{-7} to 10^{-6} g cm^{-2}. The thickness and rate-control figures reported for these conditions are typically $\pm 2\%$.[279,314] The attainment of $\pm 1\%$ accuracy for masses in the 10^{-7} to 10^{-6} g cm^{-2} range has been reported by Hillecke and Niedermayer[315] but requires consideration of the temperature dependence of the frequency. Warner and Stockbridge[316] describe instrumentation capable of measuring frequencies with an accuracy of 1 part in 10^{10}. In addition, the temperature of the quartz crystal was maintained constant within ± 0.1 to 0.01°C, which allowed the detection of mass changes in the 10^{-10} to 10^{-12} g cm^{-2} range. While this sensitivity exceeds that of microbalances, one cannot expect to attain such a temperature constancy during vacuum evaporation. Good experimental practices concerning the use of quartz-crystal oscillators for film-deposition control have been discussed in detail by Riegert.[317]

c. Monitoring of Specific Film Properties

In preparing thin films, the investigator is often interested in only one particular film property to assume a certain final value, whereas the deposition rate is of secondary importance. Such properties may be optical or electrical ones, and their attainment can be accomplished more assuredly by direct observation during the deposition process than by monitoring the mass and correlating it to the desired property. While often simpler in regard to equipment, these methods are not universally applicable, and some of them require especially prepared monitoring substrates to facilitate in situ measurements. If the latter is the case, the monitoring substrate must be positioned so that it experiences the same incidence of vapor molecules as the regular substrates. Furthermore, its thermal conductivity and mode of heating should be identical to those of the other substrates to ensure equal temperatures.

(1) Optical Monitors Optical phenomena such as light absorption, transmittance, reflectance, and related interference effects can be utilized to monitor the growth of films during vacuum deposition. The necessary equipment is relatively simple and consists basically of a light source and a photocell. Both items are preferably located outside the vacuum system, with suitable windows and optical paths provided for communication with the substrates. The choice of the quantity to be measured depends on the type of substrate and the film to be monitored. Metal films, for example, may be observed by transmittance measurements, provided they are deposited onto transparent substrates. The amount of transmitted light T_r, however, decreases rapidly with thickness so that sensitive measurements are limited to rather thin films. Furthermore, the extinction law

$$T_r = T_0 \exp\left(-\alpha d\right)$$

where α, cm^{-1}, is the adsorption coefficient, is not obeyed during the nucleation and island stage of film growth.[139] Similar considerations hold for reflectance measurements on metal films. Therefore, optical monitoring techniques are primarily used for dielectric films.

The monitoring of transparent films exploits the periodic fluctuations in light intensity which arise from multiple reflections within the film and subsequent interference. The conditions for constructive and destructive interference vary depending on the refractive indices of film and substrate materials. Also, interference maxima in transmission coincide with minima in reflectance, and vice versa. This is discussed

more extensively in the context of film thickness measurements in Chap. 11, Sec. 1. The difference in thickness monitoring is that the extreme values of intensity occur sequentially as the film thickness increases by increments which lengthen the optical path of the light beam by a quarter of the wavelength λ. Therefore, the order of a particular interference maximum or minimum can be observed directly.

Transmittance and reflectance monitoring techniques are most often employed when films are deposited for optical purposes such as beam splitters, mirrors, antireflection coatings, and interference filters. These applications usually require film thicknesses of $\lambda/4$ or multiples thereof, and the advantage of monitoring the desired film property directly is obvious. The various monitor designs developed for such purposes are discussed in Behrndt's review.[139] Steckelmacher et al.[318,319] describe a monitor arrangement with a modulated light beam so that the output of the photocell can be selectively amplified and the effect of light scattering eliminated. The design was successfully used in the fabrication of multilayer interference systems.

As for film applications in the microelectronics field, optical thickness monitoring has not been a widespread practice because the emphasis there is on electrical rather than optical properties. Transmittance measurements are usually not possible, either because the substrates are opaque or because they are mounted against a metal holder-heater plate. This leaves reflectance measurements as the most suitable approach. However, the more common types of optical monitors including commercial models[320] are intended for small (nearly perpendicular) angles of light incidence on the substrates. Consequently, the light source and photocell compete for installation space with such essential parts as pumping port, evaporation source, and heat shields. Although this problem can be resolved, the ensuing difficulties have generally discouraged the use of optical and favored other monitoring devices.

The advent of rf sputtering methods for the deposition of dielectric films has changed this situation because all the monitoring techniques based on electrical measurements are severely disturbed by the glow discharge. The renewed interest in optical monitors in conjunction with sputtering (see also Schaible and Standley[321]) led to the development of a technique which permits installation of the illuminator and photocell off to the sides of the vacuum system.[322] The arrangement is shown in Fig. 56 for an rf sputtering system as described by Davidse and Maissel.[323] The large quartz cathode in close proximity to the substrate plane necessitates a large angle of incidence θ of about 80°. Since θ approaches or exceeds Brewster's angle
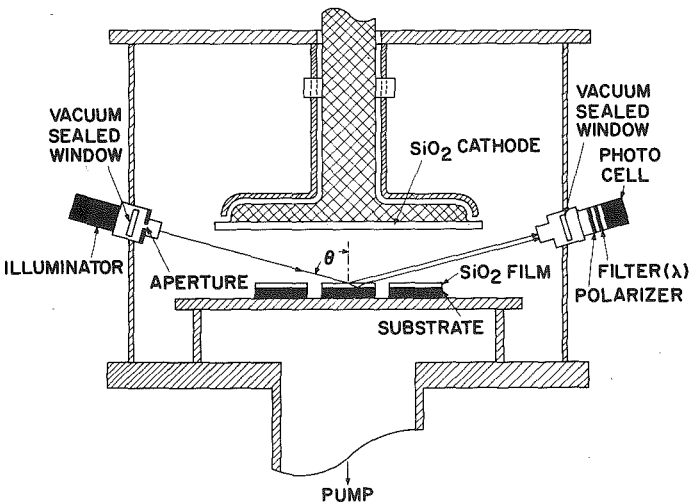
Fig. 56 Schematic of an RF sputtering system (after Davidse and Maissel[323]) with optical-thickness monitor.[322]

for the dielectric film material, the conditions for destructive and constructive interference are opposite for the parallel and perpendicular polarized components of the light beam.[324] A polarization filter in front of the photocell admits only the perpendicular component, which yields a greater difference between maximum and minimum intensity than the parallel component. An interference filter singles out one particular wavelength to be received by the photocell. If the substrate surface—in this case, silicon—is reflective, the intensity of the reflected beam as a function of thickness is given by the Eq. (16) in Chap. 11, Sec. 1c(2). The output voltage of the photocell varies in proportion and yields a recorder trace as shown in Fig. 57.
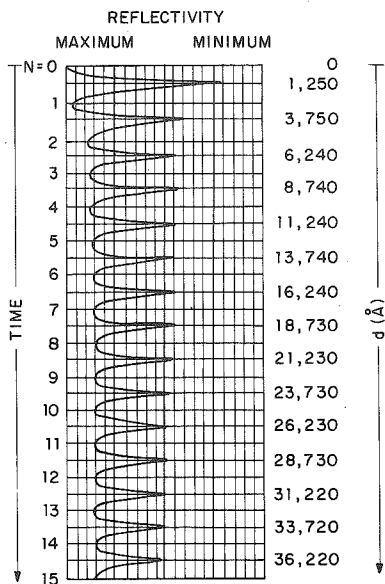
Fig. 57 Recorder trace of optical-thickness monitor shown in Fig. 56 for the deposition of RF sputtered SiO₂ on silicon (λ = 5,500 Å; θ = 79°).
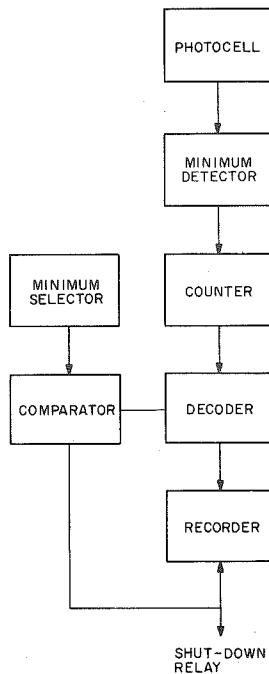
Fig. 58 Block diagram for automatic thickness control with an optical monitor.[322]

The continuous recorder trace permits the thickness to be determined for every desired fraction of a wavelength. Automatic termination of the process, however, is most easily accomplished by stopping at a preselected minimum. A suitable circuit for this function is shown in the block diagram in Fig. 58. In that case, one can obtain only film thicknesses which are multiples of λ/4 according to Eq. (15) in Chap. 11, Sec. 1c(2),

$$d = \frac{N\lambda}{2n_f \cos \theta_f} + \Delta t_\varphi + \Delta t_r$$

where $N = \frac{1}{2}, \frac{3}{2}, \frac{5}{2}, \ldots$ for interference minima, or $N = 0, 1, 2, 3$, for maxima (see Fig. 57)

n_f = refractive index of film material (1.470 for sputtered SiO₂)

θ_f = angle of refraction in the film

Δt_φ = phase-shift correction

Δt_r = reflectivity correction

The reflectivity correction can be neglected in this application since neither the angle of incidence θ nor the wavelength λ is variable.[325,326] The phase-shift correction Δt_φ arises from the fact that the incident light beam suffers two phase shifts, one of 2π at the film surface and another of different magnitude at the film-substrate interface. For SiO_2 films on silicon, the two phase shifts are nearly identical and Δt_φ may be neglected.[326,327] The phase-shift corrections for SiO_2, Al_2O_3, and silicon nitride films on several common metal surfaces including germanium have been calculated by Pliskin.[328] Their values vary from -60 to -300 Å for the perpendicular component of the light beam and hence should be considered in most cases.

The thickness monitor described has been used in the rf sputter deposition of SiO_2 onto silicon wafers. Film thicknesses between 2,000 and 30,000 Å have been controlled to within ± 1 to 2%, an accuracy which is fairly typical for optical monitors. By virtue of its installation in rather uncontested locations of the vacuum system, the monitor is also adaptable for vacuum evaporation systems. There, the most widely used dielectric material is SiO, which absorbs part of the visible spectrum. Consequently, the intensity of subsequent reflectivity maxima will decrease. Experimental curves of light transmittance through growing SiO films show an exponential decrease superimposed on the intensity variations arising from interference. This tends to reduce the difference between maxima and minima so that their distinction becomes increasingly difficult. For example, Zerbst[329] shows a transmittance curve which was essentially flat from about 8,000 Å of SiO on up. With a more sophisticated electronic sensing circuit, it is claimed that $1\text{-}\mu\text{-thick}$ SiO films could be controlled to within ± 20 Å.[330]

The utilization of interference techniques can be extended into the infrared part of the spectrum. This is of particular interest when monitoring the thickness of epitaxial silicon films, and several references are given by Steckelmacher.[279] Because of the elevated temperatures required for epitaxy, no external light source is necessary. The radiation emitted from the substrate—which may be silicon[324] or sapphire[331]—suffers interference due to partial reflection at the film surface. In the case of silicon growing on silicon, the effect is contingent upon differences in the impurity levels of film and substrate, since the refractive index of silicon varies with the free carrier concentration [see also Chap. 11, Sec. 1c(4)].

(2) Resistance Monitors The resistance R of a conductive film pattern of fixed length l and width w is given by

$$R = \rho \frac{l}{wd} \tag{83}$$

Hence, if the resistivity ρ of a film material remains constant throughout the deposition, the film thickness d can be continuously monitored by in situ resistance measurements. In its simplest form, the technique requires a glass slide or strip with two metal contacts at the ends to determine l, and an evaporation mask which confines the film deposition to a path of width w between the end contacts. The contacts must be applied prior to the experiment, either in a separate metal evaporation or by painting on a metal paste and burning it in. The monitor slide and its mask are mounted side by side with the substrates to ensure equal exposure to the evaporant vapor. The metal lands are contacted by a pair of probes to facilitate current-voltage measurements inside the vacuum system.

While easily implemented, resistance monitoring is not a reliable method to observe and control the thickness of metal films. During the early stages of film growth, the deposit consists of nuclei or partially connected islands (see Chap. 8) whose resistance does not obey Eq. (83). As the film becomes continuous, it goes through a thickness range in which the resistivity varies as a result of diminishing contributions from surface scattering (see Chap. 13). Furthermore, during the deposition of the first few hundred angstroms, the resistance vs. thickness function is also affected by the application of electric fields as shown in Fig. 18, Chap. 18. At greater film thicknesses, the inverse proportionality between R and d is satisfied, but the thickness can only be deduced if the resistivity ρ is known. Since the latter often varies substantially as the result of fluctuations in the residual gas pressure, the deposition rate, and

the substrate temperature, film-thickness values derived from resistance measurements are rarely accurate.

In view of these uncertainties, in situ resistance measurements are mainly used to monitor and control the deposition of films intended for the fabrication of resistors. In this application, film thickness and constancy of resistivity are of secondary importance. The quantity of prime interest is the sheet resistance R_s, which is defined by

$$R = R_s \frac{l}{w}$$

and represents the ratio of resistivity over thickness ρ/d. For a fixed monitor aspect ratio l/w, current-voltage measurements give a direct indication of the sheet resistance, and the desired value is obtained regardless of resistivity variations within the film because these are compensated by adjusting the final film thickness.

The usual resistance monitor arrangement involves a Wheatstone-bridge circuit as shown in the block diagram in Fig. 59. In the simplest form, the film resistance as
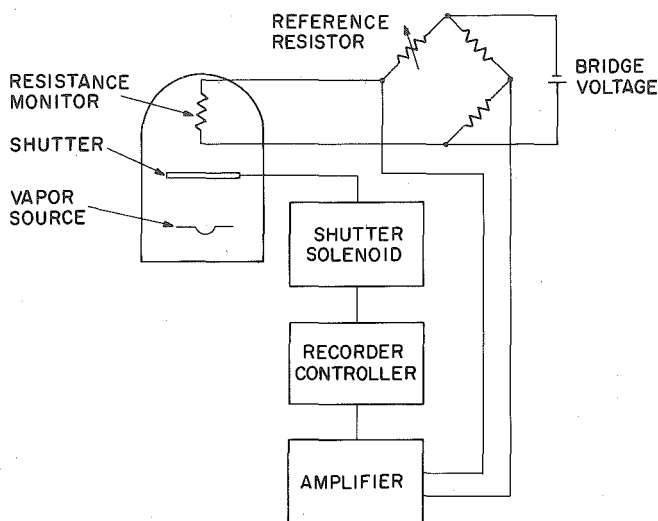
Fig. 59 Wheatstone-bridge circuit for resistance monitoring.

indicated by the unbalance of the bridge is continuously recorded on a strip chart and the shutter solenoid is actuated when the balance point is reached. During deposition, the resistance of the monitor decreases over many decades and the sensitivity of the bridge varies accordingly. Therefore, Bennett and Flanagan[332] utilized a variable reference resistor which decreased automatically in steps whenever the bridge went through the balance point. The resistance of the monitor was recorded only at these points. Steckelmacher et al.[333] employed a preset 10-turn potentiometer and altered the resistance in the ratio arm of the bridge. It has also been suggested that the reference potentiometer be driven by a motor and the evaporation rate be adjusted automatically so as to maintain the bridge balanced at all times.[279]

A more complex control system has been described by Turner et al.,[334] who used the monitor as the input resistor of a feedback amplifier. With a constant voltage applied to the resistance monitor, the output voltage of the amplifier was proportional to the film thickness (assuming constant film resistivity throughout the deposition). The same signal was given into an operational differentiator whose output voltage was proportional to the deposition rate. A trigger circuit allowed termination of the

process at a preselected level of thickness, while constant evaporation rates could be maintained through a servo-control circuit governed by the rate signal.

The conventional monitoring techniques employing Wheatstone bridges in one form or other are two-terminal resistance measurements and therefore subject to errors due to lead and contact resistances. These errors become significant only if the resistance values to be monitored are smaller than a few hundred ohms. One method to avoid this problem is the use of more complicated monitor masks which yield a long and narrow, meandering resistance path.[334] However, as the resistance path is made narrower, the definition of its width by means of an evaporation mask becomes less accurate. Slight variations in the mask-to-monitor–slide spacing produce varying degrees of vapor scattering and corresponding fluctuations in the pattern width.

A monitor configuration which allows four-terminal resistance measurements and thereby eliminates contact and lead-resistance contributions has been described by Glang, Holmwood, and Maissel.[137] As shown in Fig. 60, it consists of a round
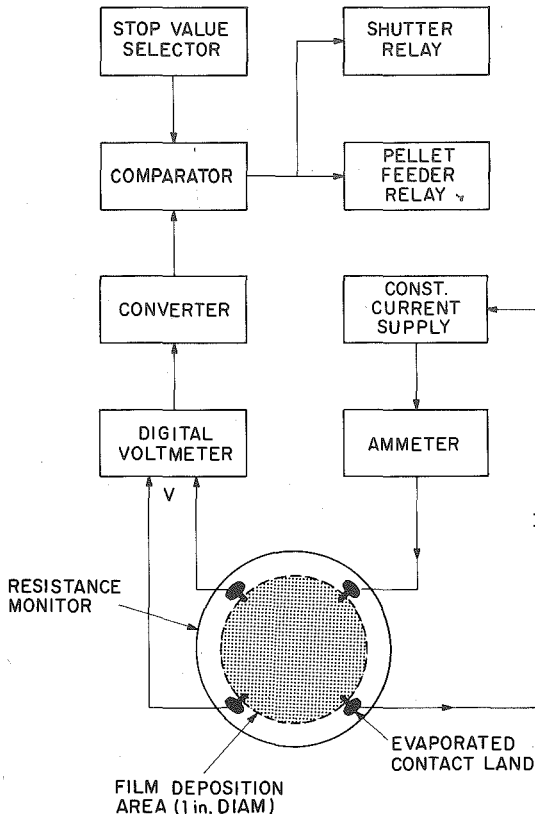
Fig. 60 Circular resistance monitor with four symmetrically located contacts, and block diagram of associated control circuit. (*After Glang, Holmwood, and Maissel.*[137])

substrate with four preevaporated metal lands. These are contacted by spring-loaded clips while the film-deposition area is defined by a mask with a circular opening. The contact lands extend narrow tips toward the center just far enough to touch the perimeter of the circular deposition area. Generally, peripheral four-point-probe resistance measurements on irregularly shaped objects require at least two different

current-voltage readings, as discussed by van der Pauw.[335]   However, because of the symmetry of this particular configuration, no cyclic switching of current and voltage terminals is necessary. If connected as shown in Fig. 60, the sheet resistance of the film is obtained from one measurement:

$$R_s = 4.53 \frac{V}{I}$$

Evaluation is further simplified by using a constant current of 4.53 mA which makes the voltage displayed by the DVM numerically identical to the sheet resistance.

In addition to being a four-terminal measurement, the technique has other advantages. It can be shown[335] that small variations in the diameter of the circular film area as caused by misregistration or variable spacing of the mask have only negligible effects on the indicated resistance value. The latter is also independent of the contact pressure applied to the lands. The technique is particularly suitable for the fabrication of integrated semiconductor circuits, an application where circular silicon wafers are the standard substrates and methods of surface insulation are readily available. Thus, the identity of regular and monitor substrates in regard to thermal conductivity, heat absorption, and surface temperature is assured. Automatic termination of the process is initiated by a comparator which receives its second input from the stop-value selector shown in Fig. 60.   The latter is a four-digit binary-coded decimal switch into which the desired termination value can be dialed.

One problem common to all resistance monitors is the danger of load damage at the beginning of a deposition, when electrical continuity between the preevaporated contacts is first established by an extremely thin film. Crittenden and Hoffman[336] introduced a technique whereby the substrate shutter remains closed while the monitor receives a certain amount of deposit. Thus, when the films on the substrates go through the critically thin stage, the condensate on the monitor is already beyond that thickness. However, their method is really a thickness-control technique which relies on the film resistivity being constant, and it does not lend itself to direct monitoring of the sheet resistance. In the flash evaporation of cermet films, the film-condensation rate is controlled fairly well by the evaporant feed rate. It is therefore possible to estimate the time required to establish a "safe" thickness of about 100 to 200 Å and delay the application of the monitor voltage accordingly.[137]   The circuit employed by Steckelmacher et al.[333] had provisions for varying the bridge voltage so that the power to be dissipated by the monitor never exceeded 50 mW.

The accuracy with which a preselected sheet-resistance value can be obtained is of the order of 1 to 2%.   The deposition stop value as represented by a preset reference resistor or binary-coded-decimal switch, and the sensitivity of the detection circuits permit, of course, a greater accuracy. In practice, these values are always slightly exceeded. If the terminating signal cuts off the source current,[337] evaporation continues at diminishing rates until the source has cooled.   The faster and more common technique is to trigger the substrate shutter, but because of its inertia the latter does not close at the same instant when the solenoid receives the actuating signal. With some experience, it is often possible to anticipate the degree of overshooting and compensate for it by slightly changing the setting of the stop-value selector.   However, freshly deposited films are likely to incur resistance changes during subsequent cooling, exposure to air, and the customary annealing processes. Hence, empirical control of the final sheet-resistance value may very well be established without considering the relatively small increment due to overshooting.

Since film resistor materials such as tantalum or Nichrome are often deposited by sputtering techniques, it is important to be aware of the fact that resistance monitors exposed to a glow discharge are subject to unpredictable fluctuations. Maissel et al.[338] found that true resistance indications ($\pm 1\%$) could be obtained only if the aspect ratio of the monitor was chosen to produce readings of less than 20 ohms.   In sputtering Nichrome, Stern[206] measured the ion current and relied essentially on constant sputtering yields to control the process. However, the system also had a built-in four-point probe which allowed in situ resistance measurements when the discharge was interrupted.

(3) Capacitance Monitors There have been few attempts to utilize capacitance measurements for evaporation monitoring. The main reason is that the most sensitive arrangement to measure the capacitance of a dielectric film would require the application of a top electrode to the growing film surface and therefore is unfeasible. The possibility of using a planar capacitor as a sensing element has been investigated by Keister and Scapple.[339] Their monitor consisted of a series of narrow parallel lines etched out of aluminum film and spaced 0.0075 in. apart on a quartz substrate. Alternate lines were connected in parallel so as to form the two electrodes of a capacitor. Upon application of an ac voltage, the displacement current spreads throughout the adjacent dielectric media. The quartz substrate alone yielded a capacitance of about 65 pF whereas the deposition of SiO added 1 to 1.5% capacitance per micron of film thickness. Thus, the technique is not very sensitive and is applicable only to relatively thick films. The error associated with thickness monitoring was between 2 and 4%. By relating the capacitance change to a change in voltage amplitude, deposition-rate measurements with an accuracy of about 4% were also made.

A monitor based on capacitance measurements in the evaporant vapor which indicates rates directly has been described by Riddle.[340] The sensing element was formed by two parallel plates, and the vacuum in between served as the dielectric. During evaporation, the vapor passing between the electrodes alters the dielectric constant and hence the capacitance. The device is reportedly capable of indicating rates from 0.1 to 100 Å s^{-1}. However, its merit would have to be judged against other and better-established vapor monitors such as ionization-rate meters, and it does not offer the advantage of monitoring a film property directly.

d. Evaporation-process Control

(1) Thickness Control Provisions for monitoring an evaporation process are usually combined with means to control film deposition. Frequently, the only requirement is to terminate the process when the film thickness or a thickness-related property has reached a certain value. The simplest way to do this is to evaporate a weighed amount of source material to completion. If the emission characteristic of the source is known, the film thickness to be expected from a given quantity of evaporant can be calculated by means of the equations and methods discussed in Sec. 5a. Nomographs for this purpose have also been published.[341] In practice, the technique requires empirical adjustment, and its utilization is limited to applications where thickness control is not critical. Greater accuracy and more positive control are offered by methods which employ a monitoring device.

As the discussion of monitors has shown, some of them give indications of the accumulated deposit thickness and are therefore directly applicable to determine when the process should be discontinued. Other devices are primarily rate indicators and require integration over the deposition time. For automatic thickness control, monitors which generate an electric signal are necessary. As shown in Table 17, most devices produce an electric output suitable for control purposes. With ionization-rate monitors, the signal must be integrated to obtain the film thickness, and circuits as well as instruments for electronic integration have been reported by Schwarz[280] and Brownell et al.[286] Process termination may be implemented by analog or digital techniques, depending on the nature of the signal and the preference of the investigator. In the former case, a recorder with an adjustable on-off control point is a convenient means for recognizing the stop value and triggering the closure of the substrate shutter. A digital control circuit is shown in Fig. 60 in conjunction with resistance monitoring.

The only devices which do not yield an electric signal are the particle-impingement monitors, and while the use of an electronic revolution counter has been suggested,[289] the idea has not been implemented as yet. Optical monitors require specialized circuitry to sense the occurrence and register the number of reflectivity maxima or minima.[318,319,330]

(2) Rate Control The control of evaporation rates is a more complex task than thickness control because it requires adjustment of the source temperature. The

TABLE 17 Evaporation Process Control

Control method	Electrical signal		Prerequisites for	
	Available	Related to	Thickness control	Rate control
Evaporation to completion.......	No	....	Weighed evaporant charge	Not applicable
Control of source temperature, power, or current.............	Yes	Evaporation rate	Rates must be integrated	Error-signal feedback
Ionization-rate monitor..........	Yes	Evaporation rate	Rates must be integrated	Error-signal feedback
Particle impingement devices....	No	....	Direct observation on pivoted models, manual stop	Direct observation on torsion-wire models, manual power adjustment
Microbalances.................	Electromagnetic or electrostatic models: yes	Deposit thickness	Strip-chart recorder, preset microswitch for automatic termination	Programmed weight increase, or second signal by electronic differentiation
Crystal oscillator...............	Yes	Deposit thickness	Counter, meter, or recorder; preset microswitch for automatic termination	Second signal by differentiation; servoloop
Optical monitors...............	With photocell: yes	Deposit thickness	Strip-chart recorder; fairly complex circuitry for automatic termination	Has not been implemented yet
Resistance monitors.............	Yes	Deposit thickness	Strip-chart recorder and preset microswitch, or digital techniques	Second signal by electronic differentiation; servoloop
Capacitance monitors...........	Yes	Deposit thickness[339] or rate[340]	Planar capacitor substrate; oscillator circuit with reference capacity and comparator[339]	Direct rate indication from Riddle's vapor capacitor[340]

simplest approach is to assume that the emission of a source remains constant through-out an evaporation if the power input does not vary and hence that the evaporant temperature does not change. This concept is applicable only if the effective source area does not vary as a result of slag formation, spreading, or contraction of the evaporant, and if there are no changes in the degree of heat transfer between the evaporant and its support. An example of rate control through a wattmeter is the radiation-heated source described by DaSilva[84] (see Fig. 18). The feasibility of this control principle has also been investigated by Bath and Steckelmacher,[342] who studied the constancy of evaporation rates produced by a resistance-heated molyb-denum boat. If the source was maintained at constant voltage, fluctuations of the molten evaporant (bismuth) caused resistance variations sufficiently severe to affect power input and rates. Although the rms current variations observed were relatively small, the exponential temperature dependence of the vapor pressure makes evapora-tion rates very sensitive to fluctuations of the source temperature. Stable rates were obtained, however, if the rms variations were used to generate an error signal which controlled the power supply and stabilized the current. The method worked satis-factorily for Bi, Cu, and MgF_2, provided relatively large charges of evaporant were employed and slag formation avoided.

One may expect to achieve the same or even better rate constancy by sensing the source temperature directly with a thermocouple and utilizing the latter to control the power supply. However, the conditions of constant evaporant surface area and heat transfer are often difficult to meet. During the evaporation of CdTe from a small effusion cell, for example, the maintenance of constant evaporation rates was accom-panied by a gradual rise of the source temperature.[76] Therefore, the control of evaporation rates is generally implemented by means of deposition-monitoring devices which, for this application, must yield an electric signal proportional to rates.

Referring back to Table 17, again, the only devices which provide rate signals directly are ionization-rate monitors and the capacitance vapor monitor described by Riddle.[340] With microbalances, crystal oscillators, and resistance monitors, it is necessary to differentiate the primary signal and derive a secondary signal proportional to the deposition rate. Control circuits incorporating electronic differentiation have been described for these three types of thickness monitors (see, for example, Cahn and Schultz[298] for microbalances; Behrndt and Love,[145] Bath,[343] and Bath, English, and Steckelmacher[344] for crystal oscillators; Turner, Birtwistle, and Hoffman[334] for resis-tance monitors). Rate control may also be achieved by programming the weight increase, a technique introduced by Hayes and Roberts.[292]

Whether the rate signal is primary or secondary with respect to the monitor, it must be compared with a stable reference signal to produce a differential output suit-able for controlling the source power. The latter function requires signal amplifica-tion. Continuous adjustment of the source power supply in response to the error signal received from the sensing device may be accomplished by means of saturable reactors or silicon-controlled rectifiers (SCRs or thyristors). The former have been used extensively in conjunction with ionization-rate monitors, and circuit diagrams have been given by various authors.[284,286,345] A servoloop control system employing crystal oscillators and saturable reactors has been described by Behrndt and Love.[145]

The use of SCRs for automatic evaporation-rate control is of more recent origin. Their mode of operation is discussed in Steckelmacher's review,[279] and a system for rate as well as thickness control utilizing a crystal oscillator as the sensing element has been described by Bath et al.[343,344] The latter article is of general interest because the system components are designed as individual modules which offer considerable flexibility in performing various evaporation-control functions. For instance, the drive signal may be derived from monitoring devices other than crystal oscillators. Furthermore, although the system was primarily intended for the control of resistance-heated sources, the control loop is sufficiently flexible to permit stable operation of other source types with different rate vs. power characteristics. The evaporation rates of electron-gun sources, for example, are commonly varied by altering the electron-emission current. Induction-heated vapor sources, too, are amenable to feedback control, although the higher cost and the space and safety requirements of

the generator and saturable reactor usually make other source types preferable. An induction-heated nickel-iron source which was servo-controlled from a resistance monitor has been described by Turner et al.[334]

Generally, the development of deposition-control equipment tends toward further automation to eliminate operator judgment and thereby increase the reproducibility of film properties. The objective is to perform the entire pump-down and deposition cycle by combining pressure and temperature sensors, rate monitors, and servomechanisms with adjustable electronic delay devices so that every step of the process is automatically initiated when certain conditions—pressures, temperatures, or evaporation rates—have been established. This trend is exemplified by the system described by English, Putner, and Holland.[346]

REFERENCES

1. Faraday, M., *Phil. Trans.*, **147**, 145 (1857).
2. Nahrwold, R., *Ann. Physik*, **31**, 467 (1887).
3. Kundt, A., *Ann. Physik*, **34**, 473 (1888).
4. See, for example, Guggenheim, E. A., "Thermodynamics. An Advanced Treatment for Chemists and Physicists," 4th ed., North Holland Publishing Company, Amsterdam, 1959.
5. Nesmeyanov, A. N., "Vapor Pressure of the Chemical Elements," Elsevier Publishing Company, New York, 1963.
6. Kubaschewski, O., and E. L. Evans, "Metallurgical Thermochemistry," Pergamon Press, New York, 1965.
7. See, for example, Lewis, G. N., and M. Randall, "Thermodynamics," 2d ed., p. 419, McGraw-Hill Book Company, New York, 1961.
8. See, for example, Darken, L. S., and R. W. Gurry, "Physical Chemistry of Metals," p. 233; McGraw-Hill Book Company, New York, 1953.
9. Rossini, F. D., "Selected Values of Thermodynamic Properties," *NBS Circular* 500, Government Printing Office, Washington, D.C., 1952.
10. Wagman, D. D., "Selected Values of Chemical Thermodynamic Properties," *NBS Technical Note* 270–1 (1965), 270-2 (1966), Government Printing Office, Washington, D.C.
11. Kelley, K. K., "High Temperature Heat Content, Heat Capacity, and Entropy Data for the Elements and Inorganic Compounds," *Bureau of Mines Bulletin* 584, Government Printing Office, Washington, D.C., 1960.
12. Kelley, K. K., and E. G. King, "Entropies of the Elements and Inorganic Compounds," *Bureau of Mines Bulletin* 592, Government Printing Office, Washington, D.C., 1961.
13. Stull, D. R., and G. C. Sinke, "Thermodynamic Properties of the Elements," Advances in Chemistry Series, no. 18, American Chemical Society, 1956.
14. Stull, D. R., "JANAF Thermochemical Data," The Dow Chemical Co., U.S. Clearinghouse, Springfield, Va., 1965/66.
15. Wicks, C. E., and F. E. Block, "Thermodynamic Properties of 65 Elements—Their Oxides, Halides, Carbides, and Nitrides," *Bureau of Mines Bulletin* 605, Government Printing Office, Washington, D.C., 1963.
16. Ulich, H., "Kurzes Lehrbuch der physikalischen Chemie," 5th ed., p. 100, Theodor Steinkopff Verlag, Leipzig, 1948.
17. Kelley, K. K., "The Free Energies of Vaporization and Vapor Pressures of Inorganic Substances," *Bureau of Mines Bulletin* 383, Government Printing Office, 1935.
18. Hohmann, E., and H. Bommer, *Z. Anorg. Allgem. Chem.*, **248**, 383 (1941).
19. Honig, R. E., *RCA Rev.*, **23**, 567 (1962).
20. Hultgren, R., R. L. Orr, P. D. Anderson, and K. K. Kelley, "Selected Values of Thermodynamic Properties of Metals and Alloys," John Wiley & Sons, Inc., New York, 1963.
21. Dushman, S., "Scientific Foundations of Vacuum Technique," John Wiley & Sons, Inc., New York, 1962.
22. See, for example, Kennard, E. H., "Kinetic Theory of Gases," McGraw-Hill Book Company, New York, 1938; or Ref. 23.
23. Parker, P., "Electronics," p. 935, Edward Arnold (Publishers) Ltd., London, 1955.
24. Chapman, S., and T. G. Cowling, "The Mathematical Theory of Non-uniform Gases," Cambridge University Press, New York, 1939.
25. Knudsen, M., *Ann. Physik*, **28**, 75, 999 (1909); **35**, 389 (1911).

26. Steckelmacher, W., *Vacuum*, **16**, 561 (1966).
27. Levenson, L. L., N. Milleron, and D. H. Davis, *Trans. 7th AVS Symp.*, 1960, p. 372, Pergamon Press, Oxford, England.
28. Hertz, H., *Ann. Physik*, **17**, 177 (1882).
29. Knudsen, M., *Ann. Physik*, **47**, 697 (1915).
30. Langmuir, I., *Physik. Z.*, **14**, 1273 (1913).
31. Knudsen, M., *Ann. Physik*, **29**, 179 (1909).
32. Knacke, O., and I. N. Stranski, *Progr. Metal Phys.*, **6**, 181 (1956).
33. Rutner, E., in E. Rutner, P. Goldfinger, and J. P. Hirth (eds.), "Condensation and Evaporation of Solids," p. 149, Gordon and Breach, Science Publishers, Inc., New York, 1964.
34. Freeman, R. D., and J. G. Edwards, Ref. 33, p. 127.
35. Hirth, J. P., and G. M. Pound, "Condensation and Evaporation, Nucleation and Growth Kinetics," The Macmillan Company, New York, 1963.
36. Winslow, G. H., Ref. 33, p. 29.
37. Dettorre, J. F., T. G. Knorr, and E. H. Hall, in C. F. Powell, J. H. Oxley, and J. M. Blocher, Jr. (eds.), "Vapor Deposition," p. 62, John Wiley & Sons, Inc., New York, 1966.
38. Polanyi, M., and E. Wigner, *Z. Physik. Chem.*, **139A**, 439 (1928).
39. Herzfeld, K. F., "Kinetische Theorie der Waerme," p. 229, vol. 3, pt. 2 of Mueller-Pouilletta, "Lehrbuch der Physik," F. Vieweg & Sons, Braunschweig, 1925.
40. Pelzer, H., in M. Volmer (ed.), "Kinetik der Phasenbildung," Theodor Steinkopff Verlag, Dresden (1939).
41. Neumann, K., *Z. Physik. Chem.*, **197A**, 16 (1950).
42. Penner, S. S., *J. Phys. Chem.*, **52**, 367, 949, 1262 (1948); **56**, 475 (1952); **65**, 702 (1961).
43. Glasstone, S., K. J. Laidler, and H. Eyring, "The Theory of Rate Processes," McGraw-Hill Book Company, New York, 1941.
44. Herzfeld, K. F., *J. Chem. Phys.*, **3**, 319 (1935).
45. Stearn, A. E., and H. Eyring, *J. Chem. Phys.*, **5**, 113 (1937).
46. Shultz, R. D., and A. O. Dekker, *J. Chem. Phys.*, **23**, 2133 (1955).
47. Mortensen, E. M., and H. Eyring, *J. Phys. Chem.*, **64**, 847 (1960).
48. Eyring, H., F. M. Wanlass, and E. M. Eyring, Ref. 33, p. 3.
49. Kossel, W., *Nachr. Ges. Wiss. Goettingen*, 1927, p. 135; *Ann. Physik*, **33**, 651 (1938).
50. Stranski, I. N., *Z. Physik. Chem.*, **136**, 259 (1928); **11B**, 421 (1931).
51. Knacke, O., and I. N. Stranski, *Ergeb. Exakt. Naturw.*, **26**, 383 (1952). For a review, see also Mayer, H., "Physik duenner Schichten," vol. II, p. 14, Wissenschaftliche Verlagsgesellschaft m.b.H., Stuttgart, 1955.
52. Hirth, J. P., and G. M. Pound, *J. Chem. Phys.*, **26**, 1216 (1957).
53. Sears, G. W., *J. Chem. Phys.*, **24**, 868 (1956); **27**, 1308 (1957).
54. Hirth, J. P., and G. M. Pound, Ref. 35, p. 138; see also Winterbottom, W. L., and J. P. Hirth, Ref. 33, p. 347.
55. Knudsen, M., *Ann. Physik*, **28**, 75, 999 (1909).
56. Mayer, H., *Z. Physik*, **52**, 235 (1929).
57. Knudsen, M., *Ann. Physik*, **52**, 105 (1917).
58. Heald, J. H., Jr., and R. F. Brown, *Ext. Abstr. 14th AVS Symp.*, 1967, p. 63, Herbick and Held Printing Co., Pittsburgh, Pa.
59. Holland, L., "Vacuum Deposition of Thin Films," John Wiley & Sons, Inc., New York, 1961.
60. Behrndt, K. H., in Bunshah, R. F. (ed.), "Techniques of Metals Research," vol. I, pt. 3, p. 1225, Interscience Publishers, Inc., New York, 1968.
61. Pirani, M., and J. Yarwood, "Principles of Vacuum Engineering," Reinhold Publishing Corporation, New York, 1961.
62. Rosenblatt, G. M., P. K. Lee, and M. B. Dowell, *J. Chem. Phys.*, **45**, 3454 (1966).
63. Yamdagni, R., and R. F. Porter, *J. Electrochem. Soc.*, **115**, 601 (1968).
64. Kohl, W. H., "Handbook of Materials and Techniques for Vacuum Devices," Reinhold Publishing Corporation, New York, 1967.
65. Olsen, L. O., C. S. Smith, and E. C. Crittenden, *J. Appl. Phys.*, **16**, 425 (1945).
66. Nicholson, J. L., *Rev. Sci. Instr.*, **34**, 118 (1963).
67. Lucas, M. S. P., C. R. Vail, W. C. Stewart, and H. A. Owen, *Trans. 8th AVS Symp.*, 1961, p. 988, The Macmillan Company, New York.
68. Massey, B. J., *Trans. 8th AVS Symp.*, 1961, p. 992; The Macmillan Company, New York.
69. Behrndt, K. H., *J. Appl. Phys.*, **33**, 193 (1962).
70. Kilgore, B. F., and R. W. Roberts, *Rev. Sci. Instr.*, **34**, 11 (1963).
71. Hale, A. P., *Vacuum*, **13**, 93 (1963).
72. Neugebauer, C. A., *J. Appl. Phys.*, **31**, 1525 (1960).

73. Layton, W. T., and H. E. Culver, *Proc. Electron. Components Conf.*, 1966, p. 225, Washington, D.C.
74. Hoffman, D. M., and J. Riseman, *Trans. 6th AVS Symp.*, 1959, p. 218, Pergamon Press, New York.
75. Roberts, G. C., and G. G. Via, U.S. Patent 3,313,914, 1967.
76. Glang, R., J. G. Kren, and W. J. Patrick, *J. Electrochem. Soc.*, **110**, 408 (1963).
77. Drumheller, C. E., *Trans. 7th AVS Symp.*, 1960, p. 306, Pergamon Press, New York.
78. Vergara, W. C., H. M. Greenhouse, and N. C. Nicholas, *Rev. Sci. Instr.*, **34**, 520 (1963); for instructions on how to make a baffled SiO source, see also De Tuerk, J. J., Jr., *J. Vacuum Sci. Technol.*, **5**, 88 (1968).
79. For binary phase diagrams, see Hansen, M., and K. Anderko, "Constitution of Binary Alloys," 2d ed., McGraw-Hill Book Company, New York, 1958; Elliott, R. P., "Constitution of Binary Alloys, First Supplement," McGraw-Hill Book Company, New York, 1965.
80. See, for example, "Guide to Scientific Instruments—1967/68," American Association for the Advancement of Science, New York.
81. Economos, G., and W. D. Kingery, *J. Am. Ceram. Soc.*, **36**, 403 (1953).
82. Johnson, P. D., *J. Am. Ceram. Soc.*, **33**, 168 (1950).
83. Kingery, W. D., *J. Am. Ceram. Soc.*, **36**, 362 (1953).
84. DaSilva, E. M., *Rev. Sci. Instr.*, **31**, 959 (1960).
85. Hauck, J. E., *Mater. Design Eng.*, no. 208, p. 85, July, 1963.
86. Hildenbrand, D. L., and W. F. Hall, Ref. 33, p. 399.
87. Ames, I., L. H. Kaplan, and P. A. Roland, *Rev. Sci. Instr.*, **37**, 1737 (1966).
88. Thompson, F. E., and J. F. Libsch, *SCP Solid State Technol.*, December, 1965, p. 50.
89. Picard, R. G., and J. E. Joy, *Electronics*, **24**, 126 (April, 1951).
90. Lewis, J. C., B. Redfern, and F. C. Cowlard, *Solid-State Electron.*, **6**, 251 (1963).
91. Rothwell, W. S., *J. Appl. Phys.*, **39**, 1840 (1968).
92. Moriya, Y., N. Okuma, and K. Sugiura, *Trans. 8th AVS Symp.*, 1961, vol. 2, p. 1055, The Macmillan Company, New York.
93. Wikel, V., *Solid State Technol.*, **11**, (2), 12 (1968).
94. Holland, L., *Vacuum*, **6**, 161 (1956).
95. Toombs, P. A. B., and A. J. Jeal, *J. Sci. Instr.*, **42**, 722 (1965).
96. Hemmer, F. J., and J. R. Piedmont, *Rev. Sci. Instr.*, **33**, 1355 (1962).
97. Holland, L., in "Thin Film Microelectronics," p. 143, John Wiley & Sons, Inc., New York, 1965.
98. Candidus, E. S., M. H. Hablanian, and H. A. Steinherz, *Trans. 6th AVS Symp.*, 1959, p. 185, Pergamon Press, New York.
99. Holland, L., British Patent 754,102, 1951.
100. Heavens, O. S., *J. Sci. Instr.*, **36**, 95 (1959).
101. Kelly, J. C., *J. Sci. Instr.*, **36**, 89 (1959).
102. Milleron, N., *Trans. 4th AVS Symp.*, 1957, p. 148, Pergamon Press, New York.
103. Unvala, B. A., and G. R. Booker, *Phil. Mag.*, **9**, 691 (1964).
104. Chopra, K. L., and M. R. Randlett, *Rev. Sci. Instr.*, **37**, 1421 (1966).
105. Berry, R. W., Proc. 3d Symp. on Electron Beam Technology, 1961, p. 359, Alloyd Electronics Corp., Cambridge, Mass.
106. Holmwood, R. A., and R. Glang, *J. Electrochem. Soc.*, **112**, 827 (1965).
107. Reichelt, W., and G. F. P. Mueller, *Trans. 8th AVS Symp.*, 1961, p. 956, Pergamon Press, New York.
108. Denton, R. A., and A. D. Greene, *Proc. 5th Electron Beam Symp.*, 1963, p. 180, Alloyd Electronics Corp., Cambridge, Mass.
109. Fowler, P., *J. Appl. Phys.*, **34**, 3538 (1963).
110. Gerstenberg, D., and P. M. Hall, *J. Electrochem. Soc.*, **111**, 936 (1964).
111. Thun, R. E., and J. B. Ramsey, *Trans. 6th AVS Symp.*, 1959, p. 192, Pergamon Press, New York.
112. Rairden, J. R., and C. A. Neugebauer, *Proc. IEEE*, **52**, 1234 (1964).
113. Brunner, W. F., and H. G. Patton, *Trans. 8th AVS Symp.*, 1961, p. 895, The Macmillan Company, New York.
114. Siddall, G., and B. A. Probyn, *Trans. 8th AVS Symp.*, 1961, p. 1017, Pergamon Press, New York.
115. Brice, J. C., and U. Pick, *J. Sci. Instr.*, **41**, 633 (1964).
116. Davey, J. E., R. J. Tiernan, T. Pankey, and M. D. Montgomery, *Solid-State Electron.*, **6**, 205 (1963).
117. Voigt, J. W., and K. W. Foster, *Rev. Sci. Instr.*, **35**, 1087 (1964).
118. Brownell, R. B., W. D. McLennan, R. L. Ramsey, and E. J. White, *Rev. Sci. Instr.*, **35**, 1147 (1964).

119. Reames, J. P., *Trans. 6th AVS Symp.*, 1959, p. 215, Pergamon Press, New York.
120. Maskalick, N. J., and C. W. Lewis, *Trans. 8th AVS Symp.*, 1961, vol. 2, p. 874, Pergamon Press, New York.
121. Blackburn, D. H., and W. Haller, *Rev. Sci. Instr.*, **36**, 901 (1965).
122. Erdman, K. L., D. Axen, J. R. McDonald, and L. P. Robertson, *Rev. Sci. Instr.*, **35**, 122 (1964).
123. Steckelmacher, W., and L. Holland, *Vacuum*, **2**, 346 (1952); see also Ref. 59.
124. von Hippel, A., *Ann. Physik*, **81**, 1043 (1926).
125. Holland, L., and W. Steckelmacher, *Vacuum*, **2**, 346 (1952).
126. Anastasio, T. A., and W. J. Slattery, *J. Vacuum Sci. Technol.*, **4**, 203 (1967).
127. Holland, L., and N. J. Newman, *Rev. Sci. Instr.*, **23**, 642 (1952).
128. Clausing, P., *Z. Physik*, **66**, 471 (1930).
129. Ruth, V., and J. P. Hirth, Ref. 33, p. 99.
130. Guenther, K. G., *Z. Angew. Phys.*, **9**, 550 (1957).
131. Learn, A. J., and R. S. Spriggs, *Rev. Sci. Instr.*, **34**, 179 (1963).
132. Ehrler, F., and Th. Kraus, *Trans. 3d Intern. Vacuum Congr.*, 1965, vol. 2, pp. 131, 135, Pergamon Press, New York.
133. Grimley, R. T., and J. LaRue, *Ext. Abstr. 14th AVS Symp.*, 1967, p. 59, Herbick and Held Printing Co., Pittsburgh, Pa.
134. Behrndt, K. H., and R. A. Jones, *Vacuum*, **11**, 129 (1961).
135. Spriggs, R. S., and A. J. Learn, *Rev. Sci. Instr.*, **37**, 1539 (1966).
136. Rohn, K., *Z. Physik*, **126**, 20 (1949).
137. Glang, R., R. A. Holmwood, and L. I. Maissel, *Thin Solid Films*, **1**, 151 (1967).
138. Beavitt, A. R., R. C. Turnell, and D. S. Campbell, *Thin Solid Films*, **1**, 3 (1967).
139. Behrndt, K. H., in G. Hass and R. E. Thun (eds.), "Physics of Thin Films," vol. 3, p. 1, Academic Press Inc., New York, 1966.
140. Oberg, P. E., R. M. Sander, and E. J. Torok, *Vacuum*, **13**, 53 (1963).
141. Bugenis, C., and L. E. Preuss, *Trans. 10th AVS Symp.*, 1963, p. 374, The Macmillan Company, New York.
142. Behrndt, K. H., and R. A. Jones, *Trans. 5th AVS Symp.*, 1958, p. 217, Pergamon Press, New York.
143. Behrndt, K. H., *Trans. 6th AVS Symp.*, 1959, p. 242, Pergamon Press, New York.
144. Behrndt, K. H., *Trans. 7th AVS Symp.*, 1960, p. 137, Pergamon Press, New York.
145. Behrndt, K. H., and R. W. Love, *Vacuum*, **12** (1962).
146. Behrndt, K. H., *Trans. 9th AVS Symp.*, 1962, p. 111, The Macmillan Company, New York.
147. Hass, G., and E. Ritter, *J. Vacuum Sci. Technol.*, **4**, 71 (1967).
148. Fisher, R. A., and J. R. Platt, *Rev. Sci. Instr.*, **8**, 505 (1937).
149. Behrndt, K. H., *Trans. 10th AVS Symp.*, 1963, p. 379, The Macmillan Company, New York.
150. Behrndt, K. H., and D. W. Doughty, *J. Vacuum Sci. Technol.*, **3**, 264 (1966).
151. Drowart, J., Ref. 33, p. 255.
152. Reichelt, W., and P. Mueller, *Vakuum-Tech.*, 1962, no. 8.
153. Holland, L., Ref. 59, p. 464.
154. Kubaschewski, O., and E. L. Evans, Ref. 6, p. 326.
155. Blackburn, P. E., M. Hoch, and H. L. Johnston, *J. Phys. Chem.*, **62**, 769 (1958).
156. Schaefer, H., and R. Hoernle, *Z. Anorg. Allgem. Chem.*, **263**, 26 (1950).
157. Tombs, N. C., and A. J. E. Welch, *J. Iron Steel Inst.*, **172**, 69 (1952).
158. Hacman, D., W. K. Huber, and G. Rettinghaus, *Ext. Abstr. 14th AVS Symp.*, 1967, p. 27, Herbick and Held Printing Co., Pittsburgh, Pa.
159. Simons, E. L., Ref. 21, p. 760.
160. Woesten, W. J., and M. G. Geers, *J. Phys. Chem.*, **66**, 1252 (1962).
161. Neuhaus, A., and W. Retting, *Z. Elektrochem.*, **62**, 33 (1958).
162. Woesten, W. J., *J. Phys. Chem.*, **65**, 1949 (1961).
163. Burmeister, R. A., Jr., and D. A. Stevenson, *J. Electrochem. Soc.*, **114**, 394 (1967).
164. de Nobel, D., *Philips Res. Rept.*, **14**, 361, 430 (1959).
165. Schoolar, R. B., and J. N. Zemel, *J. Appl. Phys.*, **35**, 1849 (1964).
166. Efstathion, A., D. M. Hoffman, and E. R. Levin, *Ext. Abstr. 13th AVS Symp.*, 1966, p. 143, Herbick and Held Printing Co., Pittsburgh, Pa.
167. Vecht, A., in G. Hass and R. E. Thun (eds.), "Physics of Thin Films," vol. 3, p. 165, Academic Press Inc., New York, 1966.
168. Hamilton, P. M., *SCP Solid State Technol.*, June, 1964, p. 15.
169. Reichelt, W., *Proc. 3d Intern. Vacuum Congr.*, 1965, vol. 2, p. 25, Pergamon Press, New York.
170. Colin, R., and P. Goldfinger, Ref. 33, p. 165.

171. Somorjai, G. A., Ref. 33, p. 417.
172. Goswami, A., and S. S. Koli, in R. Niedermayer and H. Mayer (eds.), "Basic Problems in Thin Film Physics," p. 646, Vandenhoeck and Ruprecht, Goettingen, 1966.
173. Cariou, F. E., V. A. Cajal, and M. M. Gajary, *Proc. 1967 Electron. Components Conf.*, p. 60.
174. Cox, J. T., G. Hass, and J. B. Ramsey, *J. Phys. (Paris)*, **25**, 250 (1964).
175. Reichelt, W., *Vide*, no. 106, p. 390, 1963.
176. Pliskin, W. A., and P. P. Castrucci, *Electrochem. Technol.*, **6**, 85 (1968).
177. Eisele, K. M., Ref. 171, p. 672.
178. Stull, D. R., *Ind. Eng. Chem.*, **39**, 540 (1947). The tables may also be found in the "Handbook of Chemistry and Physics," 47th ed., p. D-109, The Chemical Rubber Co., Cleveland, Ohio, 1966.
179. Darken, L. S., and R. W. Gurry, "Physical Chemistry of Metals," p. 342, McGraw-Hill Book Company, New York, 1953.
180. Quill, L. L. (ed.), "The Chemistry and Metallurgy of Miscellaneous Materials," McGraw-Hill Book Company, New York, 1950.
181. Rickert, H., Ref. 33, p. 201.
182. Knauff, K. G., Ref. 172, p. 207.
183. Lyon, T. F., Ref. 33, p. 435.
184. Weiser, K., in R. K. Willardson and H. L. Goering (eds.), "Compound Semiconductors," vol. 1, "Preparation of III-V Compounds," p. 471, Reinhold Publishing Corporation, New York, 1962.
185. Lee, P. K., and R. C. Schoonmaker, Ref. 33, p. 379.
186. Paparoditis, C., Ref. 183, p. 326.
187. Dale, E. B., G. Senecal, and D. Huebner, *Trans. 10th AVS Symp.*, 1963, p. 348, The Macmillan Company, New York.
188. Zinsmeister, G., *Vakuum-Tech.*, no. 8, p. 223, 1964.
189. Sommer, A. H., *J. Appl. Phys.*, **37**, 2789 (1966).
190. Lowe, R. M., *J. Appl. Phys.*, **39**, 2476 (1968).
191. See, for example, Kortuem, G., "Treatise on Electrochemistry," 2d ed., p. 54, Elsevier Publishing Company, New York, 1965.
192. Hultgren, R., R. L. Orr, P. D. Anderson, and K. K. Kelley, "Selected Values of Thermodynamic Properties of Metals and Alloys," John Wiley & Sons, Inc., New York, 1963.
193. Zellars, G. R., S. L. Payne, J. P. Morris, and R. L. Kipp, *Trans. Met. Soc. AIME*, **215**, 181 (1959).
194. Koller, L. R., Ref. 21, p. 691.
195. Huijer, P., W. T. Langendam, and J. A. Lely, *Philips Tech. Rev.*, **24**, 144 (1963).
196. An example of this technique is described in the leaflet BRL-No. 67-6, issued by the Bendix Research Laboratories, Southfield, Mich.
197. Finegan, J. J., and P. R. Gould, *Trans. 9th AVS Symp.*, 1962, p. 129, The Macmillan Company, New York.
198. Degenhart, H. J., and I. H. Pratt, *Trans. 10th AVS Symp.*, 1963, p. 480, The Macmillan Company, New York.
199. Swift, R. A., B. A. Noval, and K. M. Merz, *J. Vacuum Sci. Technol.*, **5**, 79 (1968).
200. Campbell, D. S., and B. Hendry, *Brit. J. Appl. Phys.*, **16**, 1719 (1965).
201. Blois, M. S., *J. Appl. Phys.*, **26**, 975 (1955).
202. Penn, T. C., and F. G. West, *J. Appl. Phys.*, **38**, 2060 (1967).
203. Lakshmanan, K., *Trans. 8th AVS Symp.*, 1961, vol. 2, p. 868, The Macmillan Company, New York.
204. Lewis, C. W., and M. Schick, Ref. 33, p. 699.
205. Wied, O., and M. Tierman, *Proc. 3d Ann. Microelectron. Symp.*, St. Louis, 1964, p. 1-C-1.
206. Stern, E., *Proc. Electron. Components Conf.*, 1966, p. 233.
207. Riddle, G. C., *Ext. Abstr. 13th AVS Symp.*, 1966, p. 89, Herbick and Held Printing Co., Pittsburgh, Pa.
208. Sauer, E., and E. Unger, *Z. Naturforsch.*, **13a**, 72 (1958).
209. For a review of residual gas effects on thin film properties, see Caswell, H. L., in G. Hass (ed.), "Physics of Thin Films," vol. 1, p. 1, Academic Press Inc., New York, 1963.
210. Clapham, P. B., *J. Sci. Instr.*, **39**, 596 (1962).
211. Wolter, A. R., *J. Appl. Phys.*, **36**, 2377 (1965).
212. Schwartz, H. J., *J. Appl. Phys.*, **34**, 2053 (1963).
213. Lu, Chih-Shun, and A. A. Milgram, *J. Vacuum Sci. Technol.*, **4**, 49 (1967).

214. Roberts, R. W., and T. A. Vanderslice, "Ultrahigh Vacuum and Its Applications," p. 167, Prentice-Hall, Inc., Englewood Cliffs, N.J., 1963.
215. Gibson, R., B. Bergsnov-Hansen, N. Endow, and R. A. Pasternak, *Trans. 10th AVS Symp.*, 1963, p. 88, The Macmillan Company, New York.
216. Hansen, N., and W. Littman, *Trans. 3d Intern. Vacuum Congr.*, 1965, vol. 2, p. 465, Pergamon Press, New York.
217. Singleton, J. H., *Trans. 3d Intern. Vacuum Congr.*, 1965, vol. 2, p. 441, Pergamon Press, New York.
218. Ritter, E., *Monatsh. Chem.*, **95**, 795 (1964).
219. Ritter, E., *J. Vacuum Sci. Technol.*, **3**, 225 (1966).
220. Anastasio, T. A., *J. Appl. Phys.*, **38**, 2606 (1967).
221. Feuersanger, A. E., A. K. Hagenlocher, and A. L. Solomon, *J. Electrochem. Soc.*, **111**, 1387 (1964).
222. Krikorian, E., *Ext. Abstr. 13th AVS Symp.*, 1966, p. 175, Herbick and Held Printing Co., Pittsburgh, Pa.
223. Schilling, R. B., *Proc. IEEE*, **52**, 1350 (1964).
224. Novice, M. A., J. A. Bennett, and K. B. Cross, *J. Vacuum Sci. Technol.*, **1**, 73 (1964).
225. Frank, R. I., and W. L. Moberg, *J. Vacuum Sci. Technol.*, **4**, 133 (1967).
226. Holland, L., Ref. 59, p. 476.
227. Herring, C. S., and A. D. Tevebaugh, *J. Electrochem. Soc.*, **110**, 119 (1963).
228. Cremer, E., and H. Pulker, *Monatsh. Chem.*, **93**, 491 (1962).
229. Ritter, E., *Opt. Acta*, **9**, 197 (1962).
230. Pizzarello, F. A., *J. Appl. Phys.*, **35**, 2730 (1964).
231. Itoh, A., *Proc. 4th Intern. Vacuum Congr.*, 1968, pt. 2, p. 536, The Institute of Physics and the Physical Society, London.
232. Miller, R. J., and C. H. Bachman, *J. Appl. Phys.*, **29**, 1277 (1958).
233. Bis, R. F., A. S. Rodolakis, and J. N. Zemel, *Rev. Sci. Instr.*, **36**, 1626 (1965).
234. Johnson, J. E., *J. Appl. Phys.*, **36**, 3193 (1965).
235. Potter, R. F., *Ext. Abstr. 13th AVS Symp.*, 1966, p. 81, Herbick and Held Printing Co., Pittsburgh, Pa.
236. Frankl, D. R., A. Hagenlocher, E. D. Haffner, P. H. Heck, A. Sandor, E. Both, and H. J. Degenhart, *Proc. Electron. Components Conf.*, 1962, p. 44.
237. Edgecumbe, J., L. G. Rosner, and D. E. Anderson, *J. Appl. Phys.*, **35**, 2198 (1964).
238. Behrndt, K. H., *J. Metals*, **14**, 208 (1962).
239. Glang, R., R. A. Holmwood, and S. R. Herd, *J. Vacuum Sci. Technol.*, **4**, 163 (1967).
240. Mader, S., *J. Vacuum Sci. Technol.*, **2**, 35 (1965).
241. Sachtler, W. M. H., G. J. H. Dorgelo, and R. Jongepier, Ref. 171, p. 218.
242. Belser, R. B., *J. Appl. Phys.*, **31**, 562 (1960).
243. Neugebauer, C. A., *J. Appl. Phys.*, **35**, 3599 (1964).
244. Campbell, D. S., and H. Blackburn, *Trans. 7th AVS Symp.*, 1960, p. 313, Pergamon Press, New York.
245. Beckerman, M., and R. E. Thun, *Trans. 8th AVS Symp.*, 1961, p. 905, Pergamon Press, New York.
246. Ostrander, W. J., and C. W. Lewis, *Trans. 8th AVS Symp.*, 1961, p. 881, Pergamon Press, New York.
247. Guenther, K. G., *Z. Naturforsch.*, **13a**, 1081 (1958).
248. Guenther, K. G., in J. C. Anderson (ed.), "The Use of Thin Films in Physical Investigations," p. 213, Academic Press Inc., New York, 1966.
249. Haenlein, E., and K. G. Guenther, *Naturwiss.*, **46**, 319 (1959).
250. Schottmiller, J. C., F. Ryan, and T. Taylor, *Ext. Abstr. 14th AVS Symp.*, 1967, p. 29, Herbick and Held Printing Co., Pittsburgh, Pa.
251. Steinberg, R. F., and D. M. Scruggs, *J. Appl. Phys.*, **37**, 4586 (1966); see also Steinberg, R. F., *Ext. Abstr. 13th AVS Symp.*, 1966, p. 171, Herbick and Held Printing Co., Pittsburgh, Pa.
252. Davey, J. E., and T. Pankey, *J. Appl. Phys.*, **39**, 1941 (1968); see also Ref. 253.
253. Houde, A. L., in K. H. Behrndt (ed.), "Vacuum Microbalance Techniques," vol. 3, p. 109, Plenum Press, New York, 1963.
254. Young, A. S., and R. J. Heritage, *Proc. 4th Intern. Vacuum Congr.*, 1968, pt. 2, p. 496, The Institute of Physics and the Physical Society, London.
255. Harris, L., and B. M. Siegel, *J. Appl. Phys.*, **19**, 739 (1948).
256. Beam, W. R., and T. Takahashi, *Rev. Sci. Instr.*, **35**, 1623 (1964).
257. Tandeski, D. A., M. M. Hanson, and P. E. Oberg, *Vacuum*, **14**, 3 (1964).
258. Marshall, R., L. Atlas, and T. Putner, *J. Sci. Instr.*, **43**, 144 (1966).
259. Androes, G. M., R. H. Hammond, and W. D. Knight, *Rev. Sci. Instr.*, **32**, 251 (1961).
260. Feldtkeller, E., *Z. Physik*, **157**, 65 (1959).

261. Beckerman, M., and R. L. Bullard, *Proc. Electron. Components Conf.*, 1962, p. 53.
262. Braun, L., and D. E. Lood, *Proc. IEEE*, **54**, 1521 (1966).
263. Layer, E. H., *Trans. 6th AVS Symp.*, 1959, p. 210, Pergamon Press, New York.
264. Wilson, R. W., and L. E. Terry, *Proc. Electron. Components Conf.*, 1967, p. 397.
265. Richards, J. L., P. B. Hart, and L. M. Gallone, *J. Appl. Phys.*, **34**, 3418 (1963).
266. Richards, J. L., Ref. 248, p. 71.
267. Mueller, E. K., *J. Appl. Phys.*, **35**, 580 (1964).
268. Zyetz, M. C., and A. M. Despres, *Ext. Abstr. 13th AVS Symp.*, 1966, p. 169, Herbick and Held Printing Co., Pittsburgh, Pa.
269. Light, T. B., E. M. Hull, and R. Gereth, *J. Electrochem. Soc.*, **115**, 857 (1968).
270. Holloway, H., J. L. Richards, L. C. Bobb, and J. Perry, Jr., *J. Appl. Phys.*, **37**, 4694 (1966).
271. Ellis, S. G., *J. Appl. Phys.*, **38**, 2906 (1967).
272. Mueller, E. K., B. J. Nicholson, and M. H. Francombe, *Electrochem. Technol.*, **1**, 158 (1963).
273. Brown, V. R., *Ext. Abstr. 13th AVS Symp.*, 1966, p. 139, Herbick and Held Printing Co., Pittsburgh, Pa.
274. Mueller, E. K., B. J. Nicholson, and G. L. E. Turner, *J. Electrochem. Soc.*, **110**, 969 (1963).
275. Himes, W., B. F. Stout, and R. E. Thun, *Trans. 9th AVS Symp.*, 1962, p. 144, The Macmillan Company, New York.
276. Carter, E. E., *Rev. Sci. Instr.*, **34**, 588 (1963).
277. Eckardt, J. R., and R. N. Peacock, *J. Vacuum Sci. Technol.*, **3**, 356 (1966).
278. Mueller, E. K., and J. L. Richards, *J. Appl. Phys.*, **35**, 1233 (1964).
279. Steckelmacher, W., in L. Holland (ed.), "Thin Film Microelectronics," p. 193, John Wiley & Sons, Inc., New York, 1965.
280. Schwarz, H., *Rev. Sci. Instr.*, **32**, 194 (1961).
281. Schwarz, H., *Arch. Tech. Messen*, **5**, 1341 (1960).
282. Dufour, C., and B. Zega, *Vide*, no. 104, p. 180, 1963.
283. Haase, O., *Z. Naturforsch.*, **12a**, 941 (1957).
284. Giedd, G. R., and M. H. Perkins, *Rev. Sci. Instr.*, **31**, 773 (1960).
285. Perkins, M. H., *Trans. 8th AVS Symp.*, 1961, p. 1025, Pergamon Press, New York.
286. Brownell, R. B., W. D. McLennan, R. L. Ramey, and E. J. White, *Rev. Sci. Instr.*, **35**, 1147 (1964).
287. Hammond, R. H., G. M. Kelly, C. H. Meyer, Jr., and J. H. Perene, Jr., "Vacuum Deposition of Refractory Thin Films and Thin Film Compounds," distributed by General Dynamics, San Diego, Calif.
288. Zega, B., *Proc. 4th Intern. Vacuum Congr.*, 1968, pt. 2, p. 523, The Institute of Physics and the Physical Society, London.
289. Beavitt, A. R., *J. Sci. Instr.*, **43**, 182 (1966).
290. Poulis, J. A., P. J. Meeusen, W. Dekker, and J. P. de Mey, in "Vacuum Microbalance Techniques," vol. 6, p. 27, Plenum Press, New York, 1967.
291. Behrndt, K. H., *Z. Angew. Phys.*, **8**, 453 (1956).
292. Hayes, R. E., and A. R. V. Roberts, *J. Sci. Instr.*, **39**, 428 (1962).
293. Gulbransen, E. A., *Rev. Sci. Instr.*, **15**, 201 (1944).
294. Wolsky, S. P., *Phys. Rev.*, **108**, 1131 (1957).
295. Wolsky, S. P., and E. J. Zdanuk, in "Vacuum Microbalance Techniques," vol. 1, p. 35, Plenum Press, New York, 1961.
296. Mayer, H., W. Schroen, and D. Stuenkel, *Trans. 7th AVS Symp.*, 1960, p. 279, Pergamon Press, New York.
297. Mayer, H., R. Niedermayer, W. Schroen, D. Stuenkel, and H. Goehre, in "Vacuum Microbalance Techniques," vol. 3, p. 75, Plenum Press, New York, 1963.
298. Cahn, L., and H. R. Schultz, in "Vacuum Microbalance Techniques," vol. 3, p. 29, Plenum Press, New York, 1963.
299. Gast, Th., *Vakuum-Tech.*, **14**, 41 (1965).
300. Gast, Th., in "Vacuum Microbalance Techniques," vol. 6, p. 59, Plenum Press, New York, 1967.
301. Pearson, S., and N. J. Wadsworth, *J. Sci. Instr.*, **42**, 150 (1965).
302. Wolsky, S. P., E. J. Zdanuk, C. H. Massen, and J. A. Poulis, in "Vacuum Microbalance Techniques," vol. 6, p. 37, Plenum Press, New York, 1967.
303. Sauerbrey, G., *Phys. Verhandl.*, **8**, 113 (1957).
304. Sauerbrey, G., *Z. Physik*, **155**, 206 (1959).
305. Lostis, M. P., *J. Phys. Radium*, **20**, 25 (1959).
306. Phelps, F. P., *Proc. 11th Ann. Symp. Frequency Control*, 1957, p. 256, Fort Monmouth, N.J.

307. Stockbridge, C. D., in "Vacuum Microbalance Techniques," vol. 5, p. 193, Plenum Press, New York, 1966.
308. Eschbach, H. L., and E. W. Kruidhof, in "Vacuum Microbalance Techniques," vol. 5, p. 207; Plenum Press, New York, 1966.
309. Niedermayer, R., N. Gladkich, and D. Hillecke, in "Vacuum Microbalance Techniques," vol. 5, p. 217, Plenum Press, New York, 1966.
310. Pulker, H. K., *Z. Angew. Phys.*, **20**, 537 (1966).
311. Pulker, H. K., and W. Schaedler, *Ext. Abstr. 14th AVS Symp.*, 1967, p. 79, Herbick and Held Printing Co., Pittsburgh, Pa.
312. Langer, A., and J. T. Patton, in "Vacuum Microbalance Techniques," vol. 5, p. 231, Plenum Press, New York, 1966.
313. Stockbridge, C. D., in "Vacuum Microbalance Techniques," vol. 5, p. 147, Plenum Press, New York, 1966.
314. Bakos, J., G. Nagy, and J. Szigeti, *J. Appl. Phys.*, **37**, 4433 (1966).
315. Hillecke, D., and R. Niedermayer, *Vakuum-Tech.*, **3**, 69 (1965).
316. Warner, A. W., and C. D. Stockbridge, in "Vacuum Microbalance Techniques," vol. 3, p. 55, Plenum Press, New York, 1963.
317. Riegert, R. P., *Proc. 4th Intern. Vacuum Congr.*, 1968, pt. 2, p. 527, The Institute of Physics and the Physical Society, London.
318. Steckelmacher, W., J. M. Parisot, L. Holland, and T. Putner, *Vacuum*, **9**, 171 (1959).
319. Steckelmacher, W., and J. English, *Trans. 8th AVS Symp.*, 1961, p. 852, Pergamon Press, New York.
320. Ross, A., *Vakuum-Tech.*, **8**, 1 (1959).
321. Schaible, P. M., and C. L. Standley, *IBM Tech. Disclosure Bull.* 6, no. 1, p. 112, 1963.
322. Description and recorder trace courtesy of J. S. Logan and E. S. Ward, IBM Corp., East Fishkill Facility, Hopewell Junction, N.Y.
323. Davidse, P. D., and L. I. Maissel, *Trans. 3d Intern. Vacuum Congr.*, 1965, vol. 2, p. 651, Pergamon Press, New York; Davidse, P. D., and L. I. Maissel, *J. Appl. Phys.*, **37**, 574 (1966).
324. Boss, D. W., W. A. Pliskin, and M. Revitz, *IBM Tech. Disclosure Bull.* 9, no. 10, p. 1389, 1967.
325. Pliskin, W. A., and R. A. Wesson, *IBM J. Res. Develop.*, **12**, 192 (1968).
326. Wesson, R. A., H. W. Young, and W. A. Pliskin, *Appl. Phys. Letters*, **11**, 105 (1967).
327. Wesson, R. A., R. P. Phillips, and W. A. Pliskin, *J. Appl. Phys.*, **38**, 2455 (1967).
328. Pliskin, W. A., *Solid-State Electron.*, **11**, 957 (1968).
329. Zerbst, H., *Vakuum-Tech.*, **12**, 173 (1963).
330. Fury, A. M., and C. L. Smith, U.S. Patent 3,059,611, 1962.
331. Dumin, D. J., *Rev. Sci. Instr.*, **38**, 1107 (1967).
332. Bennett, J. A., and T. P. Flanagan, *J. Sci. Instr.*, **37**, 143 (1960).
333. Steckelmacher, W., J. English, H. H. A. Bath, D. Haynes, J. T. Holden, and L. Holland, *Trans. 10th AVS Symp.*, 1963, p. 415, The Macmillan Company, New York.
334. Turner, J. A., J. K. Birtwistle, and R. G. Hoffman, *J. Sci. Instr.*, **40**, 557 (1963).
335. van der Pauw, L. J., *Philips Res. Rept.*, **13**, 1 (1958).
336. Crittenden, E. C., and R. W. Hoffman, *Rev. Mod. Phys.*, **25**, 310 (1953).
337. Bishop, F. W., *Rev. Sci. Instr.*, **20**, 527 (1949).
338. Maissel, L. I., R. J. Hecht, and N. W. Silcox, *Proc. Electron. Components Conf.*, 1963, p. 190.
339. Keister, F. Z., and R. Y. Scapple, *Trans. 9th AVS Symp.*, 1962, p. 116, The Macmillan Company, New York.
340. Riddle, G. C., *Proc. 4th Symp. Electron Beam Technol.*, 1962, p. 340, Alloyd Electronics Corp., Cambridge, Mass.
341. Bond, W. L., *J. Opt. Soc. Am.*, **44**, 429 (1954).
342. Bath, H. H. A., and W. Steckelmacher, *J. Sci. Instr.*, **42**, 144 (1965).
343. Bath, H. H. A., *J. Sci. Instr.*, **43**, 374 (1966).
344. Bath, H. H. A., J. English, and W. Steckelmacher, *Electron. Components*, **7**, 239 (1966).
345. Yaffe, T. H., W. C. Vergara, and H. M. Greenhouse, U.S. Patent 3,316,386, 1967.
346. English, J., T. Putner, and L. Holland, *Proc. 4th Intern. Vacuum Congr.*, 1968, pt. 2, p. 491, The Institute of Physics and the Physical Society, London.